The University of Memphis

A New Spectrum Matching-Response Spectrum in Central United States

Submitted To:

Tennessee Department of Transportation
Research Development and Technology Program

by

Shahram Pezeshk, Ph.D., P.E.
and
Farhad Sedaghati, Ph.D.

Department of Civil Engineering
The University of Memphis
spezeshk@memphis.edu

Behrooz Tavakoli, Ph.D.
Sr. Engineering Seismologist/Geologist
Bechtel Corporation

Technical Report Documentation Page

1. Report No. RES2016-24	2. Government Accession No.	3. Recipient's Catalog No.
4. Title and Subtitle A New Spectrum Matching-Response Spectrum in Central United States		5. Report Date September 19, 2018
		6. Performing Organization Code
7. Author(s) Shahram Pezeshk, Farhad Sedaghati, and Behrooz Tavakoli		8. Performing Organization Report No.
9. Performing Organization Name and Address The University of Memphis Department of Civil Engineering Memphis, TN 38152		10. Work Unit No. (TRAIS)
		11. Contract or Grant No. RES2016-24
12. Sponsoring Agency Name and Address Tennessee Department of Transportation Long Range Planning Division Suite 900, James K. Polk Building Nashville, TN 37243-0334		13. Type of Report and Period Covered
		14. Sponsoring Agency Code
15. Supplementary Notes		

16. Abstract

Central and eastern North America (CENA) is considered to be a moderately active region, but it suffers from a lack of recorded earthquakes in the magnitude-distance range of engineering interest. In this report, region-specific synthetic strong ground motion time histories are generated using a new and improved stochastic summation of Green's functions method (SSGFM) for CENA. In addition, the synthetics are used to develop ground motion prediction equations (GMPEs) for this region.For simulating large earthquakes, considering the effects of finite-fault rupture such as rupture propagation, asperities, and fault-site geometry (saturation effect) are significant and influential. The SSGFM is a straightforward approach in which the effect of rupture propagation is stochastically considered by summation over many lagged small earthquakes, without requiring any detailed information about the rupture process such as rise time, slip distribution, rupture speed, and dimensions of the fault. The summation procedure is defined to match the spectrum of the target event satisfying the scaling law of the source spectra. The effect of asperities on waveforms is brought into play by using a two-stage summation scheme through simulations. Since the concept of the source in the SSGFM developed in this report is point source, the distance defined in its framework is the distance between the site and an equivalent point source, called effective distance, in which the impact of the propagation path on seismic waves radiated from different parts of the fault is considered. However, motions come from different parts of the fault rupture in the extended source model, not a single point. This research will improve the SSGFM to convert the effective distance to the Joyner-Boore distance, which is one the most-used distance metrics in the engineering and seismology fields, for a given fault size within a region with given geometrical spreading and attenuation functions. Further, this research will improve the summation scheme of the SSGFM to define the source spectrum of large earthquakes with double-corner frequency models.

17. Key Words		18. Distribution Statement	
19. Security Classif. (of this report) Unclassified	20. Security Classif. (of this page) Unclassified	21. No. of Pages	22. Price

Form DOT F 1700.7 (8-72)   **Reproduction of completed page authorized**

DISCLAIMER

This research was funded through the State Research and Planning (SPR) Program by the Tennessee Department of Transportation and the Federal Highway Administration under Research Project Title: "Hernando Desoto I-40 Bridge Seismic Instrumentation Upgrade," RES# RES2016-26.

This document is disseminated under the sponsorship of the Tennessee Department of Transportation and the United States Department of Transportation in the interest of information exchange. The State of Tennessee and the United States Government assume no liability of its contents or use thereof.

The contents of this report reflect the views of the author(s) who are solely responsible for the facts and accuracy of the material presented. The contents do not necessarily reflect the official views of the Tennessee Department of Transportation or the United States Department of Transportation.

Executive Summary

Central and eastern North America (CENA) is considered to be a moderately active region, but it suffers from a lack of recorded earthquakes in the magnitude-distance range of engineering interest. In this report, region-specific synthetic strong ground motion time histories are generated using a new and improved stochastic summation of Green's functions method (SSGFM) for CENA. In addition, the synthetics are used to develop ground motion prediction equations (GMPEs) for this region.

For simulating large earthquakes, considering the effects of finite-fault rupture such as rupture propagation, asperities, and fault-site geometry (saturation effect) are significant and influential. The SSGFM is a straightforward approach in which the effect of rupture propagation is stochastically considered by summation over many lagged small earthquakes, without requiring any detailed information about the rupture process such as rise time, slip distribution, rupture speed, and dimensions of the fault. The summation procedure is defined to match the spectrum of the target event satisfying the scaling law of the source spectra. The effect of asperities on waveforms is brought into play by using a two-stage summation scheme through simulations. Since the concept of the source in the SSGFM developed in this report is point source, the distance defined in its framework is the distance between the site and an equivalent point source, called effective distance, in which the impact of the propagation path on seismic waves radiated from different parts of the fault is considered. However, motions come from different parts of the fault rupture in the extended source model, not a single point.

This research will improve the SSGFM to convert the effective distance to the Joyner-Boore distance, which is one the most-used distance metrics in the engineering and seismology fields, for a given fault size within a region with given geometrical spreading and attenuation functions. Further, this research will improve the summation scheme of the SSGFM to define the source spectrum of large earthquakes with double-corner frequency models.

Table of Contents

List of Figures

List of Tables

1. Introduction

1.1 Introduction

Near source and large-magnitude recordings of ground motions are of great interest to both seismologists and engineers, particularly for performing site-specific or regions-specific probabilistic seismic hazard assessment (PSHA). For instance, engineers use strong ground motion time histories to design important or irregular structures such as long-span bridges, liquefied natural gas tanks, and high-rise buildings to be able to withstand a possible damaging high magnitude earthquake (e.g., Haji-Soltani, 2017; Haji-Soltani and Pezeshk, 2017). In nonlinear dynamic structural analysis and performance-based design, a large number of input ground motions is required to determine the response of the structure. To modify recorded time histories to be representative of the target analysis condition, different methods such as spectral matching and ground motion scaling can be employed (Shahbazian and Pezeshk, 2010; Rezaeian, 2010; Yamamoto and Baker, 2013). The main shortcoming of these modifications is that they can intensively change the characteristics of the recorded time histories; and as a result, the response of the structure could be distorted (Luco and Bazzurro, 2007). Therefore, generating realistic synthetic time histories that have similar features of actual recorded time histories can be considered as an alternative approach of great need. Moreover, simulated time histories for regions of low seismicity with sparse large magnitude-close distance recordings are essential to develop ground motion prediction equations (GMPEs) (e.g., Tavakoli and Pezeshk, 2005; Pezeshk *et al*., 2011, Pezeshk, *et al*., 2015, Shahjouei and Pezeshk, 2016; Pezeshk *et al*. 2018a). GMPEs have relatively simple functional forms to predict median ground motion intensity measures (GMIMs) using input parameters such as magnitude, distance, and local site conditions. This can happen for tectonically active areas such as California, Japan, Turkey, or Iran (e.g., Boore *et al.,* 2014; Campbell and Bozorgnia, 2014; Sedaghati and Pezeshk, 2016a; Sedaghati and Pezeshk, 2016b; Sedaghati and Pezeshk, 2017) where there are plenty of strong ground motion data. However, empirical methods alone cannot be used to develop GMPEs that are valid for moderate-to-large magnitudes for regions with limited strong ground-motion data. An example of such regions is central and eastern North America (CENA), which is a stable

continental regime with abundant recordings of ground motions from mainly distant small- and moderate-magnitude events, but with limited ground-motion recordings from large-magnitude earthquakes.

In this study, we develop improved procedures that can use either observed small to moderate earthquakes considered as empirical Green's functions (EGFs) or synthetic weak motions to synthesize large-magnitude earthquakes. As an application of these procedures, we apply them to simulate strong ground motion time histories within CENA. To this end, the stochastic summation of Green's function method (SSGFM) is implemented. This report provides improvements over existing methodologies, which will be explained later in detail. In the SSGFM, a specific number of small earthquakes are scaled, shifted, and then added together to construct three-component broadband time histories for a large target earthquake. The scaling factor normalizes the input motion to the unit excitation. Then, the number of required input motions to add and the delay times are defined to satisfy the scaling law of the source spectra. This summation scheme is called stochastic summation since no detailed information about the fault such as the geometry, location of the hypocenter, slip distribution, or rise time is required. The required input parameters for this approach are only values of the stress drop and the moment magnitude of both target and small events.

The uncertainty of modeling path and site effects can be removed by using observed small earthquakes acting as EGFs. In seismology and earthquake engineering, ground motion recordings carry the information and details about the source, path, and site. If an earthquake is small in magnitude, the source approximately acts as an impulsive force; and therefore, the observed recording is called an EGF. In fact, EGFs contain the impacts of the propagation path (including geometrical spreading and attenuation) as well as the local site (amplification and near-site distance independent) on radiated seismic waves (Hartzell, 1978; Wu, 1978). Green's functions describe the response of the Earth as the displacement (velocity, or acceleration) observed at the site of interest because of a point force applying at the source. Having the source time function, the displacement at the site of interest can be obtained by convolving the source time function with the Green's function (Aki and Richards, 2002; Frankel, 2017). The elastic displacement at an observation point, time t, and distance x, $u(x, t)$, due to a displacement discontinuity, $u(\xi, \tau)$, over a surface Σ where ξ is a point on the fault and τ is the rupture time, can be expressed as (Aki and Richard, 2002)

$$U(x,t) = \int_{-\infty}^{\infty} \int_{\Sigma} \left(c \left| u(\xi,\tau) \right| GF(x,t;\xi,\tau) v d\Sigma \right) d\tau \qquad (1\text{-}1)$$

where c is the elastic constants, GF is the Green's function, and v is the unit normal to the fault surface. In the far-field, this integral then can be expressed as

$$U(x,t) = \int_{0}^{W} \int_{0}^{L} \dot{D}(t;y,z) * GF(x,t;y,z) dy dz \qquad (1\text{-}2)$$

in which (y, z) are a point on the fault plane, L is the length of the fault, and W is the width of the fault. D is the slip time function, dot represents its differentiation with time, and * represents the convolution operator. Therefore, the total displacement can be obtained from the convolution of the slip velocity time function with the Green's function in the time domain. If the earthquake dimension is much smaller than the wavelength of interest, or the source-to-site distance is much longer than the wavelength of interest, then fault is considered as a point and thus the above-mentioned integral can be rewritten as

$$U(x,t) = \dot{D}(t) * GF(x,t) \qquad (1\text{-}3)$$

The large earthquake with a huge rupture area can be broken into small subfaults (m elements along the length and n elements along the width) considered as point sources, and the ground motion can be obtained from (Frankel, 2017)

$$U(x,t) = \sum_{i=1}^{m} \sum_{j=1}^{n} \dot{D}(t-T_{ij}) * GF(x,t-T_{ij}) \qquad (1\text{-}4)$$

in which T_{ij} accounts for the delay between different subfaults because of the rupture propagation and different distance of site to subfaults.

1.2 **Background**

There are several approaches that aim to generate accurate and realistic large magnitude ground motions at a given site. These approaches are generally classified as deterministic or physics-based, stochastic, and hybrid (Ólafsson *et al.*, 2001; Douglas and Aochi, 2008) which are explained in more detail in the following pages. It should be emphasized that the intent of these methods is not to generate synthetic time histories to fit recorded time histories in every detail

and wiggle for wiggle, but to capture realistic features and characteristics of the observed time histories.

Two source models are defined in synthesizing ground motions: the point-source model and the finite-fault source model. In the point-source model, the distance between the site and source is sufficiently long, compared to the size of the fault, to consider the fault as a point source. Thus, seismic waves are effectively radiated from a single point in which the source-to-site distance and radiation angle are clearly defined. In this case, the form of the ω^n spectrum (e.g., ω-square or ω-cube models) can accurately mimic the slip velocity function. The seismic moment and corner frequency (or stress drop) are the only two parameters required to have the shape of source spectrum. However, in the near-field region particularly for large magnitude earthquakes, the single point-source turns into a finite-fault rupture in which the effects of rupture propagation, asperities, directivity, source-to-site geometry, saturation (source-to-site distance), hanging wall, and fling step should be considered. In the finite-fault model, the slip initiates due to a shear dislocation at a specific point, called the hypocenter, and spreads out within the fault at a particular rate, called rupture velocity. Thus, the rupture time is the time needed for the rupture to propagate across the entire fault. Each point on the fault begins to slip once the rupture front arrives at that point, and the time required for that point to obtain the complete slip is called the rise time. Asperity means roughness and indicates a region (patch) on a fault that is locked or stuck and resists against breaking (Aki, 1984). In fact, the friction between the two sides of the fault is highest on asperities (slip heterogeneities). During an earthquake, rupture usually begins from an asperity and the most released energy of the earthquake comes from the asperities that become unlocked or unstuck. Saturation is a result of the effect of the propagation path on seismic waves coming from different parts of the finite-fault. In fact, the parts of the fault that are closer to the site have higher influence on the total energy captured at the site, since longer parts of the fault are highly attenuated because of the geometrical spreading and attenuation functions (Yenier and Atkinson, 2014; Tavakoli *et al*., 2018). The fling step is the permanent ground displacement caused by the relative movement of the two sides of the fault. The permanent ground displacement is gradually decreased with increasing the distance from the fault. The details associated with the fling step can be evaluated from geodetic surveys using GPS measurements. It should be mentioned that the fling step effect is removed by doing baseline correction and filtering; hence, a particular data processing

approach is required to obtain this information (Dabaghi, 2014). The hanging wall (HW) effect is a result of the geometry of the ruptured fault and shortcomings of the source-to-site distances such as the Joyner-Boore distance or rupture distance. Regarding this effect for two sites having identical rupture distances, the site located on the HW region experiences larger ground motions compared to the second site located on the footwall (FW) region (Abrahamson and Somerville, 1996; Donahue and Abrahamson, 2014). This happens because the effective distance of the site on the HW region is less than the effective distance of the site on the FW region. The directivity effect is caused by the direction of rupture propagation and location of the site. If the rupture propagation moves towards the site, forward directivity case, we will have a time series with a larger amplitude which is compressed in time. On the other hand, if the rupture propagates away from the site, backward directivity case, we will have a time series with shorter amplitude, but longer duration compared to the forward directivity case.

1.2.1 Deterministic Approach

The first approach to generate synthetic ground motion time histories is to theoretically model the accurate realistic source time function, the path effect, and the local site condition, and then incorporate the effects of each term on seismic waves. Methods using this approach are known as "theoretical methods" and the function containing the path effect and local site condition terms are called "Green's function," "synthetic Green's function," or "Impulse Response" (Aki, 1968; Haskell, 1969; Wu, 1981). To explain it simply in the elasto-dynamic wave theory, the term "Green's function" is defined as the displacement (or velocity or acceleration) at a specific point due to application of a point-force load at another point (see Figure 1-1). The propagation term can be modeled using various methods such as finite element methods (FEM; e.g., Moczo *et al*., 2007) or finite difference methods (FDM; e.g., Boore, 1973). One of the main difficulties in modeling Green's function is accounting for scattering effects (Zeng, 1991; Zeng *et al*., 1993). In methods using the deterministic approach, dynamic or kinematic source models are convolved with the deterministic Green's function obtained from 1D or 3D velocity-density structure of the crust. These methods are often very computationally expensive.

1.2.2 Stochastic Approach

The simple and computationally efficient second approach which is very popular, known as "stochastic ground motion simulation," assumes that the simulated ground motion is a zero-mean Gaussian process (Yamamoto and Baker, 2011). This approach uses a Gaussian white noise which is a stationary random process and has a zero mean and a relatively constant spectral density over all frequencies. The most famous technique to simulate ground motions using the stochastic assumption is to combine a windowed Gaussian signal (white noise) with the duration of a desired earthquake at a given site, T_{gm}, (that is, the sum of the rupture duration, T_c, which is related to the inverse of the corner frequency and the path-dependent duration, T_p) transformed into the frequency domain and multiplied with the ground motion Fourier amplitude spectrum (FAS) obtained from appropriate seismological parameters; and then, transformed back into the time domain, which is known as "the stochastic method" (Boore, 1983; Boore, 2003). In the stochastic method, the obtained result is not necessarily required to transform back into the time domain, and GMIMs can be directly determined using the random vibration theory (RVT) from the Fourier amplitude spectrum (FAS) of seismic waves. Although it is difficult to account for physical definitions such as directivity, 3-D crustal structure, and surface waves, this approach is very popular since it requires fewer input parameters and fewer details about the source, path, and site functions, as well as it is computationally very fast compared to either physics-based or hybrid approaches. The main issue of this approach is that it is very difficult to account for the time and frequency domain nonstationary features of time series. The temporal nonstationary, caused by the transient nature of the earthquake phenomenon, indicates that the amplitude or intensity of seismic ground motions incrementally grows to reach the strong shake phase and then progressively is attenuated to zero. The spectral nonstationary, arising from the attenuation and evolving nature of seismic waves during propagation through the path and site, implies that frequency contents of earthquake ground motions vary with time and each part or phase of time series have different frequency amplitudes and frequency phases. The temporal and spectral nonstationary features are of great importance in the nonlinear dynamic response of structures, since the behavior of structures is also nonstationary (Papadimitrios, 1990; Conte, 1992).

The main assumption about the stochastic point-source model is that the source is focused at a point and the acceleration time series constructed at a given site includes both

random and deterministic aspects of ground motion shaking. By deterministic aspects, the average FAS which is a function of magnitude and distance is defined. From stochastic aspects, motions are treated as noise with the given deterministic spectrum. Note that the point source model is reasonable, once the distance between the source and site is much larger than the dimensions of the source (Boore, 1983, 2003; Boore and Atkinson, 1987; Atkinson and Boore, 1995; Atkinson and Boore, 1997; Atkinson and Silva, 2000). The steps to synthesize ground motions by the stochastic point source model are (Boore, 2003; Atkinson *et al*., 2009):

1. Constructe a normally distributed random Gaussian signal (white noise) with zero mean and unit variance.

2. Multiply the signal from step (1) by a window function with a given time equal to the total ground motion duration at the site of interest.

3. Calculating the Fourier transform of the windowed signal from step (2).

4. Normalize the result from step (3) so that the RMS amplitude spectrum of the windowed Gaussian signal equals unity.

5. Calculate the theoretical or deterministic point-source FAS using equation (1-10), employing the seismological characteristics of the region of interest.

6. Multiply the result from step (5) by the normalized windowed Gaussian spectrum estimated from step (4) to obtain the FAS of the motion at the given site.

7. Calculate the inverse Fourier transform (IFT) of the spectrum from step (6) to acquire the simulated accelerogram or seismogram (time histories) or use the RVT to estimate GMIMs of interest such as peak ground acceleration (PGA), 5% pseudo-spectral acceleration (PSA), and peak ground velocity (PGV).

The main deficiency of the stochastic point-source model is near source simulations for large earthquakes in which the impacts of finite-fault rupture containing directivity, rupture propagation, asperities, and source-receiver geometry are significant on the amplitudes, duration, and frequency content of strong ground motions (Beresnev and Atkinson, 1997). One important issue of point-source ground motion simulations is that they monotonically grow with reducing distance. Thus, the concept of the stochastic point-source was improved by using the effective distance instead of the hypocentral distance and using more complex source models such as

double-corner frequencies (Boore, 2009; Boore *et al*., 2014). An equivalent point-source model is like the point-source model, but it uses the effective distance instead of other definitions of source-to-site distance such as the Joyner-Boore or rupture distances. The effective distance is an imaginary distance between the station and a virtual point, such that the energy captured by the station from that virtual point is equal to the energy captured by the station from an actual extended-fault rupture. We will comprehensively go through the details of this concept in Chapter 4. Simulated ground motions from equivalent point-source model saturate at very close distance because the effective distance increases with increasing magnitude resulting in counterbalancing the effect of very large magnitude. In fact, the effect of a very large earthquake is counterbalanced with the effect of its associated large effective distance. Yenier and Atkinson (2014) showed that an equivalent point-source model, in which the concept of effective distance is used through a point-source model analysis, can precisely predict the mean ground motions even for very large earthquakes (> 6) at very short distances (< 20 km).

The stochastic finite-fault method (Beresnev and Atkinson, 1997; Beresnev and Atkinson, 1998) is another method based on the stochastic approach to capture the effects of finite-fault ruptures by summation of delayed weak ground motions in the time domain. One technique to model the rupture propagation effect of finite-fault is to partition the fault into smaller parts, called subfaults, and then scale, shift with appropriate delay times mimicking the rupture propagation, and linearly add the contribution of all subfaults on the site of interest to construct the strong ground motion time history at that site (Hartzell, 1978; Wu, 1978; Kanamori, 1979; Irikura, 1983; Joyner and Boore, 1986). In the stochastic finite-fault framework, weak ground motions are obtained employing the stochastic point source method, and the delay times are defined based on the source information and source-site location.

The SMSIM (Boore, 2003; Boore, 2005) and the EXSIM (Motazedian and Atkinson, 2005; Atkinson *et al*., 2009) algorithms simulate strong ground motions based on the stochastic point-source and stochastic finite-fault approaches, respectively. The input parameters required to describe the source term in the stochastic finite-fault method are magnitude, stress drop, length and width of the fault, strike, dip, depth, and slip function, which can be distributed randomly or by a given pattern. For the stochastic point source model only two parameters out of seismic moment, stress drop, and corner frequency are required to define the source. It should be noted that time domain calculations are 10 times faster in SMSIM than EXSIM and frequency domain

calculations using the RVT for a large magnitude event can be 1,000 times faster with SMSIM compared with EXSIM.

The stochastic approach is most applicable at high frequencies (HFs) since ground motions show stochastic features at short periods (short wavelengths); whereas low frequencies (LFs) have a deterministic nature and their behavior cannot be accurately modeled with the stochastic approach. For instance, the coherent features of the source such as radiation pattern at LFs cannot be captured with the stochastic method. Thus, the stochastic approach is often used to simulate the HF portion of ground motions in the broadband ground motion simulation procedure.

1.2.3 Hybrid Approach

The third approach is the hybrid approach which combines the deterministic LF part with the stochastic HF part to simulate broadband time histories (Graves and Pitarka, 2010). At LFs, the nature of ground motions is deterministic, and simulation process matches both waveform and spectral amplitude of the simulated with observed recording. Deterministic simulations can be obtained by having the rupture model and seismic velocity structure of the region of interest. However, at HFs, the nature of ground motions is stochastic and only the spectral amplitude of the simulated ground motion and the observed recording can be matched, not their waveforms. The reason why this transition from deterministic to stochastic behavior around 1 Hz is observed is that the source radiation and wave propagation are coherent at LFs (very long wavelengths), but they are incoherent at HFs (very short wavelengths) (Sato and Fehler, 1998; Graves *et al*., 1999). With increasing frequency (decreasing wave lengths), the impact of small scale heterogeneities in the earthquake rupture and crustal propagation path on seismic wave makes the high frequency portion of ground motions behave stochastically (Sato and Fehler, 1998; Hutching and Viegas, 2012). Thus, the deterministic LF synthetics are combined with the stochastic HF synthetics in the frequency domain around a matching frequency of 1 Hz to produce realistic broadband ground motions (Graves and Pitarka, 2010; Frankel, 2017).

1.3 Stochastic Summation of Green's Function Method (SSGFM)

Observed small earthquakes (sub-events, sub-sources, sub-faults, or element earthquakes), in which the source acts like an impulse (point dislocation source), can capture the realistic effects of velocity structure, propagation path (both attenuation and geometrical spreading), and local site (both amplification and near site diminution). Of course, there is no earthquake to possess an exact impulsive point source; however, if the earthquake is small; and consequently, the fault is small, the rupture time is very short and cannot affect time histories (Hutchings, 1992). For instance, Aki (1982) demonstrated that the displacement seismogram recorded for the Parkfield earthquake of 1966 at a station located at 80 m from the fault break followed a simple impulsive shape and Hutchings (1987) showed that the San Fernando earthquake's aftershocks of 1971 which were recorded at the near source stations approxinately have an impulsive point source shape. If the source is impulsive, the response of the medium captured at the observation point associated with the impulsive force at the source is called Green's function. Thus, small-event recordings are called "empirical Green's function (EGF)" (Hartzell, 1978; Wu, 1978). Using equation (1-2), if the earthquake dimension is much smaller than the wavelength of interest or the source-to-site distance is much longer than the wavelength of interest, then fault displacement at the observation point, x, and time, t, can be obtained as

$$u(x,t) = \int_A \mu S(t)(s_p n_p + s_q n_q) dA * GF(x,t) \tag{1-5}$$

in which the term $s_p n_p + s_q n_q$ is the focal mechanism, μ is the rigidity, and $S(t)$ represents the slip function. When the periods of observed waves are much longer than the duration of the fault, the source acts like a time-independent impulse function. Thus, the slip function can be replaced with a unit Heaviside step function. Substituting integral with total area A and displacement with e, equation of EGF can be expressed as

$$e(x,t) = \mu H(t-t_0)\bar{s}A(s_p n_p + s_q n_q) * GF(x,t) = M_0^e(s_p n_p + s_q n_q)H(t-t_0) * GF(x,t) \tag{1-6}$$

where $\bar{s}$ is the average slip on the fault, t_0 represents the origin time, and M_0 denotes the seismic moment of the EGF. The Heaviside function is zero before the origin time, thus

$$e(x,t) = \begin{cases} M_0^e(s_p n_p + s_q n_q) * GF(x,t) & t > t_0 \\ 0 & t \le t_0 \end{cases} \tag{1-7}$$

Now, we can explain why EGFs are used to solve the representation of ground motions. To this end, we divide the fault area into a discrete summation of subsources. Therefore, equation (1-5) can be substituted by a discrete sum over N subsources with area A_i so that the summation of all subsource areas is equal to total area A as

$$U(x,t) = \sum_{i=1}^{N} \mu A_i S_i(t)(s_p n_p + s_q n_q) * GF_i(x,t; y,z) \tag{1-8}$$

Using equation (1-7), we can replace the focal mechanism (since both small and large earthquakes should have similar focal mechanism) and the elastodynamic Green's function for each subsource as

$$U(x,t) = \sum_{i=1}^{N} \frac{\mu A_i S_i(t)}{M_{i0}^e} e_{in}(x,t) = \sum_{i=1}^{N} \xi_i e_{in}(x,t) \tag{1-9}$$

where ξ_i is the scaling factor for subsource i.

The impacts of the propagation path are very sophisticated and cannot be modeled with simple layered crustal models, particularly at HFs (>1 Hz) where seismic waves are very sensitive to small-scale heterogeneities within the crust and upper mantle due to having short wavelengths. Seismic waves captured at an observation point contain direct, reflected, refracted, scattered, and surface waves attenuated through the path by scattering and anelastic attenuation, exposed to energy focusing and defocusing because of lateral change of path properties, amplified within the path and particularly near the site, and highly attenuated close to the observation point. Employing EGFs instead of mathematical determinations can precisely and simply account for all these effects. Note that essentially EGFs describe the combined effects of the source and propagation path since no earthquake has true impulsive source function. EGFs are important tools to study earthquake source, to study crustal attenuation, to model finite rupture, to analyze site response, and to generate future great earthquakes (Hutchings and Viegas, 2012). For instance, EGFs are used to investigate the earthquake source process, having one recorded small earthquake and one recorded larger earthquake from a particular fault at a specific station, by de-convolving the small earthquake from the large event.

Simulation of large earthquakes using EGFs is an appealing approach since deploying EGFs removes the uncertainty of the propagation path and local site effects (Hartzell, 1978; Wu,

1978; Heaton and Hartzell, 1988; Hutchings and Wu, 1990). These EGFs inherently include the impacts of the propagation path and site on all kind of body waves (such as direct, reflected, refracted, and converted body waves), scattered waves, and surface waves. Another advantage of this approach is that it is not computationally expensive. Most importantly, EGFs intuitively account for the temporal and spectral nonstationary characteristics of seismic ground motions. Thus, through using EGFs it is not required to define any window functions to consider the temporal nonstationary effects or to define any filters to account for the spectral nonstationary effects like the other methods. In addition, the effects of fling step and HW, inherently included in the EGFs, accumulate in the final simulation due to the summation.

There are several different techniques to use a recording of a small earthquake and generate a recording of a large earthquake in which the primary idea is to account for the realistic propagation effects on seismic waves. Some techniques employ just one EGF for simulations, but others use a number of EGFs with similar focal mechanisms like the target focal mechanism to capture the effects of path on seismic waves coming from different parts of the fault. Another primary difference among these techniques is the procedure to model the source. The earthquake source can be defined as a point source model, kinematic model, quasi-dynamic model, and dynamic model (Hutching and Viegas, 2012). After assigning the source model, simulation can be performed using only one large event or as a combination of smaller earthquakes (composite source model or multiple-event source model). Most EGFs methods use a composite source model which is defined as a linear combination of EGFs. Different investigators combine these different classifications to obtain their simulations. For instance, Boore (1999) used the point source model with only one event. He modified and scaled the spectrum of the small earthquake to match the spectrum of the target event and then incorporated the phase information of the target event to simulate the ground motion of the target event. He mentioned that the scaling approach should account for the difference between source spectra and the difference between the duration of shakings. The main deficiency of this case is that the effect of rupture propagation cannot be taken into account. Joyner and Boore (1986), Wennerberg (1990), Tumarkin and Archuleta (1994), Ordaz *et al.* (1995), and Boore (2009) (to improve EXSIM) used the point source model combined with the composite source model. In fact, a number of small earthquakes are stochastically added to one another somehow to match the spectrum of the target event. One advantage of the first two methods is that it is not necessary to have a small

earthquake as an input motion. Therefore, signal to noise ratio (SNR) is not influential since the SNR of larger earthquakes is often acceptable. Another important advantage of these approaches is that there is no need to have detailed information about the fault and rupture process. Irikura (1986), Somerville *et al.* (1991), Hartzell, (1992), and Frankel (1995) employed the kinematic source model combined with the composite source model. To this end, the spectrum of the target event is constructed by summation of the contributions from all parts of the fault rupture. Therefore, a large earthquake can be defined as a space-time convolution of the impulse response or Green's function with a relevant slip velocity function (Burridge and Knopoff, 1964; Wu, 1978; Wu, 1981; Aki, 1982). The slip function which is a function of time and location on the fault plane explains how the fault displacement occurs during an earthquake (see equations (1-1) through (1-4)). This method requires general knowledge about the actual rupture process such as the rupture velocity, slip distribution, slip velocity, and initiation point of the rupture. In addition, small earthquakes used as input motions should be small enough to be considered as EGFs. Thus, one disadvantage of this method is to deal with poor quality data due to low SNR at LFs since the SNR of small earthquakes is often below the noise level. Quasi-dynamic and dynamic source models are more complicated and are involved with the physics of the rupture process. Boatwright (1981), Hutching (1992), and Hutching (1994) combined the quasi-dynamic source model with the composite source to simulate strong ground motions from EGFs. The low SNR of EGFs is also an issue while using these source models. In essence, the background noise energy is much higher than LF energy for small earthquakes; therefore, methods which require using small earthquakes as EGFs are restricted to frequencies approximately greater than 0.5 Hz (Jarpe and Kasameyer, 1996). Deterministic approaches can accurately simulate the LF portion of seismic waves. Thus, in several studies, the deterministic (physics-based) LF synthetics merged with HF portions of EGFs are utilized to generate broadband Green's functions having high quality LF and HF portions (Hutchings and Viegas, 2012).

The stochastic summation of Green's functions method (SSGFM), which is a simple and straightforward method, is a combination of point source model and composite source model. Thus, it does not require detailed information about the rupture process. In this regard, small earthquakes are stochastically added to reach the target event spectrum. Note that this method employs only one small earthquake as input. The SSGFM just relies on seismic scaling relations to randomly mimic the rupture propagation. For large earthquakes, considering the effect of

finite fault rupture such as rupture propagation, asperities, and saturation effect are necessary to produce realistic synthetics. However, for a future large earthquake, the details of rupture process are unknown. In this approach, the target fault is divided into many identical sub-faults having the same characteristic of the small event fault to stochastically and randomly produce the effect of rupture propagation. Compared to the stochastic finite fault approach, the SSGFM only requires magnitude and stress drop.

There are several limitations of using the SSGFM, such as:

1. EGFs cannot capture variations in focal mechanism; thus, the mechanism of the EGFs and target event should be the same.

2. The effects of basins and/or nonlinear site responses cannot be taken into account. Therefore, this method, like many other simulation methods, is used to synthesize ground motions for the generic rock site and then using appropriate transfer function, the motions can be brought up to the surface. Basins result in reflecting and focusing of seismic waves at the edges and then these trapped waves turn into surface waves and cause elongation of the duration of ground motions (Sedaghati *et al.*, 2018). Thus, 2D or 3D models are required to account for the effects of the sedimentary basins on ground motions.

3. The assumption of point source may break down in particular cases such as the near-field region of large earthquakes. Several studies showed that the source spectrum may need to have two corner frequencies to be realistic (Boatwright, 1994; Atkinson and Boore, 1995; Atkinson and Sonley, 2003; Boatwright and Seekins, 2011; Archuleta and Ji, 2016). Thus, we propose an improvement to partially account for the finiteness of the fault dimension using double corner frequency source models in case that the source spectrum cannot be modeled with a single corner frequency model.

4. The SSGFM assumes that the Green's functions from different parts of the faults are identical (see Figure 1-2). However, the effect of geometrical spreading and attenuation function on different distances between the source and subfaults results in different Green's functions from different parts of the fault. We will address this issue and develop conversion equations between the effective distance and the Joyner-Boore distance to correct for this effect.

5. The main difficulty to deal with small earthquakes is the signal to noise ratio (SNR) issue since the LF part of small magnitude earthquakes are heavily contaminated by noise (Sedaghati and Pezeshk, 2016c; Nazemi *et al*., 2017; Pezeshk *et al*., 2018a). Moreover, there are many sites in which no recordings of even small earthquakes exist. To overcome this difficulty, we will extend the SSGFM to sites for which no small earthquake recordings are available by using synthetic Green's functions (Somerville *et al*., 1991; Kamae *et al*., 1998). In this regard, we use synthetic weak ground motions using the stochastic method of Hanks and McGuire (1981) and Boore (1983) implemented in SMSIM by Boore (2003) and Boore (2005). Then, the simulated weak motions are used within the SSGFM in place of EGFs as seed motions to produce strong ground-motion time histories. Synthetic weak motions are produced for a point-source model, and then the effects of finite fault for large earthquakes are incorporated using the SSGFM. It should be mentioned that is preferred to use EGFs instead of synthetic weak motions as seed motions, since they do not require any detailed descriptions of the propagation path and site such as geometrical spreading and attenuation functions, amplification factor, or velocity structure. However, the advantage of using the simulated seed motions is that the resultant strong ground motions are region-specific and can be used in developing GMPEs.

The SSGFM can be employed along other approaches such as hybrid methods, stochastic finite-fault method, or even stochastic point-source methods to simulate ground-motion time histories. The choice of which approach to employ depends on the user and applications. The equivalent point-source approach is very simple and fast and by using the effective distance can fairly account for the effects of the finite-fault source model. On the other hand, the finite-fault approach is more sophisticated and can capture many effects of finite-fault source model such as rupture inhomogeneity. The stochastic point-source method is 10 times and 1,000 times faster than the stochastic finite-fault method in the time and frequency domains, respectively. The SSGFM is easier since it does not need any information about the source, but it accounts for the most finite-fault effects. The stochastic methods are very useful in simulating path-specific ground motions for use in developing GMPEs; whereas the hybrid and deterministic approaches are often used for event-path-specific or path-specific simulations.

It should be emphasized that the most powerful approach to simulate strong ground-motion time histories is to use the physic-based and hybrid broadband methods (Graves and Pitarka, 2010; Frankel, 2017). However, methods based on the physic-based and hybrid approaches require many input parameters associated with the source of future earthquakes for which detailed information about the rupture process is unknown. Further, these methods are still computationally expensive. The SSGFM resolves these issues. Moreover, the physic-based and hybrid broadband methods generate event-path-specific or path-specific events. On the other hand, the stochastic point-source or stochastic finite-fault models are used for generic or region-specific applications. One advantage of the SSGFM is to be employed for both region-specific applications and path-specific applications. The main application of region-specific ground motions is for use in developing GMPEs.

1.3.1 Formulation

The FAS which is the Fourier transform of a seismic wave radiated from a point source and recorded by an instrument at a given site can be obtained as (Boore, 1983; Boore, 2003)

$$Y(M_0, f, R) = S(M_0, f) \times P(f, R) \times G(f) \times I(f) \tag{1-10}$$

where $S(M_0, f)$, $P(f, R)$, $G(f)$, and $I(f)$ denote the source function, path term, site effect, and instrument response, respectively. M_0 is the seismic moment, R is the source-to-site distance (km) and f represents frequency (Hz).

The FAS of a target event (large magnitude) and the FAS of a subfault (small event) having the same focal mechanism and propagation path and recorded at a particular site can be written as

$$Y_{\text{target}}(f, R) = S_{\text{target}}(f) \times P(f, R) \times G(f) \times I(f)$$
$$Y_{\text{small}}(f, R) = S_{\text{small}}(f) \times P(f, R) \times G(f) \times I(f) \tag{1-11}$$

and by dividing the FAS of the target by the FAS of the sub-event, we get

$$\text{Transfer function: } H(f) = \frac{Y_{\text{target}}(f, R)}{Y_{\text{small}}(f, R)} = \frac{S_{\text{target}}(f)}{S_{\text{small}}(f)} \tag{1-12}$$

Therefore, for co-located events the ratio of record spectra can reasonably approximate with the ratio of source spectra. According to this equation, the transfer function is a filter in the frequency domain, and by getting the inverse Fourier transform (IFT), we have

$$Y_{\text{target}}(f,R) = H(f) \times Y_{\text{small}}(f,R) \rightarrow IFT \rightarrow Y_{\text{target}}(t,R) = H(t) * Y_{\text{small}}(t,R) \qquad (1\text{-}13)$$

The convolution of two discrete finite functions can be written as a summation as

$$Y_{\text{target}}(t,R) = Y_{\text{small}}(t,R) * H(t) = Y_{\text{small}}(t,R) * \sum_{i=1}^{N} \delta(t-\theta_i) = \sum_{i=1}^{N} Y_{\text{small}}(t-\theta_i,R) \qquad (1\text{-}14)$$

in which N is the total number of small events, θ_i represents the time shift, and i denotes the counter over the number of the small events. Therefore, in the SSGFM, the target fault area is divided into small identical sub-faults (see Figure 1-3). Then, ground motions generated by these sub-faults are scaled and shifted and finally are summed together to produce a ground motion for the target event (Hartzell, 1978; Irikura, 1983; Irikura, 1986; Joyner and Boore, 1986; Wennerberg, 1990; Tumarkin and Archuleta, 1994; Ordaz *et al.,* 1995; Kohrs *et al.,* 2005). The summation can be written as

$$Y_t(t) = \xi \sum_{i=1}^{N} Y_s(t-\tau_i) \qquad (1\text{-}15)$$

where $Y_t(t)$ gives the amplitude of the postulated earthquake, ξ represents the scaling factor to normalize the small earthquake to the unit excitation, N denotes the number of sub-events, τ_i is the rupture time (delay time) for event ith (rupture j starts radiating at τ_i), and $Y_s(t)$ gives the amplitude of the observed small earthquake. The abovementioned equation can be written in the frequency domain as

$$Y_t(\omega) = \xi Y_s(\omega) \sum_{i=1}^{N} \exp(-i\omega\tau_i) \qquad (1\text{-}16)$$

Therefore, this method requires three steps. First, the scaling factor should be obtained. Then, the number of sub-events required should be determined. Finally, a probability distribution function (pdf) should be defined to generate rupture times (delays). There are several schemes for performing the SSGFM according to different definitions for these three steps. Note that although this method is a composite source model for simulating a large earthquake, it looks at the source as a single point. In this regard, the summation parameters are obtained using the

scaling relations of the source spectrum. Therefore, the only parameters needed from the small and target events are the stress drop and seismic moment values (see Figure 1-4).

Different single-stage summation schemes are proposed for the SSGFM. Joyner and Boore (1986) proposed a summation scheme corresponding to a uniform distribution for delay times. The problem with the Joyner and Boore scheme was that it creates holes in the spectrum. Then, Wennerberg (1990) improved the transfer function; however, it overestimated the spectrum at HFs. Tumarkin and Archuleta (1994) improved the transfer function by choosing a complex transfer function to incorporate the phase difference between the small event and the target event. This transfer function again overestimated the HF spectrum. Ordaz *et al*. (1995) suggested a transfer function in which its spectrum matches the target spectrum in the whole frequency range. We will explain and compare these methods in Chapter 2.

Time histories of simulated events using the single-stage scheme have a simple form with a single peak in which most of the energy is concentrated. For large earthquakes such as the 2011 **M**9.0 Tohoku, Japan earthquake (Ghofrani *et al*., 2013) and the 2010 **M**8.8 Maule, Chile earthquake (Frankel, 2017), the rupture propagation is often very complex and heterogeneous. There are some parts of the fault that radiate seismic waves stronger than other parts, which are known as asperities (Boatwright, 1988). To take into account the effect of asperities on simulated strong ground-motion time histories, a two-stage summation scheme has been introduced (Wennerberg, 1990; Kohrs *et al*., 2005). We will implement a two-stage summation scheme as well as a single-stage summation scheme to generate different time histories with random source characteristics.

1.3.2 **Improvement 1 – Extension of the Source Function**

To explain how to extend the source model in the SSGFM, we shall begin to describe the source model from scratch. In this regard, we require defining the rupture time and the rise time to obtain the source time function for a linear fault with a length of *L*. The rupture time, T_R, is the time required for the rupture propagation along the fault. The rise time, T_D, is the time required for any dislocation points on the fault to reach its maximum amount. These times can be approximately estimated by

$$T_R = L / V_R = L / (y\beta)$$
$$T_D = \mu D_0 / (\beta \Delta \sigma) \tag{1-17}$$

where V_R is the rupture velocity assuming to be about 0.6 to 1.0 ($= y$) times the shear wave velocity, μ is the rigidity of the material in the vicinity of the source, β is the shear wave velocity, and $\Delta\sigma$ is the stress drop parameter. D_0 is the average slip (dislocation) on the fault. The source time function is then defined as the convolution of two boxcar functions associated with the velocities finite rupture time and the finite rise time. The velocity functions have a boxcar shape since the displacement functions have a ramp shape. Thus, the source time function generally is a trapezoid. The Fourier transform of a boxcar function is a sinc function as follows

$$F(\omega) = \int_{-T/2}^{T/2} \frac{1}{T} e^{i\omega t} dt = \frac{1}{i\omega T} \left(e^{i\omega T/2} - e^{-i\omega T/2} \right) = \frac{\sin(\omega T / 2)}{\omega T / 2} = \mathrm{sinc}(\omega T / 2) \tag{1-18}$$

Therefore, the FAS of the source time function can be written as the multiplication of two sinc functions as follows

$$|S(\omega)| = M_0 \left| \mathrm{sinc}(\omega T_R / 2) \right| \left| \mathrm{sinc}(\omega T_D / 2) \right| \tag{1-19}$$

in which M_0 is the seismic moment to scale the low-frequency level and can be obtained from (Burridge and Knopoff, 1964; Madariaga, 1977)

$$M_0 = \mu \int_S D(x, y) dS = c \mu D_0 A \tag{1-20}$$

where A is the fault area and c is a constant related to the fault shape factor. Then, getting the natural logarithm from both sides, we have

$$\log |S(\omega)| = \log M_0 + \log\left[\mathrm{sinc}(\omega T_R / 2) \right] + \log\left[\mathrm{sinc}(\omega T_D / 2) \right] \tag{1-21}$$

The sinc(x) function can be approximated by

$$\mathrm{sinc}(x) = \begin{cases} 1 & x \le 1 \\ 1/x & x > 1 \end{cases} \tag{1-22}$$

The logarithm of the FAS of the source time function is shown in Figure 1-5. Schematic plot for the approximation of theoretical source time function can be written as

$$\log |S(\omega)| = \begin{cases} \log M_0 & \omega < 2/T_R \\ \log M_0 - \log(T_R/2) - \log(\omega) & 2/T_R < \omega < 2/T_D \\ \log M_0 - \log(T_R T_D/4) - 2\log(\omega) & 2/T_D < \omega \end{cases} \tag{1-23}$$

Note that with increasing the fault dimension, the rupture time, the rise time, and the seismic moment grows; thereby, the corner frequencies decrease (Aki, 1967; Brune, 1970; Brune, 1971). This model is called a double corner frequency (DCF) model. For far-field stations, since the path-dependent duration increases, and the fault length is very small to the source to site distance, the rise time and the rupture time are supposed to be identical; and thus, the source function is like a triangle. This source time function yields a single corner frequency (SCF) model with corner frequency of $2/T_R$.

It should be mentioned that the impact of the width can be taken into account by adding another boxcar function for the rupture time along the width for large magnitude earthquakes and near-field stations. This assumption leads to a new source time function with three corner frequencies having another segment with spectral falloff (decay rate) of ω^{-3} at high frequencies after the segment with spectral falloff of ω^{-2}. This was a simplistic source model. Next, we will discuss a realistic model.

By years passing, the stress strain is accumulated on the fault, and it releases in a sudden failure of the fault, which decreases the stress compared to the initial condition and radiating seismic waves. Regarding the stress formula and stress-strain relation, we have

$$\varepsilon = \frac{\delta u}{u} \approx \frac{D_0}{L} \rightarrow \Delta\sigma = \mu\frac{D_0}{L} \tag{1-24}$$

and using equation (1-20), the stress can be written as

$$\Delta\sigma = c\frac{M_0}{LA} \tag{1-25}$$

in which u and δu are initial length and the deformation after slip, respectively. Based on the fault shape and rupture dip, the scaling relationship is obtained as (Eshelby, 1957; Keilis-Borok, 1959)

$$\Delta\sigma = \begin{cases} \dfrac{7}{16}\dfrac{M_0}{R^3} & \text{circle source} \\[3mm] \dfrac{2}{\pi}\dfrac{M_0}{W^2 L} & \text{rectangular source - dip 90} \end{cases} \qquad (1\text{-}26)$$

The idea of the convolution of the rise time and rupture time functions was first proposed by Aki (1967). Aki (1967) used the far-field displacement components of *P* and *S* waves at long distances associated with a shear-fault source obtained by Haskell (1964) and Haskell (1966) as the solution of the elastic wave equations in an infinite, isotropic, and homogenous medium (a medium with a constant stiffness). The elastodynamic wave equation (combining the Newton's second law, the Hooke's law for the relationship between stress and strain components, and strain equations) in time, *t*, and space, *x* in 3D, in the Cartesian coordinates, (x_1, x_2, x_3), is written as follows (Madariaga, 1976)

$$\mu\nabla^2 u(x,t) + (\mu+\lambda)\nabla(\nabla.u(x,t)) + f(x,t) = \rho\frac{\partial^2 u(x,t)}{\partial t^2} \qquad (1\text{-}27)$$

where $u(x,t)$ notes the particle displacement due to the wave propagation, μ is the shear modulus (rigidity), λ indicates the elastic constant, and ρ is the mass density. $f(x,t)$ is the force, a function of location and time, expressed as follows

$$f(x,t) = D(t)\delta(x-x_0)\vec{f} \qquad (1\text{-}28)$$

in which $S(t)$ is the source time function, δ is the Dirac delta function, and $\vec{f}$ is the unit vector representing the direction of the applied force. ∇ is the gradient operator or a first order partial differential operator, ∇ denotes the divergence operator which maps a vector function to a scalar function, and ∇^2 represents the Laplace operator or Laplacian which is a second order partial differential equation considering all dimensions of space. In this medium with explained characteristics, the velocity of *P*-wave (α) and *S*-wave (β) can be defined as $\alpha = \sqrt{(\lambda + 2\mu)/\rho}$ and $\beta = \sqrt{\lambda/\rho}$, respectively. Further, the wavelength for the *P*-wave (λ_P) and *S*-wave (λ_S) is given by $\lambda_P = 2\pi\alpha/\omega$ and $\lambda_S = 2\pi\beta/\omega$, respectively.

The general solution to this equation with homogenous initial conditions, zero initial displacement and velocity, in the time-space domain but in the spherical coordinates, (R, θ, φ), is given by (Madariaga, 1997; Aki and Richards, 2002; Madariaga, 2007)

$$u(R,t) = \frac{\mu}{4\pi\rho}\left[\vec{f}.\nabla\nabla(R)\right]\int\limits_{R/\alpha}^{\min(t,R/\beta)}\tau\dot{D}(t-\tau)d\tau$$

$$+\frac{\mu}{4\pi\rho\alpha^2}\frac{1}{R}\left[(\vec{f}.\nabla R)\nabla R\right]\dot{D}(t-R/\alpha) \qquad (1\text{-}29)$$

$$+\frac{\mu}{4\pi\rho\beta^2}\frac{1}{R}\left[\vec{f}-(\vec{f}.\nabla R)\nabla R\right]\dot{D}(t-R/\beta)$$

in which R is distance from the point source and $\dot{D}$ is the derivative of the source function describing the energy pulse radiated from the point source. In this equation, the first term on the right-hand side is the near-field displacement, the second term is the far-field displacement for P-waves, and the third term is the far-field displacement for S-waves. Thus, the near-filed solution for the elastodynamic Green's function in a homogenous, isotropic, and unbounded medium is expressed as

$$u^N(x,t) = \frac{1}{4\pi\rho}\frac{1}{R^3}(3\gamma_i\gamma_j - \delta_{ij})\int\limits_{R/\alpha}^{\min(t,R/\beta)}\tau\dot{M}(t-\tau)d\tau \qquad (1\text{-}30)$$

in which $\dot{M}$ is the moment rate function (MRF) obtained from the derivative of the seismic moment function as follows

$$M(t) = \mu D(t)S \qquad (1\text{-}31)$$

where S is the fault area, but for the point source is supposed to be 1. γ_i is defined as x_i/R. Regarding this equation, the near field is composed of both P-waves and S-waves. Thus, it includes both radial and transverse motions. The total duration of this term is $(R/\beta - R/\alpha) + T$ in which T is the duration of the nonzero source term.

The far-field situation occurs when the distance from the point source is more than several wavelengths. Then, the far-field displacement for P-waves is radial and can be written as (Haskell, 1964; Randall, 1973)

$$u_P(R,t) = \frac{1}{4\pi\rho\alpha^3}\frac{1}{R}\dot{M}(t-R/\alpha)\sin(2\theta)\sin(\varphi) \qquad (1\text{-}32)$$

where θ is the polar angle and φ is the azimuthal angle in the spherical coordinates. In this equation, $\sin(2\theta)\cos(\varphi)$ expresses the radiation pattern for P-waves. As can be seen from the abovementioned equation, P-waves are attenuated as R^{-1}. They propagate with the speed of α.

22

These waves move radially (longitudinally) indicating that the direction of the waves and particle motions are the same. Furthermore, the term inside the moment rate function indicates that if the source starts radiating at zero, P-waves arrive to the observation point at time R/α.

The far-field displacement for S-waves, which is transverse and has two components known as SH and SV (see Figure 1-6), is given by (Haskell, 1964; Randall, 1973)

$$u_{SH}(R,t) = \frac{1}{4\pi\rho\beta^3}\frac{1}{R}\dot{M}(t-R/\beta)\cos(2\theta)\sin(\varphi)$$

$$u_{SV}(R,t) = \frac{1}{4\pi\rho\beta^3}\frac{1}{R}\dot{M}(t-R/\beta)\cos(\theta)\cos(\varphi)$$

(1-33)

According to this equation, S-waves are attenuated with a rate of R^{-1}. They propagate with the speed of β. These waves move perpendicular to the direction of particle motions; and therefore, they are called transverse waves. Furthermore, the term inside the moment rate function indicates that if the source starts radiating at zero, S-waves arrive at the observation point at time R/β. In fact, they reach the observation point after P-waves, since $\alpha > \beta$.

It is interesting to note that regarding equations (1-32) and (1-33), the far-field displacement caused by S-waves is higher than P-waves because $\alpha > \beta$. In general, the far-field displacement can be given by (Aki and Richards, 2002; Madariaga, 2007)

$$U_C(R,t) = \frac{1}{4\pi\rho V_C^3}\frac{R_{\theta\varphi}}{R}\dot{M}(t-R/V_C)$$

(1-34)

in which c can be P (radial component) or S (transverse component), R is the distance between the point source and observer, and $R_{\theta\varphi}$ is the radiation pattern. Boore and Boatwright (1984) estimated radiation of 0.52 and 0.63 for P- and S-waves, respectively. Having the far-field displacement function in the time-space domain, the Fourier transform of the response of the source in the frequency-space can be obtained by

$$\tilde{U}_C(R,\omega) = \frac{1}{4\pi\rho V_C^3}\frac{R_{\theta\varphi}}{R}\tilde{\dot{M}}(\omega)e^{-i\omega R/V_C}$$

(1-35)

where $\tilde{\tilde{M}}$ is the Fourier transform of the MRF.

Aki (1967) isolated and removed the path propagation term (geometrical spreading term, $1/R$) from the total far-field displacement. Therefore, what remains shows the spectral response

of the source. Using the scaling of seismic moments with earthquake sizes (seismic moment increases with increasing the earthquake dimensions), he observed that the low frequency level of the source time function equals the total moment of the source. He also found that the autocorrelation function of dislocation velocity can express the spectrum of the MRF. He assumed that the displacement source time function linearly increases up to the maximum dislocation (ramp shape); and thus, its derivative giving the velocity source time function is like a boxcar function. The autocorrelation function has a triangular shape and its Fourier transform match the source spectrum obtained from the solution of the elastic wave equations. He called this spectrum the "ω-square model" due to the decay rate of ω^{-2} at high frequencies. Figure 1-7 demonstrates the schematic plot of the dislocation and velocity functions as well as the autocorrelation function for a shear-fault source.

The above discussion regards a simplified source model. However, it is somewhat different in reality. Brune (1970) suggested using the effective stress that results in accelerating the two sides of the fault to the time function to obtain source time function. In fact, he assumed that the earthquake dislocation is a tangential stress pulse, and the stress pulse that sends out shear waves can be modeled with a function similar to the boxcar function. Then, the tangential displacement can be obtained by integrating the stress pulse function which is associated with the velocity function. To this end, he accounted for the edge effects of dislocation surface (effects of finite-fault source) on the velocity function. Therefore, he proposed an exponential function instead of a boxcar, known as Brune's pulse, as follows

$$\dot{D}(t) = (\sigma / \mu)\beta e^{-t/T_D} \tag{1-36}$$

and the displacement can be obtained by integration as follows

$$D(t) = (\sigma / \mu)\beta T_D (1 - e^{-t/T_D}) \tag{1-37}$$

in which D is the displacement (slip) source time function, $\dot{D}$ is its derivative representing the slip velocity source time function, σ is the effective shear wave stress, t is time, and T_D is the rise time defined above. Figure 1-8 depicts displacement and velocity source time functions proposed by Brune (1970).

Boore (1983) then organized the process to obtain the source term based on the work of Aki (1967) and Brune (1970). In the point-source approach of simulating ground motions, the

shape of the displacement, velocity, and source acceleration spectra is scaled with the seismic moment (or magnitude) using the single corner frequency (SCF) model given by

$$\text{Displacement: } S(\omega) = CM_0 \frac{1}{1+\left(\dfrac{\omega}{\omega_C}\right)^2} = CM_0 \frac{1}{1+\left(\dfrac{f}{f_C}\right)^2}$$

$$\text{Velocity: } \quad S(\omega) = CM_0 \frac{(\omega)}{1+\left(\dfrac{\omega}{\omega_C}\right)^2} = CM_0 \frac{(2\pi f)}{1+\left(\dfrac{f}{f_C}\right)^2} \qquad (1\text{-}38)$$

$$\text{Acceleration: } S(\omega) = CM_0 \frac{(\omega)^2}{1+\left(\dfrac{\omega}{\omega_C}\right)^2} = CM_0 \frac{(2\pi f)^2}{1+\left(\dfrac{f}{f_C}\right)^2}$$

where M_0 is the seismic moment (dyne-cm), related to the moment magnitude, **M**, and can be obtained by (Hanks and Kanamori, 1979)

$$\mathbf{M} = \frac{2}{3}\log(M_0) - 10.7 \qquad (1\text{-}39)$$

and f_C is the source corner frequency (Hz) related to the stress drop (bar), $\Delta\sigma$, by (Brune, 1970; Brune, 1971)

$$f_C = 4.9 \times 10^6 \beta \left(\Delta\sigma / M_0\right)^{1/3} \qquad (1\text{-}40)$$

in which β is the shear-wave velocity (km/s) in the source area. The corner frequency is related to the rise time as $f_c = 1/T_D$ (Hanks and McGuire, 1981). $\Delta\sigma$ in the literature is referred to as stress drop, effective stress, dynamic stress drop, Brune stress drop, or rms stress drop and controls the strength of the HF radiation (Boore, 1983). C is a constant accounting for the effects of the radiation pattern as follows

$$C = \frac{R_{\varphi\theta}FV}{4\pi\rho\beta_s^{\,3}R_0} \qquad (1\text{-}41)$$

in which $R_{\varphi\theta}$ is the radiation pattern depending on the fault orientation, slip direction, and direction to the receiver (average value of 0.63 for S-waves based on Boore and Boatwright, 1984), F denotes the free surface effect (considered as 2 which is correct only for SH waves), V denotes a coefficient for partitioning the total shear-wave energy into horizontal component

$(1/\sqrt{2})$, ρ represents the density near the source, and R_0 is a reference distance (assumed to be 1). Regarding the equation of source spectrum, at LFs the seismic moment controls the spectral amplitude, while the stress drop and the seismic moment control the spectral amplitude at HFs. This is the simplest and most widely used source model known as the Aki-Brune omega-square model (Aki, 1967; Brune, 1970; Brune, 1971).

To find the source time function, Brune (1970) came up with equation (1-37) by solving equation (1-34). However, this is one of the solutions for the far-field displacement. There are infinite ad hoc source time functions which can satisfy equation (1-34) (Beresnev and Atkinson, 1997). Three of these functions are

$$
\begin{aligned}
D_0(t) &= D_0(1 - e^{-t/T_R}) \\
D_1(t) &= D_0\left[1 - (1 + t/T_R)e^{-t/T_R}\right] \\
D_2(t) &= D_0\frac{\left[2 - \left(1 + (1 + t/T_R)^2\right)e^{-t/T_R}\right]}{2}
\end{aligned}
\tag{1-42}
$$

in which D_0 is the maximum total slip of the fault. Then, the derivative of the displacement source time function can be expressed as

$$
\dot{D}_n(t) = \frac{D_0}{n!T_R}\left(\frac{t}{T_R}\right)^n e^{-t/T_R} \qquad n = 0,\ 1,\ 2
\tag{1-43}
$$

Figure 1-8 illustrates the displacement source time function and the slip velocity time function. As can be seen, $n = 0$ has a discontinuity at $t = 0$ in the velocity source time function; thus, it is physically unrealistic. Substituting equation (1-43) into (1-34), we obtain the general form of the far-field displacement in the time domain as

$$
U_C(R,t) = \frac{\mu A}{4\pi\rho V_C^3}\frac{R_{\theta\varphi}}{R}\left[\frac{D_0}{n!T_R}\left(\frac{t - R/\beta}{T_R}\right)^n e^{-(t-R/\beta)/T_R}\right] = \frac{R_{\theta\varphi}M_0}{4\pi\rho V_C^3 R}\frac{1}{n!T_R}\left(\frac{t - R/\beta}{T_R}\right)^n e^{-(t-R/\beta)/T_R} \tag{1-44}
$$

and by getting a Fourier Transform the general form of the far-field displacement in the frequency domain can be expressed as (Tumarkin and Archuleta, 1994; Beresnev and Atkinson, 1997)

$$\left|U_C(R,\omega)\right| = \frac{R_{\theta\varphi}M_0}{4\pi\rho V_C^3 R} \frac{1}{\left[1+\left(\omega/\omega_c\right)^2\right]^{\frac{(n+1)}{2}}} = CM_0 \frac{1}{\left[1+\left(\omega/\omega_c\right)^2\right]^{\frac{(n+1)}{2}}} \qquad (1\text{-}45)$$

where ω_c is the corner frequency defined as $2\pi/T_r$. If $n = 1$ the source spectrum is called the ω-square model, and if $n = 2$, the source spectrum is called the ω-cube model.

The general form of scaling relationship, equation (1-26), can also be expressed as (Tumarkin *et al.*, 1994)

$$M_0 = C_M R^\delta \Delta\sigma \qquad (1\text{-}46)$$

where C_M is a constant of proportionality and δ is the seismic moment scaling exponent. Since the corner frequency is inversely proportional to the earthquake dimension as $f_c = C_f R^{-1}$ (Brune, 1970; Madariaga, 1976), the above-mentioned equation can be rewritten as (Kanamori and Rivera, 2004)

$$\begin{aligned} M_0 f_C^\delta &\propto \Delta\sigma \\ M_0 f_C^\delta &= M_0 f_C^{(3+\varepsilon)} = C\Delta\sigma \qquad \varepsilon \le 1 \end{aligned} \qquad (1\text{-}47)$$

in which C is a constant. Assuming $\delta = 3$ results in equation (1-40) of Brune (1970) and, $\delta = 4$ was used by Nuttli (1983).

As mentioned earlier, the near-field point-source model may need to have more than one corner frequency to account for the effect of dimensions, rise time, and rupture time to match apparent MRFs (observed source spectra) (Archuleta and Ji, 2016). Some researchers observed that the source spectrum of large earthquakes is better defined with a double corner frequency (DCF) point-source model which has a sag between two corner frequencies (Joyner, 1984; Boore, 1986; Atkinson and Boore, 1995; Atkinson and Sonley, 2003; Yenier and Atkinson, 2014). Even for small to moderate earthquakes, the source spectrum may need two corner frequencies to match the apparent MRFs. For instance, several investigators observed that the MRF of moderate earthquakes occurring in northeastern North America show a double corner frequency model (e.g., Boatwright, 1994; Atkinson and Boore, 1995; Atkinson and Sonley, 2003; Boatwright and Seekins, 2011). Moreover, Archuleta and Ji (2016) concluded that the attenuation-corrected apparent MRF for earthquakes with $3.3 < \mathbf{M} < 5.3$ that occurred in California (from the NGA-West2 database) has two corner frequencies, between which the

spectrum decays as ω^{-1} and the effect of ignoring attenuation results in incorrectly obtaining a single corner frequency MRF.

Boore *et al.* (2014) generalized double corner frequency (DCF) source models into multiplicative and additive models. The basic assumptions about these generalized models are that the acceleration spectrum decay rate is proportional to f^2 at LF; whereas, it has a constant level at HF equal to the HF level of SCF with a particular stress drop.

The multiplicative double corner frequency (MDCF) model for acceleration is obtained by multiplication of two spectra as (Boore *et al.,* 2014)

$$S(f) = CM_0 (2\pi f)^2 \frac{1}{\left(1 + \left(\frac{f}{f_a}\right)^{pf_a}\right)^{pd_a}} \frac{1}{\left(1 + \left(\frac{f}{f_b}\right)^{pf_b}\right)^{pd_b}} \qquad (1\text{-}48)$$

where *pf* and *pd* represent the power of frequency and the power of denominator, respectively. The subscripts *a* and *b* are related to the first (lower) and second (higher) corner frequencies, respectively. Since the HF level of the acceleration spectrum of DCF and SCD models are equal, it requires the following constraints

$$pf_a \times pd_a + pf_b \times pd_b = 2$$
$$f_a^{pf_a \times pd_a} \times f_b^{pf_b \times pd_b} = f_c^2 \qquad (1\text{-}49)$$

f_c is known using equation (1-40). The additive double corner frequency (ADCF) model for acceleration is constructed by summation of two spectra as (Boore *et al.,* 2014)

$$S(f) = CM_0 (2\pi f)^2 \left[\frac{1 - \varepsilon}{\left[1 + \left(\frac{f}{f_a}\right)^{pf_a}\right]^{pd_a}} + \frac{\varepsilon}{\left(1 + \left(\frac{f}{f_b}\right)^{pf_b}\right)^{pd_b}} \right] \qquad (1\text{-}50)$$

where ε is a weighting factor in the range of 0 to 1 for assigning the contribution of each SCF spectrum. The HF level of the acceleration spectrum of DCF and SCD models should be equal; thus, it imposes the following constraints

$$pf_a \times pd_a = pf_b \times pd_b = 2$$
$$(1-\varepsilon)f_a^2 + \varepsilon f_b^2 = f_c^2$$

(1-51)

Therefore, if one of the corner frequencies is specified, the other one can be obtained from equations (1-49) and (1-51) for a given f_c. One significant difference between the SCF and DCF models is the difference between their source durations. In the SCF the source duration is defined as $1/f_c$; while in the DCF models the duration is defined as $0.5/f_a+0.5/f_b$. Longer duration of DCF models results in decreasing the amplitude and consequently in decreasing the response spectra obtained from these models.

1.3.3 Improvement 2 – Incorporating the Effective Distance

One important effect of finite-fault rupture is distance-magnitude saturation caused by the fault-site geometry and effect of propagation path. The saturation effect indicates the reduction of ground motion amplitude because of motions coming from different parts of the fault with different distances which are larger than the closest distance to the site such as the rupture or Joyner-Boore distances. To account for the effect of saturation, we will introduce a new effective distance. In this regard, the finite-fault source is partitioned into small elements in which each element is a point source and summation of radiated energy from all these small elements produce the final ground motion shaking generated by the finite-fault source (homogenous energy radiation from the fault). In fact, all points of the finite source model radiate uniform energy with equal intensity. We are looking for an effective point that if the whole finite fault is modeled in that point gives the same results and identical total energy as the finite source model (Yenier and Atkinson, 2014). Note that elements that are located with shorter distances have a higher contribution to the total energy captured at the station compared to elements with longer distance, due to the presence of the geometrical spreading and anelastic attenuation.

The path function in the frequency domain, which intuitively accounts for the geometrical spreading and attenuation terms, is used for estimating the effective distance. In this regard, distances from site to sub-faults take appropriate weights based on geometrical spreading and attenuation functions. Short period (high frequency) seismic waves have random phases; therefore, they are considered as incoherent waves and to obtain the total energy for the entire extended-fault we should sum the energy spectrum (squared amplitude spectrum) of each

segment. This approach is similar to what Boore (2009) has done to modify the SMSIM software.

We first derive general distance conversion equations to convert the Joyner-Boore distance to the effective distance and vice versa. Then, using seismological and geological characteristics of CENA such as geometrical spreading and attenuation functions, fault dimensions, and fault location, converted effective distances are obtained for different magnitude-JB distance bins. These effective distances will be incorporated in the SSGFM to capture the effect of saturation resulted from the fault-site geometry in Chapter 6.

1.4 Objectives and Scope of the Study

The main objective of this study is to develop an improved method to simulate broadband synthetic strong ground motion time histories using small magnitude events. The new improved method is used to generate realistic and appropriate time series in CENA having the key features of ground motions expected in this region for generic hard rock sites. In CENA where no detailed information about the faults such as slip distribution, geometry of the fault, and asperity location can predict for future earthquakes, the SSGFM is a simple, convenient, and fast technique to simulate strong ground motion time histories because it stochastically captures the effect of rupture propagation for large earthquakes. We propose two important modifications to improve the SSGFM. First, we introduce a new distance metric "effective distance," to capture the effect of propagation path on seismic waves coming from different parts of the fault resulting in saturation. Special attention is focused on reducing uncertainties. Moreover, we propose a new summation scheme to incorporate DCF source models, which is important for large earthquakes. We will combine the new proposed improvement for the SSGFM in a MATLAB code to generate synthesized waveforms. The MATLAB code will be verified using synthetics and real observed recordings including mainshock and foreshock/aftershock data. As an application to our code, we will use it to simulate synthetic broadband strong ground motions within CENA. In this regard, we employ synthetic weak ground motions as input motions to the code. The advantage of using these synthetic weak motions instead of EGFs is that the resultant strong ground motion time histories are region-specific, constructed based on the seismological characteristics of CENA. Thus, they can be used in development of GMPEs for this region. To

this end, we simulate weak motions using SMSIM for small earthquakes with **M**3.5, **M**4.0, and **M**4.5 which can be effectively considered as a point source. The SSGFM is implemented to simulate synthetic time histories for moment magnitudes of **M**5.0 to **M**8.0 in 0.5 increments using the generated weak motions at the JB distance range of 1 to 1000 km. Synthesized large magnitude time histories generated based on this proposal will be validated against existing GMPEs developed for CENA. The simulated ground motions are then employed for GMPE development. Furthermore, the simulated ground motions can be use in linear/nonlinear structural dynamic analysis/design, performance-based design, and seismic hazard analysis.

1.5 Organization of the Report

This report has 7 chapters. This chapter includes the background and general explanation and framework about the report. The remaining chapters are organized as follows:

In Chapter 2, distinct techniques proposed for producing synthetic time series using the SSGFM are described, and a comparison between advantages and disadvantages of those methods is performed. Finally, an alternative new rupture time probability function will be developed and will be shown why it works better. Then, this chapter presents the two-stage SSGFM in which the future large earthquake is divided into a few patches and small earthquakes are triggered inside these patches to account for the effect of asperities.

Chapter 3 discusses how to extend the SSGFM to DCF source model since this method is a scaling approach and it is not necessarily required to use small earthquakes. In fact, it is possible to generate synthetic time series for earthquakes with magnitudes of interest using any recorded earthquakes with different magnitudes which obey various source models such as DCF source models.

Chapter 4 describes some adjustment factors to convert between point-source and extended-fault models. In this regard, an effective distance or center of released energy, in which we define a virtual point providing the same amount of energy at the station as a finite-fault would provide, is defined that can account for the effect of propagation path on seismic waves. The SSGFM simulates ground motions at the center of energy. Therefore, using the presented conversion equations between the effective distance and the Joyner-Boore distance, the effective

distance is converted to the JB distance which is one the most widely used distance metrics in earthquake engineering and seismology.

In Chapter 5, multiple MATLAB functions are written to generate synthetic large earthquake time histories including different methods proposed and developed for producing synthetic time histories using input ground motion as seeds. Then, the written codes are validated using synthetic and real earthquake data. To this end, we use the shock and foreshock/aftershock data as large and small earthquakes and compare the simulated time histories with the observed data in terms of amplitude (PGA and PGV), frequency content, significant duration (Trifunac and Brady, 1976), and elastic response spectra, PSAs (Bozorgnia *et al.*, 2010).

Chapter 6 employs the written codes based on the explained approaches to simulate ground motions in CENA. One of the difficulties of using empirical Green's functions is that recordings of small earthquakes should be available. So, what if there is no recording available at the site of interest? Furthermore, most recordings of small earthquakes are contaminated with noise. In this regard, we simulate region-specific synthetic weak motions to be used as seeds (input motions) within the framework of the SSGFM. The simulated time histories are then used to develop a suite of GMPEs for CENA. Derived GMPEs are validated against real observations and predicted mean values of PGA, PSA, and PGV from existing GMPEs developed for this region.

Finally, Chapter 7 summarizes significant results and conclusions presented in this report. Recommendations for future studies are also presented.

1.6 Figures
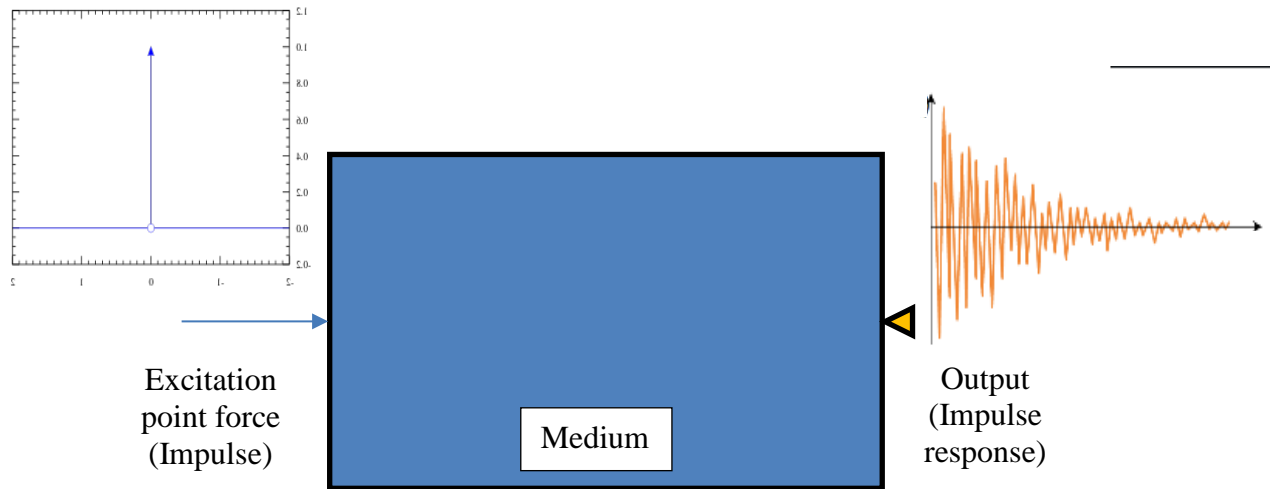
Figure 1-1. Impulse response function (Definition of Green's function). The triangle on the right

of the medium is a sensor to capture the response such as a seismometer or accelerometer.
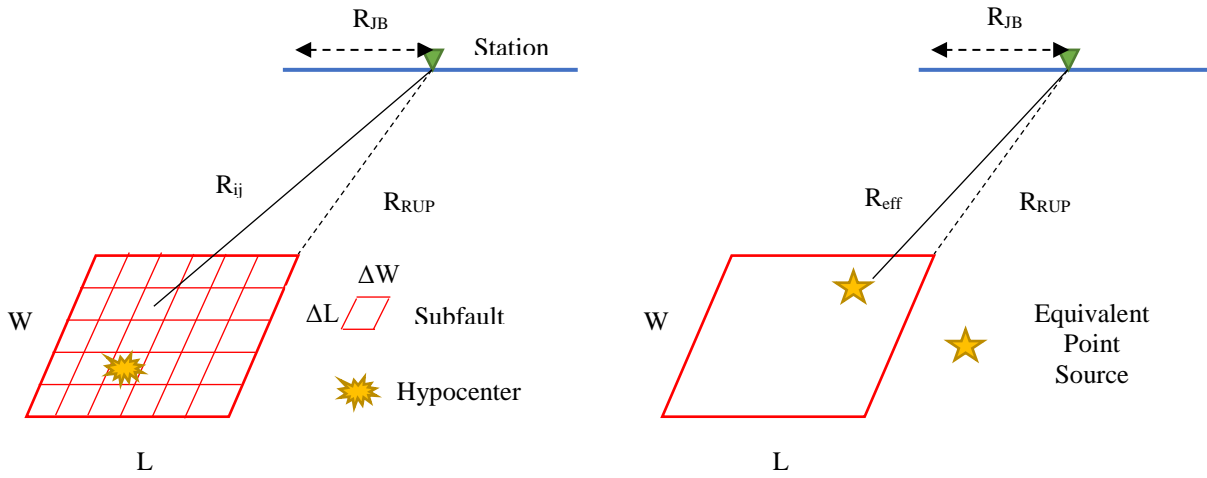
Figure 1-2. The difference between the effective distance with the other distances.
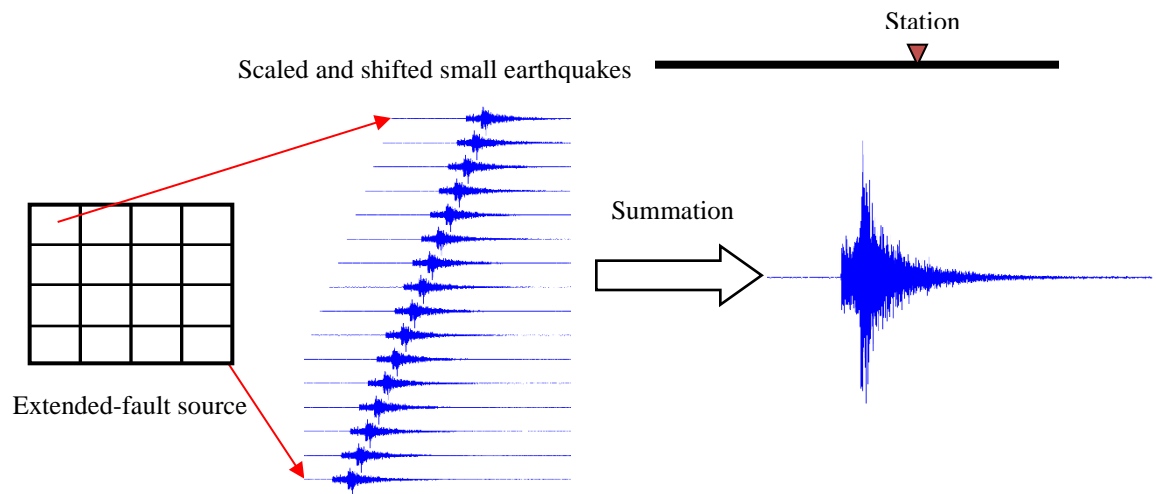
Figure 1-3. Schematic diagram of a predicted strong ground motion using the SSGFM.
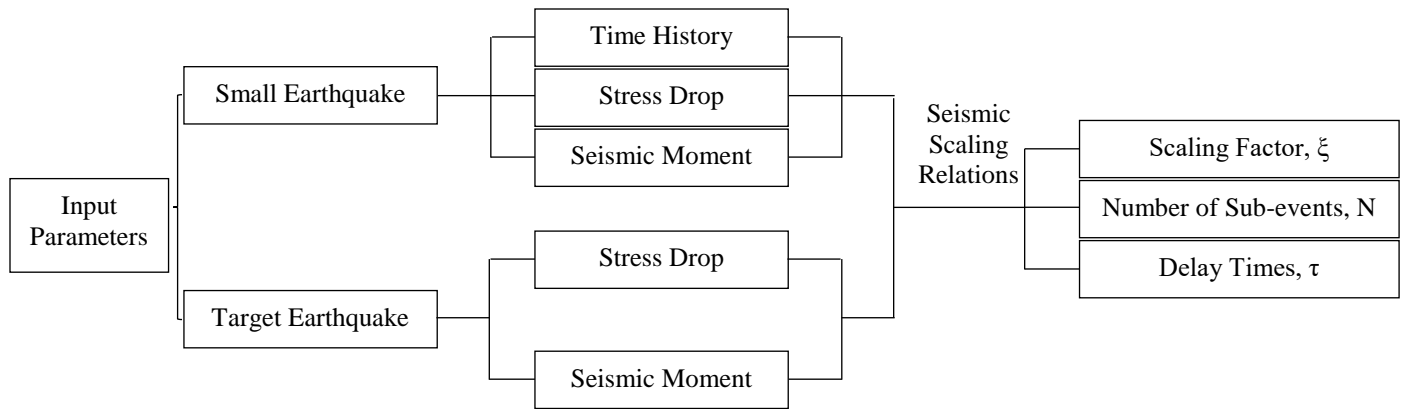
Figure 1-4. Schematic illustration of different steps for simulation of large earthquakes (target) using the SSGFM.
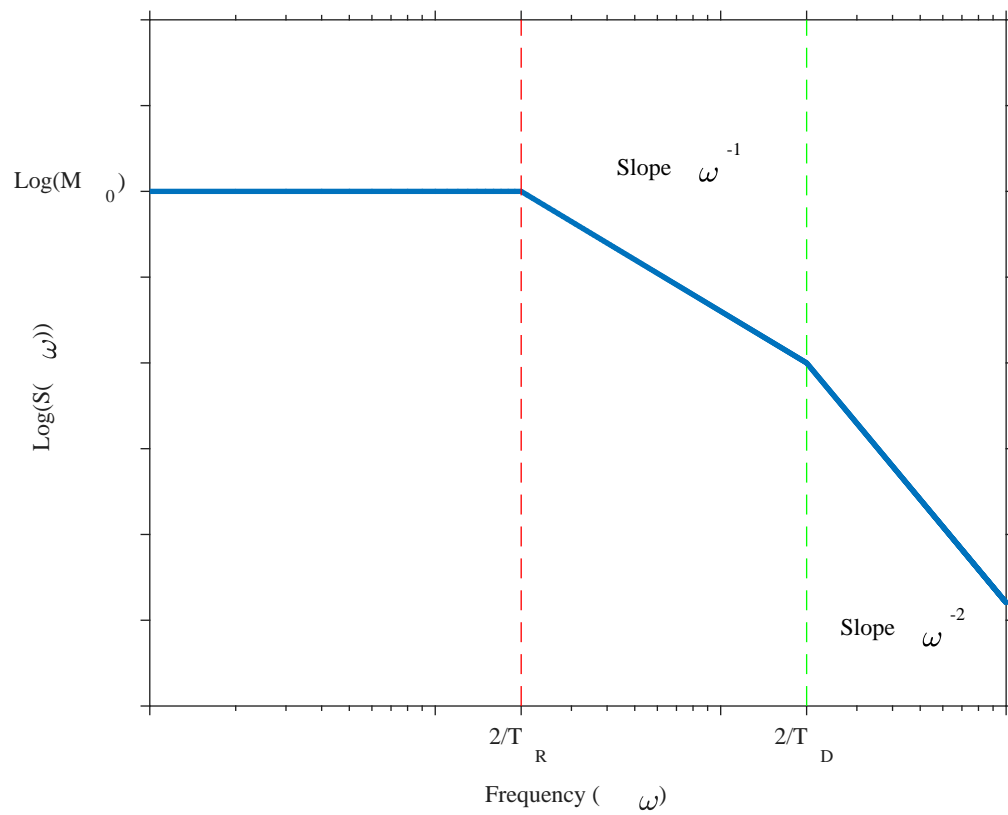
Figure 1-5. Schematic plot for the approximation of theoretical source time function.
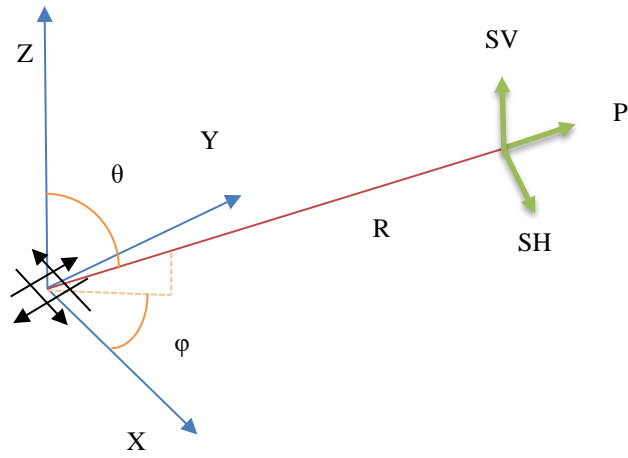
Figure 1-6. Radiation of *P* and *S*-waves from a double-couple point source (shear-dislocation).

Dislocation source time function

D_0

Velocity source time function

T

Autocorrelation function

-T   0   T
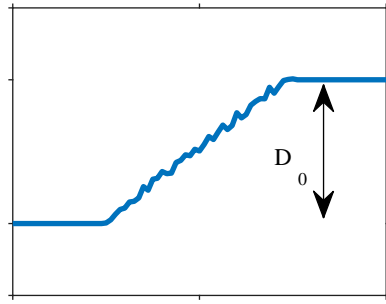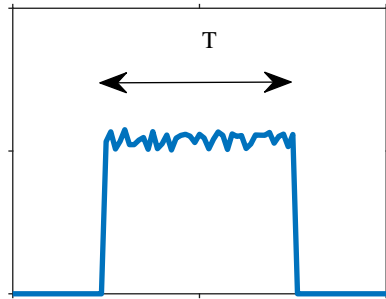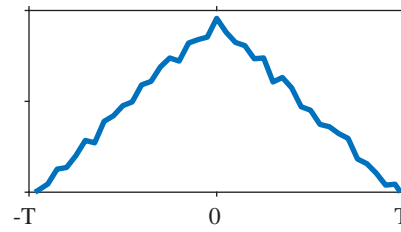
Figure 1-7. Schematic plot of the displacement, velocity, and autocorrelation functions. D_0 is the total final slip and T is the rise time.
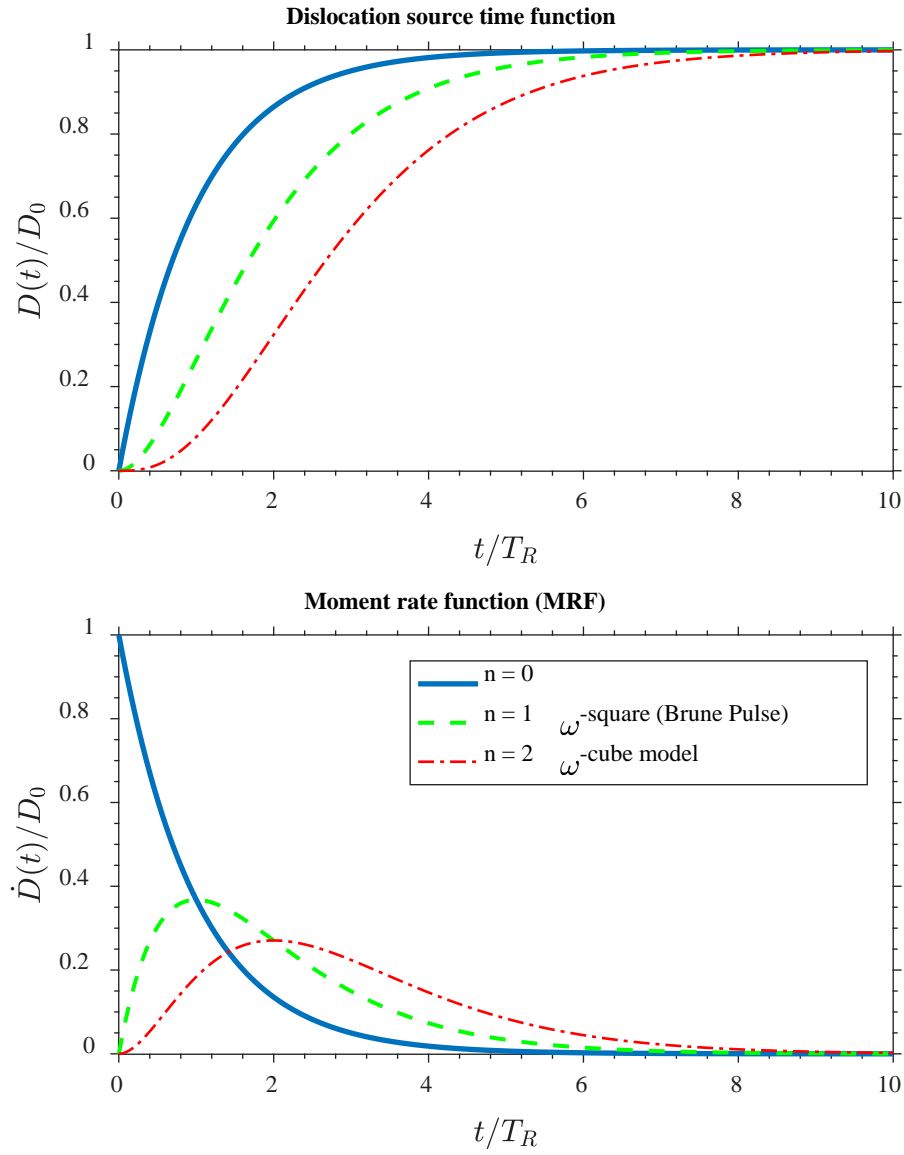
Figure 1-8. Theoretical general form of displacement source time function and slip velocity source time function.

2. Generalization of the Stochastic Summation Schemes for the Single Corner Frequency Source Spectral Model

2.1 Introduction

The stochastic summation of Green's functions method (SSGFM) scheme is a simple and straightforward technique which requires a recorded small earthquake time history plus stress drop and moment magnitude values of both small and target events. In essence, the target fault area is partitioned into a large number of identical sub-faults representing the small earthquake fault area. The displacement pulse radiated from each sub-fault can be treated as Brune's pulse in the far field. In other words, a hierarchical set of smaller earthquakes make a large earthquake. In fact, strong motion records for a high-magnitude earthquake can be defined as a summation (linear combination) of delayed (lagged or shifted) and scaled small-event time histories (Hartzell, 1978; Irikura, 1983; Irikura, 1986; Munguia and Brune, 1984; Joyner and Boore, 1986; Boatwright, 1988; Wennerberg, 1990; Tumarkin and Archuleta, 1994; Ordaz *et al.,* 1995; Kohrs *et al.,* 2005). Therefore, the process can be characterized in 3 steps. The first and second steps are to find the number of sub-events and the scaling factor, respectively. The scaling factor is a factor that scales the small earthquake to a unit excitation (Wu, 1978; Wu, 1981). The third and the most important step is to produce a probability distribution function to generate rupture times (delay times) for sub-events to account for rupture propagation. Thus, it is required to find the scaling factor, the number of cells, and the rupture times where the expected spectrum matches the spectrum of the target event, to attain realistic accurate synthetic time histories.

In the SSGFM, three components of a large earthquake can be simultaneously simulated in the whole frequency range using a linear combination of a specific number of shifted and scaled small earthquakes' time histories. Hence, the amplitude of the target event (total seismic signal at a particular site) in the time domain, $Y_t(t)$, can be written as

$$Y_t(t) = \xi[Y_s(t-\tau_1) + Y_s(t-\tau_2) + \cdots + Y_s(t-\tau_N)] = \xi\sum_{i=1}^{N} Y_s(t-\tau_i), \qquad (2\text{-}1)$$

where $Y_t(t)$ gives the amplitude of the postulated earthquake (total seismic signal at a particular site), ξ represents the scaling factor, N denotes the number of sub-events, and $Y_s(t)$ gives the

amplitude of the observed small earthquake (the signal of sub-events at that site). τ_i is the rupture time for sub-event ith (rupture i starts radiating at τ_i). In fact, each subevent begins to radiate at rupture time τ_i. Delay times generally describe the effect of directivity and rupture velocity (Hartzell, 1978). Since there are no specific restrictions for the rupture times and no assumptions for the fault size and position of nucleation for a future earthquake, this summation called a stochastic (or random) summation scheme. The aforementioned equation can be written in the frequency domain as

$$Y_t(\omega) = \xi Y_s(\omega) \sum_{i=1}^{N} \exp(-i\omega\tau_i).$$ (2-2)

Delay times in the time domain equation, implying the rupture propagation, are turned into phase shifts (exponential term) in the frequency domain equation. Regarding different source models like single and double corner frequencies, diverse rupture time probability functions will be introduced. In the following, we will explain how to define N, ξ, and τ_i to obey scaling relations corresponding to the widely used source models such as the ω-squared model (Aki, 1967; Brune, 1970).

In this chapter, how one can obtain these three parameters (ξ, N, and $p(t)$ to generate delay times) to simulate a postulated major earthquake are explained. In this regard, some mathematical definitions are reviewed first. Then, the procedures proposed by Joyner and Boore (1986), Wennerberg (1990), Tumarkin and Archuleta (1994), and Ordaz *et al.* (1995) are described.

2.2 **Mathematical Definitions**

The expected value of a function, $g(x)$, over a specific probability distribution function (pdf), $f_x(x)$, is defined as

$$E[g(x)] = \int_{-\infty}^{+\infty} g(x) f_x(x) dx$$ (2-3)

The Fourier transform of a function is defined as

$$Fourier\{\varphi(t)\} = \phi(f) = \int_{0}^{T} \varphi(t) e^{-i\omega t} dt$$ (2-4)

The inverse Fourier of a function is defined as

$$InverseFourier\{\phi(f)\} = \varphi(t) = \frac{1}{2\pi}\int_0^T \phi(f)e^{i\omega t}d\omega \tag{2-5}$$

The energy (power spectrum) of a function in the time domain, using the convolution (*), is defined as

$$Energy = \varphi(t) * \varphi^*(t) \tag{2-6}$$

in which the superscript * indicates the complex conjugate function. The energy (power spectrum) of a function in the frequency domain is defined as

$$Energy = \phi(f) \times \phi^*(f) \tag{2-7}$$

Based on the aforementioned equations, the expected power spectrum for the simulated seismic wave in the frequency domain can be written as

$$E\left[Y_t(\omega) \times Y_t^*(\omega)\right] = Y_t^{\,2}(\omega) = \xi^2 Y_s^{\,2}(\omega)E\left[\sum_{j=1}^N e^{-i\omega\tau_j} \times \sum_{k=1}^N e^{+i\omega\tau_k}\right] = \\ \xi^2 Y_s^{\,2}(\omega)E\left[\sum_{j=1}^N e^{-i\omega\tau_j}\right]E\left[\sum_{k=1}^N e^{+i\omega\tau_k}\right] \tag{2-8}$$

and using equation (2-3)

$$Y_t^{\,2}(\omega) = \xi^2 Y_s^{\,2}(\omega)\left[\sum_{j=1}^N \int_0^T p(\tau_j)e^{-i\omega\tau_j}d\tau_j\right]\left[\sum_{k=1}^N \int_0^T p(\tau_k)e^{+i\omega\tau_k}d\tau_k\right] \tag{2-9}$$

Therefore, the expected energy of the simulated seismic wave is

$$Y_t^2(\omega) = \xi^2 Y_s^2(\omega) \times \begin{cases} \sum_{j=1}^N \left[\int_0^T p(\tau_k)d\tau_k\right]^2 & j=k \\ \sum_{j=1}^N\sum_{k=1}^N \int_0^T p(\tau_j)e^{-i\omega\tau_j}d\tau_j\int_0^T p(\tau_k)e^{+i\omega\tau_k}d\tau_k & j \neq k \end{cases} \tag{2-10}$$

Since

$$\int_0^T p(t)dt = 1 \\ |p(\omega)| = \int_0^T p(t)e^{\pm i\omega t}dt \tag{2-11}$$

we obtain

$$Y_t^2(\omega) = \xi^2 Y_s^2(\omega) \left[N + N(N-1) |p(\omega)|^2 \right] \tag{2-12}$$

Finally, by taking a square root from both sides, we have

$$Y_t(\omega) = \left[\xi \sqrt{N + N(N-1) |p(\omega)|^2} \right] Y_s(\omega) = \left[\xi N \sqrt{\frac{1 + (N-1) |p(\omega)|^2}{N}} \right] Y_s(\omega) \tag{2-13}$$

Thus, $p(\omega)$ is the spectrum (Fourier transform) of the probability distribution function (pdf) of rupture times.

2.3 One-stage Stochastic Summation Schemes for the Single Corner Frequency Source Spectral Model

2.3.1 Joyner and Boore (1986) Scheme

First, it should be mentioned that Boore and Joyner did not introduce any particular procedure for the SSGFM, but they showed how to constrain the LF and HF predictions using the seismic scaling relations with a uniform distribution of random delay times over the rupture duration of the target event. In this scheme, N identical sub-events scaled by a factor, ξ, are added together using random rupture times with a uniform distribution over the source duration, T_c. Hence, the pdf can be written as

$$p(t) = \frac{1}{T_c} \tag{2-14}$$

Next, taking a Fourier transform from the pdf of delay times, we get

$$\int_0^{T_c} p(t) e^{-i\omega t} dt = \text{sinc}(\omega T_c / 2) = \frac{\sin(\omega T_c / 2)}{\omega T_c / 2} \tag{2-15}$$

Therefore, the spectrum of the simulated event is

$$Y_t(\omega) = \left[\xi \sqrt{N + N(N-1)\left(\frac{\sin(\omega T_c/2)}{\omega T_c/2} \right)^2} \right] Y_s(\omega) \tag{2-16}$$

Then, the low and high frequency limits are used to constrain the summation as follows

$$\frac{Y_t(\omega)}{Y_s(\omega)} = \left[\xi N \right] \qquad \text{if } \omega \to 0$$

$$\frac{Y_t(\omega)}{Y_s(\omega)} = \left[\xi \sqrt{N} \right] \qquad \text{if } \omega \to \infty \tag{2-17}$$

As expected, the aforementioned equation shows that the spectra of sub-events are added coherently at very low frequencies and are added incoherently at very high frequencies to construct the target spectrum. Since the path, the site, and the instrument effects are the same for both events, they can be removed. Of course, there are some discrepancies between path and site effects for both events due to directivity, geometrical spreading, and scattering and intrinsic attenuation. But these variations are assumed to be insignificant and ignorable. Thus, the ratio of the amplitude of the target event to the sub-event for a ω-square source spectrum can be written as

$$\frac{Y_t(\omega)}{Y_s(\omega)} = \frac{S_t(\omega)}{S_s(\omega)} = \frac{\dfrac{M_t}{1 + \left(\omega/\omega_{ct} \right)^2}}{\dfrac{M_s}{1 + \left(\omega/\omega_{cs} \right)^2}} \tag{2-18}$$

So, we have

$$\frac{Y_t(\omega)}{Y_s(\omega)} = \frac{M_t}{M_s} \qquad \text{if } \omega \to 0$$

$$\frac{Y_t(\omega)}{Y_s(\omega)} = \frac{M_t}{M_s} \left(\frac{\omega_{ct}}{\omega_{cs}} \right)^2 \qquad \text{if } \omega \to \infty \tag{2-19}$$

Then, assuming both events have similar stress drop values (similarity assumption) with a scaling relation of $Mf_c^3 = $ constant, N and ξ can be obtained from equations (2-17) and (2-19) as follows

$$N = \left(\frac{M_t}{M_s} \right)^{4/3}$$

$$\xi = \left(\frac{M_t}{M_s} \right)^{-1/3}$$

(2-20)

Now, we have N, ξ, and rupture times generating from a uniform distribution in the interval of 0 to the duration of the target event, $T_{ct} = 1/f_{ct}$. This model is essentially a Haskell (1964) rupture where the slip velocity and rupture velocity are constant and the slip is the same all over the fault plane. To perform a numerical example for this scheme and the other schemes which are later explained in the remaining of this report, the following values to simulate a target event from a small event supposing both have identical stress drop values (assumption of similarity) is used

$$M_t = 1$$
$$M_s = 0.001$$
$$f_{ct} = 1$$
$$f_{cs} = 10$$

(2-21)

To do simulation, we use a sampling rate of 200 samples/sec (step size of 0.005 sec). Hence, the Nyquist frequency is 100 Hz (half of the sampling rate). Since the corner frequency of the target event is 1 Hz, the duration of the target event is 1 sec. Consequently, all the generated rupture times are placed between 0 to 1 sec. Figure 2-1 illustrates the distribution of the generated rupture times for one realization. To produce rupture times with a uniform distribution, first random numbers are generated over 0 to 1 and they are then scaled to the interval of 0 to T_{ct}. Then, N and ξ are determined. Finally, using equation (2-1), the simulated event is produced. Figure 2-2 presents 10 specific runs (simulations or realizations) of the Joyner-Boore scheme using the numerical example as well as the root mean square (rms) average spectrum from 10 different simulations. It should be mentioned that different realizations are similar but not identical due to the random nature of the generated rupture times for each realization. Again, we emphasize that what is shown in the plots as simulation indicates only 10 specific simulations and running another simulation would produce a slightly different spectrum.

Although the Joyner-Boore scheme predicts LFs and HFs of the target spectrum very well, the main problem of this scheme is that there are no constraints at intermediate frequencies

46

particularly near the corner frequency; and consequently, in this frequency range the simulation differs from the target event. Moreover, the appearance of the *sinc* function in the simulation process creates several holes (a periodic set of zeroes) in the simulated spectrum, particularly at frequencies above the corner frequency of the target event. Another flaw in this scheme is that stress drop values are supposed to be equal for the sub-event and target event, but in reality, they can be different.

2.3.2 Wennerberg (1990) Scheme

To find the pdf of rupture times covering the duration of the larger event, Wennerberg supposed that the density function has an amplitude spectrum equal to the ratio of the ω-square spectra of the target event to the sub-event and has a zero phase (non-causal). In fact, he assumed that the sub-event and target event have identical or very similar phases. In Wennerberg (1990), he assumes that the ratio of the spectra is

$$\frac{Y_t(\omega)}{Y_s(\omega)} = \left[\xi \sqrt{N + N(N-1)|P(\omega)|^2} \right] \approx \xi N |p(\omega)| \qquad \text{when } N \text{ is large} \qquad (2\text{-}22)$$

and then using equation (2-18), the following equations are obtained

$$p(\omega) = \frac{1 + \left(\omega \big/ \omega_{cs} \right)^2}{1 + \left(\omega \big/ \omega_{ct} \right)^2} \qquad (2\text{-}23)$$

$$\xi N = \frac{M_t}{M_s}$$

As can be seen, there is no specific equation to obtain the number of summands and the scaling factor and these two parameters are dependent. Therefore, one can acquire the scaling factor supposing a large number for the number of summands. Also, getting inverse Fourier transform from the amplitude of the density function in the frequency domain gives the zero-phase probability distribution (ZPD) for delay times as follows

$$p(t) = \left(\frac{\omega_t}{\omega_s} \right)^2 \left[\delta(t) + \frac{\omega_s{}^2 - \omega_t{}^2}{2\omega_t} e^{-\omega_t|t|} \right] \qquad (2\text{-}24)$$

in which $\delta(t)$ is the delta function. Since this function is ZPD, the shape of this function is symmetric around the y axis.

For the numerical example, values already described in the Joyner and Boore section are used. Wennerberg suggested using a large number for the number of sub-events. Here, we use 10,000 to be similar to other schemes. Then, the scaling factor can be obtained using the equation (2-23). To generate rupture times, the method proposed in the Appendix of Wennerberg (1990) is used. In this regard, first he calculated the cumulative distribution function (cdf) from the pdf using $P(t) = \int_{-\infty}^{t} p(t)dt$. Then, using differentiation he provided three equations to obtain rupture times. These equations are

$$
t = \frac{1}{\omega_t} \ln\left(\frac{2P}{1 - \left(\omega_t/\omega_s\right)^2} \right) \qquad 0 \leq P \leq \frac{1}{2}\left(1 - \left(\omega_t/\omega_s\right)^2\right)
$$

$$
t = 0 \qquad \frac{1}{2}\left(1 - \left(\omega_t/\omega_s\right)^2\right) \leq P \leq \frac{1}{2}\left(1 + \left(\omega_t/\omega_s\right)^2\right) \qquad (2\text{-}25)
$$

$$
t = \frac{1}{\omega_t} \ln\left(\frac{1 - \left(\omega_t/\omega_s\right)^2}{2(1-P)} \right) \qquad \frac{1}{2}\left(1 + \left(\omega_t/\omega_s\right)^2\right) \leq P \leq 1
$$

Since the cdf is always less than or equal to 1, we generate 10,000 random numbers (seeds) in the interval of [0, 1] as representative values from the cdf. Afterwards, rupture times are derived using the abovementioned equations corresponding to the generated P values. Figure 2-3 shows the distribution of the generated rupture times.

This distribution has a single peak at 0 sec and the most energy is distributed here. It is also symmetric around the y axis. Since the generated rupture times are symmetric, they compensate the effect of delays and the phase effectively stays zero. In this approach, approximately half of the rupture times are negative, and it is unrealistic. Hence, all rupture times are shifted by a constant value equal to the rupture duration ($T_{ct} = 1/f_{ct}$) to be properly treated and be appropriately applied for simulations. Another point is that there are rupture times which are larger than the total rupture duration, but those sub-events are rare. Note that $p(t)$ should not be

truncated to remove those rupture times because this process introduces a boxcar window and yields in holes in synthetized spectra.

Afterwards, the value of either N or ξ is assumed and the other value is determined. Finally, using equation (2-1), the simulated event is produced. Figure 2-4 presents 10 specific runs of the Wennerberg scheme using the numerical example.

The most important part of a spectrum for engineers and engineering applications is the high frequency part, and since there is no constraint at HFs, the simulated spectrum would be overestimated. Thus, this scheme has a huge deficiency in the HF part of the simulated spectrum that cannot be matched with the target event. For instance, using the number of summands proposed by Joyner and Boore (1986) overestimated the spectrum by a factor of $\sqrt{2}$ at HFs.

2.3.3 Tumarkin and Archuleta (1994) Scheme

To obtain values of scaling factor and number of sub-events, Tumarkin and Archuleta (1994) defines just one constraint and it is like the Wennerberg constraint. Hence, the number of sub-events is considered to be a large number and the scaling factor can be obtained by the following equation

$$\xi N = \frac{M_t}{M_s} \tag{2-26}$$

As opposed to the Wennerberg (1990) scheme in which he supposed that the transfer function is non-causal (zero-phase), Tumarkin and Archuleta (1994) introduced a transfer function which is causal and considers the phase difference between the source spectra of small and target events. Using the complex form of the source spectrum, the transfer function is defined as the ratio of the complex source spectra of target event to sub-event as follows

$$p(\omega) = \frac{S_t(\omega)}{S_s(\omega)} = \frac{\left(1 + i\dfrac{\omega}{\omega_{cs}}\right)^2}{\left(1 + i\dfrac{\omega}{\omega_{ct}}\right)^2} \tag{2-27}$$

The inverse Fourier transform of the above-mentioned equation is

$$p(t) = \left(\frac{\omega_t}{\omega_s}\right)^2 \left[\delta(t) + \left[2(\omega_s - \omega_t) + (\omega_s - \omega_t)^2 t\right] e^{-\omega_t t} H(t)\right] \qquad (2\text{-}28)$$

The cumulative distribution function (cdf) from the pdf using $P(t) = \int_{-\infty}^{t} p(t)dt$ can be written as

$$P(t) = \left[1 - \left[1 - \left(\frac{\omega_t}{\omega_s}\right)^2 + t\omega_t\left(1 - \frac{\omega_t}{\omega_s}\right)^2\right] e^{-\omega_t t}\right] H(t) \qquad (2\text{-}29)$$

To generate rupture times, we first construct a $t - P(t)$ table like normal distribution for various t values. The step size for t values in the table must be less than the step size of the small event. Then, like previous schemes, we generate N random numbers implying values of P. Finally, the corresponding t value can be reached from each P value (seed) using the constructed $t - P(t)$ table. Figure 2-5 displays the distribution of 10000 generated rupture times based on the Tumarkin and Archuleta (1994) transfer function for one realization.

The distribution starts from 0 and the transfer function, unlike other schemes, does not produce any negative rupture time. The shape of the distribution is very similar to a simple source time function for a large event (see Figure 1-5). Then, assuming 10000 sub-evens, we find the value of the scaling factor and using equation (2-26), the simulated event is produced. Figure 2-6 depicts 10 simulated spectra compared with the target and sub-event spectra as well as rms average spectra.

Even though the time domain distribution of the Tumarkin and Archuleta (1994) scheme is different than the Wennerberg (1990) scheme, they have similar spectra in the frequency domain due to the identical shape (amplitude) of their transfer functions in the frequency domain. Like the Wennerberg scheme, this scheme overestimates the spectrum at HFs. This overestimation of spectrum at HFs yields in higher maximum amplitude (such as PGA or PSA) in the time domain.

2.3.4 **Ordaz *et al.* (1995) Scheme**

In this scheme, the authors define a transfer function in such a way that the obtained expected spectrum exactly matches the theoretical spectrum in the whole frequency band. To this

end, N and ξ can be computed using the LF and HF restrictions. In essence, the spectral ratio of the expected target event over the small event can be written as

$$\frac{Y_t(\omega)}{Y_s(\omega)} = \left[\xi\sqrt{N + N(N-1)|p(\omega)|^2} \right] \qquad (2\text{-}30)$$

Since $p(\omega) = \int_0^T p(t)e^{-i\omega t}dt$, it can be shown that

$$
\begin{aligned}
p(\omega) &= 1 & \text{if } \omega \to 0 \\
p(\omega) &= 0 & \text{if } \omega \to \infty
\end{aligned}
\qquad (2\text{-}31)
$$

Therefore, the spectral ratios at very LF and very HF range can be written as

$$
\begin{aligned}
\frac{Y_t(\omega)}{Y_s(\omega)} &= \xi N & \text{if } \omega \to 0 \\[2mm]
\frac{Y_t(\omega)}{Y_s(\omega)} &= \xi\sqrt{N} & \text{if } \omega \to \infty
\end{aligned}
\qquad (2\text{-}32)
$$

This procedure is very similar to the Joyner and Boore procedure (see equation (2-17)) but Ordaz *et al.* (1995) calculate N and ξ in a general form with the possibility of having different stress drop values for the small and target events. Now, using the ratio of the amplitude of the target event to the sub-event, equations (2-18) and (2-19), we can get

$$
\begin{aligned}
N &= \left(\frac{\omega_{ct}}{\omega_{cs}} \right)^4 \\[2mm]
\xi &= \frac{\left(\dfrac{M_t}{M_s} \right)}{N}
\end{aligned}
\qquad (2\text{-}33)
$$

Then, using the equation between seismic moment, stress drop, and corner frequency (see equation (1-40), the scaling law), N and ξ can be obtained by

$$
\begin{aligned}
N &= \left(\frac{M_t}{M_s} \right)^{4/3} \left(\frac{\Delta\sigma_t}{\Delta\sigma_s} \right)^{-4/3} \\[2mm]
\xi &= \left(\frac{M_t}{M_s} \right)^{-1/3} \left(\frac{\Delta\sigma_t}{\Delta\sigma_s} \right)^{4/3}
\end{aligned}
\qquad (2\text{-}34)
$$

At the intermediate frequency range, the spectral ratio can be written as

$$\frac{Y_t(\omega)}{Y_s(\omega)} = \frac{M_t}{M_s}\frac{1+\left(\omega/\omega_{cs}\right)^2}{1+\left(\omega/\omega_{ct}\right)^2} = \left[\xi\sqrt{N+N(N-1)|p(\omega)|^2}\right] \tag{2-35}$$

After simplifying the abovementioned equation, the Fourier transform of the pdf function of rupture times is derived as

$$|p(\omega)| = \frac{\sqrt{1+\dfrac{2\omega^2}{\omega_{cs}^2+\omega_{ct}^2}}}{1+\left(\dfrac{\omega}{\omega_{ct}}\right)^2} \tag{2-36}$$

Supposing that $p(\omega)$ is real, then the pdf function of rupture time can be obtained by getting the inverse Fourier transform as

$$p(t) = \frac{1}{2\pi}\int_{-\infty}^{\infty}\frac{\sqrt{1+\dfrac{2\omega^2}{\omega_{cs}^2+\omega_{ct}^2}}}{1+\left(\dfrac{\omega}{\omega_{ct}}\right)^2}e^{i\omega t}d\omega \tag{2-37}$$

The first step to use this scheme is to determine N and ξ that for the numerical example are 10,000 and 0.1. Then, we need rupture times to perform a summation. To generate rupture times, we use a procedure explained in Appendix A of Ordaz *et al.* (1995). They did not find any analytical solution for the inverse of the cdf of rupture time. However, they provide an equation to numerically find the cdf of rupture times as

$$P(t) = 0.5+0.5\left(1-e^{-\omega_t t}\right)\sqrt{1-a}+\frac{1}{\pi}\sqrt{a}\int_{1/\sqrt{a}}^{\infty}\frac{\sqrt{y^2-\dfrac{1}{a}}}{y(y^2-1)}\left(1-e^{-\omega_t ty}\right)dy \qquad t \geq 0 \tag{2-38}$$

$$P(-t) = 1-P(t)$$

Like the Tumarkin and Archuleta (1994) scheme, we construct a $t - P(t)$ table for various t values. Afterwards, we generate 10000 random numbers in the interval of [0, 1] acting as P values. Then, rupture times are determined using the $t - P(t)$ table for generated P values. Figure

2-7 shows the distribution of generated rupture times with the pdf proposed by Ordaz *et al.* (1995). As can be seen, it goes to infinity from both tails. Therefore, the generated rupture times are shifted by a constant value equal to the duration of the target event. There are a very small number of rupture times that are placed out of the total duration of the target event (less than 5%). Note that the rupture times should not be truncated to consider only the rupture times within the duration, since it introduces a boxcar in the time domain and a *sinc* function in the frequency domain resulting in a periodic set of zeroes. Figure 2-8 demonstrates 10 simulated spectra compared with the target and sub-event spectra as well as the rms average spectra. As can be seen, the spectrum of simulation matches the expected spectrum of the target event at the whole frequency band.

2.3.5 TSP1 Scheme

Coherent (smooth) portions of the source process generate LF waves, while incoherent (small scale heterogeneities) portions of the source process produce HF waves. In fact, a slip on a fault has two parts. The first part is a uniform slip (background slip) with a uniform stress drop over the entire fault. This part describes the LF seismic radiation. The second part is related to irregular slips over a heterogeneous fault to explain the HF radiation, particularly for large earthquakes (Aki, 1984). Thus, the overall fault rupture process is heterogeneous and it should be taken into account in the modeling of the source. These heterogeneities on the fault plane are called asperities, defined as strong patches resisting against breaking during a large earthquake.

To construct the spectrum of a large earthquake, subevent spectra are coherently added at LFs while they are incoherently added at HFs. In the middle frequency range, the feature of incremental transition from complete coherence at LFs to complete incoherence at HF is called partial coherency (Haskell, 1964; Tumarkin and Archuleta, 1994). Thus, the target spectrum, $S_t(\omega)$, can be expressed by the summation of scaled source spectra as

$$\left|S_t(\omega)\right|^{\varepsilon(\omega)} = \left|\xi_1 S_1(\omega)\right|^{\varepsilon(\omega)} + \left|\xi_2 S_2(\omega)\right|^{\varepsilon(\omega)} + \ldots + \left|\xi_N S_N(\omega)\right|^{\varepsilon(\omega)} \tag{2-39}$$

and once all subevents have identical source spectra, $S_s(\omega)$, we have

$$\left|S_t(\omega)\right|^{\varepsilon(\omega)} = N\left|\xi S_s(\omega)\right|^{\varepsilon(\omega)} \tag{2-40}$$

where $\varepsilon(\omega)$ is the power for raising each subevent spectrum. Using the coherent summation at LFs and incoherent summation at HF, two constraints can be put on the power function as

$$\omega \to 0 \Rightarrow \varepsilon(\omega) \to 1 \Rightarrow \left|S_t(\omega)\right| = N\left|\xi S_s(\omega)\right|$$
$$\omega \to \infty \Rightarrow \varepsilon(\omega) \to 2 \Rightarrow \left|S_t(\omega)\right|^2 = N\left|\xi S_s(\omega)\right|^2 \tag{2-41}$$

Therefore, the ratio of source spectra can be written as

$$\left|\frac{S_t(\omega)}{S_s(\omega)}\right| = \xi N^{1/\varepsilon(\omega)} \tag{2-42}$$

To generalize the summation scheme, we suppose that the spectrum has the general form of

$$\left|S(\omega)\right| = CM_0 \frac{1}{\left[1+\left(\omega/\omega_c\right)^{pf}\right]^{pd}} \tag{2-43}$$

Hence, the source spectral ratio is given by

$$\left|\frac{S_t(\omega)}{S_s(\omega)}\right| = \frac{\dfrac{M_t}{\left[1+\left(\omega/\omega_{ct}\right)^{pf}\right]^{pd}}}{\dfrac{M_s}{\left[1+\left(\omega/\omega_{cs}\right)^{pf}\right]^{pd}}} \tag{2-44}$$

So, the limits for the LF and HF ranges can be obtained from

$$\omega \to 0 \Rightarrow \left|\frac{S_t(\omega)}{S_s(\omega)}\right| = \frac{M_t}{M_s}$$
$$\omega \to \infty \Rightarrow \left|\frac{S_t(\omega)}{S_s(\omega)}\right| = \frac{M_t}{M_s}\left(\frac{\omega_{ct}}{\omega_{cs}}\right)^{pf \cdot pd} \tag{2-45}$$

By equality of equations (2-42) and (2-45), we obtain

$$\xi N = \frac{M_t}{M_s}$$
$$\xi \sqrt{N} = \frac{M_t}{M_s}\left(\frac{\omega_{ct}}{\omega_{cs}}\right)^{pf \cdot pd} \tag{2-46}$$

Thus, the scaling factor and the number of small events are generally determined from

$$N = \left(\frac{\omega_{cs}}{\omega_{ct}} \right)^{2pf \cdot pd}$$

$$\xi = \frac{M_t / M_s}{N} = \frac{M_t / M_s}{\left(\dfrac{\omega_{cs}}{\omega_{ct}} \right)^{2pf \cdot pd}}$$

(2-47)

If both events have similar stress drop values and the scaling of the source dimension and the seismic moment is as follows

$$M_0 f_C^{\delta} = \text{constant}$$

(2-48)

Note that many studies concluded that the δ should be equal to 3 and the other values are artifacts caused by the limited frequency band of data (e.g., Abercrombie, 1995; Hiramatsu *et al*., 2002). Using this equation, we get

$$N = \left(\frac{M_t}{M_s} \right)^{2pf \cdot pd / \delta}$$

$$\xi = \left(\frac{M_t}{M_s} \right)^{1 - 2pf \cdot pd / \delta}$$

(2-49)

To evaluate the power function, we should use the equilibrium for the middle frequency range as

$$\left| \frac{S_t(\omega)}{S_s(\omega)} \right| = \xi N^{1/\varepsilon(\omega)} = \frac{M_t}{M_s} \frac{\left[1 + \left(\omega / \omega_{cs} \right)^{pf} \right]^{pd}}{\left[1 + \left(\omega / \omega_{ct} \right)^{pf} \right]^{pd}}$$

(2-50)

Substituting N and ξ in the abovementioned equation, the power function can be obtained from

$$\varepsilon(\omega) = \frac{\ln N}{\ln N + \ln \left(\dfrac{\left[1 + \left(\omega / \omega_{cs} \right)^{pf} \right]^{pd}}{\left[1 + \left(\omega / \omega_{ct} \right)^{pf} \right]^{pd}} \right)} = \frac{1}{1 + \dfrac{\ln \left[1 + \left(\omega / \omega_{cs} \right)^{pf} \right] - \ln \left[1 + \left(\omega / \omega_{ct} \right)^{pf} \right]}{2pf \ln \left(\omega_{cs} / \omega_{ct} \right)}}$$

(2-51)

55

It is interesting to note that the power function is independent of *pd* (the power of the denominator) and *δ,* but dependent on *pf* (the power of frequency). However, by changing *δ*, the corner frequencies vary. Figure 2-9 illustrates the variation of epsilon with frequency for different cases with different corner frequencies.

It should be noted that Boore (2009) and Atkinson *et al*. (2009) used this approach to modify the EXSIM software to generate results matching the results of SMSIM. However, they used a transfer function in the middle frequency based on the ratio of the target to small event source spectrum. But here, we define $N^{(1/\varepsilon)}$ to automatically consider the effect of coherent, incoherent, and transition region at the same time.

Thus, the spectral ratios can be defined as

$$\left|\frac{S_t(\omega)}{S_s(\omega)}\right| = \xi N^{1/\varepsilon(\omega)}$$

$$\frac{Y_t(\omega)}{Y_s(\omega)} = \left|\frac{S_t(\omega)}{S_s(\omega)}\right| = \left[\xi\sqrt{N + N(N-1)|P(\omega)|^2}\right]$$

(2-52)

Therefore, by equality of these ratios, we have

$$p(\omega) = \sqrt{\frac{N^{2/\varepsilon(\omega)} - N}{N^2 - N}} = \sqrt{\frac{N^{(2/\varepsilon(\omega)-1)} - 1}{N - 1}}$$

$$p(t) = \frac{1}{2\pi}\int_{-\infty}^{\infty}\sqrt{\frac{N^{(2/\varepsilon(\omega)-1)} - 1}{N - 1}}e^{i\omega t}d\omega$$

(2-53)

where the *ε* is determined using equation (2-51). To determine the rupture times using the TSP1 method, we first construct a *t* – *P(t)* table. Then, we generate random numbers in the interval of [0, 1]. These random numbers are used as *P(t)* and using the constructed table, relevant rupture times, *t*, are picked.

2.3.6   **Classic ω2 source spectrum with the scaling assumption of Mf 3=Cσ**

Briefly speaking, the steps required for the SSGFM employing the TSP1 scheme is as follows

    1.   Select the seed input ground motion and its magnitude and stress drop.

    2.   Choose the magnitude and stress drop of the large magnitude event.

3. Determine ξ: to scale (normalize) the input seed to a unit excitation

$$\xi = \frac{M_t/M_s}{N} = \frac{M_t/M_s}{\left(\dfrac{\omega_{cs}}{\omega_{ct}}\right)^4} = \left(\frac{M_t}{M_s}\right)^{-\frac{1}{3}}\left(\frac{\Delta\sigma_t}{\Delta\sigma_s}\right)^{\frac{4}{3}}$$

(2-54)

4. Calculate N: the number of required subfaults to reach the target spectrum

$$N = \left(\frac{\omega_{cs}}{\omega_{ct}}\right)^4 = \left(\frac{M_t}{M_s}\right)^{\frac{4}{3}}\left(\frac{\Delta\sigma_t}{\Delta\sigma_s}\right)^{-\frac{4}{3}}$$

(2-55)

5. Generate τ: delay times to simulate the rupture propagation

$$p(t) = \frac{1}{2\pi}\int_{-\infty}^{\infty}\sqrt{\frac{N^{(2/\varepsilon(\omega)-1)}-1}{N-1}}e^{i\omega t}d\omega$$

(2-56)

where

$$\varepsilon(\omega) = \frac{1}{1+\dfrac{\ln\left[1+\left(\omega/\omega_{cs}\right)^2\right]-\ln\left[1+\left(\omega/\omega_{ct}\right)^2\right]}{4\ln\left(\omega_{cs}/\omega_{ct}\right)}}$$

(2-57)

6. Finally, add scaled and delayed motions from subfaults to construct the ground motion of the target event.

Figure 2-10 and Figure 2-11 depict the distribution of rupture times and 10 realizations using those generated rupture times using the TSP1 method, respectively, for the numerical example. It should be emphasized that this scheme is the same as the Ordaz *et al.* (1995) scheme and the only difference is the procedure to obtain the pdf for generating rupture times. This method has been tested with other examples provided in the Appendix A.

2.3.7 General Comparison between One-stage Schemes

To generally compare these schemes, Figure 2-12 demonstrates the plots for the expected spectra of all schemes in addition to the spectra of the target event and small event. The Joyner and Boore (1986) method underestimates the expected spectrum in the intermediate frequency range and contains holes; however, it matches the target spectrum at LFs and HFs. The

Wennerberg (1990) and Tumarkin and Archuleta (1994) spectra are completely identical and they overestimate spectra at the HF range. Of course, the difference between these two schemes appears in the time domain, since the pdf function proposed by the Wennerberg (1990) scheme does not introduce any phase delay, but there a phase delay in the Tumarkin and Archuleta (1994) function. Although the Ordaz *et al*. (1995) and TSP1 spectra completely match the target spectrum, the shape of simulated time histories will be somehow unrealistic due to concentration of the energy at a single peak in the middle.

2.4 Two-stage Stochastic Summation Schemes for the Single Corner Frequency Source Spectral Model

Generally, there are two different views to model an idealized heterogeneous composite fault plane which is a rectangular including small circles (Aki, 1982). In the first view, the "asperity model," each circle is considered as a patch with very strong cohesion against the break. Then, each circular patch slips independently and generates HF waves (Wesson *et al.,* 1973; Kanamori and Stewart, 1978; Li and Dmowska, 1981). In the second view, circles indicate cracks which can break and a slip occurs on them; however, the remaining regions will be unbroken after the rupture (Das and Aki, 1977). This model is known as the "barrier model" (Aki *et al.,* 1977). Barriers cause an irregular slip distribution, and thereby an irregular stress drop distribution (Irikura, 1983). Of course, a realistic fault plane may consist of a combination of patches and barriers (Aki, 1982). For large earthquakes such as the 2011 **M**9.0 Tohoku, Japan earthquake (Ghofrani *et al*., 2013) and the 2010 **M**8.8 Maule, Chile earthquake (Frankel, 2017), the rupture propagation is often very complex and heterogeneous. There are some parts on the fault that radiate seismic waves stronger than other parts which are known as asperities (Boatwright, 1988). During an earthquake, rupture usually begins from an asperity and the most released energy of the earthquake comes from the asperities that become unlocked or unstuck. By expanding the rupture area, more than one asperity would be required to mimic the realistic behavior of the earthquake (Archuleta and Ji, 2016).

The obvious problem of all one-stage schemes is that they produce similar time histories with a concentrated energy in the half duration of the target event. In fact, generated rupture times for the target event are distributed very simply and predictably similar to the source

complexity of the sub-event in one-stage schemes. However, several observations indicate that the rupture times' distribution for a major earthquake is quite complex. In other words, a single peak carries most of the energy of the earthquake in the one-stage method; however, the moment rate functions for large earthquakes are not this simple (Wennerberg, 1990).

To take into account the effect of asperities on simulated strong ground-motion time histories, Wennerberg (1990) suggested using a two-stage summation to create more realistic source time functions. In this strategy, first a few random patches are introduced. Second, a large number of rupture times corresponding to small sub-events inside the initial patches is generated to cluster the energy around produced rupture times in the first stage. In other words, many scaled and shifted small sub-events are summed together to generate medium magnitude auxiliary events. Then, these medium magnitude auxiliary events are scaled, shifted, and added together to simulate the final large target event. By creating several intermediate-magnitude events (corresponding to patches inside the fault area), the complexity of the moment rate function of the source gets more realistic.

The concept of the two-stage scheme is similar to the concept of the one-stage scheme. In fact, scaled and lagged identical small earthquakes (EGFs) are added together to construct the spectrum of the target event. The difference with the one-stage scheme is that a few rupture times are generated at the first step over the total duration of the target event. Then, many new rupture times are generated over the duration of smaller earthquakes between the target and small earthquakes. These generated delay times in the second stage are distributed around the rupture times produced in the first stage. Different simulations (or realizations) with various initial rupture times are not similar and can account for different rupture processes due to a large earthquake. In fact, the rupture times having energy concentrated around them are generated at the first stage. These delay times somehow act like asperities on the fault of the target event. According to the definition of the two-stage scheme the time histories of the target spectrum from equation (2-1) can be generalized as

$$Y_t(t) = \xi \sum_{i=1}^{N_1} \sum_{j=1}^{N_2} Y_s(t - \tau_{1i} - \tau_{2j})$$
(2-58)

where τ_{1i} and τ_{2j} are the rupture times generated within the first and second stage, respectively. N_1 and N_2 are the number of rupture times in the first and second stage, respectively. Note that

the total number of subevents is equal to the multiplication of the number of patches by the number of subevents within each patch. Thus

$$N = N_1 \times N_2 \qquad (2\text{-}59)$$

The Fourier transform of the aforementioned equation is expressed as

$$Y_t(\omega) = \xi Y_s(\omega) \sum_{i=1}^{N_1} \sum_{j=1}^{N_2} e^{-i\omega(\tau_{1i}+\tau_{2j})} \qquad (2\text{-}60)$$

The expected power spectrum for the simulated seismic signal in the frequency domain can be written as

$$E\left[Y_t(\omega) \times Y_t^*(\omega)\right] = Y_t^2(\omega) = \xi^2 Y_s^2(\omega) E\left[\sum_{i=1}^{N_1} e^{-i\omega\tau_{1i}} \times \sum_{k=1}^{N_1} e^{+i\omega\tau_{1k}} \times \sum_{j=1}^{N_2} e^{-i\omega\tau_{2j}} \times \sum_{kk=1}^{N_2} e^{+i\omega\tau_{2kk}}\right] =$$

$$\xi^2 Y_s^2(\omega) E\left[\sum_{i=1}^{N_1} e^{-i\omega\tau_{1i}}\right] E\left[\sum_{k=1}^{N_1} e^{+i\omega\tau_{1k}}\right] E\left[\sum_{j=1}^{N_2} e^{-i\omega\tau_{2j}}\right] E\left[\sum_{kk=1}^{N_2} e^{+i\omega\tau_{2kk}}\right]$$

$$(2\text{-}61)$$

After calculations, we get

$$Y_t^2(\omega) = \xi^2 Y_s^2(\omega)\left[N_2 + N_2(N_2-1)|p_2(\omega)|^2\right]\left[N_1 + N_1(N_1-1)|p_1(\omega)|^2\right] \qquad (2\text{-}62)$$

in which $p_1(\omega)$ and $p_2(\omega)$ are the spectrum (Fourier transform) of the pdf of rupture times for the first and second stages, respectively. Finally, the amplitude spectrum of the target event can be written as

$$Y_t(\omega) = \left[N\xi \sqrt{\frac{\left[1+(N_2-1)|p_2(\omega)|^2\right]}{N_2}} \sqrt{\frac{\left[1+(N_1-1)|p_1(\omega)|^2\right]}{N_1}}\right] Y_s(\omega) \qquad (2\text{-}63)$$

Again, the problem of not accounting for the directivity effect and not accounting for the nonlinear soil response still exist in this approach; however, the distribution of the rupture times does not look simple like the one-stage method.

2.4.1 **Wennerberg (1990) Scheme**

The constraints for the LF and HF are similar to the Wennerberg (1990) one-stage. The difference is how to generate the rupture times. The pdf to produce rupture times is also similar similar to the Wennerberg (1990) one-stage, but it is used to generate rupture times in two different stages. First, using the ZPD, a few (N_1) rupture times associated with the significant subevent ruptures are generated. Then, in the second stage, many (N_2) new rupture times are produced using the ZPD and are distributed over intervals centered on each produced rupture time in the first stage. In this regard, we need to consider some auxiliary events (patches) with a magnitude between the small and target magnitudes. These patches can be defined with a specific corner frequency, ω_d, as follows

$$\omega_d = N_1^{1/4}\omega_{ct} \tag{2-64}$$

where N_1 is a random small value (like 10) selected by the user and $\omega_t < \omega_d < \omega_s$. Then, the ZPDs for stage one and two are defined as

$$
\begin{aligned}
P_1(t) &= \left(\frac{\omega_t}{\omega_d}\right)^2 \left[\delta(t) + \frac{\omega_d^2 - \omega_t^2}{2\omega_t}e^{-\omega_t|t|}\right] \\
P_2(t) &= \left(\frac{\omega_d}{\omega_s}\right)^2 \left[\delta(t) + \frac{\omega_s^2 - \omega_d^2}{2\omega_d}e^{-\omega_d|t|}\right]
\end{aligned}
\tag{2-65}
$$

For the numerical example, we employ values already described in the Joyner and Boore (1986) section. Figure 2-13 and Figure 2-14 illustrate the distribution of rupture times for one realization and 10 realizations using those generated rupture times using the Wennerberg two-stage scheme, respectively. The distribution of delay times unlike the Wennerberg one-stage summation has more than one peak. In fact, the energy generated from the second stage is clustered around the rupture times generated in the first stage. However, as the one-stage scheme of Wennerberg (1990), this scheme also has a huge deficiency in the HF part of the simulated spectrum that cannot be matched with the target event. For instance, using the number of summands proposed by Joyner and Boore (1986) overestimated the spectrum by a factor of $\sqrt{2} \cdot \sqrt{2} = 2$ at HFs. It is interesting to note that the overestimation is multiplied since it occurs at both stages. Although, the generated rupture times seem more realistic, this procedure includes too much HF. Therefore, this scheme gets even worse than its original one-stage scheme.

2.4.2 **Kohrs *et al.* (2005) Scheme**

This scheme is the extension of the Ordaz *et al.* (1995) scheme from one-stage to two-stage. The LF and HF constraints for the two-stage scheme are the same as the one-stage scheme, but rupture times are generated in two different stages to capture the variability of different rupture processes (different rupture scenarios). Within the framework of the two-stage scheme, the spectral ratio of the expected target event over the small event can be written as

$$\frac{Y_t(\omega)}{Y_s(\omega)} = \left[N\xi \sqrt{\frac{\left[1+(N_2-1)|p_2(\omega)|^2\right]}{N_2}} \sqrt{\frac{\left[1+(N_1-1)|p_1(\omega)|^2\right]}{N_1}} \right] \tag{2-66}$$

Since $p(\omega) = \int_0^T p(t)e^{-i\omega t}dt$, it can be shown that

$$\begin{aligned} p(\omega) &= 1 && \text{if } \omega \to 0 \\ p(\omega) &= 0 && \text{if } \omega \to \infty \end{aligned} \tag{2-67}$$

Therefore, the spectral ratios at very LF and very HF range can be written as

$$\begin{aligned} \frac{Y_t(\omega)}{Y_s(\omega)} &= \xi N && \text{if } \omega \to 0 \\ \frac{Y_t(\omega)}{Y_s(\omega)} &= \xi \sqrt{N} && \text{if } \omega \to \infty \end{aligned} \tag{2-68}$$

Thus, for the scaling of the LF and HF range, we obtain the same results as the one-stage scheme

$$N = N_1 N_2 = \left(\frac{\omega_{ct}}{\omega_{cs}}\right)^4 = \left(\frac{M_t}{M_s}\right)^{4/3} \left(\frac{\Delta\sigma_t}{\Delta\sigma_s}\right)^{-4/3}$$

$$\xi = \frac{\left(\dfrac{M_t}{M_s}\right)}{N} = \left(\frac{M_t}{M_s}\right)^{-1/3} \left(\frac{\Delta\sigma_t}{\Delta\sigma_s}\right)^{4/3} \tag{2-69}$$

At the intermediate frequency range, the spectral ratio can be written as

$$\frac{Y_t(\omega)}{Y_s(\omega)} = \left[N\xi \sqrt{\frac{\left[1+(N_2-1)|p_2(\omega)|^2\right]}{N_2}} \sqrt{\frac{\left[1+(N_1-1)|p_1(\omega)|^2\right]}{N_1}} \right] = \frac{M_t}{M_s} \frac{1+\left(\omega/\omega_{cs}\right)^2}{1+\left(\omega/\omega_{ct}\right)^2} \tag{2-70}$$

Hence,

$$\sqrt{\frac{\left[1+(N_2-1)\left|p_2(\omega)\right|^2\right]}{N_2}}\sqrt{\frac{\left[1+(N_1-1)\left|p_1(\omega)\right|^2\right]}{N_1}}=\frac{1+\left(\omega/\omega_{cs}\right)^2}{1+\left(\omega/\omega_{ct}\right)^2}=\frac{1+\left(\omega/\omega_{cs}\right)^2}{1+\left(\omega/\omega_{cd}\right)^2}\times\frac{1+\left(\omega/\omega_{cd}\right)^2}{1+\left(\omega/\omega_{ct}\right)^2} \quad (2\text{-}71)$$

in which ω_{cd} or f_{cd} is an auxiliary variable to define the corner frequency of the virtual event between the small and target events defined as

$$N_1=\left(\frac{\omega_{cd}}{\omega_{ct}}\right)^4 \rightarrow \omega_{cd}=N_1^{1/4}\omega_{ct}$$

$$N_2=\left(\frac{\omega_{cs}}{\omega_{cd}}\right)^4 \rightarrow \omega_{cd}=N_2^{-1/4}\omega_{cs}$$

$$(2\text{-}72)$$

Then, by assuming a reasonable number of N_1 such as 10, the corner frequency of the virtual (or auxiliary) event can be determined. Note that in the first step a few rupture times are generated over the whole duration of the target event. Assuming the two pdfs are independent, one solution can be obtained from the equality of the first terms on both sides and from the equality of the second terms on both sides. Then, the pdfs can be expressed as

$$p_1(t)=\frac{1}{2\pi}\int_{-\infty}^{\infty}\frac{\sqrt{1+\dfrac{2\omega^2}{\omega_{cd}^2+\omega_{ct}^2}}}{1+\left(\dfrac{\omega}{\omega_{ct}}\right)^2}e^{i\omega t}d\omega$$

$$p_2(t)=\frac{1}{2\pi}\int_{-\infty}^{\infty}\frac{\sqrt{1+\dfrac{2\omega^2}{\omega_{cs}^2+\omega_{cd}^2}}}{1+\left(\dfrac{\omega}{\omega_{cd}}\right)^2}e^{i\omega t}d\omega$$

$$(2\text{-}73)$$

Figure 2-15 and Figure 2-16 show the distribution of rupture times and 10 realizations using those generated rupture times using the Kohrs *et al.* (2005) two-stage scheme, respectively. As can be seen, the simulated spectrum matches perfectly the target spectrum in the whole frequency range.

2.4.3 TSP2 Scheme

This method is similar to the TSP1 method (and so similar to Ordaz *et al.*, 1995) and the only difference is to produce the rupture times in two steps. Therefore, the LF and HF constraints are the same as equation (2-47). Then, using the general equations of (2-42) and (2-63), the spectral ratios can be written as

$$\left|\frac{S_t(\omega)}{S_s(\omega)}\right| = \left|\frac{S_t(\omega)}{S_d(\omega)}\right|\left|\frac{S_d(\omega)}{S_s(\omega)}\right| = \xi_1\xi_2 N_1^{1/\varepsilon(\omega)} N_2^{1/\varepsilon(\omega)} \tag{2-74}$$

in which

$$
\left.\begin{aligned}
N_1 &= \left(\frac{\omega_d}{\omega_t}\right)^4 \\
\xi_1 &= \frac{M_t / M_d}{N_1} \\
N_2 &= \left(\frac{\omega_s}{\omega_d}\right)^4 \\
\xi_2 &= \frac{M_d / M_s}{N_2}
\end{aligned}\right\}
\rightarrow
\left\{\begin{aligned}
N &= N_1.N_2 = \left(\frac{\omega_s}{\omega_t}\right)^4 \\
\xi &= \xi_1.\xi_2 = \frac{M_t / M_s}{N}
\end{aligned}\right.
\tag{2-75}
$$

If the N_1 value is supposed, then N_2 and ξ can be obtained. Thus, using equation (2-62)

$$p_1(\omega) = \sqrt{\frac{N_1^{(2/\varepsilon_1(\omega)-1)} - 1}{N_1 - 1}} \rightarrow p(t) = \frac{1}{2\pi}\int_{-\infty}^{\infty}\sqrt{\frac{N_1^{(2/\varepsilon_1(\omega)-1)} - 1}{N_1 - 1}}e^{i\omega t}d\omega$$

$$p_2(\omega) = \sqrt{\frac{N_2^{(2/\varepsilon_2(\omega)-1)} - 1}{N_2 - 1}} \rightarrow p(t) = \frac{1}{2\pi}\int_{-\infty}^{\infty}\sqrt{\frac{N_2^{(2/\varepsilon(\omega)-1)} - 1}{N_2 - 1}}e^{i\omega t}d\omega \tag{2-76}$$

where

$$\varepsilon_1(\omega) = \frac{1}{1 + \dfrac{\ln\left[1 + (\omega/\omega_{cd})^{pf}\right] - \ln\left[1 + (\omega/\omega_{ct})^{pf}\right]}{2pf \ln(\omega_{cd}/\omega_{ct})}}$$

$$\varepsilon_2(\omega) = \frac{1}{1 + \dfrac{\ln\left[1 + (\omega/\omega_{cs})^{pf}\right] - \ln\left[1 + (\omega/\omega_{cd})^{pf}\right]}{2pf \ln(\omega_{cs}/\omega_{cd})}} \tag{2-77}$$

To determine the rupture times using the TSP2 method, we first construct a $t - P(t)$ table. Then, we generate random numbers in the interval of [0, 1]. These random numbers are used as $P(t)$ and using the constructed table, relevant rupture times, t, are picked.

2.4.4 Classic ω2 source spectrum with the scaling assumption of Mf 3=Cσ

To determine equations for this case, we substitute *pf* and *pd* exponents with 2 and 1, respectively. Thus, the steps needed for the SSGFM employing the TSP2 scheme is as follows

1. Select the seed input ground motion and its magnitude and stress drop.
2. Choose the magnitude and stress drop of the large magnitude event.
3. Determine ξ: to scale (normalize) the input seed to a unit excitation

$$\xi = \frac{M_t/M_s}{N} = \frac{M_t/M_s}{\left(\frac{\omega_{cs}}{\omega_{ct}}\right)^4} = \left(\frac{M_t}{M_s}\right)^{-\frac{1}{3}}\left(\frac{\Delta\sigma_t}{\Delta\sigma_s}\right)^{\frac{4}{3}} \tag{2-78}$$

4. Calculate N: the number of required subfaults to reach the target spectrum

$$N = \left(\frac{\omega_{cs}}{\omega_{ct}}\right)^4 = \left(\frac{M_t}{M_s}\right)^{\frac{4}{3}}\left(\frac{\Delta\sigma_t}{\Delta\sigma_s}\right)^{-\frac{4}{3}} \tag{2-79}$$

5. Suppose a small value to represent the number of patches (N_1). 10 is a good number to choose. Then, N_2 can be found using $N = N_1 \cdot N_2$. Note that with increasing the value of N_1, the distribution of rupture times generated using the two-stage scheme becomes more similar to the one-stage scheme.
6. Compute the corner frequency of the auxiliary event using the following equation

$$N_1 = \left(\frac{\omega_{cd}}{\omega_{ct}}\right)^4 \rightarrow \omega_{cd} = N_1^{1/4}\omega_{ct} \tag{2-80}$$

7. Generate τ_{1i}: delay times in the first stage to simulate the rupture propagation of patches using the following distribution

$$p_1(t) = \frac{1}{2\pi}\int_{-\infty}^{\infty}\sqrt{\frac{N_1^{(2/\varepsilon_1(\omega)-1)}-1}{N_1-1}}e^{i\omega t}d\omega \tag{2-81}$$

65

where

$$\varepsilon_1(\omega) = \cfrac{1}{1 + \cfrac{\ln\left[1+\left(\omega/\omega_{cd}\right)^2\right] - \ln\left[1+\left(\omega/\omega_{ct}\right)^2\right]}{4\ln\left(\omega_{cd}/\omega_{ct}\right)}} \qquad (2\text{-}82)$$

8. Generate τ_{2j}: delay times in the second stage to simulate the rupture propagation of small events distributed around the patches using the following distribution

$$p_2(t) = \frac{1}{2\pi}\int_{-\infty}^{\infty}\sqrt{\frac{N_2^{\left(2/\varepsilon_2(\omega)^{-1}\right)} - 1}{N_2 - 1}}\,e^{i\omega t}d\omega \qquad (2\text{-}83)$$

where

$$\varepsilon_2(\omega) = \cfrac{1}{1 + \cfrac{\ln\left[1+\left(\omega/\omega_{cs}\right)^2\right] - \ln\left[1+\left(\omega/\omega_{cd}\right)^2\right]}{4\ln\left(\omega_{cs}/\omega_{cd}\right)}} \qquad (2\text{-}84)$$

9. Finally, add scaled and delayed motions from subfaults to construct the ground motion of the target event as follows

$$Y_t(t) = \xi\sum_{i=1}^{N_1}\sum_{j=1}^{N_2}Y_s\left(t - \tau_{1i} - \tau_{2j}\right) \qquad (2\text{-}85)$$

Figure 2-17 and Figure 2-18 demonstrate the distribution of rupture times and 10 realizations using those generated rupture times using the TSP2 scheme, respectively, for the numerical example. Again, we note that this scheme is the same as the Kohrs *et al.* (2005) scheme and the only difference is the procedure to obtain the pdfs for generating rupture times. This method has been tested with other examples provided in the Appendix A.

2.4.5 **General Comparison between Two-stage Schemes and One-stage Schemes**

Figure 2-19 displays the difference between various two-stage schemes to obtain the expected target spectra. As previously explained, the TSP2 and Kohrs *et al.* (2005) schemes are exactly the same and both match the target spectrum in the whole frequency range and the only

difference between them is the procedure to construct the summation schemes. The Wennerberg (1990) two-stage scheme overestimates the HF portion by a factor of 2.

Since the TSP1 and the Ordaz *el al*. (1995) schemes are the same and also the TSP2 and the Kohrs *et al*. (2005) schemes are the same, we selected the TSP1 and TSP2 schemes to compare the difference between these two approaches. Figure 2-20 presents the rupture times generated by TSP1 (the one-stage scheme) and TSP2 (the two-stage scheme) for three different realizations. Although both schemes match the target spectrum in the whole frequency range, the rupture times generated by them are completely different. For the one-stage scheme, all three different realizations have similar patterns with maximum energy concentrated in the middle. On the other hand, each realization of the two-stage scheme is different than the others describing the strength of this scheme to account for different rupture scenarios.

2.5 **Figures**
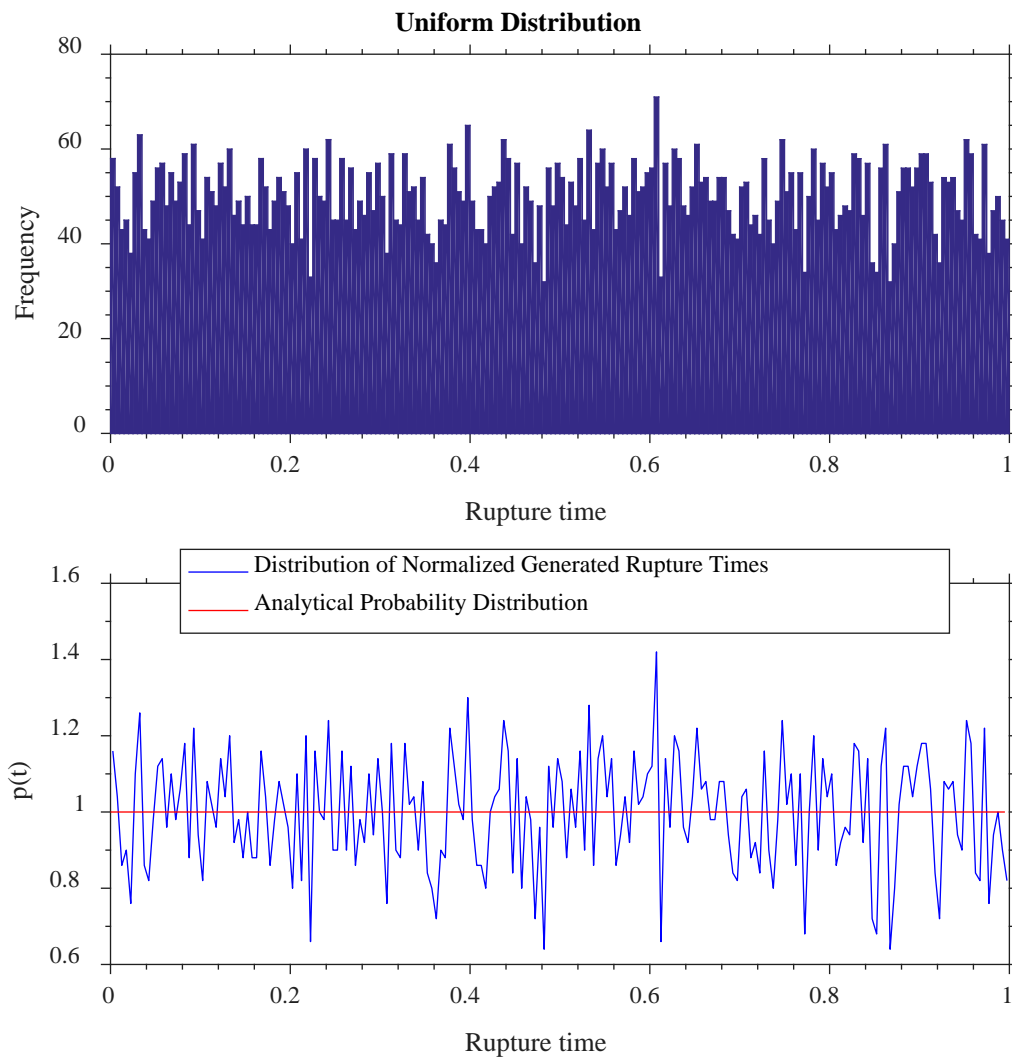
Figure 2-1. The distribution of the generated rupture times using the Joyner and Boore (1986) scheme
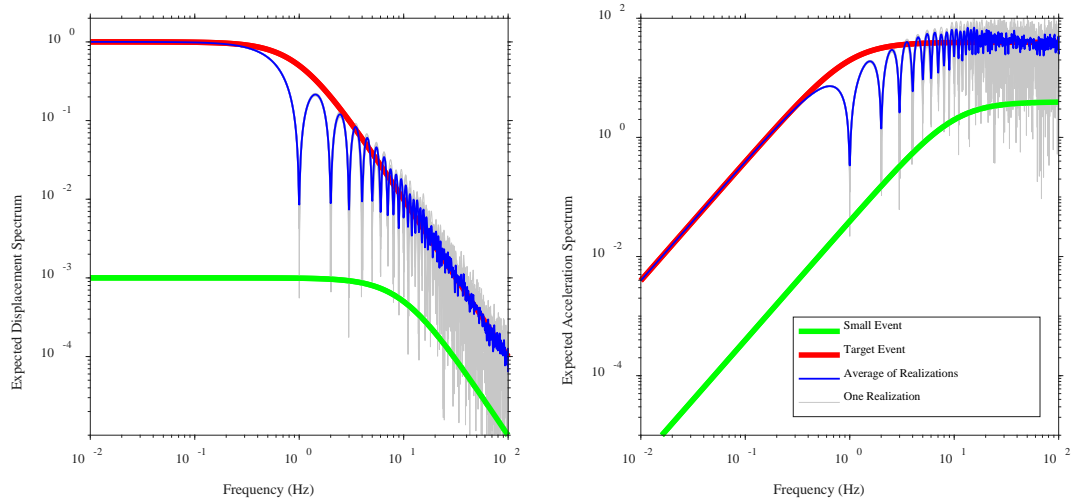
Figure 2-2. 10 different realizations using the Joyner and Boore (1986) scheme and rms average spectrum
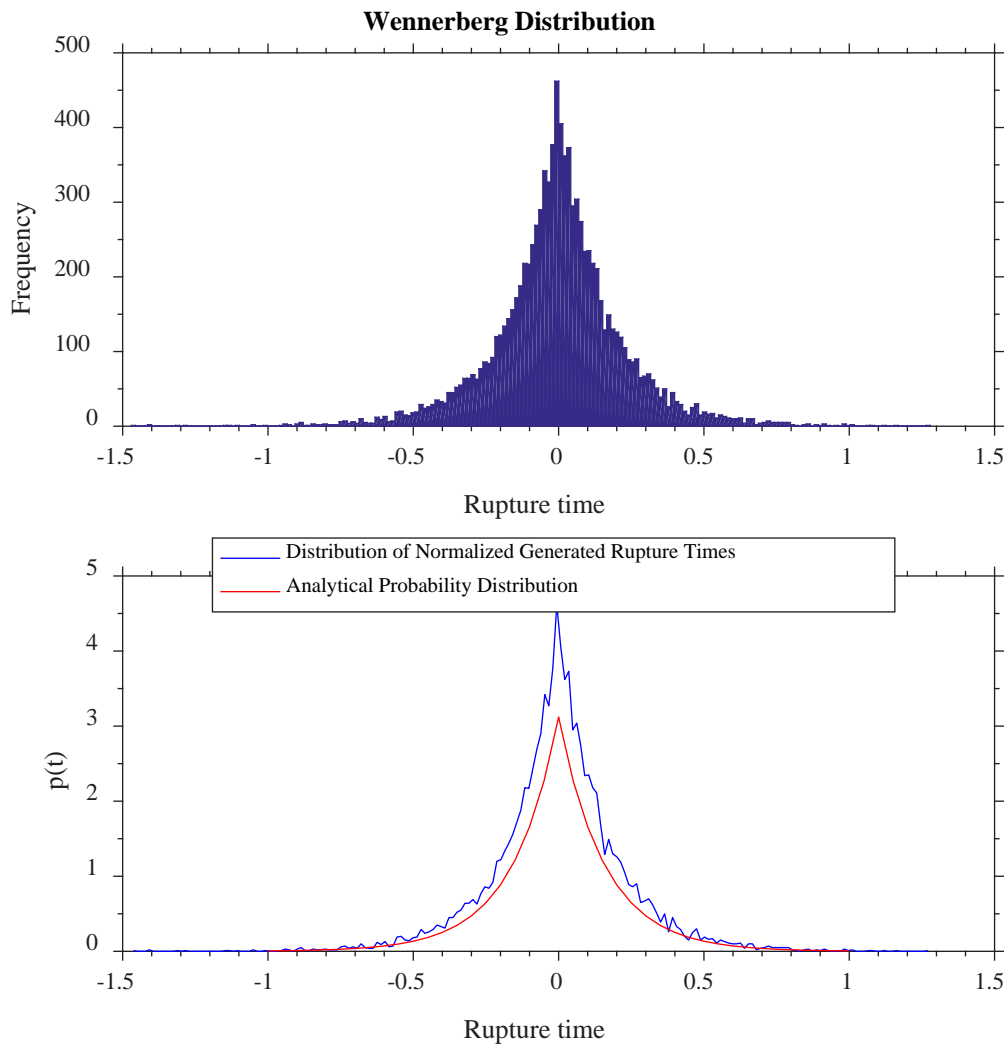
Figure 2-3. The distribution of the generated rupture times using the Wennerberg (1990) scheme
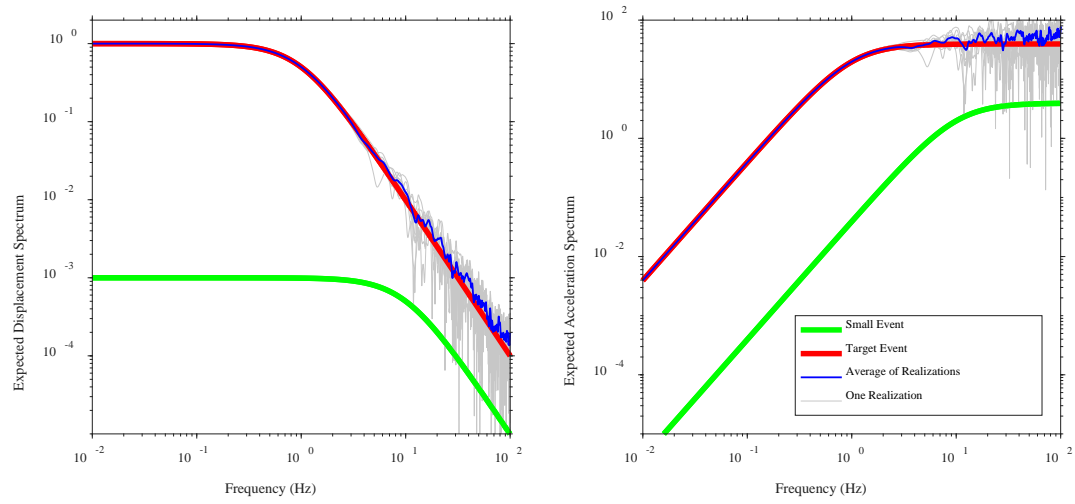
Figure 2-4. 10 different realizations using the Wennerberg (1986) scheme and rms average spectrum
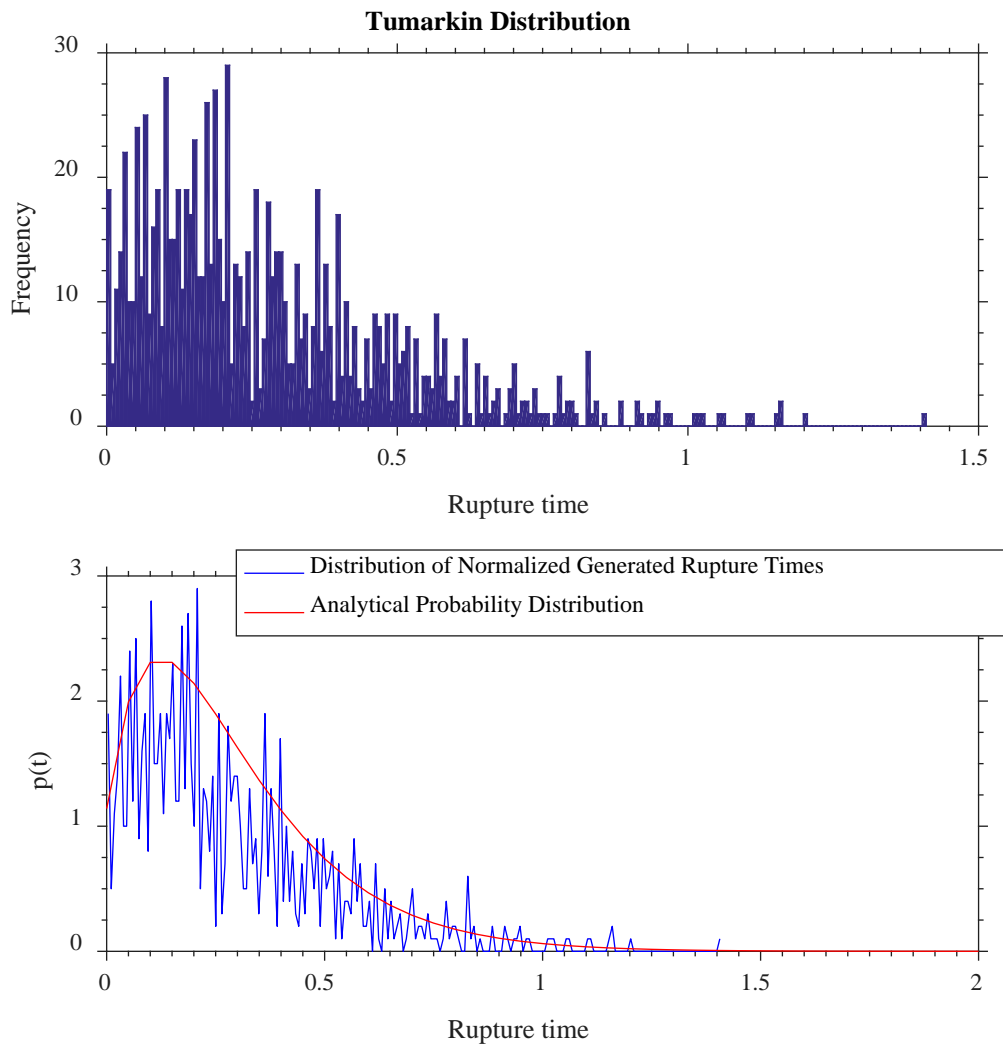
Figure 2-5. The distribution of the generated rupture times using the Tumarkin and Archuleta (1994) scheme
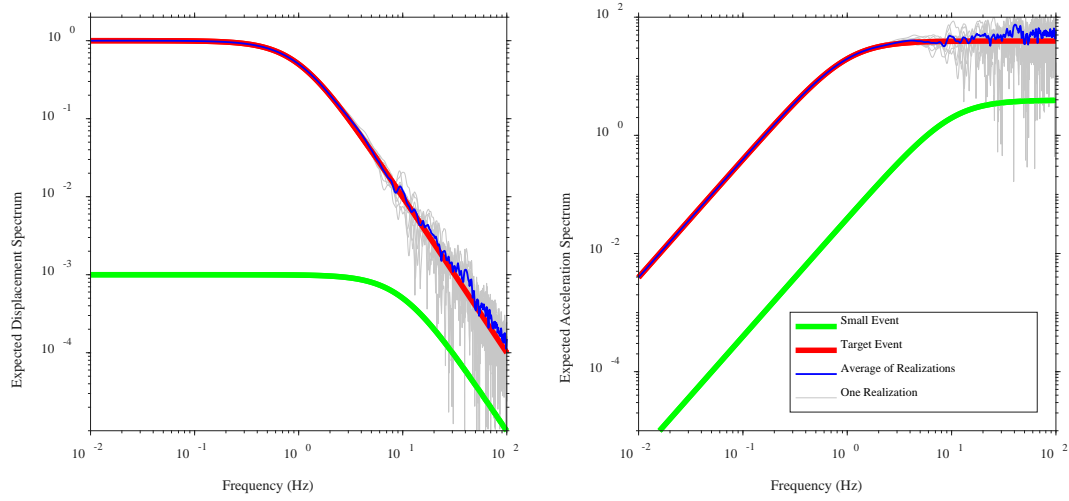
Figure 2-6. 10 different realizations using the Tumarkin and Archuleta (1994) scheme and rms
average spectrum
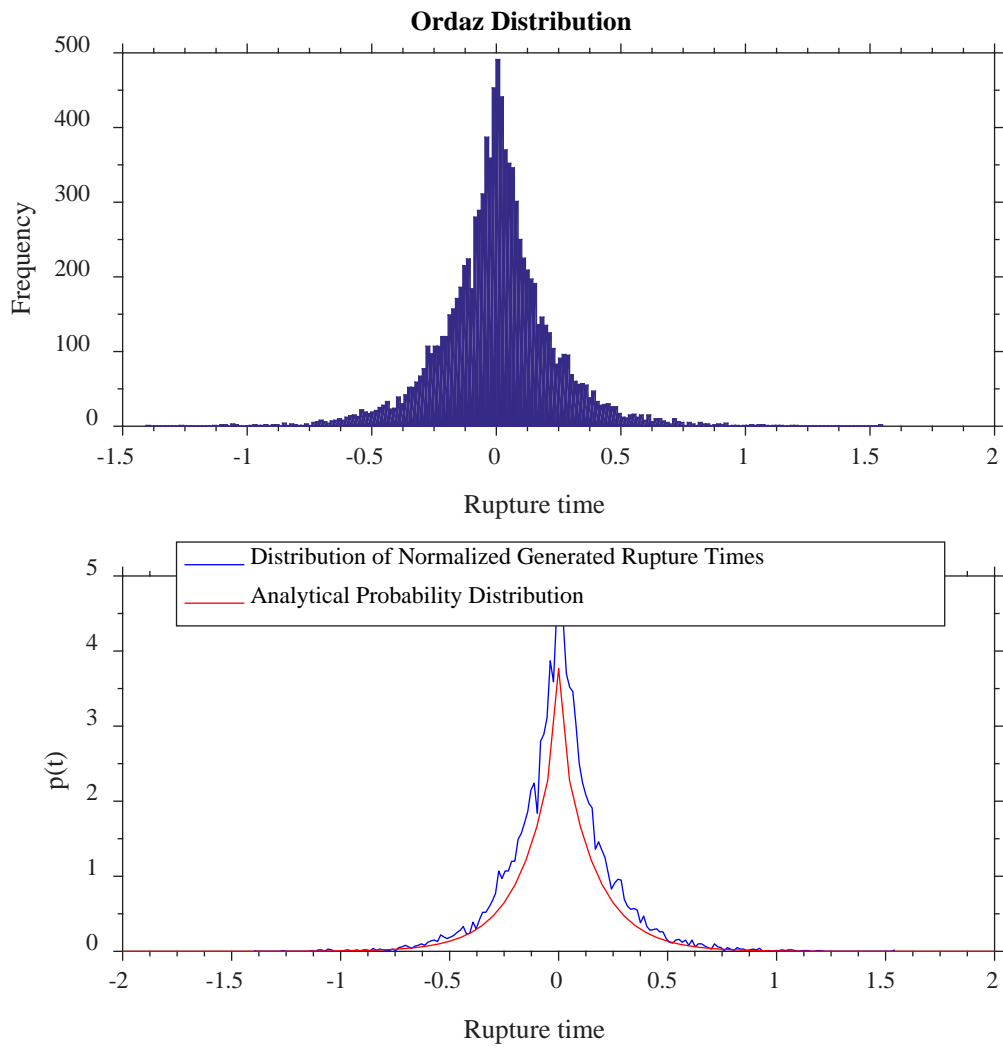
Figure 2-7. The distribution of the generated rupture times using the Ordaz *el al.* (1995) scheme

Figure 2-8. 10 different realizations using the Ordaz *et al.* (1995) scheme and rms average spectrum
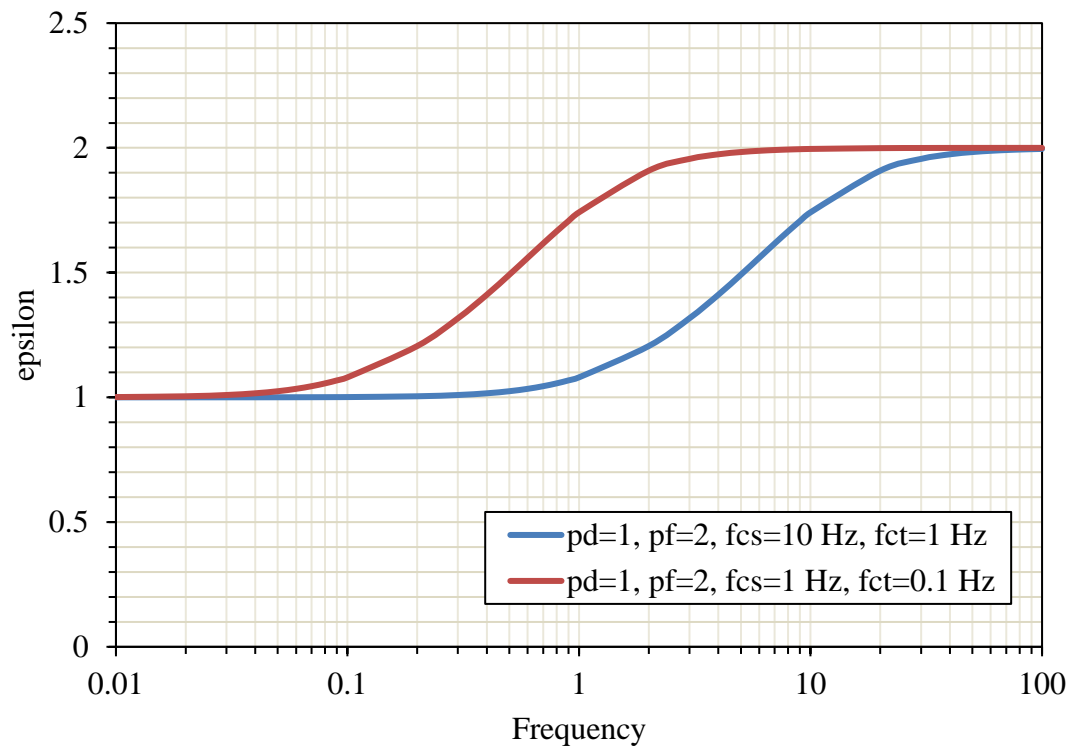
Figure 2-9. Variation of epsilon with frequency
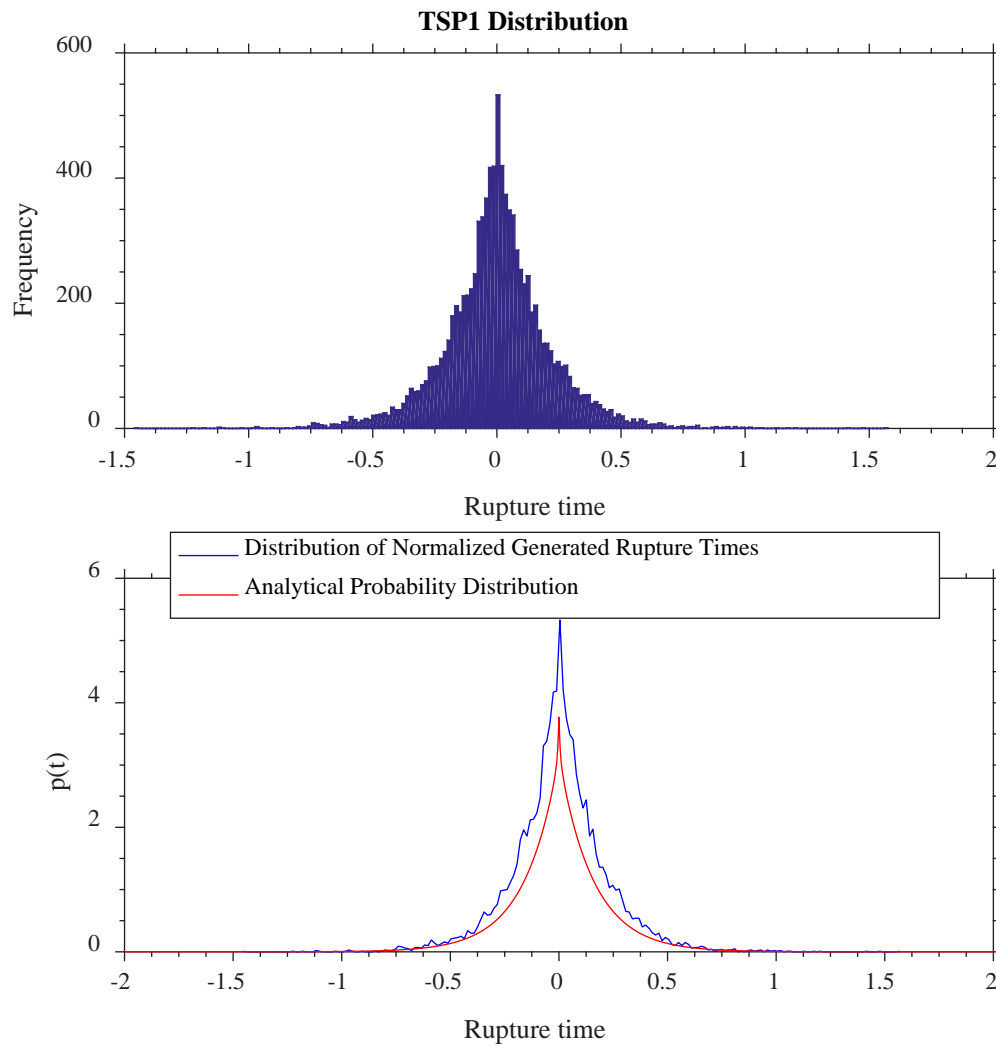
Figure 2-10. The distribution of the generated rupture times using the TSP1 scheme
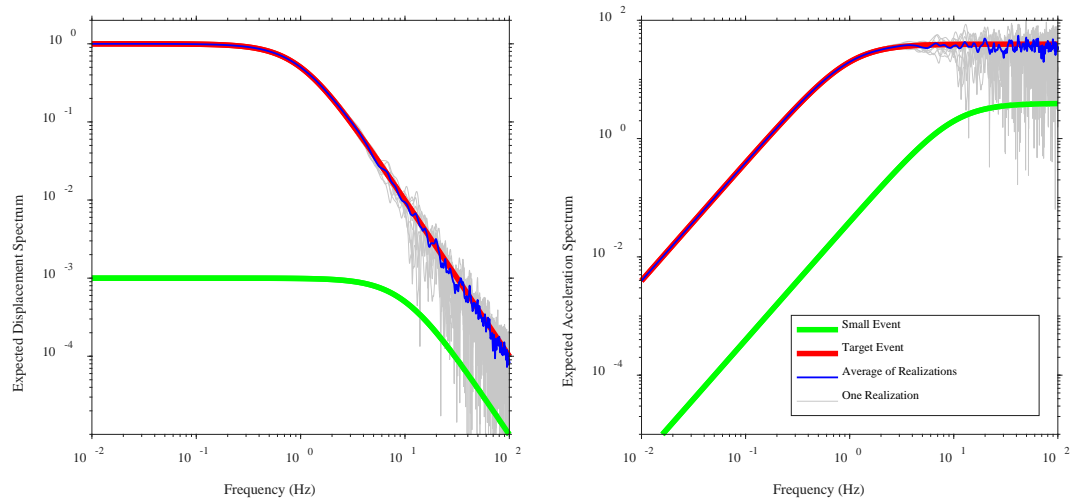
Figure 2-11. 10 different realizations using the TSP1 scheme and rms average spectrum
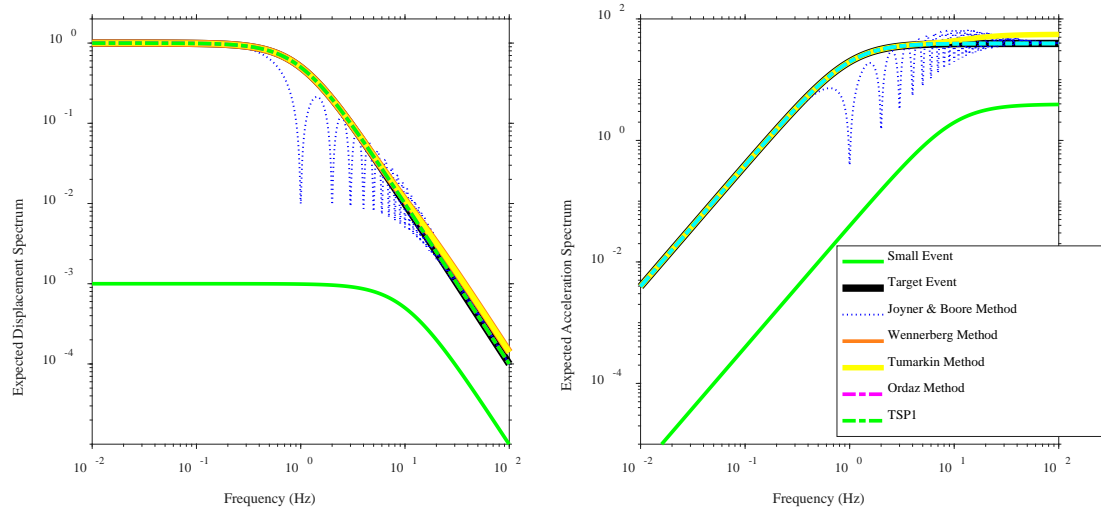
Figure 2-12. Comparison of expected Fourier amplitudes determined from different one-stage summation schemes
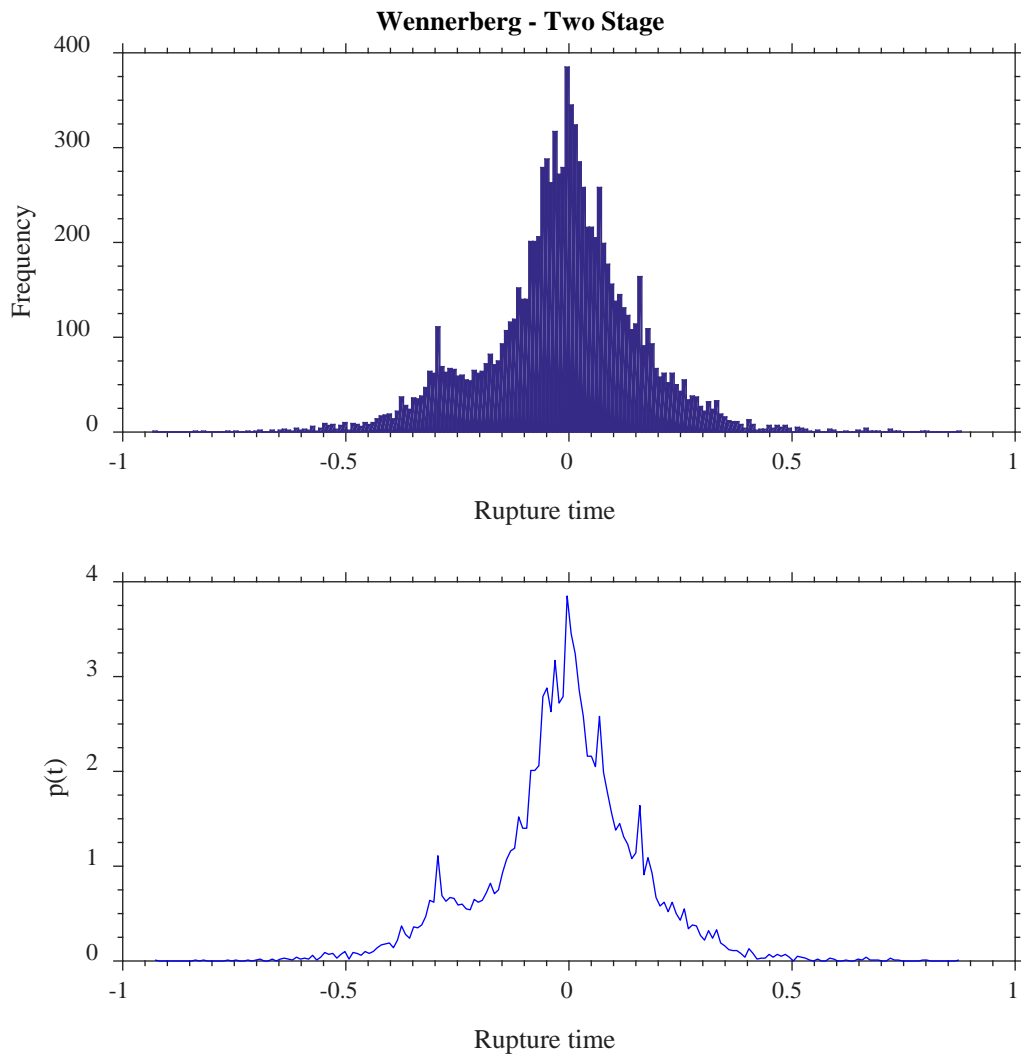
Figure 2-13. The distribution of the generated rupture times using the Wennerberg (1990) two-stage scheme
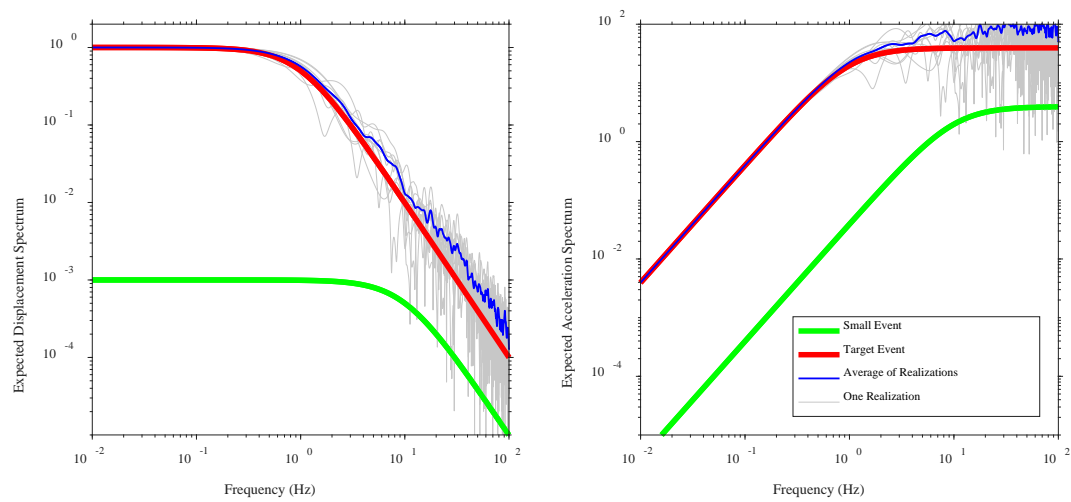
Figure 2-14. 10 different realizations using the Wennerberg (1990) two-stage scheme and rms average spectrum

Kohrs Distribution
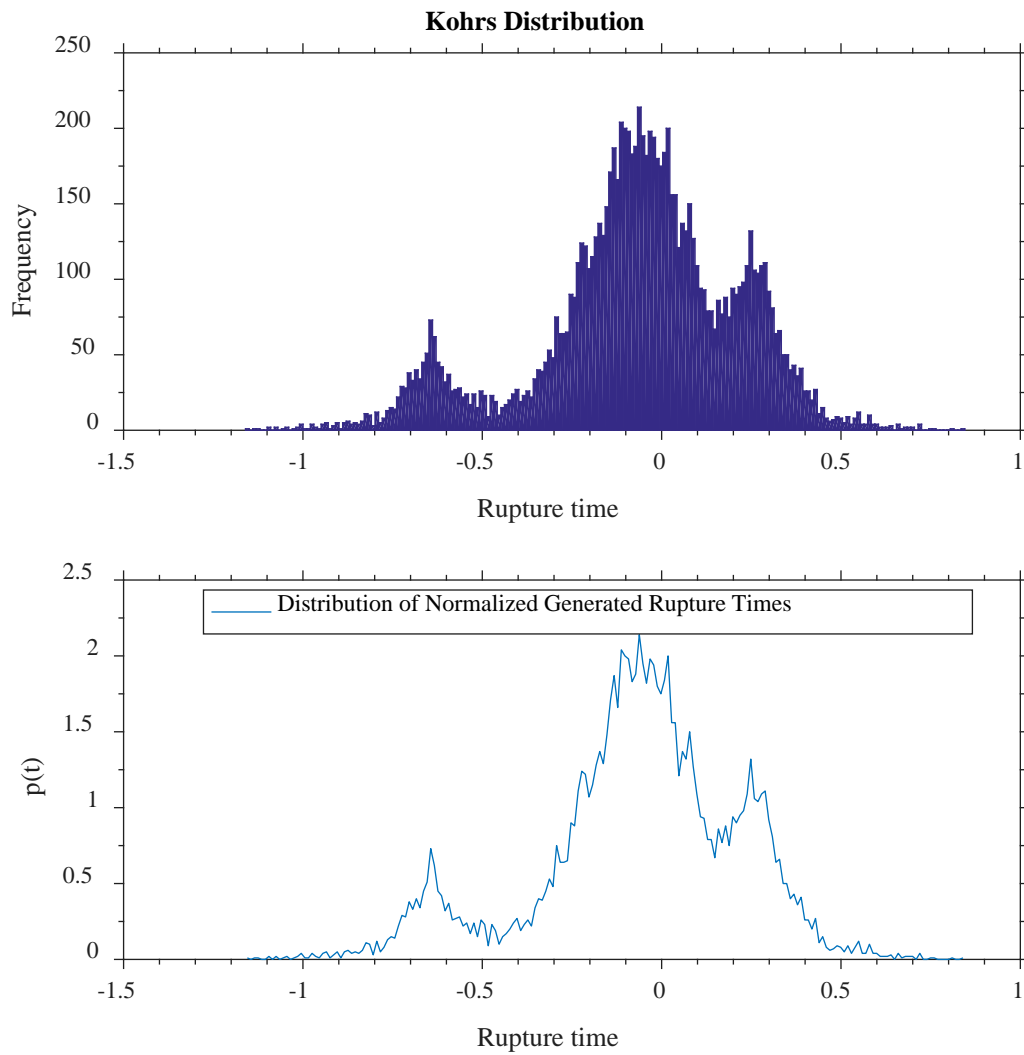
Figure 2-15. The distribution of the generated rupture times using the Kohrs *et al*. (2005) two-stage scheme
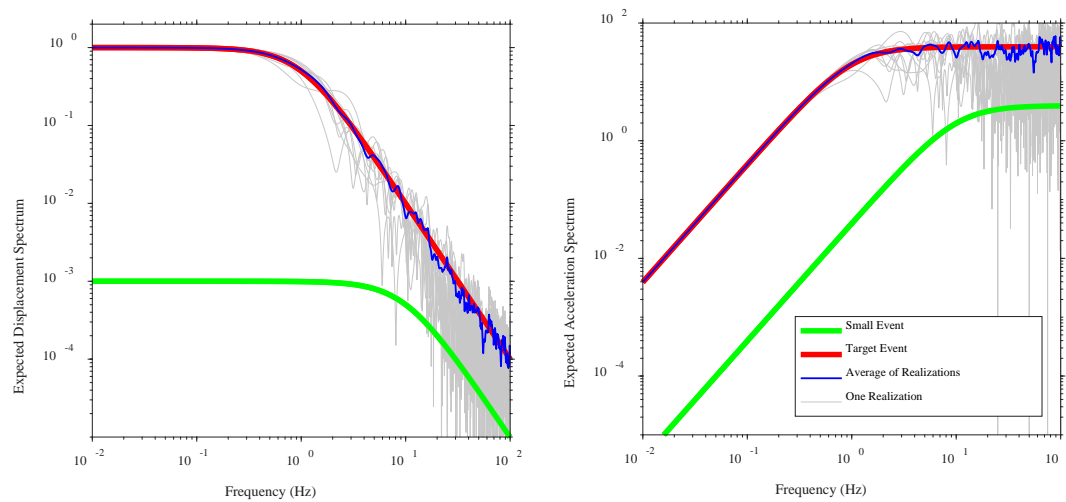
Figure 2-16. 10 different realizations using the Kohrs *et al*. (2005) two-stage scheme and rms average spectrum
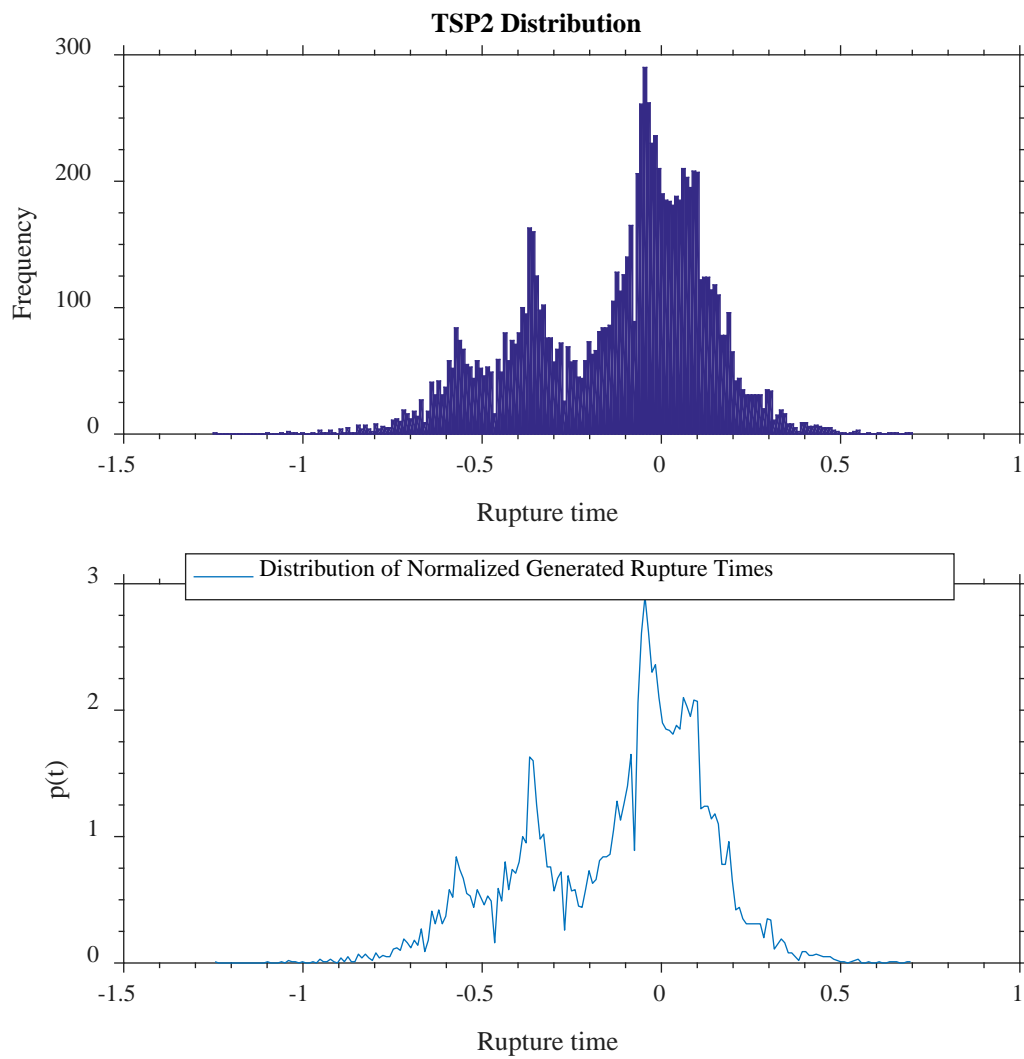
Figure 2-17. The distribution of the generated rupture times using the TSP2 scheme
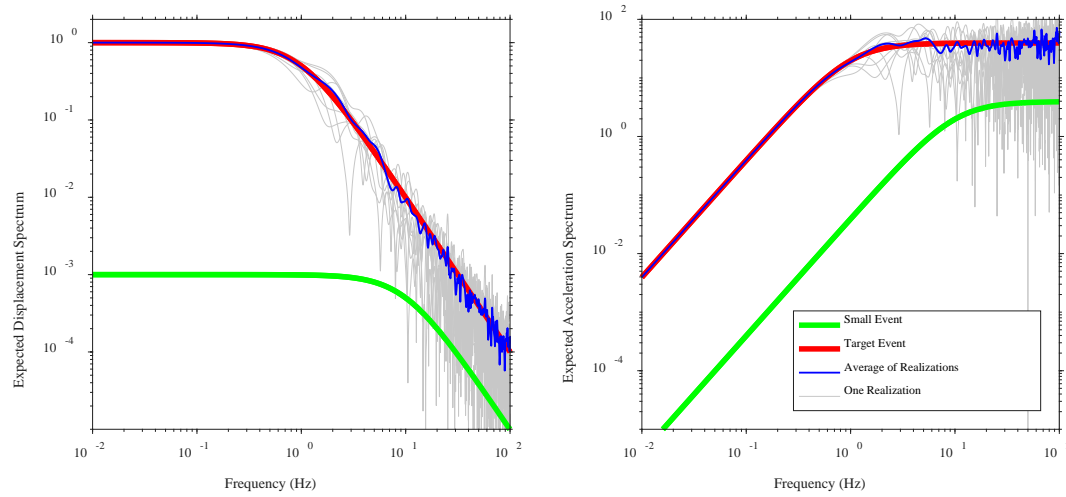
Figure 2-18. 10 different realizations using the TSP2 scheme and rms average spectrum
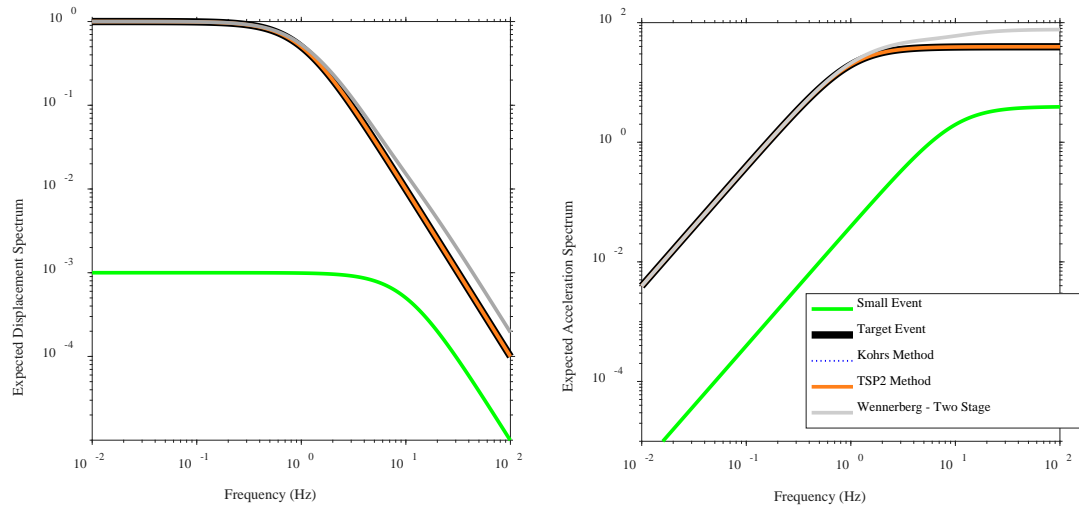
Figure 2-19. Comparison of expected Fourier amplitudes determined from different two-stage summation schemes
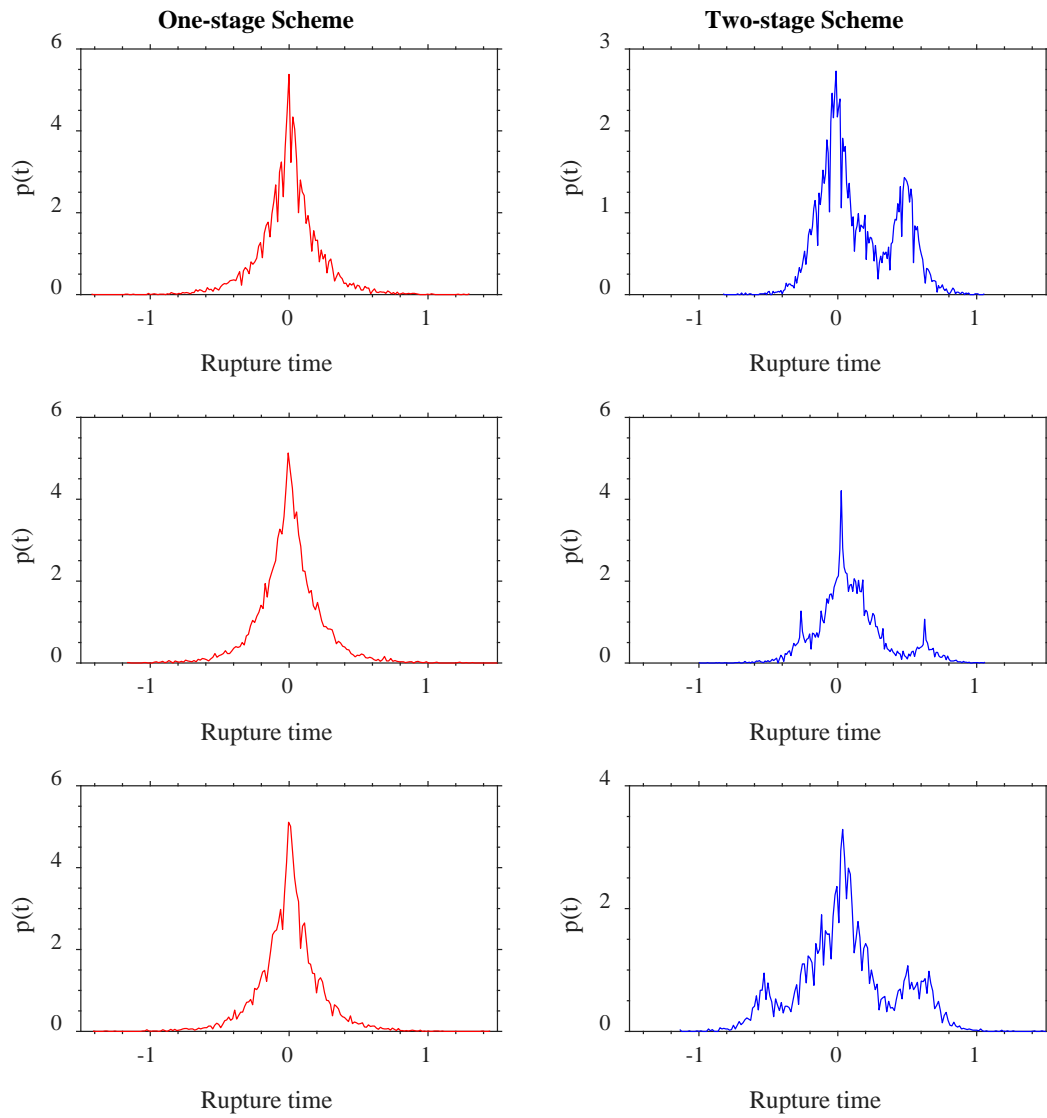
Figure 2-20. Comparison of rupture times generated using TSP1 and TSP2 (one- and two-stage summation schemes, respectively)

3. Generalized Stochastic Summation Schemes Extended for the Double Corner Frequency Source Spectral Model

3.1 Introduction

The single corner frequency (SCF) ω-square (Brune shape) source model is constructed based on a circular fault (Haskell, 1969; Savage, 1972; Haddon, 1992). In reality, a ruptured fault can be a rectangular or has a complex shape. In addition to the shape of the rupture, fault roughness (asperity) and inhomogeneities on the fault cause departure from the SCF ω-square model. Different models have been proposed to capture these effects on the source spectral shape (e.g., Hartzell and Brune, 1979; McGarr, 1981; Papageorgiou and Aki, 1983; Boatwright, 1988). Therefore, the near-field point-source model may need to have more than one corner frequency to account for the effect of dimensions, rise time, rupture time, and asperities to match observed source spectra (Archuleta and Ji, 2016). Some researchers observed that the source spectrum of large earthquakes is better characterized with a double corner frequency (DCF) point-source model which has a spectral sag between two corner frequencies (Joyner, 1984; Boore, 1986; Atkinson and Boore, 1995; Atkinson and Sonley, 2003; Yenier and Atkinson, 2014). Even for small to moderate earthquakes, the source spectrum may need two corner frequencies to match the apparent moment rate functions (MRFs). For instance, several investigators observed that the MRFs of moderate earthquakes that occurred in northeastern North America follow a DCF model (e.g. Boatwright, 1994; Atkinson and Boore, 1995; Atkinson and Sonley, 2003; Boatwright and Seekins, 2011). Furthermore, Archuleta and Ji (2016) concluded that even small to moderate earthquakes (having $3.3 < \mathbf{M} < 5.3$) are better described with DCF source models.

In the SSGFM, the finite-fault source is divided into sub-events or sub-sources, representing small earthquakes which can be treated as point sources. Atkinson (1993), Atkinson and Boore (1995), and Boore *et al*. (2014) analyzed recordings from earthquakes recorded within eastern and North America (ENA) with magnitudes more than 4 and showed that there is a sag in the middle frequency range of the source spectrum. This source spectrum shape can be modeled with two different corner frequencies, and thus, the SCF is no longer valid. Yenier and Atkinson (2014) also observed that the Fourier amplitude spectrum (FAS) obtained from the Landers, CA

earthquake (1992/06/28) with a moment magnitude of 7.28 and the Northridge earthquake (1994/01/17) with a moment magnitude of 6.69 successfully match the DCF point-source model. In the SSGFM, we usually employ earthquakes with magnitude around 4.5 to 5.5 as the EGFs because for smaller magnitude earthquakes the signal to noise ratio (SNR) is very low. Therefore, the signal is lost in the noise particularly for the low frequency range since the frequency contents of small earthquakes have less contribution from the low frequency range (Sedaghati and Pezeshk, 2016c). For moderate-magnitude earthquakes, the assumption of having a SCF sub-source may be violated. Therefore, it is required to generalize and update the pdf for generating rupture times in order to be used once the selected EGF is defined with a DCF source model to match the target spectrum which has two corner frequencies as well.

The question is why is this departure from SCF to DCF source models important and does it have a significant effect on simulations? Duration is an important feature of seismic waves which has significant impact on response spectral amplitudes. In essence, shorter durations lead to higher response spectral amplitudes, whereas longer durations yield smaller response spectral amplitudes (Atkinson *et al*., 2009). One important difference between the SCF and DCF models is the difference between their source durations. In the SCF the source duration is defined as $1/f_c$, while in the DCF models the duration is defined as $1/f_a + 1/f_b$. Since the energy should be constant, a longer duration of DCF models results in a lower spectral acceleration (response spectra) compared to SCF models (Boore, 2014).

In this chapter, we will show that it is not necessary to have the SCF assumption for the source model. In this regard, we will describe how to extend the SSGFM to be employed for earthquakes with DCF source models.

3.2 **Multiplicative Double Corner Frequency Source Models**

The Fourier acceleration spectrum for a multiplicative double corner frequency (MDCF) source model is obtained by multiplication of two spectra as (Boore *et al.,* 2014)

$$S(f) = CM_0 (2\pi f)^2 \frac{1}{\left(1 + \left(\dfrac{f}{f_a}\right)^{pf_a}\right)^{pd_a}} \frac{1}{\left(1 + \left(\dfrac{f}{f_b}\right)^{pf_b}\right)^{pd_b}} \qquad (3\text{-}1)$$

where M_0 and f are seismic moment and frequency, respectively, and C is a constant related to the radiation pattern. pf and pd represent the power of frequency and the power of denominator. The subscripts a and b are related to the first (lower) and second (higher) corner frequencies, respectively. Therefore, f_a and f_b are the first and second corner frequencies. Since the LF and HF level of the Fourier acceleration spectrum of the DCF source model should match the LF and HF level of the Fourier acceleration spectrum of the SCF ω-square source model, it imposes the following constraints to be satisfied

$$
\begin{aligned}
pf_a \times pd_a + pf_b \times pd_b &= 2 \\
f_a^{pf_a \times pd_a} \times f_b^{pf_b \times pd_b} &= f_c^2
\end{aligned}
\tag{3-2}
$$

where f_c is computed using equation (1-40).

3.2.1 One-stage Summation Scheme

Based on the equation of the FAS of the MDCF source model, the small and target spectra can be written as

$$
S_t(f) = CM_{0t}(2\pi f)^2 \frac{1}{\left(1+\left(\dfrac{f}{f_{at}}\right)^{pf_{at}}\right)^{pd_{at}}} \frac{1}{\left(1+\left(\dfrac{f}{f_{bt}}\right)^{pf_{bt}}\right)^{pd_{bt}}}
$$

$$
S_s(f) = CM_{0s}(2\pi f)^2 \frac{1}{\left(1+\left(\dfrac{f}{f_{as}}\right)^{pf_{as}}\right)^{pd_{as}}} \frac{1}{\left(1+\left(\dfrac{f}{f_{bs}}\right)^{pf_{bs}}\right)^{pd_{bs}}}
\tag{3-3}
$$

and by dividing the spectra, the spectral ratio of source functions can be obtained from

$$
\frac{Y_t(f)}{Y_s(f)} = \frac{M_{0t}}{M_{0s}} \frac{\left(1+\left(\dfrac{f}{f_{as}}\right)^{pf_{as}}\right)^{pd_{as}} \left(1+\left(\dfrac{f}{f_{bs}}\right)^{pf_{bs}}\right)^{pd_{bs}}}{\left(1+\left(\dfrac{f}{f_{at}}\right)^{pf_{at}}\right)^{pd_{at}} \left(1+\left(\dfrac{f}{f_{bt}}\right)^{pf_{bt}}\right)^{pd_{bt}}} = \frac{M_{0t}}{M_{0s}} G
\tag{3-4}
$$

where G is

$$G = \frac{\left(1+\left(\dfrac{f}{f_{as}}\right)^{pf_{as}}\right)^{pd_{as}} \left(1+\left(\dfrac{f}{f_{bs}}\right)^{pf_{bs}}\right)^{pd_{bs}}}{\left(1+\left(\dfrac{f}{f_{at}}\right)^{pf_{at}}\right)^{pd_{at}} \left(1+\left(\dfrac{f}{f_{bt}}\right)^{pf_{bt}}\right)^{pd_{bt}}} \qquad (3\text{-}5)$$

to avoid writing a complex expression in the following equations. Thus, we can find the limits of the spectral ratio when frequency goes to zero and infinity as

$$\frac{Y_t(f)}{Y_s(f)} = \frac{M_{0t}}{M_{0s}} \qquad\qquad\qquad\qquad\qquad\qquad if \ f \to 0$$

$$\frac{Y_t(f)}{Y_s(f)} = \frac{M_{0t}}{M_{0s}} \frac{(f_{at})^{pf_{at}\,pd_{at}}}{(f_{as})^{pf_{as}\,pd_{as}}} \frac{(f_{bt})^{pf_{bt}\,pd_{bt}}}{(f_{bs})^{pf_{bs}\,pd_{bs}}} = \frac{M_{0t}}{M_{0s}} \frac{(f_{ct})^2}{(f_{cs})^2} \qquad if \ f \to \infty$$

$$(3\text{-}6)$$

Also, using the expected target spectrum, as explained previously in Chapter 2 equation (2-13), the spectral ratio of the target event to the small event can be written as

$$\frac{Y_t(f)}{Y_s(f)} = \left[\xi N \sqrt{\frac{1}{N} + (1-\frac{1}{N})|p(\omega)|^2} \right]$$

$$\frac{Y_t(f)}{Y_s(f)} = [\xi N] \qquad\qquad if \ f \to 0 \qquad\qquad (3\text{-}7)$$

$$\frac{Y_t(f)}{Y_s(f)} = \left[\xi \sqrt{N} \right] \qquad\qquad if \ f \to \infty$$

Therefore, by equality of the limits of equations (3-6) and (3-7) for the very LF and very HF, the scaling factor and number of small events can be found as

$$N = \left(\frac{f_{cs}}{f_{ct}}\right)^4$$

$$\xi = \frac{M_t/M_s}{N} = \frac{M_t/M_s}{\left(\dfrac{f_{cs}}{f_{ct}}\right)^4} \qquad\qquad (3\text{-}8)$$

As can be seen, since the LF and HF of the SCF and DCF source models match each other, the scaling factor and number of summands have not been changed and can be obtained like the SCF source model. Now, if the pdf to generate rupture times is obtained, we will have a

complete solution. In order to derive the pdf of rupture times, we use the equality of equations (3-4) and (3-7) in the middle frequency range as follows

$$\frac{Y_t(f)}{Y_s(f)} = \left[\xi N \sqrt{\frac{1}{N} + (1 - \frac{1}{N})|p(\omega)|^2} \right] = \frac{M_{0t}}{M_{0s}} G \tag{3-9}$$

After simplifying the above-mentioned equation, the Fourier transform of the pdf of rupture times is derived as

$$|p(\omega)| = \sqrt{\frac{NG^2 - 1}{N - 1}} \tag{3-10}$$

Supposing that $p(\omega)$ is real, then the pdf of rupture times can be obtained by getting the inverse Fourier transform as

$$p(t) = \frac{1}{2\pi} \int_{-\infty}^{\infty} \sqrt{\frac{NG^2 - 1}{N - 1}} e^{i\omega t} d\omega \tag{3-11}$$

in which G is the function defined in equation (3-5).

To perform a numerical example for this scheme, we use the following values to simulate a target event from a small event, supposing both have identical stress drop values (assumption of similarity)

$$
\begin{aligned}
M_t &= 1.0 \\
M_s &= 0.001 \\
pf_a &= pf_b = 2.0 \\
pd_a &= pd_b = 0.5 \\
f_{ct} &= 1.0, f_{at} = 0.2 \rightarrow f_{bt} = 5.0 \\
f_{cs} &= 10.0, f_{as} = 4.0 \rightarrow f_{bs} = 25.0
\end{aligned}
\tag{3-12}
$$

To do simulation, we use a sampling rate of 200 samples/sec (step size of 0.005 sec). Hence, the Nyquist frequency is 100 Hz (half of the sampling rate). Since the corner frequencies of the target event are 0.2 and 5.0 Hz, the duration of the target event is $0.5/0.2 + 0.5/5.0 = 2.6$ sec. However, the SCF source model with similar characteristics has a source duration of 1.0 sec. This increase of duration causes the reduction of PGA and PSA values if the energy is constant. Figure 3-1 depicts the difference between the spectra of MDCF and SCF source models for both

small and target events. As can be seen, in the middle frequency range, there is a spectral sag for the MDCF source model; however, the MDCF source spectra match the SCF source spectra at very LFs and very HFs for both small and target events.

Figure 3-2 demonstrates simulated spectra from 10 different realizations as well as spectra of small and target events following a MDCF source model. It is interesting to note that each simulation can be soemwhat distinct from the target spectrum, while simulations on average perfectly match the target spectrum in the whole frequency range of interest. The average simulation is the root mean square (rms) mean of all different realizations. Different numbers of simulations (*e.g.*, 10, 40, and 640) are suggested for averaging and matching the target frequency with higher accuracy (Boore, 2003; Boore, 2009). This figure describes that the average spectrum from even a small number of simulations (10) can roughly match the target spectrum in the entire frequency range. Figure 3-3 illustrates the rupture times generated by the one-stage scheme of the MCDF source model for three different realizations. Since the scheme is performed in only one stage, the distributions of generated rupture times are pretty similar and the maximum energy is released in the half source duration for all realizations. Therefore, this scheme cannot appropriately account for the variability of different rupture propagation scenarios as well as asperities. Hence, we extend this method to the two-stage scheme in the next section.

3.2.2 Two-stage Summation Scheme

The whole concept of the two-stage summation scheme has been comprehensively described in Chapter 2 Section 4. Therefore, here only important equations to implement this scheme are explained.

The spectral ratio of the target event to the small event can be written as the ratio of the source spectra using equation (3-4). On the other hand, the expected spectral ratio of the target event to the small event can be written as (from equations (2-60) thorough (2-63))

$$\frac{Y_t(f)}{Y_s(f)} = \left[N\,\xi\sqrt{\frac{\left[1+(N_2-1)|p_2(\omega)|^2\right]}{N_2}}\sqrt{\frac{\left[1+(N_1-1)|p_1(\omega)|^2\right]}{N_1}} \right]$$

$$\frac{Y_t(f)}{Y_s(f)} = \left[\xi N\right] \qquad if \;\; f \to 0$$

$$\frac{Y_t(f)}{Y_s(f)} = \left[\xi\sqrt{N}\right] \qquad if \;\; f \to \infty$$

(3-13)

in which N_1 and N_2 are the number of main patches and the number of small events inside each patch, respectively, and $N = N_1\, N_2$. $p_1(\omega)$ and $p_2(\omega)$ are pdfs to produce rupture times for the first and second stage over the total target source duration and over the auxiliary source duration, respectively. Similar to the two-stage scheme for the SCF source model, we assume a small number like 10 for the number of main patches.

The LF and HF limits are the same as the one-stage scheme. Thus, equation (3-8) can be used to obtain the scaling factor and number of subevents. Then for the intermediate frequency range, by equality of equations (3-13) and (3-4), we get

$$\frac{Y_t(f)}{Y_s(f)} = \left[N\,\xi\sqrt{\frac{\left[1+(N_1-1)|p_1(\omega)|^2\right]}{N_1}}\sqrt{\frac{\left[1+(N_2-1)|p_2(\omega)|^2\right]}{N_2}} \right] =$$

$$\frac{M_{0t}}{M_{0s}}\frac{\left(1+\left(\dfrac{f}{f_{as}}\right)^{pf_{as}}\right)^{pd_{as}}\left(1+\left(\dfrac{f}{f_{bs}}\right)^{pf_{bs}}\right)^{pd_{bs}}}{\left(1+\left(\dfrac{f}{f_{at}}\right)^{pf_{at}}\right)^{pd_{at}}\left(1+\left(\dfrac{f}{f_{bt}}\right)^{pf_{bt}}\right)^{pd_{bt}}} =$$

$$\frac{M_{0t}}{M_{0s}}\left[\frac{\left(1+\left(\dfrac{f}{f_{ad}}\right)^{pf_{ad}}\right)^{pd_{ad}}\left(1+\left(\dfrac{f}{f_{bd}}\right)^{pf_{bd}}\right)^{pd_{bd}}}{\left(1+\left(\dfrac{f}{f_{at}}\right)^{pf_{at}}\right)^{pd_{at}}\left(1+\left(\dfrac{f}{f_{bt}}\right)^{pf_{bt}}\right)^{pd_{bt}}}\right]\left[\frac{\left(1+\left(\dfrac{f}{f_{as}}\right)^{pf_{as}}\right)^{pd_{as}}\left(1+\left(\dfrac{f}{f_{bs}}\right)^{pf_{bs}}\right)^{pd_{bs}}}{\left(1+\left(\dfrac{f}{f_{ad}}\right)^{pf_{ad}}\right)^{pd_{ad}}\left(1+\left(\dfrac{f}{f_{bd}}\right)^{pf_{bd}}\right)^{pd_{bd}}}\right]$$

(3-14)

in which f_{ad} and f_{bd} are the corner frequencies of an auxiliary event with a MDCF source model, and pf_{ad}, pf_{bd}, pd_{ad}, and pd_{bd} are its exponents somehow, they satisfy

$$pf_{ad} \times pd_{ad} + pf_{bd} \times pd_{bd} = 2$$
$$f_{ad}^{\,pf_{ad} \times pd_{ad}} \times f_{bd}^{\,pf_{bd} \times pd_{bd}} = f_{cd}^{\,2}$$

(3-15)

where f_{cd} is a variable to characterize the main corner frequency of the virtual event between the small and target events, defined as

$$N_1 = \left(\frac{f_{cd}}{f_{ct}}\right)^4 \rightarrow f_{cd} = N_1^{1/4} f_{ct}$$

$$N_2 = \left(\frac{f_{cs}}{f_{cd}}\right)^4 \rightarrow f_{cd} = N_2^{-1/4} f_{cs}$$

(3-16)

Assuming the two pdfs are independent, one solution can be obtained from the equality of the first term on both sides and from the equality of the second term on both sides of equation (3-14). Then, the pdfs can be expressed as

$$p_1(t) = \frac{1}{2\pi} \int_{-\infty}^{\infty} \sqrt{\frac{N_1 L_1^{\,2} - 1}{N_1 - 1}} e^{i\omega t} d\omega$$

$$p_2(t) = \frac{1}{2\pi} \int_{-\infty}^{\infty} \sqrt{\frac{N_2 L_2^{\,2} - 1}{N_2 - 1}} e^{i\omega t} d\omega$$

(3-17)

in which L_1 and L_2 are two functions defined as

$$L_1 = \frac{\left(1+\left(\frac{f}{f_{ad}}\right)^{pf_{ad}}\right)^{pd_{ad}} \left(1+\left(\frac{f}{f_{bd}}\right)^{pf_{bd}}\right)^{pd_{bd}}}{\left(1+\left(\frac{f}{f_{at}}\right)^{pf_{at}}\right)^{pd_{at}} \left(1+\left(\frac{f}{f_{bt}}\right)^{pf_{bt}}\right)^{pd_{bt}}}$$

$$L_2 = \frac{\left(1+\left(\frac{f}{f_{as}}\right)^{pf_{as}}\right)^{pd_{as}} \left(1+\left(\frac{f}{f_{bs}}\right)^{pf_{bs}}\right)^{pd_{bs}}}{\left(1+\left(\frac{f}{f_{ad}}\right)^{pf_{ad}}\right)^{pd_{ad}} \left(1+\left(\frac{f}{f_{bd}}\right)^{pf_{bd}}\right)^{pd_{bd}}}$$

(3-18)

To test the proposed two-stage scheme for the MDCF source model, we use the similar assumptions mentioned in equation (3-12). For the auxiliary event, we use the following assumptions

$$pf_{ad} = pf_{bd} = 2.0$$
$$pd_{ad} = pd_{bd} = 0.5$$
$$N_1 = 10 \rightarrow f_{cd} = N_1^{1/4} f_{ct} = 1.7783 \tag{3-19}$$

For the corner frequencies, we suppose the lower corner frequency and then obtain the upper one using equation (3-15) as

$$f_{ad} = 1.5058 \rightarrow f_{bd} = 2.1000 \tag{3-20}$$

Figure 3-4 presents 10 different realizations generated using the two-stage summation scheme for the MDCF source model and the rms average simulation. As can be seen, the average simulation is in good agreement with the target spectrum in the entire frequency band of interest. However, the average spectrum from 10 realizations is not as smooth as the one-stage summation of the MDCF source model. Therefore, it is recommended to employ more realizations to obtain the average simulation in order to have a smoother result. Figure 3-5 demonstrates three different distributions of generated rupture times for the two-stage summation scheme with the MDCF source model. It is obvious that the complexity of the source rupture can be modeled using this scheme and the energy is well distributed over the source duration without concentration of the energy in the half of the duration. Hence, each realization simulated using this scheme is completely different than the next realization; and as a result, the variability of the rupture process and effect of asperities can be included in this summation scheme.

3.3 Additive Double Corner Frequency Source Models

The Fourier acceleration spectrum for an additive double corner frequency (ADCF) source model is obtained by summation of two spectra as (Boore *et al.,* 2014)

$$S(f) = CM_0 (2\pi f)^2 \left[\frac{1-\varepsilon}{\left(1+\left(\dfrac{f}{f_a}\right)^{pf_a}\right)^{pd_a}} + \frac{\varepsilon}{\left(1+\left(\dfrac{f}{f_b}\right)^{pf_b}\right)^{pd_b}} \right] \tag{3-21}$$

where ε is a weighting factor in the range of 0 to 1 for assigning the contribution of each SCF spectrum. The LF and HF level of the Fourier acceleration spectrum of the ADCF source model

must match the LF and HF level of the Fourier acceleration spectrum of the SCF source model. Thus, it imposes the following constraints

$$pf_a \times pd_a = pf_b \times pd_b = 2$$
$$(1-\varepsilon)f_a^2 + \varepsilon f_b^2 = f_c^2$$

(3-22)

in which f_c is determined using equation (1-40); therefore, if one of the corner frequencies and epsilon are specified, the other corner frequency can be obtained from the aforementioned equation.

3.3.1 One-stage Summation Scheme

Based on the equation of the FAS of the DCF source model, the small and target spectra can be written as

$$S_t(f) = CM_{0t}(2\pi f)^2 \left[\frac{1-\varepsilon_t}{\left(1+\left(\frac{f}{f_{at}}\right)^{pf_{at}}\right)^{pd_{at}}} + \frac{\varepsilon_t}{\left(1+\left(\frac{f}{f_{bt}}\right)^{pf_{bt}}\right)^{pd_{bt}}} \right]$$

$$S_s(f) = CM_{0s}(2\pi f)^2 \left[\frac{1-\varepsilon_s}{\left(1+\left(\frac{f}{f_{as}}\right)^{pf_{as}}\right)^{pd_{as}}} + \frac{\varepsilon_s}{\left(1+\left(\frac{f}{f_{bs}}\right)^{pf_{bs}}\right)^{pd_{bs}}} \right]$$

(3-23)

and by dividing the spectra, the spectral ratio of the target event to the small event can be written as

$$\frac{Y_t(f)}{Y_s(f)} = \frac{M_{0t}}{M_{0s}} \frac{\left[\dfrac{1-\varepsilon_t}{\left(1+\left(\dfrac{f}{f_{at}}\right)^{pf_{at}}\right)^{pd_{at}}} + \dfrac{\varepsilon_t}{\left(1+\left(\dfrac{f}{f_{bt}}\right)^{pf_{bt}}\right)^{pd_{bt}}}\right]}{\left[\dfrac{1-\varepsilon_s}{\left(1+\left(\dfrac{f}{f_{as}}\right)^{pf_{as}}\right)^{pd_{as}}} + \dfrac{\varepsilon_s}{\left(1+\left(\dfrac{f}{f_{bs}}\right)^{pf_{bs}}\right)^{pd_{bs}}}\right]} = \frac{M_{0t}}{M_{0s}} G^* \qquad (3\text{-}24)$$

where G^* is

$$G^* = \frac{\left[\dfrac{1-\varepsilon_t}{\left(1+\left(\dfrac{f}{f_{at}}\right)^{pf_{at}}\right)^{pd_{at}}} + \dfrac{\varepsilon_t}{\left(1+\left(\dfrac{f}{f_{bt}}\right)^{pf_{bt}}\right)^{pd_{bt}}}\right]}{\left[\dfrac{1-\varepsilon_s}{\left(1+\left(\dfrac{f}{f_{as}}\right)^{pf_{as}}\right)^{pd_{as}}} + \dfrac{\varepsilon_s}{\left(1+\left(\dfrac{f}{f_{bs}}\right)^{pf_{bs}}\right)^{pd_{bs}}}\right]} \qquad (3\text{-}25)$$

to avoid writing a complex expression in the following equations. Thus, we can find the limits of the spectral ratio when frequency approaches to zero and infinity as

$$\frac{Y_t(f)}{Y_s(f)} = \frac{M_{0t}}{M_{0s}} \qquad\qquad\qquad\qquad\qquad\qquad\qquad if\ f \to 0$$

$$\frac{Y_t(f)}{Y_s(f)} = \frac{M_{0t}}{M_{0s}} \frac{(1-\varepsilon_t)f_{at}^{pf_{at}pd_{at}} + (\varepsilon_t)f_{bt}^{pf_{bt}pd_{bt}}}{(1-\varepsilon_s)f_{as}^{pf_{as}pd_{as}} + (\varepsilon_s)f_{bs}^{pf_{bs}pd_{bs}}} = \frac{M_{0t}}{M_{0s}} \frac{(f_{ct})^2}{(f_{cs})^2} \qquad if\ f \to \infty \qquad (3\text{-}26)$$

Moreover, using the expected target spectrum, as explained previously in equation (3-7), the spectral ratio of the target event to the small event can be written as

$$\frac{Y_t(f)}{Y_s(f)} = \left[\xi N \sqrt{\frac{1}{N} + (1-\frac{1}{N})|p(\omega)|^2} \right]$$

$$\frac{Y_t(f)}{Y_s(f)} = \left[\xi N \right] \qquad \text{if} \ \ f \to 0 \qquad\qquad (3\text{-}27)$$

$$\frac{Y_t(f)}{Y_s(f)} = \left[\xi \sqrt{N} \right] \qquad \text{if} \ \ f \to \infty$$

Hence, by equality of the limits of equations (3-26) and (3-27) for the very LF and very HF, the scaling factor and number of summands can be found as

$$N = \left(\frac{f_{cs}}{f_{ct}} \right)^4$$

$$\xi = \frac{M_t/M_s}{N} = \frac{M_t/M_s}{\left(\dfrac{f_{cs}}{f_{ct}} \right)^4} \qquad\qquad (3\text{-}28)$$

Again, since the LF and HF spectrum of the SCF source model matches the LF and HF spectrum of the DCF source model, the scaling factor and number of small events are the same and can be obtained like the SCF source model. Thus, if the pdf to generate rupture times is determined, a complete solution is obtained. In order to compute the pdf of rupture times, we use the equality of equations (3-24) and (3-27) in the middle frequency range as follows

$$\frac{Y_t(f)}{Y_s(f)} = \left[\xi N \sqrt{\frac{1}{N} + (1-\frac{1}{N})|p(\omega)|^2} \right] = \frac{M_{0t}}{M_{0s}} G^* \qquad\qquad (3\text{-}29)$$

After simplifying the abovementioned equation, the Fourier transform of the pdf of rupture times is derived as

$$|p(\omega)| = \sqrt{\frac{NG^{*2}-1}{N-1}} \qquad\qquad (3\text{-}30)$$

Supposing that $p(\omega)$ is real, the pdf of rupture times can be obtained by getting inverse Fourier transform as

$$p(t) = \frac{1}{2\pi} \int_{-\infty}^{\infty} \sqrt{\frac{NG^{*2}-1}{N-1}} e^{i\omega t} d\omega \qquad\qquad (3\text{-}31)$$

in which G^* is the function defined in equation (3-25).

To perform a numerical example for this scheme, we use the following values to simulate a target event from a small event supposing both events have identical stress drop values (assumption of similarity)

$$
\begin{aligned}
&M_t = 1.0 \\
&M_s = 0.001 \\
&pf_a = pf_b = 2.0 \\
&pd_a = pd_b = 1.0 \\
&f_{ct} = 1.0, \ f_{at} = 0.1603 \rightarrow f_{bt} = 2.8676 \\
&f_{cs} = 10.0, \ f_{as} = 1.5740 \rightarrow f_{bs} = 16.0016 \\
&eps_{ct} = 0.1189 \\
&eps_{cs} = 0.3846
\end{aligned}
\tag{3-32}
$$

In these equations, we used the approach suggested by Boore *et al.* (2014) to obtain epsilon and f_a using the following equations derived by Atkinson and Silva (2000) for ENA

$$
\begin{aligned}
\log f_a &= 2.181 - 0.496\mathbf{M} \\
\log \varepsilon &= 0.605 - 0.255\mathbf{M}
\end{aligned}
\tag{3-33}
$$

assuming that the target event has a magnitude of 6 and the small event has a magnitude of 4.

To perform simulation, we employ a sampling rate of 200 samples/sec (step size of 0.005 sec). Thus, the Nyquist frequency is 100 Hz (half of the sampling rate). Because the corner frequencies of the target event are 0.1603 and 2.8676 Hz, the duration of the target event is 0.5/0.1603 + 0.5/2.8676 = 3.2930 sec. Note that the SCF source model with similar characteristics has a source duration of 1.0 sec. Duration increase causes the decease of PGA and PSA values assuming the energy is constant. Figure 3-6 compares the source spectra of the ADCF model with the SCF model for target and small events. The ADCF source model has a considerable spectral sag at the middle frequency range and this sag increases with increasing the magnitude of the event. Figure 3-7 shows the rms average of 10 different simulations compared with each other as well as the spectrum of the target event. It is clear that the average simulation is in good agreement with the target spectrum in the whole frequency range and can perfectly mimic the spectral sag between two corner frequencies. Figure 3-8 displays three different distributions of rupture times. Again, since this is a one-stage scheme the maximum energy is

focused in the middle; therefore, this summation scheme results in similar simulations. Thus, to capture the variability of the rupture process and the effect of asperities, this scheme is extended to a two-stage summation.

3.3.2 Two-stage Summation Scheme

The spectral ratio of the target event to the small event can be written as the ratio of the source spectra using equation (3-24). The expected spectral ratio of the target event to the small event can be written the same as the two-stage summation scheme for the MDCF source model equation (3-13).

The LF and HF limits are the same as the one-stage scheme of the ADCF source model. Therefore, equation (3-28) can be used to obtain the scaling factor and number of small events. Then for the intermediate frequency range, we have

$$\frac{Y_t(f)}{Y_s(f)} = \left[N\,\xi\sqrt{\frac{\left[1+(N_1-1)\left|p_1(\omega)\right|^2\right]}{N_1}}\sqrt{\frac{\left[1+(N_2-1)\left|p_2(\omega)\right|^2\right]}{N_2}}\,\right] =$$

$$\frac{M_{0t}}{M_{0s}}\frac{\left[\dfrac{1-\varepsilon_t}{\left(1+\left(\dfrac{f}{f_{at}}\right)^{pf_{at}}\right)^{pd_{at}}}+\dfrac{\varepsilon_t}{\left(1+\left(\dfrac{f}{f_{bt}}\right)^{pf_{bt}}\right)^{pd_{bt}}}\right]}{\left[\dfrac{1-\varepsilon_s}{\left(1+\left(\dfrac{f}{f_{as}}\right)^{pf_{as}}\right)^{pd_{as}}}+\dfrac{\varepsilon_s}{\left(1+\left(\dfrac{f}{f_{bs}}\right)^{pf_{bs}}\right)^{pd_{bs}}}\right]} =$$

$$\frac{M_{0t}}{M_{0s}}\left[\frac{\left[\dfrac{1-\varepsilon_t}{\left(1+\left(\dfrac{f}{f_{at}}\right)^{pf_{at}}\right)^{pd_{at}}}+\dfrac{\varepsilon_t}{\left(1+\left(\dfrac{f}{f_{bt}}\right)^{pf_{bt}}\right)^{pd_{bt}}}\right]}{\left[\dfrac{1-\varepsilon_d}{\left(1+\left(\dfrac{f}{f_{ad}}\right)^{pf_{ad}}\right)^{pd_{ad}}}+\dfrac{\varepsilon_d}{\left(1+\left(\dfrac{f}{f_{bd}}\right)^{pf_{bd}}\right)^{pd_{bd}}}\right]}\right]\left[\frac{\left[\dfrac{1-\varepsilon_d}{\left(1+\left(\dfrac{f}{f_{ad}}\right)^{pf_{ad}}\right)^{pd_{ad}}}+\dfrac{\varepsilon_d}{\left(1+\left(\dfrac{f}{f_{bd}}\right)^{pf_{bd}}\right)^{pd_{bd}}}\right]}{\left[\dfrac{1-\varepsilon_s}{\left(1+\left(\dfrac{f}{f_{as}}\right)^{pf_{as}}\right)^{pd_{as}}}+\dfrac{\varepsilon_s}{\left(1+\left(\dfrac{f}{f_{bs}}\right)^{pf_{bs}}\right)^{pd_{bs}}}\right]}\right] \quad (3\text{-}34)$$

where f_{ad} and f_{bd} are the corner frequencies of an auxiliary event with a ADCF source model, and pf_{ad}, pf_{bd}, pd_{ad}, and pd_{bd} are its exponents satisfying the following constraints

$$pf_{ad} \times pd_{ad} = pf_{bd} \times pd_{bd} = 2$$
$$(1-\varepsilon_d)f_{ad}^2 + \varepsilon_d f_{bd}^2 = f_{cd}^2 \quad (3\text{-}35)$$

in which f_{cd} is a variable to specify the main corner frequency of the virtual event between the small and target events defined as

$$N_1 = \left(\frac{f_{cd}}{f_{ct}}\right)^4 \rightarrow f_{cd} = N_1^{1/4} f_{ct}$$

$$N_2 = \left(\frac{f_{cs}}{f_{cd}}\right)^4 \rightarrow f_{cd} = N_2^{-1/4} f_{cs}$$

(3-36)

Assuming these two pdfs are independent, one solution can be acquired from the equality of the first term on both sides and from the equality of the second term on both sides of equation (3-34). Then, the pdfs can be expressed as

$$p_1(t) = \frac{1}{2\pi} \int_{-\infty}^{\infty} \sqrt{\frac{N_1 J_1^2 - 1}{N_1 - 1}} e^{i\omega t} d\omega$$

$$p_2(t) = \frac{1}{2\pi} \int_{-\infty}^{\infty} \sqrt{\frac{N_2 J_2^2 - 1}{N_2 - 1}} e^{i\omega t} d\omega$$

(3-37)

in which L_1 and L_2 are two functions defined as

$$J_1 = \dfrac{\left[\dfrac{1-\varepsilon_t}{\left[\left(1+\left(\dfrac{f}{f_{at}}\right)^{pf_{at}}\right)^{pd_{at}}\right]} + \dfrac{\varepsilon_t}{\left(1+\left(\dfrac{f}{f_{bt}}\right)^{pf_{bt}}\right)^{pd_{bt}}}\right]}{\left[\dfrac{1-\varepsilon_d}{\left[\left(1+\left(\dfrac{f}{f_{ad}}\right)^{pf_{ad}}\right)^{pd_{ad}}\right]} + \dfrac{\varepsilon_d}{\left(1+\left(\dfrac{f}{f_{bd}}\right)^{pf_{bd}}\right)^{pd_{bd}}}\right]}$$

$$J_2 = \dfrac{\left[\dfrac{1-\varepsilon_d}{\left[\left(1+\left(\dfrac{f}{f_{ad}}\right)^{pf_{ad}}\right)^{pd_{ad}}\right]} + \dfrac{\varepsilon_d}{\left(1+\left(\dfrac{f}{f_{bd}}\right)^{pf_{bd}}\right)^{pd_{bd}}}\right]}{\left[\dfrac{1-\varepsilon_s}{\left[\left(1+\left(\dfrac{f}{f_{as}}\right)^{pf_{as}}\right)^{pd_{as}}\right]} + \dfrac{\varepsilon_s}{\left(1+\left(\dfrac{f}{f_{bs}}\right)^{pf_{bs}}\right)^{pd_{bs}}}\right]}$$

(3-38)

To numerically test the proposed two-stage scheme for the ADCF source model, we use the similar assumptions mentioned in equation (3-32). For the auxiliary event, we use the following assumptions

$$pf_{ad} = pf_{bd} = 2.0$$
$$pd_{ad} = pd_{bd} = 1.0$$
$$N_1 = 10 \rightarrow f_{cd} = N_1^{1/4} f_{ct} = 1.7783$$

(3-39)

For the corner frequencies, we suppose the lower corner frequency and epsilon, and then obtain the upper one using equation (3-35) as

$$f_{ad} = 1.5058, \ eps_d = 0.2138 \rightarrow f_{bd} = 2.1000$$

(3-40)

Figure 3-9 depicts 10 different realizations generated using the two-stage summation scheme for the ADCF source model as well as the rms average simulation. As can be seen, the

average simulation satisfactorily matches the target spectrum in the whole frequency range of interest. It should be noted that the average spectrum from 10 realizations is not as smooth as the one-stage summation of the ADCF source model. Thus, we suggest using more realizations to obtain the average simulation. Figure 3-10 illustrates distributions of generated rupture times for three different realizations using the two-stage summation scheme following the ADCF source model. As can be seen, the complexity of the source rupture can be captured using this scheme and the energy is distributed over the source duration without concentration of the energy in the middle. Thus, each simulation from this scheme is totally distinct from another simulation, resulting in capturing the variability of the rupture process and the effect of asperities in this scheme.

3.4 Figures
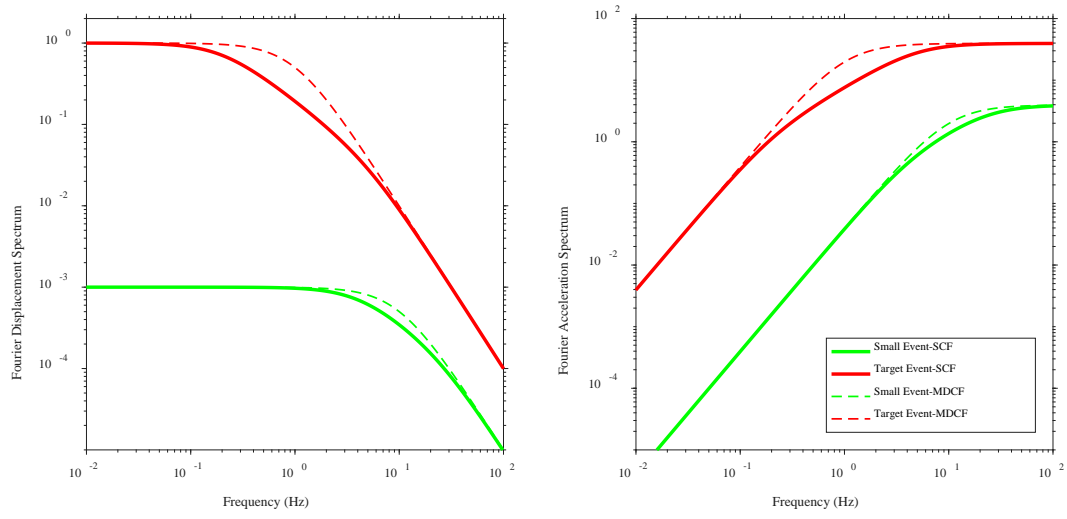
Figure 3-1. Comparison of the SCF source model ($f_{cs} = 10$ and $f_{ct} = 1$ Hz) with the MDCF source model ($f_{as} = 4$, $f_{bs} = 25$, $f_{at} = 0.2$, and $f_{bt} = 5$ Hz) for the small and target spectra.
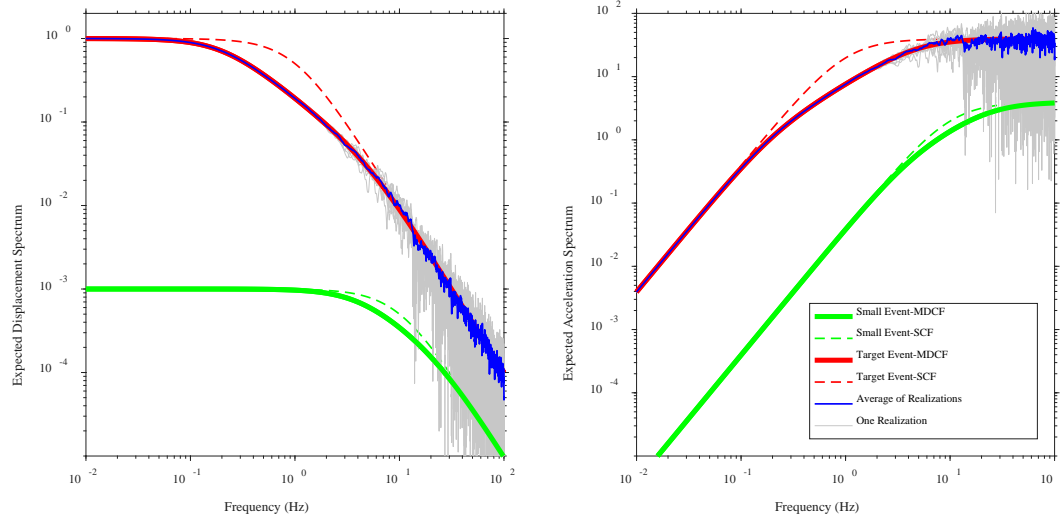
Figure 3-2. Spectra from 10 different realizations generated using the proposed one-stage summation scheme for the MDCF source model and rms average spectrum from 10 realizations compared to the target spectrum.
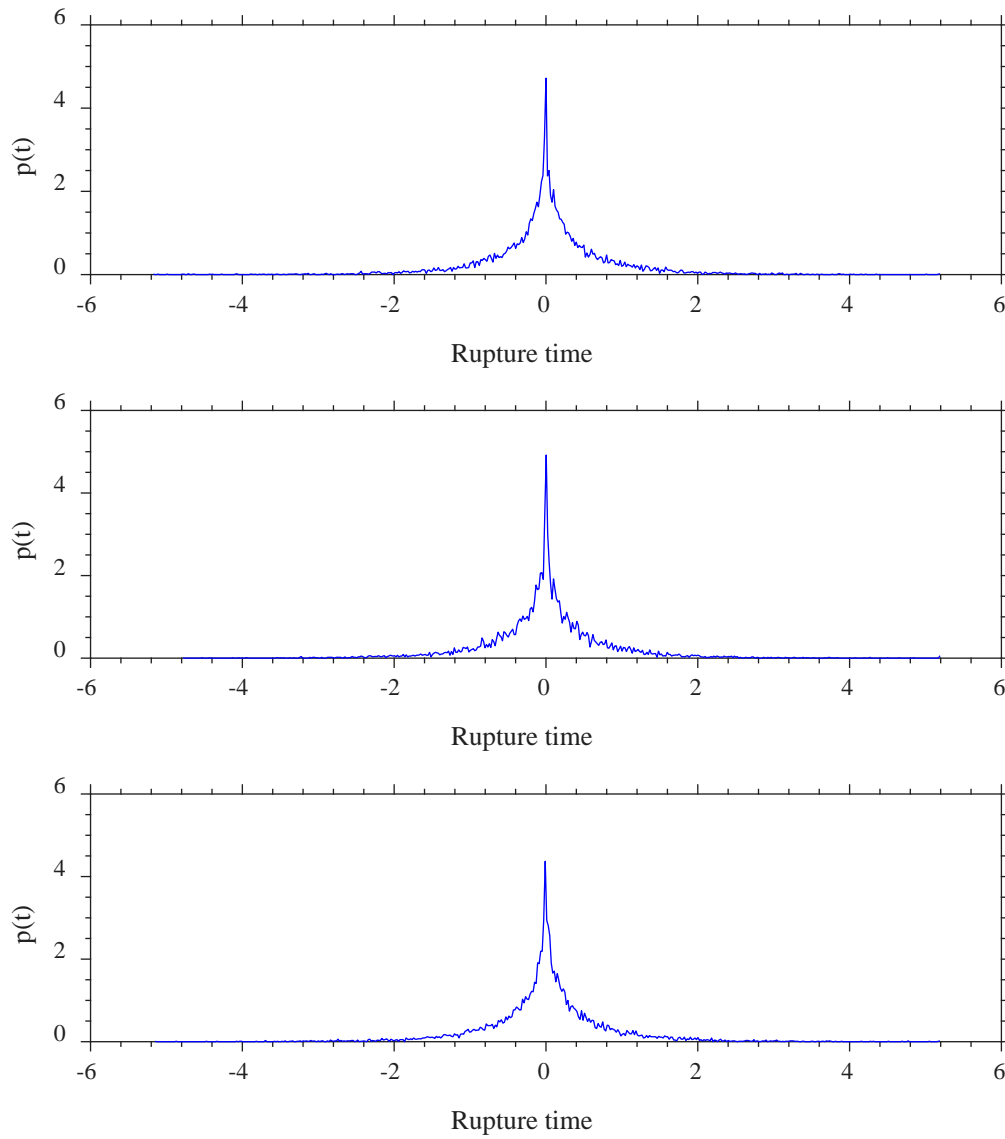
Figure 3-3. Three different distributions for rupture times generated using the proposed one-stage summation scheme for the MDCF source model.
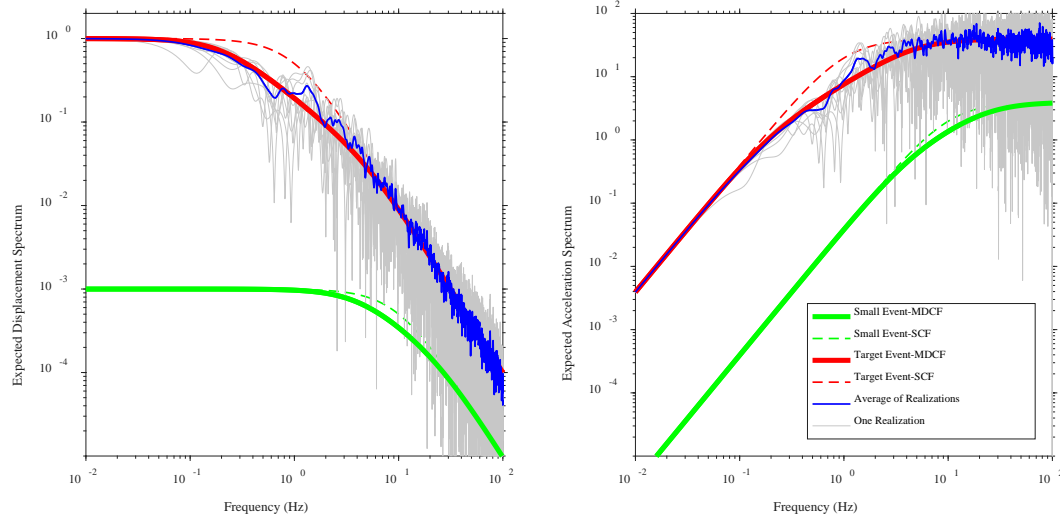
Figure 3-4. Spectra from 10 different realizations generated using the proposed two-stage summation scheme for the MDCF source model and rms average spectrum from 10 realizations compared to the target spectrum.
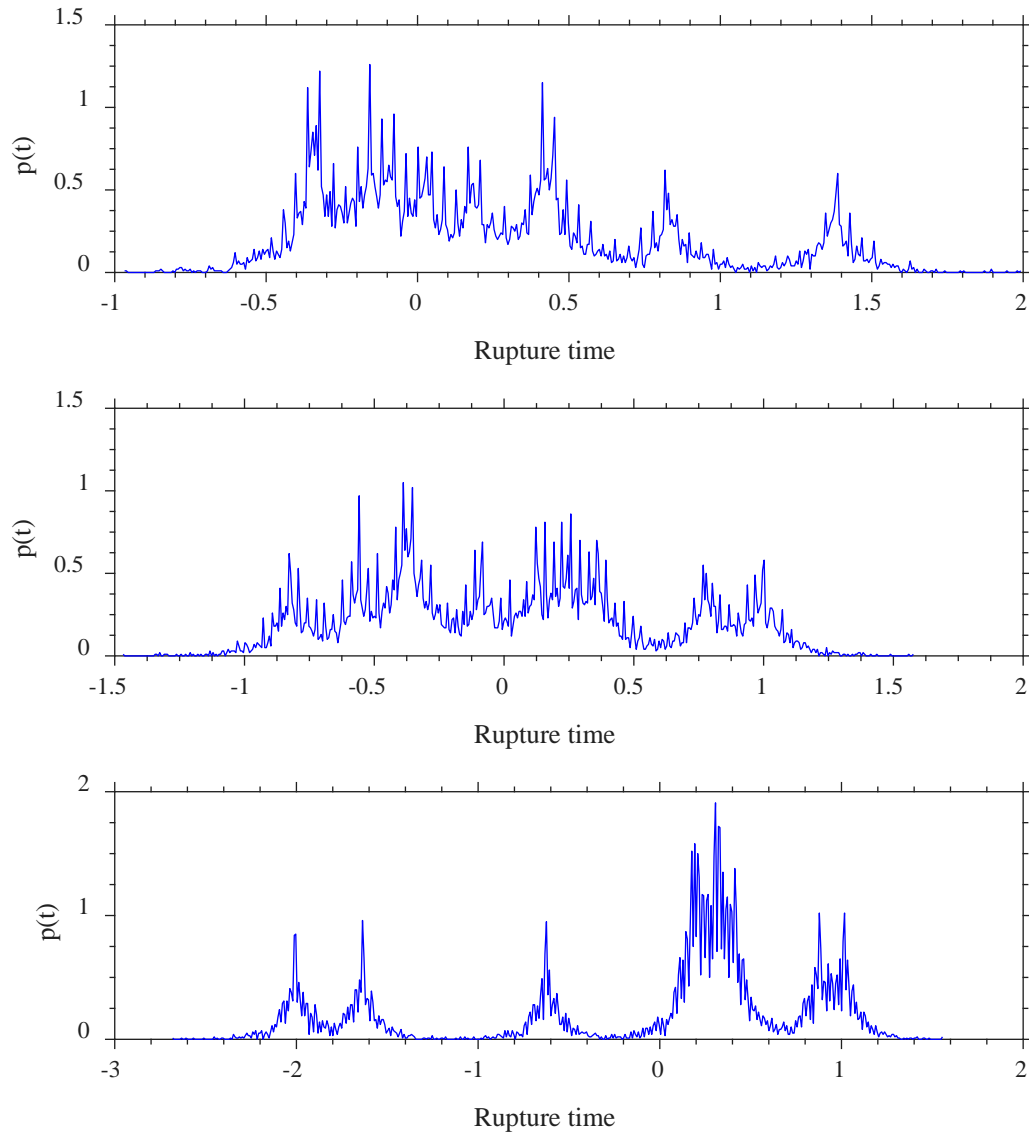
Figure 3-5. Three different distributions for rupture times generated using the proposed two-stage summation scheme for the MDCF source model.
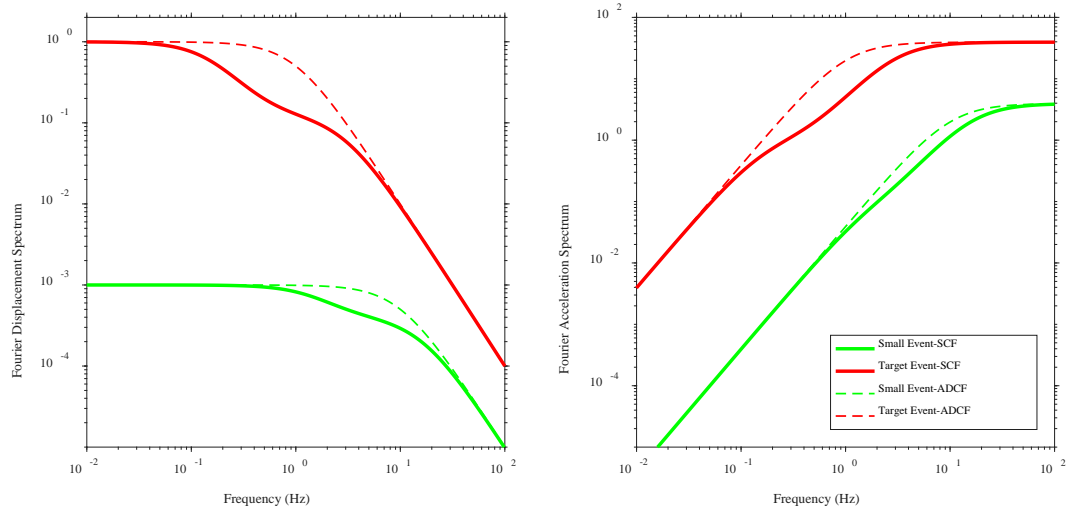
Figure 3-6. Comparison of the SCF source model ($f_{cs} = 10$ and $f_{cs} = 1$ Hz) with the ADCF source model ($f_{as} = 1.5740$, $f_{bs} = 16.0016$, $f_{at} = 0.1603$, $f_{bt} = 2.8676$ Hz, $\varepsilon_s = 0.3846$, and $\varepsilon_t = 0.1189$) for the small and target spectra.
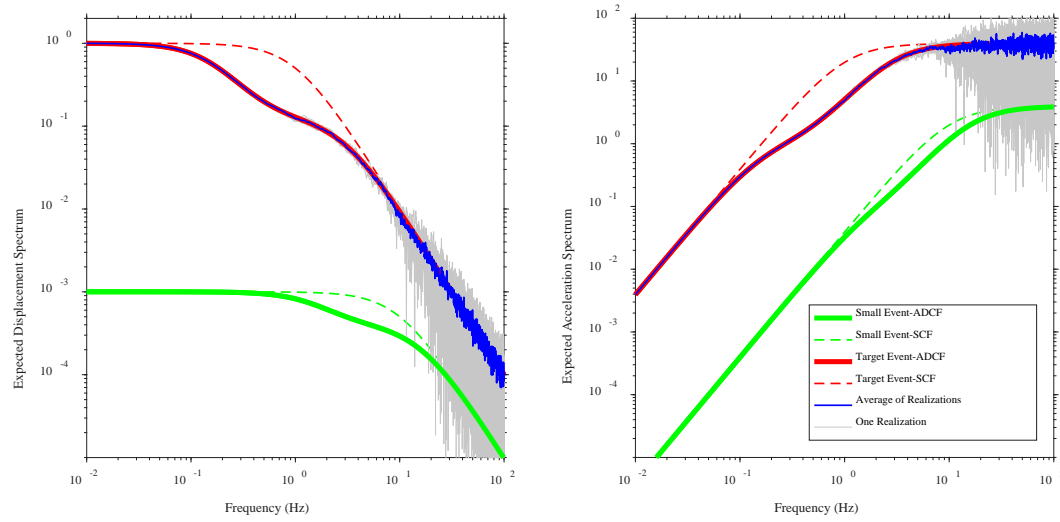
Figure 3-7. Spectra from 10 different realizations generated using the proposed one-stage summation scheme for the ADCF source model and rms average spectrum from realizations compared to the target spectrum.
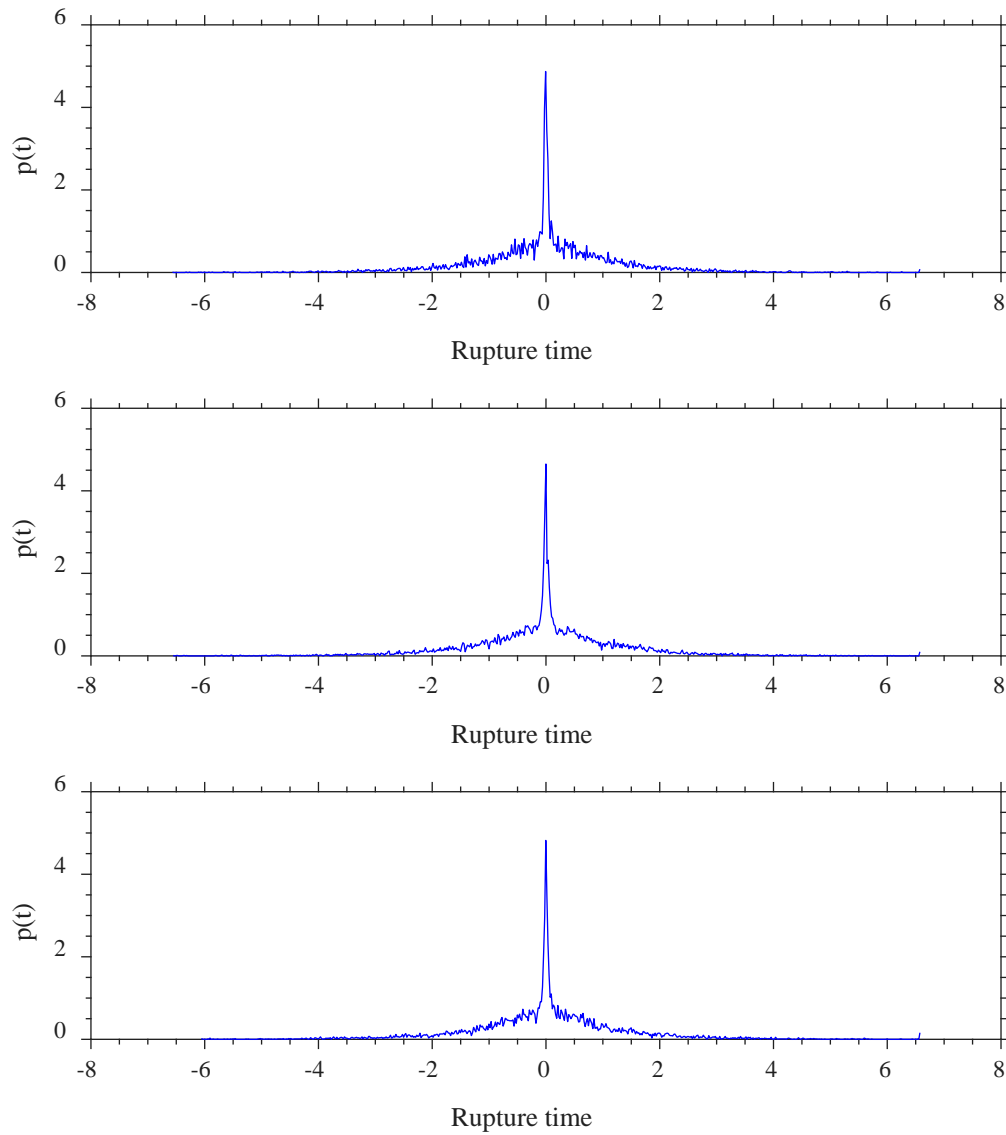
Figure 3-8. Three different distributions for rupture times generated using the proposed one-stage summation scheme for the ADCF source model.
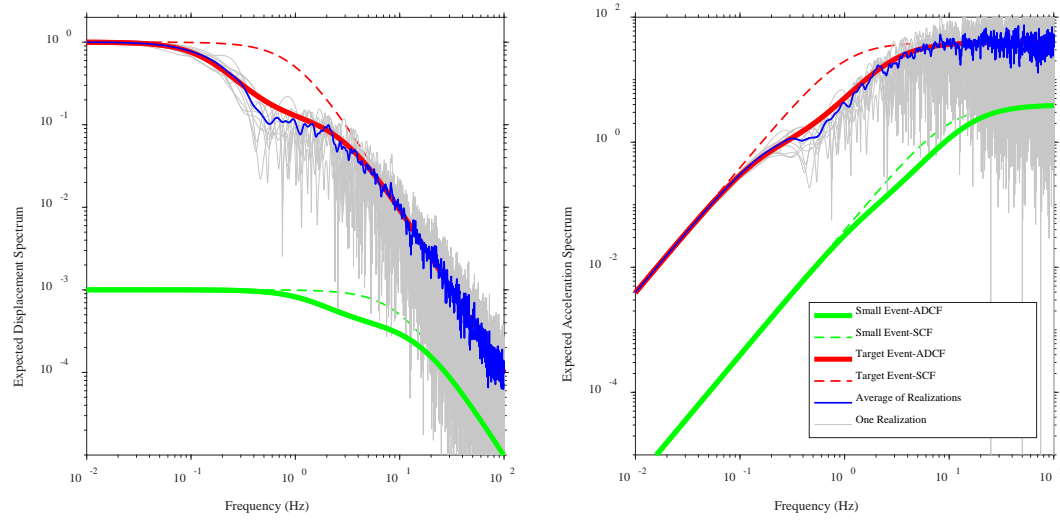
Figure 3-9. Spectra from 10 different realizations generated using the proposed two-stage summation scheme for the ADCF source model and rms average spectrum from realizations compared to the target spectrum.
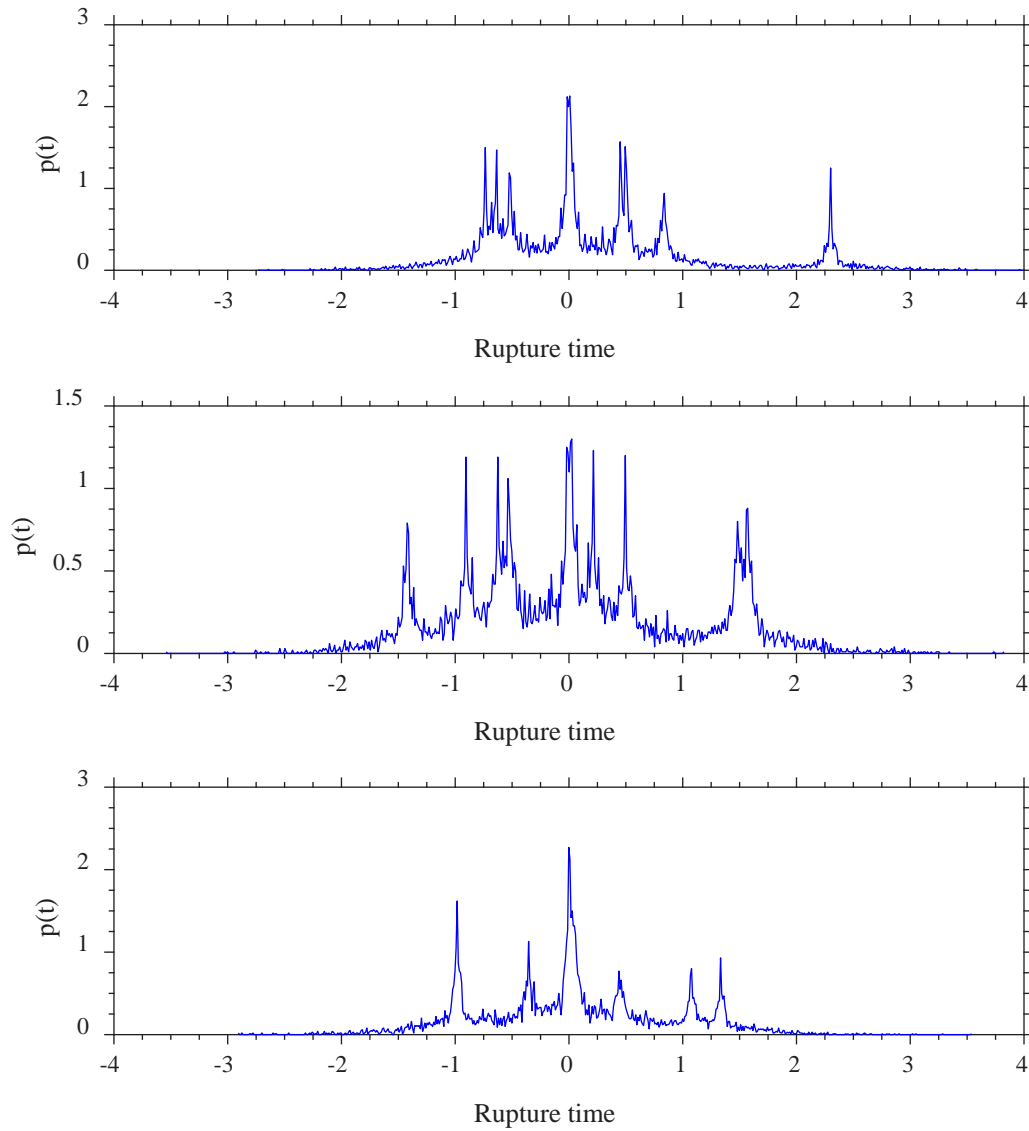
Figure 3-10. Three different distributions for rupture times generated using the proposed two-stage summation scheme for the ADCF source model.

4. An Improvement for Considering the Effects of Finite-Fault Sources on the Source-to-site Distance

4.1 Introduction

The Joyner-Boore distance (the closest distance to the surface projection of an extended fault, R_{JB}) or rupture distance (the closest distance to an extended fault, R_{RUP}) are commonly used in ground-motion prediction equations (GMPEs) to capture the effect of finite-fault ruptures, particularly for near-source recordings. In probabilistic seismic hazard analysis (PSHA), the spatial distribution of earthquakes within a large areal seismic source, where the traces of faults are unknown, is described by associating them with point-source models. Therefore, it is necessary to convert the extended fault-based distance metrics defined in GMPEs into the point source-based distance measures such as epicentral (R_{EPI}) or hypocentral (R_{HYP}) distances for use in PSHA. In other words, in the PSHA integrals, each potential event has a distance R_{EPI} from the site, but to get the ground motions for that event, the R_{EPI} must be converted into a R_{JB} for the magnitude of the event, and that R_{JB} is then used in the GMPE to get the ground motions. Various methods have been proposed to convert extended-fault source distance metrics into point-source distance metrics and vice versa.

Scherbaum *et al*. (2004) have developed the empirical distance conversion relations for three types of generic, strike-slip, and all dipping fault scenarios using simulated fault ruptures and observation points around the faults. In the Scherbaum *et al*. (2004) approach, the extended-fault rupture scenarios are generated based on the magnitude, the selected dip angle, and the hypocenter locations on the fault rupture, which are randomly chosen from a truncated normal distribution. Then, the observation points for each of the simulated extended-faults are randomly and uniformly chosen between 0 and 360 degrees about the fault rupture to calculate various distance measures [e.g., R_{EPI} from the site] with respect to R_{JB} distance and earthquake magnitude. Since the R_{JB} distance is always smaller than or equal to other distance measures, the positive residuals between various measures of distance and R_{JB} distance are used to determine the distance conversion relations. To this end, polynomial functional forms are provided to estimate the mean converted distance metrics as well as their standard errors by fitting a gamma

probability distribution function to residuals, which are defined as the difference between the R_{JB} distance and R_{EPI} or R_{HYP} distances.

This simulation-based approach calculates the converted R_{EPI} or R_{HYP} distances for a specific R_{JB} distance by ignoring the effect of wave propagation path from each portion of the entire fault to the site. The wave propagation path affects the mean converted distance, particularly for large fault ruptures by assigning non-uniform weighting factors (e.g., $R^{-\gamma}$ propagation decay where γ is the geometrical spreading exponent) to source-to-site distances. The Scherbaum *et al*. (2004) approach predicts large values of other distance measures near the fault ruptures, such as epicentral distance (R_{EPI}), for an initial-fixed value of $R_{JB,}$ compared to those approaches that involve GMPEs in the process of averaging possible epicenters or hypocenters (e.g., EPRI, 2004). The direct use of these distance conversion relations may not be considered suitable for evaluating ground motions, particularly for the areal seismic source models used in PSHA studies.

EPRI (2004) used GMPEs developed for central and eastern United States (CEUS) to provide the empirical point-source distance conversion equations for various measures of distance defined in the CEUS GMPEs. These distance conversion equations are used to adjust various source-to-site distances in areal seismic sources with unknown traces of faulting for PSHA studies in the CEUS. In EPRI (2004) approach, unknown extended-fault ruptures within a given areal seismic source are modeled to be an equal combination of 90˚-dip strike-slip faults and 40˚-dip reverse faults with uniform random orientations distributed in azimuth from 0 to 360 degrees about the earthquake epicenter and with uniform random depth constrained to a maximum depth of 25 km. Then, two most widely used distances, the R_{JB} distance and the R_{RUP} distance are calculated using an appropriate geometry for each randomly simulated fault rupture about the earthquake with moment magnitude of **M** and epicentral distance of R_{EPI} from the site.

Since seismic energy is released from the entire extended-fault rupture during a large earthquake, R_{JB} or R_{RUP} distances are used in appropriate R_{JB}- or R_{RUP}-based GMPEs to compute the geometric-mean ground motion intensity measure (GMIM) of interest such as peak ground acceleration as a measure of energy density of shaking for both strike-slip or reverse fault rupture models. The expected geometric-mean GMIM is used in those corresponding GMPEs to back-calculate the appropriate average R_{JB} or R_{RUP} distance and associated uncertainties with respect

117

to GMIM of interest. The EPRI (2004) distance conversion relations may be sensitive to the selection of GMPEs and the frequency of ground motions. These GMPE-based conversion equations need to be modified for areal seismic sources that a preferred fault orientation or explicit modeling of finite ruptures is warranted.

The USGS distance conversion approach used in the USGS hazard maps for the CEUS (Petersen *et al*., 2008) assumes that energy is released from the earthquake epicenter rather than the crust around the entire fault rupture during a large earthquake. In the USGS hazard maps, areal seismic source models are defined to account for future random earthquakes in areas with little or no historical seismicity for the PSHA study. Within areal source zones, a finite-fault vertical strike-slip fault is defined for each grid cell of source zones, and the fault rupture is located on the center of each grid cell. The virtual fault strike is randomly oriented in azimuth from 0 to 360 degrees about the earthquake epicenter, and the mean R_{JB} distance is calculated for a fixed R_{EPI} distance using the laws of sine and cosine. The dimension of a fault rupture varies for each magnitude increment and is obtained from the Wells and Coppersmith (1994) empirical relationships. Note that the USGS distance conversion relationships are applicable for the vertical fault ruptures, and may not be used for dipping fault ruptures and the regions with various geologic structures.

Bommer and Akkar (2012) have suggested directly developing pairs of GMPEs for both point and extended-source distance measures from the same ground-motion dataset. They performed a simple PSHA study and demonstrated that GMIMs obtained from the R_{JB}-based ground-motion models relative to R_{EPI}-based ground-motion models underestimate the hazard for areal seismic sources. The current GMPEs developed in the United States region have often used the R_{JB} or R_{RUP} distances from extended-fault sources of moderate-to-large magnitude earthquakes. In order to use these extended fault-based GMPEs for the case of areal seismic sources within the low-to-moderate seismicity, which tend to dominate hazard models in a PSHA study, the extended-fault distances should be converted into the point-source distances (R_{EPI} or R_{HYP}) if the point source-based GMPE models are not available.

The objective of this study is to develop an analytical approach to convert the distance measures defined for the extended-fault source-based GMPEs into various point source-based distance metrics for use in the PSHA study. The USGS and EPRI approaches use the R_{EPI}

distance as a reference distance metric and the R_{JB} distance as a target distance metric to link for two distance metrics between a point source and an extended fault source. In contrast with the EPRI and USGS approaches, we define Joyner-Boore (JB) surfaces containing virtual sites on a bathtub shape with identical R_{JB} distances around an extended-fault source as a reference distance, and then, analytically derive the average R_{EPI} and R_{HYP} using the laws of sines and cosines.

In this study, instead of using virtual faults, which are randomly oriented about a fixed earthquake epicenter (e.g., USGS and EPRI approaches), the virtual sites with a constant R_{JB} distance are taken around a fixed fault to improve the computational efficiency in the hazard models. The averaging distance conversion process are combined with region-specific geometrical spreading and anelastic attenuation functions following the Boore (2009) approach to assign a suitable weighting factor for distance conversion and to adjust the resultant point-source distance metrics into new effective R_{EPI} or R_{HYP} distance metrics that may be entered in current extended-fault source-based GMPEs for use in the PSHA studies as well as stochastic ground-motion simulations. The proposed region-specific distance conversion approach is able to model the effects of the seismic propagation path along the desired range of strikes and dip angles from available information about the tectonic region, which are not accounted in the other available methods.

As an implementation in the seismic hazard assessment, a simple PSHA study is performed within a simple circular areal source zone associated with both low and high-seismicity scenarios using a suite of published R_{RUP}-based GMPEs to demonstrate the effect of using inconsistent source-to-site distance metrics on hazard curves at a given site.

4.2 General Distance Conversion Equations

The R_{JB} distance is chosen as the primary reference metric in this study and the other distance matrices are converted as target distance metrics using the law of sines and cosines. The general distance conversion equations are analytically derived for both vertical and dipping fault rupture scenarios. The analytical distance conversion approach developed in this study has two different aspects compared to the USGS approach.

First, the proposed analytical approach is obtained based on positioning virtual sites around an arbitrary fault rupture, while the USGS approach simulates random-oriented vertical fault ruptures for a given site to obtain distance conversion equations. In essence, the distance conversion results should be insensitive either if the site is constant and the fault rotates around the center of the fault (virtual faults model) or if the fault is constant and the site rotates around the fault (virtual sites model). However, using the virtual sites model would improve the computational efficiency in the hazard models.

Second, the USGS approach fixes the epicentral distance on the center of fault, and then derives the distance conversion equations to obtain the average R_{JB} distance. On the other hand, in the proposed analytical approach the R_{JB} distance is fixed, and then the distance conversion equations are derived for various distance metrics. The advantage of using a fixed R_{JB} distance for a known fault and a given azimuth is that there is only one station for a R_{JB} distance, but the station for a fixed epicentral distance can be moved based on the location of epicenter. Due to this difficulty, the USGS approach limits itself by assuming that the epicenter is always in the center of the fault.

Figure 4-1 shows the Joyner-Boore (JB) surface about a vertical strike-slip fault and earthquake hypocenter locations, which are dependent to the moment magnitude and are defined by a truncated normal distribution. The location of possible observation points (virtual sites) having the same R_{JB} distances from an extended fault with a vertical dip angle are modeled with two semi-circles with radius of R_{JB} at the end points of the fault, and two straight lines parallel to fault. All the virtual sites on this bathtub-shaped JB surface have an identical R_{JB} distance to the fault. In this figure, θ_0 is the angle between the fault line and the line connecting the middle of the fault length and the point located on the boundaries between the semi-circles and parallel lines to the center of the fault length.

The JB surface becomes more complicated for dipping faults since there is a surface projection for the width of the fault. Figure 4-2 shows the JB surface around a dipping fault. For an extended fault with a width of W and a dip angle of δ, the surface projection of the fault has a width of $W\cos(\delta)$. In this case, the location of possible observation points having the same R_{JB} distances are modeled with four quarter-circles with radius R_{JB} and two parallel lines to the fault

length and two parallel lines to the width projection on the ground surface. All the observation points on this JB surface have an identical R_{JB} distance to the fault surface projection.

In this figure, the parameter of θ_0 is the angle between the line passing the center of the width projection and parallel to the fault length and the lines connecting the boundaries between the quarter-circles and parallel lines with the fault length to the center of the fault surface projection. The parameter of θ_1 is the angle between the line passing the center of the fault width projection and parallel with the fault length and the lines connecting the boundaries between the quarter-circles and parallel lines with the fault width projection to the center of the fault surface projection.

The JB surface has significant advantage that allows us to choose directly the R_{JB} distance defined in the R_{JB}-based GMPEs as the primary reference metric to convert to all other distance metrics.

4.2.1 Vertical Strike-slip Faults

Suppose that we have an arbitrary extended-fault rupture produced by a given earthquake, and observation points (virtual sites) with a constant R_{JB} distance of interest (see

Figure 4-1) on the JB surface. We begin with a relationship between R_{JB} and R_{HYP}, which is controlled by the depth of earthquake as a function of moment magnitude, and the influence of the depth is decreased with increasing distance.

For each observation point with a particular azimuth (θ), the geometry relation between R_{JB} distance and R_{HYP} distance using the law of sines and cosines is expressed by the following equation

$$< R_{HYP} >_\theta = \int\limits_{Z_{TOR}}^{Z_{TOR}+W} \int\limits_{-L/2}^{L/2} \sqrt{\left[\left(R_C^2 + x^2 - 2xR_C \cos(\theta)\right) + z^2\right]} p(x)p(z)dxdz \qquad (4\text{-}1)$$

where $< R_{HYP} >_\theta$ is the mean hypocentral distance for a particular θ, and R_C is an auxiliary distance between the center of the fault and the observation point, which is defined as

$$R_C = \begin{cases} \sqrt{(L/2)^2 + R_{JB}^2 - 2(L/2)R_{JB}\cos\left[180 - \left(\theta + \arcsin\left(\dfrac{\sin(\theta)L/2}{R_{JB}}\right)\right)\right]} & \text{if } 0 \le \theta < \theta_0 \\[4mm] R_{JB}\Big/\sin(\theta) & \text{if } \theta_0 \le \theta \le 90 \end{cases}$$

$$(4\text{-}2)$$

in which $\theta_0 = \arctan\left(\dfrac{R_{JB}}{L/2}\right)$, x is a variable on the fault length, and z is a variable on the fault

depth with probability distribution functions of $p(x)$ and $p(z)$, respectively. These probability

distribution functions can be defined somehow to mimic the characteristics of the fault rupture.

The term Z_{TOR} is the depth to the top of the fault rupture. If the azimuth angle of the site is

unknown, the average distance over all virtual sites is estimated by integrating over all possible

azimuth angles, which is defined as the following expression

$$<R_{HYP}> = \int_0^{2\pi} <R_{HYP}>_\theta \, p(\theta) d\theta \qquad (4\text{-}3)$$

where $<R_{HYP}>$ is the mean hypocentral distance over all azimuth angles, and $p(\theta) = \dfrac{1}{2\pi}$

is the probability distribution of azimuth θ in degree. Since the JB surface for vertical strike-slip

faults has four identical quarters (see Figure 4-1), the integration over θ may be performed for a

range of 0 to $\pi/2$ with $p(\theta) = 2/\pi$.

The mean hypocentral distance, equation (4-1), can be modified to derive the mean

epicentral distance by removing the first integral and z and $p(z)$ terms as follows

$$<R_{EPI}>_\theta = \int_{-L/2}^{L/2} \sqrt{\left[\left(R_C^2 + x^2 - 2xR_C\cos(\theta)\right)\right]} \, p(x) dx \qquad (4\text{-}4)$$

4.2.2 Dipping Faults

For a dipping fault with a dip angle of δ, the position of the observation points are located

in three different portions of the JB surface including the lines parallel to the fault length, the

quarter circles, and the lines parallel to the width projection (see Figure 4-2). As can be seen in

Figure 4-2, virtual sites around the JB surface of dipping faults can be located on either hanging

wall (HW) side or footwall (FW). The mean hypocentral distance for a particular azimuth angle

of θ, $<R_{HYP}>_\theta$, is obtained by averaging over all hypocentral distances. Thus, the mean hypocentral distance is expressed by the following equation

$$<R_{HYP}>_\theta = \int_{Z_{TOR}}^{Z_{TOR}+W\sin(\delta)W\cos(\delta)} \int_{0}^{L/2} \int_{-L/2}^{L/2} \sqrt{\left[\left(R_C^2+x^2-2xR_C\cos(\theta)\right)+z^2\right]} p(x)p(y)p(z)dxdydz \quad (4\text{-}5)$$

in which x, y, and z are respectively variables on the length, width of the fault surface projection, and the depth of the possible hypocenters, and $p(x)$, $p(y)$, and $p(z)$ are their probability distribution functions, respectively. The probability distribution functions are defined regarding the characteristics of the given fault rupture. Note that the boundary conditions for the integrals can be changed based on these characteristics. For instance, if there is any *prior* information or assumption about the focal depth location, the boundary condition of integral can take into account those assumptions. In equation (4-5), R_C is an auxiliary distance between the observation point and the middle of the fault length within the width of the fault surface projection, which has the possible epicentral point on it, and is defined as

$$R_C = \begin{cases} \dfrac{R_{JB}+L/2}{\cos(\theta')} & \text{if } 0 \le |\theta| < \theta_1 \\[3mm] \sqrt{\left[y^2+(L/2)^2\right]+R_{JB}^2-2R_{JB}\sqrt{y^2+(L/2)^2}\cos(\gamma)} & \text{if } \theta_1 \le |\theta| \le \theta_0 \\[3mm] \dfrac{R_{JB}+y}{\sin(\theta')} & \text{if } \theta_0 < |\theta| < 90 \end{cases} \quad (4\text{-}6)$$

where

$$\theta_0 = \arctan\left[\frac{\dfrac{W\cos(\delta)}{2}+R_{JB}}{L/2}\right]$$

$$\theta_1 = \arctan\left[\frac{W\cos(\delta)/2}{R_{JB}+L/2}\right] \quad (4\text{-}7)$$

$$\gamma = 180 - \left(\arcsin\left(\frac{\sin(|\theta'-\alpha|)\sqrt{y^2+(L/2)^2}}{R_{JB}}\right)+|\theta'-\alpha|\right)$$

in which

123

$$\alpha = \arctan\left[\frac{y}{L/2}\right] \tag{4-8}$$

and θ' is defined as the angle between a line parallel to the fault length and the line connecting the virtual site and the middle of the fault line within the width of the fault surface projection, which has the possible epicentral point on it (see Figure 4-2), and is obtained from

$$\theta' = \begin{cases} \arctan\left[\dfrac{y - \left[\dfrac{W\,\cos(\delta)}{2} - \tan(|\theta|)\left(R_{JB} + L/2\right)\right]}{R_{JB} + L/2}\right] & \text{if } 0 \leq \theta < \theta_1 \\[4mm] \arctan\left[\tan(|\theta|)\left(\dfrac{y + R_{JB}}{\dfrac{W\,\cos(\delta)}{2} + R_{JB}}\right)\right] & \text{if } \theta_0 < \theta < 90 \end{cases} \tag{4-9}$$

For virtual sites in which $\theta_1 \leq \theta \leq \theta_0$, θ' can be obtained from a system of equations with three equations and three unknowns (ox, oy, and θ', see Figure 4-2) as

$$\tan(\theta) = \frac{\dfrac{W\,\cos(\delta)}{2} + oy}{L/2 + ox}$$

$$\tan(\theta') = \frac{y + oy}{L/2 + ox} \tag{4-10}$$

$$ox^2 + oy^2 = R_{JB}^2$$

Finally, if the azimuth of the site is unknown, we make an average over all possible azimuths as follows

$$<R_{HYP}> = \int_0^{2\pi} <R_{HYP}>_\theta \, p(\theta) d\theta \tag{4-11}$$

Since the JB surface is symmetric along a perpendicular line on the center of fault length, the integration over θ can be done for a range of $-\pi/2$ to $\pi/2$ with $p(\theta) = 1/\pi$.

Similar to the vertical strike-slip fault case, the mean epicentral distance can be derived by removing the first integral and the z and $p(z)$ terms from equation (4-5). To determine the rupture distance R_{RUP} for a fault with a dip angle of δ and an azimuth angle of θ, the relationships

between the R_{RUP} distance and the R_{JB} distance provided by Kaklamanos *et al*. (2011) can be used in equation (4-5) for conversion distance process.

Equations to obtain the uncertainties for distance conversion equations and how to propagate these uncertainties to calculate the total standard deviation of GMPEs can be found in Tavakoli *et al*. (2018).

4.3 A General Effective Distance Conversion Equations

The general distance conversion equations developed in previous section are independent of region-specific material properties. The problem of employing R_{JB} and R_{RUP} in point-source ground-motion simulations to develop a GMPE is that they can only account for the geometry of the extended-fault rupture model instead of capturing any detailed geological and seismological features (Goda and Atkinson, 2014; Yenier and Atkinson, 2014). Yenier and Atkinson (2014) have analyzed earthquake data with moderate to large magnitudes from different regions and concluded that if the equivalent point-source model, in which the effective distance is considered as the primary distance metric, is employed, the apparent source response spectra of those earthquakes can be modeled with a simple far-field Brune point-source model. Thus, the average ground motions for large earthquakes can be acceptably simulated using the equivalent point-source model based on the effective distance even for the sites located at very close distances to the fault rupture.

The effective distance is the distance between a given site and a virtual point which substitutes the whole fault and can mimic extended-fault rupture effects. The extended-fault rupture can be subdivided into small elements (subfaults) considered as point sources and the radiated energy from all subfaults are incoherently added up to produce the total energy of the shaking at each virtual site. In fact, all subfaults of the extended-fault rupture radiate uniform energy with equal intensity (assuming homogenous energy radiation from the fault). This energy is theoretically proportional to the amplitude of the ground-motion captured at the site of interest and decreases with increasing distance due to spreading over an increasing either spherical area in a homogeneous whole space or cylindrical surface in a homogenous half space, scattering, and intrinsic absorption (Boore, 2003; Chapman and Godbee, 2012).

Different schemes have been introduced to capture the effects of extended-fault ruptures on distance metrics, GMPEs, or ground-motion simulation approaches (e.g., Singh *et al*., 1989; Kanamori *et al*., 1993; Ohno *et al*. 1993; Andrew, 2001; Boore, 2009). Following the Boore (2009) approach, we use the propagation path function in the frequency domain, which intuitively accounts for the geometrical spreading and anelastic attenuation terms, to construct the effective point-source distance conversion equation.

The general distance conversion equations, which are calculated based on the uniform weighted average of distances from virtual sites, should be modified to include the effect of geometrical spreading decay and attenuation as suitable weighting factors for the process of averaging. In fact, an effective point on an extended-fault rupture should be chosen to give an identical total energy at a given site if this point compared to an extended-fault rupture. In this regard, the distances from virtual sites to subfaults take appropriate non-uniform weights associated with geometrical spreading and attenuation functions. The following general region-specific distance conversion equation is developed to estimate effective point source-based distance metrics (e.g., effective R_{HYP} and R_{EPI} instead of R_{HYP} and R_{EPI}), in place of the extended-fault distance metrics (e.g., R_{JB} and R_{RUP}), which not only accounts for the geometry of the given fault but also considers the effects of the propagation path on radiated seismic waves

$$G(R_{EFF})\exp\left(\frac{-\pi f R_{EFF}}{Q(f)V_S}\right) =$$

$$\left[\int_0^{2\pi}\int_{Z_{TOR}}^{Z_{TOR}+W\sin(\delta)}\int_0^{W\cos(\delta)}\int_{-L/2}^{L/2}\left\{\left[G(\gamma)\times\exp\left(\frac{-\pi\gamma f}{Q(f)V_S}\right)\right]\right\}^2 p(x)p(y)p(z)p(\theta)dxdydzd\theta\right]^{0.5} \quad (4\text{-}12)$$

where G is the geometrical spreading function, Q, V_s, and f are quality factor, shear-wave velocity, and reference frequency in the attenuation function, respectively. The term γ is the distance between the observation point and possible epicenter or hypocenter locations on the fault, which is defined as

$$\gamma = \sqrt{\left[\left(R_C^2 + x^2 - 2xR_C\cos(\theta)\right) + z^2\right]} \quad (4\text{-}13)$$

The R_C is the auxiliary distance and $p(x)$, $p(y)$, $p(z)$, and $p(\theta)$ are the probability distribution functions as defined in previous equations. Equation (4-12) can be simply turned

into a summation over the length and width of the fault and the azimuth of the observation points. This equation should be solved with a trial and error approach.

To determine the effective distance for a given reference frequency, a general table for the attenuation term is developed based on the geometrical spreading and quality factor functions in the region of under study, and discretized effective distances within the range of interest using the left hand-side of equation (4-12). Then, for a given R_{JB} distance, all distances from the observation point to each subfault, obtained from equation (4-13), are substituted into the right hand-side of equation (4-12). Simplified value of the right hand-side of equation (4-12) gives the resultant effect of anelastic attenuation and geometrical spreading decay terms for a virtual point on the fault that produces the same level of energy intensity as the combination of all subfaults generate at the observation point. Finally, using the developed attenuation table for the left hand-side, the effective distance corresponding to the simplified value of the right hand-side is found.

For a given moment magnitude and R_{JB} distance, there is only one point that can be considered as an equivalent point source at a specified source-to-site azimuth. Therefore, the effective distance conversion approach has no uncertainty for a given azimuth unlike the general distance conversion approach according to averaging with uniform weights in which all points on the fault potentially can be a hypocenter. However, the uncertainty is brought into play for the effective distance conversion approach through averaging over all azimuth angles around the fault. Of course, this uncertainty is considerably smaller than the uncertainty of the general distance conversion averaging over all azimuths around the fault.

4.4 An Example of Point Source-Based Distance Conversions

The distance conversion equations that have already explained are generic and can be used for both shallow and deep earthquakes, small and very large earthquakes, and even for induced earthquakes. Therefore, conversion results depend on the input parameters and their assumptions such as the geometry of the fault, location of the fault, pattern of possible hypocenters or epicenters on the fault, and quality factor and geometrical spreading functions of the region of interest. To investigate the effects of using point source-based distance conversions on ground motions, we select prevalent assumptions about the fault and region and employ them as input parameters in the general distance conversion equations. These results are based on the

assumed input parameters describing in the following and the analyst should modify these parameters according to the characteristics of the fault and the region of under study.

The geometry of extended-fault sources is often modeled by a rectangular shape with a width, W, a length, L, and a dip angle of δ. The rupture width and length of a fault plane are determined based on empirical relationships (Wells and Coppersmith, 1994; Mai and Beroza, 2000; Somerville *et al*., 2001), which are scaled by earthquake magnitude. In this example, we use the global empirical relationships obtained by Wells and Coppersmith (1994). It should be mentioned that the dimensions of simulated faults are much smaller for a given large magnitude if the Somerville *et al*. (2001) relationships, which are derived based on the data from the CEUS, are used.

The next step is to place the fault rupture in a specific location. Earthquake focal depths are assumed to have a non-uniform distribution such as truncated normal distribution or Weibull distribution (Scherbaum *et al*., 2004; Mai *et al.*, 2005; Ma and Atkinson, 2006). In this example, we used the results from Scherbaum *et al*. (2004) in which earthquake hypocenter locations are dependent to the moment magnitude and are defined by a truncated normal distribution with a mean hypocentral depth of $h_{avg} = a + b\mathbf{M}$ in km and a standard deviation of σ, where the constant values of a, b, and σ are obtained from Table I of the Scherbaum *et al.* (2004) study.

Note that this depth distribution and the empirical relationships of Wells and Coppersmith (1994) are consistent since both have been obtained from the same dataset. The estimated hypocentral depth is used to set the center of the fault plane in the simulations. Therefore, the depth to the top of the fault rupture, Z_{TOR}, can be determined by $Z_{TOR} = h_{center} - W/2$ where h_{center} is the distance from the ground surface to the center of fault plane. Then, possible hypocenters within the simulated fault ruptures are randomly distributed with a uniform distribution along the fault length and width. Those fault ruptures whose upper edges are extended above the ground surface, are shifted down to lie on the surface with Z_{TOR} of zero.

For the vertical strike-slip fault case in this example, it is assumed that the probability distribution of earthquake hypocenter locations on the fault length and width is uniform; thus, $p(x) = 1/L$ and $p(z) = 1/W$. Similar to the vertical strike-slip fault case, it is assumed that the probability distribution of earthquake hypocenter locations is uniform on the length, depth, and surface projection of the width. Now, the general distance conversion for the case of uniform-

weighted average can be used to obtain the converted distance. In this regard, the integration is transferred to summation by discretizing the fault plane. We used 20 subfaults along the length and 20 subfaults along the width of each fault. Thus, there is a total of 400 subfaults for each simulated fault. The center of each subfault is considered as a possible hypocenter. If the azimuth of the site is unknown, equations (4-3) and (4-11) are used to average over all virtual sites around the simulated fault. In this regard, virtual sites are located at every two degrees.

Figure 4-3 and Figure 4-4 demonstrate the mean converted hypocentral and epicentral distances with respect to R_{JB} distances up to 1000 km for a vertical strike-slip fault model and a 50°-dip normal fault, respectively, for the selected magnitudes of **M**5.5, **M**6.5, and **M**7.5. The comparison between the mean converted hypocentral and epicentral distances for different dip angles demonstrates that the depth distribution of the events and the dip angle of faults control the distance saturation for earthquakes and close site distances.

Since the R_{JB} distance metric is smaller than the R_{HYP} and R_{EPI} distance metrics, the mean residuals of ε_{HYP} and ε_{EPI} are always positive. ε_{HYP} and ε_{EPI} are the residuals for the converted hypocentral and epicentral distances given by

$$
\begin{aligned}
\varepsilon_{HYP} &= R_{HYP} - \sqrt{R_{JB}^2 + Z_{TOR}^2} \\
\varepsilon_{EPI} &= R_{EPI} - R_{JB}
\end{aligned}
\tag{4-14}
$$

Figure 4-5 and Figure 4-6 show the histogram (frequency) distributions of residuals and the fitted gamma probability distributions for earthquakes with magnitudes of **M**5.5, **M**6.5, and **M**7.5, and a R_{JB} distance of 20 km for vertical and normal faults, respectively. The gamma distribution provides the best fit to the distance residuals since the distribution of the residuals for the virtual site when the azimuth is 0° is uniform while the distribution of the residuals once the azimuth is 90° (the virtual site is perpendicular to the fault line) is exponential. Thus, the combination of these two probability distributions is better captured by a gamma-distributed random variable. The frequency of residual values shows that the mean and variance of gamma distributions, which are related to the shaping parameters of gamma distribution, are function of magnitude and distance. These observations are in good agreement with Scherbaum *et al.* (2004), in which the distance conversion relationships and residuals are numerically determined using regression analysis on Monte-Carlo simulated data. These distance conversions are based on the uniform-weighted average of distances from parts of fault to each observation point.

In order to estimate the non-uniform-weighted average of distances and to capture the effect of propagation path on the range of distances, an effective point should be chosen on an extended-fault rupture. To achieve this objective, the point source-based distance conversions explained previously are modified to incorporate the effect of geometrical spreading and attenuation functions as weighting factors into the mean distance metrics. To obtain the converted effective distances, geometrical spreading and attenuation functions as well as the shear-wave velocity and the reference frequency are required to define the seismological parameters of the region of interest in addition to previous assumptions about the fault plane.

Far-field body-wave and surface-wave geometrical spreading functions are ideally modeled by $G(R) = R^{-1}$, and $G(R) = R^{-0.5}$ for a whole-space and half-space, respectively (Ou and Herrmann, 1990; Chapman and Godbee, 2012). Some researchers (e.g., Atkinson, 2004; Atkinson and Boore, 2006; Atkinson and Boore, 2014) have shown that the geometrical spreading exponent decay for body-wave should be higher than R^{-1} due to the effects of crustal layering and heterogeneities. They have indicated that the rate of $R^{-1.3}$ describes better the decay of ground-motion amplitudes with distance. There are some other studies that show the geometric spreading function may be frequency dependent (Frankel, 2015; Sedaghati and Pezeshk, 2016c). Attenuation function which is the inverse of the quality factor, Q, is a combined effect of scattering and intrinsic attenuation (Wennerberg, 1993; Boore, 2003). The scattering attenuation, caused by heterogeneities within the Earth such as irregular topography, cracks, and faults, redistributes the wave energy. The intrinsic or absorption caused by friction and viscosity through the propagation path dissipates the energy of seismic waves and converts it into heat. Q is an important parameter describing the characteristics of the medium through which seismic waves propagate (Sato and Fehler, 1998).

The quality factor of $Q = \max\ (1000,\ 893\,f^{0.32})$ and the geometrical spreading function of $G(R) = R^{-1.3}$ for $R < 70$; $R^{+0.2}$ for $70 < R < 140$; and $R^{-0.5}$ for $R > 140$ estimated by Atkinson (2004) are employed in this example to demonstrate the effect of energy decay in the effective distance conversion equations. These models are consistent with the Pezeshk *et al*. (2011) GMPE since we use this GMPE to show the effect of using effective distance on hazard curves. Further, the crustal shear-wave velocity of $V_s = 3.7$ km/sec is used in this example case. The reference frequency of 10 Hz is chosen; however, the distance conversion results are fairly insensitive to the choice of frequency, which is in good agreement with Boore (2009). The combined effect of

geometrical spreading and attenuation functions indicates that the subfaults with shorter distances from the virtual site have higher contribution to the total energy captured at the site than the subfaults with longer distances.

After selecting the appropriate seismological parameters for the region where the site is located, the effective distances are obtained using equation (4-12) for moment magnitudes of 4.5, 5.0, 5.5, 6.0, 6.5, 7.0, 7.5, and 8.0 and R_{JB} distances of 1, 2, 3, 5, 7, 10, 12, 15, 20, 30, 40, 50, 60, 70, 80, 100, 120, 150, 200, 250, 300, 400, 500, 600, 700, 800, and 1000 km. Again, we use summation instead of integration by discretizing the fault into 20 subfaults along the length and 20 subfaults along the width (400 subfaults in total). Figure 4-7 and Figure 4-8 illustrate the effective hypocentral and epicentral distance averaged over all virtual sites with respect to R_{JB} distances up to 1000 km for a vertical strike-slip fault model and a 40˚-dip reverse fault, respectively. The three selected magnitudes of **M**5.5, **M**6.5, and **M**7.5 are used to model the dimension of fault rupture. In Figure 4-7 and Figure 4-8, a direct comparison between the converted effective distances for **M**5.5, **M**6.5, and **M**7.5 is unreasonable since Z_{TOR} for each magnitude is different and is dependent on both the fault center location and the width of the fault. For instance, in Figure 4-8, the converted effective distances for **M**5.5, **M**6.5, and **M**7.5 are very similar. In fact, this similarity does not mean that the effective distance for different magnitude should be in the same range; because the depths to the top of the rupture for these magnitudes are approximately 6.71, 5.11, and 1.53 km, respectively.

The plots of distance conversion in Figure 4-7 and Figure 4-8 also show a bump around R_{JB} of 50 km particularly for large magnitudes. This bump is caused by the assumed trilinear geometrical spreading function in which the middle part is $R^{+0.2}$. For a given fault with **M**7.5 and R_{JB} of 50 km, the distance from the site to each grid center varies from 50 km to a few hundred kilometers. Thus, incorporating the middle part of the geometrical spreading function into the averaging process leads to estimating higher effective distance.

Comparison of the uniform and non-uniform-weighted average of distances in conversion process indicates that the distance conversions are dependent upon not only the geometry of fault, and the earthquake size, but also the geometric spreading of a given region. The non-uniform-weighted averaging on distances lead to increase the ground motions at near distances compared with uniform mean distance conversion approaches.

Table 4-1, Table 4-2, and Table 4-3 tabulate the average effective hypocentral distance for vertical strike-slip faults, 50˚-dip normal faults, and 40˚-dip reverse faults, respectively for this example case. Table 4-4, Table 4-5, and Table 4-6 list the average effective epicentral distance for vertical strike-slip faults, 50˚-dip normal faults, and 40˚-dip reverse faults, respectively. These magnitude-effective distance conversion tables are used to convert the fault-based GMPEs into the point source-based GMPEs, which can be applied for areal seismic sources defined in a PSHA study.

4.5 Comparison with Previous Studies

The effective distances derived from the example for the vertical case are compared with the vertical-fault USGS distance conversion approach (Peterson *et al*., 2008) shown in Figure 4-9. The USGS distance conversion approach used in the U. S. seismic hazard maps, which only consider the random-ordinated geometry of a vertical fault, is not saturated at close distance; and therefore, ground-motion amplitudes monotonically increase with decreasing the R_{JB} distance. The USGS approach is also insensitive to the magnitude of earthquakes at close distances. For instance, at a R_{JB} distance of 1 km, the USGS approach results in an R_{EPI} distance of 1.6 km for the three selected magnitudes of **M**5.5, **M**6.5, and **M**7.5, that is inconsistent with the magnitude and distance-saturation of ground motions for a large earthquake.

The magnitude and distance-saturation of ground motion for a large earthquake indicate that an observation point (or a virtual site) close to a fault can effectively see the closest portions of the extended fault, and most of the fault rupture further away from the site are not involved in the effective distance conversion, particularly by increasing magnitude and decreasing the source-to-site distance. Therefore, the effective epicentral distance developed in this study, which is a function of dip angle of fault and the distance ranges, gives the smaller R_{JB} distance values (higher ground-motion amplitudes) than the vertical-fault USGS distance conversion and the larger R_{JB} distance values (lower ground-motion amplitudes) than the mean epicentral distance (Scherbaum *et al*., 2004) at short distances for the R_{JB}-based GMPEs.

The effective distances derived from the example are also compared with the EPRI distance conversion (EPRI, 2004) for the CEUS as shown in Figure 4-10. The EPRI (2004) distance conversion equations are constructed based on the GMPEs developed for the CEUS to

132

partially capture the effect of total energy release from a large fault rupture, the random-oriented geometry of fault to include the effect of unknown fault rupture models in a specific area, and the Somerville *et al.* (2001) empirical relationship to define the earthquake rupture area. Since the EPRI (2004) distance conversions are developed for given a set of GMPEs developed for the CEUS, it may not be appropriate for areas in which regional GMPEs are not available or different GMPEs and source scaling are assigned to perform PSHA.

The EPRI (2004) approach is also developed for areas that the orientations of faults are unknown. Thus, there is no specific solution when a specific fault orientation is desired and the analyst should use the average distance conversion as the final result. Comparison of the vertical and reverse-combined effective distance conversion derived from the example with the EPRI (2004) approach (see Figure 4-10) shows that the converted distances for the R_{JB} distances of about 10 km and larger are in good agreement. However, for the near-fault observation points, the magnitude and distance-saturation of ground motions for a given large earthquake are not satisfactorily presented in the EPRI (2004) approach, because the earthquake epicenter is assumed to be located at the center of fault (centered epicenters) or the epicenter of an earthquake is uniformly distributed along the length of the rupture (random epicenters).

It is anticipated that the effective distance is saturated at very small distances because seismic waves radiated from the small portions of the entire rupture dominate recorded ground motions at the site. Thus, to account for the effects of the magnitude and distance-saturation, the impact of propagation path on seismic waves should be incorporated into the development of distance conversions to obtain the effective points referred as *Effective Epicenters* or *Effective Hypocenters* for extended fault ruptures. These effective points can be used for modeling earthquakes as point sources in PSHA.

4.6 Applications for GMPEs

The effective distance can be used for the development of stochastic GMPEs, which are obtained directly from the point-source spectrum modeling through the stochastic method (Boore, 1983; Boore, 2003). The point-source stochastic method is based on an important assumption that the total energy of earthquakes is released from the center point of a postulated fault rupture, and thus, the magnitude-distance saturation of ground motions at close distances

for large earthquakes are mostly ignored. Ignoring these saturation effects on ground motions from the point source models may lead us to estimate unrealistically high ground motions at the near source-to-site distances compared to the actual extended-fault source models (Boore, 2009; Yenier and Atkinson, 2014).

One way to overcome this problem is to find the effective hypocenters on the fault for each R_{JB} distance using the observation points (virtual sites) around a postulated fault rupture, and then using the effective distance in the stochastic point-source ground-motion simulation methods to develop GMPEs. Boore (2009) has used this approach for a specific simple case study, when the location of a fixed vertical fault and a fixed site are known, and earthquakes are uniformly distributed within the fault rupture, to modify the distances used in the point source-based simulation program and to capture the effect of extended-fault source for simulation of ground-motions. Yenier and Atkinson (2014) have also shown that the far-field Brune point-source spectrum can be used within the equivalent point-source approach with effective distance to simulate observed spectra of large ($M > 6$) earthquakes.

The advantage of the general effective distance conversion (equation (4-12)) developed in this study is that ground motions for large earthquakes generated by extended-source models can be modeled by the equivalent point-source model that incorporates the extended-fault saturation term into the ground-motion simulations for any arbitrary input parameters and functions such as fault dimensions, location of the fault with respect to virtual sites, probability distribution of focal depths, and geometrical spreading and anelastic attenuation functions corresponding to the study region.

Figure 4-11 illustrates the effective R_{HYP} distance conversion for a given suit of R_{RUP}-based GMPE (Pezeshk, *et. al.*, 2011), which has developed from a point-source stochastic model (Boore, 2003) for two selected magnitudes of $M5.5$ and $M7.5$ and two spectral periods of 0.2 sec and 1.0 sec. The discrepancy of ground motions between the R_{RUP}-based GMPE and the effective region-specific distance conversion at close distances and large earthquakes is described by the fact that the total energy of ground motions is released within a large fault rupture area compared to a finite-fault depth point defined on fault. The discrepancy between the effective R_{HYP} and R_{RUP}-based models increases for a magnitude scenario of $M7.5$. Figure 4-11 also explains that the finite-fault factor, *h*, is magnitude and distance dependent. For example,

the corrected distance-scaling curve of the GMPE with the effective distance for a magnitude of **M**5.5 is placed above the uncorrected distance-scaling curve; while, it comes below the uncorrected distance-scaling curve of the GMPE for a magnitude of **M**7.5. This implies that the finite-fault factor is lower for lower magnitude and it increases with increasing magnitude and distance.

4.7 **Analytical Equations for Finite-fault Factor**

To account for the effects of magnitude and distance saturation at close distances in stochastic point-source simulations or GMPE functional forms, the effective hypocentral distance is often connected to the closest distance from the rupture surface as follows

$$R_{eff} = \sqrt{R_{RUP}^2 + h^2}$$ (4-15)

where h is known as the finite-fault factor (Boore *et al.*, 2014), equivalent point-source depth, pseudo-depth, or fictitious depth (Atkinson and Silva, 2000; Yenier and Atkinson, 2014). For a vertical fault, the rupture distance, R_{RUP}, is simply expressed as a function of the R_{JB} distance, which is given by

$$R_{RUP} = \sqrt{R_{JB}^2 + Z_{TOR}^2}$$ (4-16)

For a given magnitude and R_{JB} distance, Z_{TOR} can be estimated from the dimensions of the fault and the location of the fault center. For a vertical strike-slip fault, the effective distance (R_{eff}) in equation (4-15) can be obtained from Table 4-1 for a given magnitude and R_{JB} distance. We developed an analytical equation to obtain finite-fault factor for all magnitude ranging from **M**4.5 to **M**8 in 0.5 magnitude unit increments at R_{JB} and the effective R_{HYP} distances tabulated in Table 4-1.

Different models have been proposed to obtain the finite-fault depth at close distances (Atkinson and Silva, 2000; Halldorsson and Papageorgiou, 2005; Yenier and Atkinson, 2014) from ground-motion databases. These empirical-based models are used to validate the analytical-based model developed in this study. The finite-fault depth is logarithmically modeled as a function of magnitude at a given R_{JB} distance. For example, using equations (4-15) and (4-16), the finite-fault factor, h, for a specified R_{JB} distance is given by the following equation

$$\log(h) = a + b\mathbf{M} \tag{4-17}$$

with a standard deviation of σ in log 10 units. Table 4-7 lists all regression coefficients for different R_{JB} distances up to 50 km. However, the model can be prolonged for any arbitrary input parameters and functions corresponding to the region of under study. The finite-fault factor indicates that the R_{eff} distance from a site can never physically be a value less than h.

Figure 4-12 is a comparison between the analytical-based finite-fault factor obtained in this study versus magnitudes obtained at different Joyner-Boore distances with the empirical-based equations proposed by other researchers. The analytical-based finite-fault factor model at a R_{JB} distance of 1 km is in good agreement with models of Atkinson and Silva (2000) and Halldorsson and Papageorgiou (2005), which are developed based on ground-motion recordings with distances less than 30 km. As shown in this figure, the finite-fault depth model developed in this study not only is magnitude dependent, but also is distance dependent. However, at long distances, non-uniform weighting factors approaches uniform weighting factors since the effect of grid centers location on the fault becomes insignificant. Yenier and Atkinson (2014) used data with distances up to 500 km, and thus, their proposed model is regressed for all distances particularly for long distances for which the finite-fault depth is larger. We preferred to model the finite-fault factor versus magnitude at each R_{JB} distance instead of generally regress at all R_{JB} distances. Note that the proposed analytical-based model is derived for a vertical fault with dimensions and seismological parameters explained in the example case. For other dip angles and different tectonic regions this equation may be varied and can be re-evaluated using equation (4-12). It should be also mentioned that the finite fault factor is significantly affected by the azimuth. For instance, for a vertical strike-slip fault, the site located on the middle of the fault has the lowest finite fault factor for a given R_{JB}, while the site located at the ends of the fault has the highest finite fault factor for the considered R_{JB}. In fact, our model is an average on all over azimuth angles around the fault.

4.8 Applications for PSHA

The impact of using the effective distance on R_{JB}-based or R_{RUP}-based GMPEs is illustrated through a simple PSHA study for a given large areal source. In general, PSHAs are performed using integration over areal sources in which sources are subdivided into small cells

as point sources. Delineation of areal seismic sources is often used for the regions with the low to moderate seismicity such as CENA, where the lack of information on the geometry of active faults is anticipated.

In the PSHA process, the distance between each cell and the site is defined as epicentral or hypocentral distances. As stated previously, GMPEs are often developed based on distance metrics such as R_{JB} and R_{RUP} to account for the effects of extended ruptures rather than distance metrics such as R_{EPI} and R_{HYP} that represent point-source models.

One way to have consistency between distance metrics used in GMPEs and distance metrics used in the PSHA process for areal seismic sources is to develop a table of effective distance for the pairs of magnitude-JB distance bins using the distance-conversion equation (4-12). For example, Table 4-1 lists the magnitude-effective distance pairs for a random-ordinated vertical-fault source of earthquakes at different Joyner-Boore distances with assumptions and seismological parameters mentioned previously.

In order to demonstrate the influence of using an effective distance on the PSHA results at a given site, a circular areal seismic source with a radius of 100 km is considered in which a rock site is located at the center of areal source similar to Bommer and Akkar (2012). The seismicity of areal source is assumed to follow a truncated exponential recurrence. For two low and high-seismicity scenarios, the seismic activity rates are set to 0.5 and 5 events/year, and b-values are set to 1 and 0.85, respectively. The maximum and minimum moment magnitudes are truncated between **M**5.0 and **M**8.0, respectively. The R_{RUP}-based GMPEs developed by Pezeshk *et al.* (2011) for the CENA are applied for these two simple PSHA study scenarios to demonstrate the effects of using inconsistent source-to-site distance metrics on the seismic hazard curves.

Figure 4-13 and Figure 4-14 depict the effect of using various source-to-site distance metrics on seismic hazard curves at two spectral periods of 0.2 sec and 1.0 sec for the low and high-seismicity scenarios, respectively. The comparison between seismic hazard curves displays that the effective R_{EPI} distance metric conversion in GMPEs that are developed based on the R_{JB} or R_{RUP}-based distance metrics results in significantly higher ground-motion hazards in PSHA calculations, particularly at the lower probability of exceedance that are often used for the design of significant facilities such as nuclear power plants.

The following example shows the reason of higher ground-motion hazards for modeling earthquakes as hypocenters or epicenters in a PSHA study. As listed in Table 4-1 and Table 4-4 for a vertical strike-slip earthquake of magnitude $\mathbf{M}$7.0, the effective R_{HYP} and R_{EPI} distance conversion values for a sample R_{JB} distance of 15 km are about R_{HYP} = 24.83 km and R_{EPI} = 21.67 km, respectively. In the PSHA study of areal seismic sources, the distance value of 15 km should be considered as an effective hypocentral or epicentral distances. The effective R_{HYP} and R_{EPI} distances of 15 km are equivalent to the R_{JB} distance of about 5.5 km and 9.5 km, respectively (see Table 4-1 and Table 4-4). Therefore, for example, if the R_{EPI} distance is used in PSHA, a distance of about 9 km should be entered into the fault source-based GMPE to obtain the adjusted value of R_{JB} distance, which is consistent with the total energy of earthquake on extended-fault sources distributed uniformly within the areal source. The equivalent smaller R_{JB} distances for the epicentral distances in the areal seismic source lead to increasing the seismic hazard results in a PSHA study, particularly at low probability of exceedance and long spectral periods of motions.

The effective distance concept explains that it is never possible to place the site on the equivalent point source and this is exactly what distance saturation means. For instance, if the site is located on the center of the fault, the site sees the effect of many subfaults around itself. Therefore, in areal source hazard calculations, the minimum effective distance does not approach zero but it saturates with magnitude and distance to capture the effects of radiated seismic waves from different parts of the fault as well as the propagation path.

4.9 Tables

Table 4-1. The effective R_{HYP} distance for vertical strike-slip faults.

JB Distance	Magnitude							
	4.5	5	5.5	6	6.5	7	7.5	8
1	8.84	9.10	9.21	9.32	10.07	11.48	11.88	13.04
2	8.98	9.52	9.77	10.24	10.86	12.39	13.75	17.37
3	9.67	9.68	9.98	10.46	11.43	12.89	15.47	20.07
5	10.36	10.38	11.15	11.73	12.88	14.68	17.73	23.97
7	11.58	11.64	12.45	13.04	14.32	16.51	19.94	27.01
10	13.51	13.93	14.55	15.55	17.27	19.56	23.86	31.14
12	14.94	15.47	16.09	17.26	18.86	21.62	25.69	33.79
15	17.68	18.05	18.59	19.73	21.72	24.83	29.07	37.32
20	22.19	22.48	23.08	24.27	26.55	29.82	34.72	42.90
30	31.52	31.85	32.51	33.78	36.17	40.51	45.33	53.28
40	41.25	41.53	42.17	43.50	46.16	50.69	55.21	70.65
50	51.08	51.35	52.01	53.31	56.04	59.97	63.40	87.43
60	60.97	61.17	61.86	63.19	65.42	67.35	81.65	107.46
70	70.80	71.11	71.70	73.15	76.43	83.66	100.39	129.72
80	80.70	81.05	81.61	83.07	86.28	93.51	111.63	138.22
100	100.61	100.91	101.53	102.95	106.19	113.43	130.98	155.21
120	120.58	120.87	121.46	122.89	126.10	134.89	148.33	171.09
150	150.52	150.78	151.38	152.79	155.92	162.74	176.32	198.88
200	200.46	200.73	201.31	202.71	205.87	212.83	227.04	251.48
250	250.41	250.66	251.28	252.67	255.84	262.89	277.52	303.32
300	300.38	300.64	301.23	302.62	305.81	312.93	327.82	354.65
400	400.34	400.61	401.21	402.60	405.79	412.99	428.27	456.50
500	500.32	500.57	501.18	502.58	505.79	513.00	528.51	557.71
600	600.30	600.56	601.18	602.56	605.76	613.03	628.68	658.54
700	700.30	700.56	701.16	702.55	705.76	713.03	728.81	759.16
800	800.29	800.55	801.15	802.53	805.76	813.04	828.89	859.63
1000	1000.28	1000.54	1001.13	1002.52	1005.76	1013.05	1029.03	1060.31

Table 4-2. The effective R_{HYP} distance for normal 50°-dip faults.

JB Distance	Magnitude							
	4.5	5	5.5	6	6.5	7	7.5	8
1	10.44	10.49	10.58	10.72	11.02	11.40	12.80	16.59
2	10.63	11.02	11.11	11.28	11.69	12.62	15.54	22.45
3	11.38	11.54	11.60	11.94	12.39	13.95	17.24	25.56
5	11.91	12.07	12.71	13.05	14.01	15.75	20.01	29.48
7	13.21	13.39	14.02	14.62	15.74	18.02	22.44	32.45
10	15.21	15.64	16.44	17.04	18.55	20.87	25.86	36.27
12	16.71	17.06	18.14	18.77	20.59	23.18	28.05	38.61
15	19.06	19.88	20.56	21.81	23.34	26.31	31.30	41.97
20	23.57	24.02	24.74	26.19	28.24	31.29	36.61	47.19
30	32.82	33.35	34.31	35.90	38.15	41.51	46.99	56.64
40	42.43	43.08	44.06	45.62	48.00	51.74	56.75	64.60
50	52.18	52.86	53.88	55.43	57.86	61.35	65.00	80.97
60	62.07	62.61	63.62	65.29	67.06	68.59	74.34	106.13
70	71.88	72.53	73.62	75.45	78.50	83.56	92.16	120.32
80	81.87	82.50	83.56	85.39	88.32	93.35	101.87	130.10
100	101.67	102.35	103.44	105.22	108.18	113.14	122.73	144.77
120	121.58	122.26	123.31	125.12	128.09	134.49	142.95	159.48
150	151.48	152.14	153.20	154.93	157.85	162.57	170.17	187.89
200	201.39	202.07	203.14	204.88	207.80	212.57	220.27	238.71
250	251.37	252.02	253.07	254.88	257.78	262.56	270.32	289.30
300	301.29	301.96	303.05	304.81	307.75	312.56	320.38	339.74
400	401.27	401.92	402.98	404.78	407.72	412.53	420.41	440.35
500	501.25	501.90	502.96	504.75	507.69	512.54	520.45	540.75
600	601.23	601.89	602.96	604.74	607.68	612.52	620.48	641.03
700	701.19	701.86	702.96	704.72	707.66	712.52	720.49	741.24
800	801.18	801.85	802.95	804.72	807.65	812.52	820.49	841.41
1000	1001.18	1001.83	1002.92	1004.71	1007.65	1012.51	1020.50	1041.64

Table 4-3. The effective R_{HYP} distance for reverse 40°-dip faults.

JB Distance	Magnitude							
	4.5	5	5.5	6	6.5	7	7.5	8
1	10.60	10.61	10.69	11.05	12.12	13.61	14.34	18.60
2	11.09	11.10	11.30	11.39	12.50	14.39	17.39	26.79
3	11.20	11.26	11.28	11.97	13.24	15.45	19.21	31.29
5	12.11	12.17	12.48	13.35	14.34	17.28	22.12	36.64
7	12.69	13.30	13.59	14.76	16.29	19.11	24.47	40.23
10	15.00	15.41	15.99	16.78	18.64	22.03	27.98	44.44
12	16.60	16.77	17.13	18.28	20.74	24.04	30.35	46.92
15	19.20	19.47	19.95	21.28	23.35	27.11	33.41	50.33
20	23.38	23.78	24.49	25.78	28.32	32.18	38.93	55.40
30	32.53	32.88	33.89	35.31	38.09	42.59	49.19	63.97
40	42.04	42.54	43.59	45.14	48.00	52.63	58.64	83.29
50	51.82	52.38	53.24	54.94	57.88	62.04	66.29	113.96
60	61.66	62.20	63.19	64.85	67.05	68.87	80.61	130.78
70	71.52	72.07	73.05	74.91	78.42	84.89	97.21	138.73
80	81.43	81.95	82.92	84.84	88.24	94.74	107.43	145.48
100	101.30	101.85	102.83	104.64	108.08	114.48	130.14	158.54
120	121.22	121.78	122.74	124.54	127.99	136.67	146.99	173.30
150	151.13	151.68	152.66	154.45	157.78	163.82	174.51	202.67
200	201.03	201.58	202.60	204.37	207.74	213.86	224.81	253.89
250	251.00	251.53	252.50	254.34	257.68	263.88	274.96	304.88
300	300.95	301.49	302.48	304.30	307.66	313.88	325.09	355.68
400	400.90	401.46	402.42	404.25	407.63	413.89	425.23	456.87
500	500.89	501.41	502.40	504.24	507.62	513.89	525.35	557.70
600	600.87	601.40	602.40	604.21	607.60	613.89	625.41	658.32
700	700.85	701.38	702.38	704.20	707.59	713.89	725.46	758.78
800	800.83	801.38	802.38	804.19	807.57	813.89	825.49	859.15
1000	1000.82	1001.38	1002.36	1004.18	1007.57	1013.89	1025.53	1059.70

Table 4-4. The effective R_{EPI} distance for vertical strike-dip faults.

JB Distance	Magnitude							
	4.5	5	5.5	6	6.5	7	7.5	8
1	1.21	1.35	1.54	1.85	2.39	3.19	4.34	5.61
2	2.22	2.39	2.70	3.12	3.79	4.97	6.64	8.85
3	3.22	3.43	3.78	4.33	5.12	6.49	8.54	11.49
5	5.23	5.46	5.88	6.61	7.61	9.23	12.02	15.89
7	7.23	7.47	7.92	8.78	10.01	11.84	14.95	19.60
10	10.23	10.47	10.97	11.95	13.48	15.62	19.14	24.65
12	12.23	12.47	13.00	14.02	15.70	18.05	21.74	27.82
15	15.23	15.47	16.01	17.10	18.97	21.67	25.62	32.08
20	20.23	20.47	21.03	22.19	24.29	27.48	31.81	38.68
30	30.23	30.48	31.05	32.27	34.67	38.69	43.43	50.48
40	40.23	40.48	41.07	42.32	44.92	49.32	53.82	66.38
50	50.24	50.48	51.08	52.35	55.04	59.01	62.53	84.98
60	60.24	60.49	61.08	62.38	64.70	66.77	79.93	103.18
70	70.24	70.49	71.09	72.47	75.72	82.92	99.59	128.89
80	80.24	80.49	81.09	82.47	85.67	92.86	110.87	137.46
100	100.24	100.49	101.08	102.47	105.67	112.85	130.48	154.54
120	120.24	120.49	121.08	122.47	125.67	134.46	147.90	170.61
150	150.24	150.49	151.08	152.47	155.57	162.36	175.89	198.27
200	200.24	200.49	201.08	202.47	205.59	212.55	226.73	251.00
250	250.24	250.49	251.08	252.48	255.61	262.66	277.26	302.93
300	300.24	300.49	301.08	302.48	305.64	312.74	327.61	354.33
400	400.24	400.49	401.08	402.48	405.66	412.83	428.08	456.26
500	500.24	500.49	501.08	502.48	505.67	512.89	528.37	557.51
600	600.24	600.49	601.08	602.48	605.69	612.93	628.56	658.37
700	700.24	700.49	701.08	702.48	705.69	712.95	728.72	759.01
800	800.24	800.49	801.08	802.48	805.69	812.97	828.81	859.50
1000	1000.24	1000.49	1001.08	1002.48	1005.69	1013.01	1028.95	1060.21

Table 4-5. The effective R_{EPI} distance for normal 50°-dip faults.

JB Distance	Magnitude							
	4.5	5	5.5	6	6.5	7	7.5	8
1	1.87	2.30	2.93	3.93	5.39	7.49	10.16	12.65
2	2.97	3.42	4.12	5.19	6.84	9.31	12.87	18.26
3	3.98	4.49	5.24	6.36	8.11	10.73	14.64	21.52
5	6.05	6.58	7.39	8.58	10.42	13.25	17.51	25.71
7	8.07	8.63	9.49	10.75	12.66	15.59	20.06	28.86
10	11.07	11.67	12.58	13.91	15.94	18.96	23.63	32.95
12	13.08	13.69	14.61	16.00	18.07	21.18	25.92	35.45
15	16.08	16.71	17.66	19.09	21.24	24.45	29.29	39.03
20	21.09	21.73	22.69	24.21	26.48	29.81	34.81	44.60
30	31.10	31.73	32.76	34.34	36.75	40.35	45.52	54.72
40	41.12	41.75	42.78	44.41	46.93	50.72	55.60	63.32
50	51.12	51.76	52.79	54.45	57.05	60.58	64.32	76.42
60	61.13	61.76	62.81	64.49	66.52	68.29	72.31	103.99
70	71.15	71.81	72.88	74.72	77.75	82.81	91.14	118.81
80	81.14	81.80	82.88	84.70	87.71	92.71	100.95	129.02
100	101.14	101.80	102.88	104.69	107.67	112.61	121.85	143.93
120	121.14	121.80	122.87	124.68	127.65	133.86	142.36	158.65
150	151.14	151.79	152.86	154.62	157.52	162.19	169.65	187.09
200	201.14	201.79	202.86	204.62	207.54	212.27	219.86	238.08
250	251.14	251.79	252.86	254.63	257.55	262.32	270.00	288.78
300	301.14	301.79	302.86	304.64	307.55	312.36	320.10	339.29
400	401.14	401.79	402.86	404.65	407.56	412.38	420.21	440.00
500	501.14	501.79	502.86	504.65	507.59	512.41	520.29	540.48
600	601.14	601.79	602.86	604.65	607.59	612.42	620.32	640.79
700	701.14	701.79	702.87	704.65	707.59	712.44	720.36	741.04
800	801.14	801.79	802.87	804.65	807.59	812.45	820.38	841.22
1000	1001.14	1001.79	1002.87	1004.65	1007.60	1012.46	1020.41	1041.50

Table 4-6. The effective R_{EPI} distance for reverse 40°-dip faults.

JB Distance	Magnitude							
	4.5	5	5.5	6	6.5	7	7.5	8
1	1.62	1.98	2.60	3.65	5.35	7.99	11.27	14.05
2	2.69	3.08	3.76	4.89	6.80	9.93	14.73	21.76
3	3.69	4.15	4.86	6.05	8.05	11.40	16.76	26.65
5	5.72	6.19	6.98	8.25	10.39	13.97	19.88	32.72
7	7.73	8.23	9.05	10.41	12.62	16.34	22.56	36.74
10	10.74	11.25	12.11	13.54	15.88	19.75	26.25	41.40
12	12.74	13.27	14.13	15.62	18.02	21.97	28.61	44.10
15	15.75	16.28	17.17	18.69	21.21	25.26	32.03	47.81
20	20.76	21.28	22.21	23.78	26.42	30.66	37.56	53.29
30	30.76	31.29	32.23	33.89	36.71	41.26	48.18	62.55
40	40.77	41.29	42.25	43.95	46.87	51.63	57.91	77.25
50	50.77	51.30	52.26	53.98	56.99	61.30	65.91	110.85
60	60.77	61.30	62.27	64.01	66.48	68.61	79.35	129.70
70	70.78	71.32	72.32	74.18	77.68	84.26	96.51	137.81
80	80.78	81.31	82.32	84.17	87.64	94.13	106.76	144.62
100	100.78	101.31	102.30	104.15	107.59	114.03	129.51	157.88
120	120.77	121.30	122.30	124.14	127.57	136.15	146.58	172.47
150	150.77	151.30	152.30	154.11	157.44	163.50	174.16	201.92
200	200.77	201.30	202.30	204.11	207.46	213.60	224.51	253.30
250	250.77	251.30	252.30	254.12	257.48	263.67	274.74	304.38
300	300.77	301.30	302.30	304.12	307.48	313.70	324.89	355.26
400	400.77	401.30	402.30	404.12	407.50	413.75	425.09	456.55
500	500.77	501.30	502.30	504.13	507.51	513.78	525.22	557.45
600	600.77	601.30	602.30	604.13	607.51	613.80	625.31	658.08
700	700.77	701.30	702.30	704.13	707.52	713.81	725.36	758.59
800	800.77	801.30	802.30	804.13	807.52	813.83	825.40	858.99
1000	1000.77	1001.30	1002.30	1004.13	1007.52	1013.85	1025.47	1059.55

Table 4-7. The coefficients of the finite-fault depth versus magnitude and its uncertainty

R_{JB}	a	b	σ
1	0.1075	0.1275	0.0210
2	0.0062	0.1513	0.0149
3	-0.0255	0.1600	0.0357
5	-0.1342	0.1825	0.0320
7	-0.1513	0.1901	0.0343
10	-0.2206	0.2076	0.0189
12	-0.2828	0.2198	0.0135
15	-0.2475	0.2197	0.0198
20	-0.2638	0.2287	0.0191
30	-0.3195	0.2468	0.0143
40	-0.3730	0.2643	0.0223
50	-0.3730	0.2706	0.0405

4.10 Figures
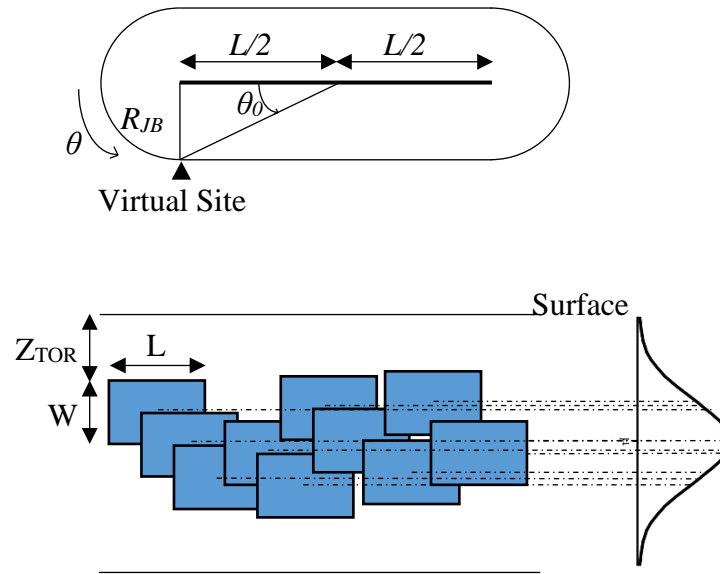
Figure 4-1. JB surface for a vertical strike-slip fault. The line in the middle of JB surface is the fault length of L. The triangle is the locations of possible observation points (sites or stations) having the same R_{JB} distances from the extended fault. The earthquake hypocenter locations are defined by a truncated normal distribution; however, any probability density function of the hypocenter (e.g., Weibull distribution), which the hypocenter is weighted toward the bottom of the fault, not centered can be used in the distance conversion approach
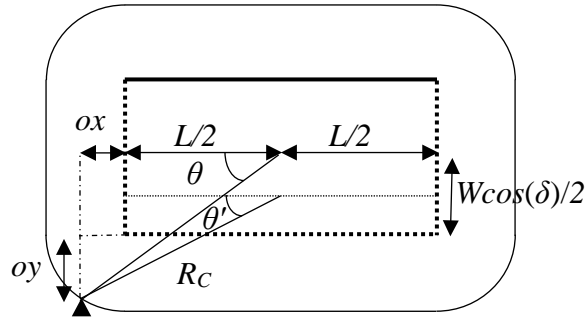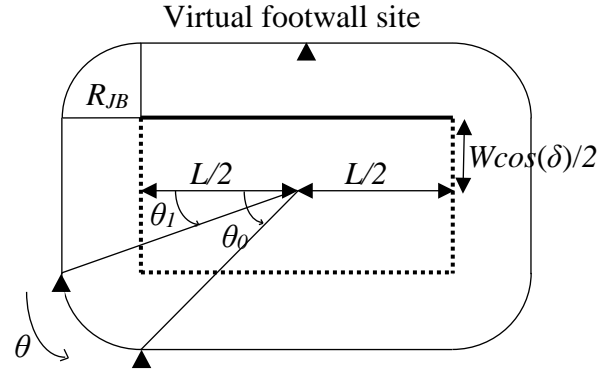
Virtual hanging wall site for the case $\theta_1 < \theta < \theta_0$

Figure 4-2. JB surface for a dipping fault. The rectangular inside is the fault projection on the surface. The triangle is the locations of possible observation points (sites or stations) having the same R_{JB} distances from the extended fault

147
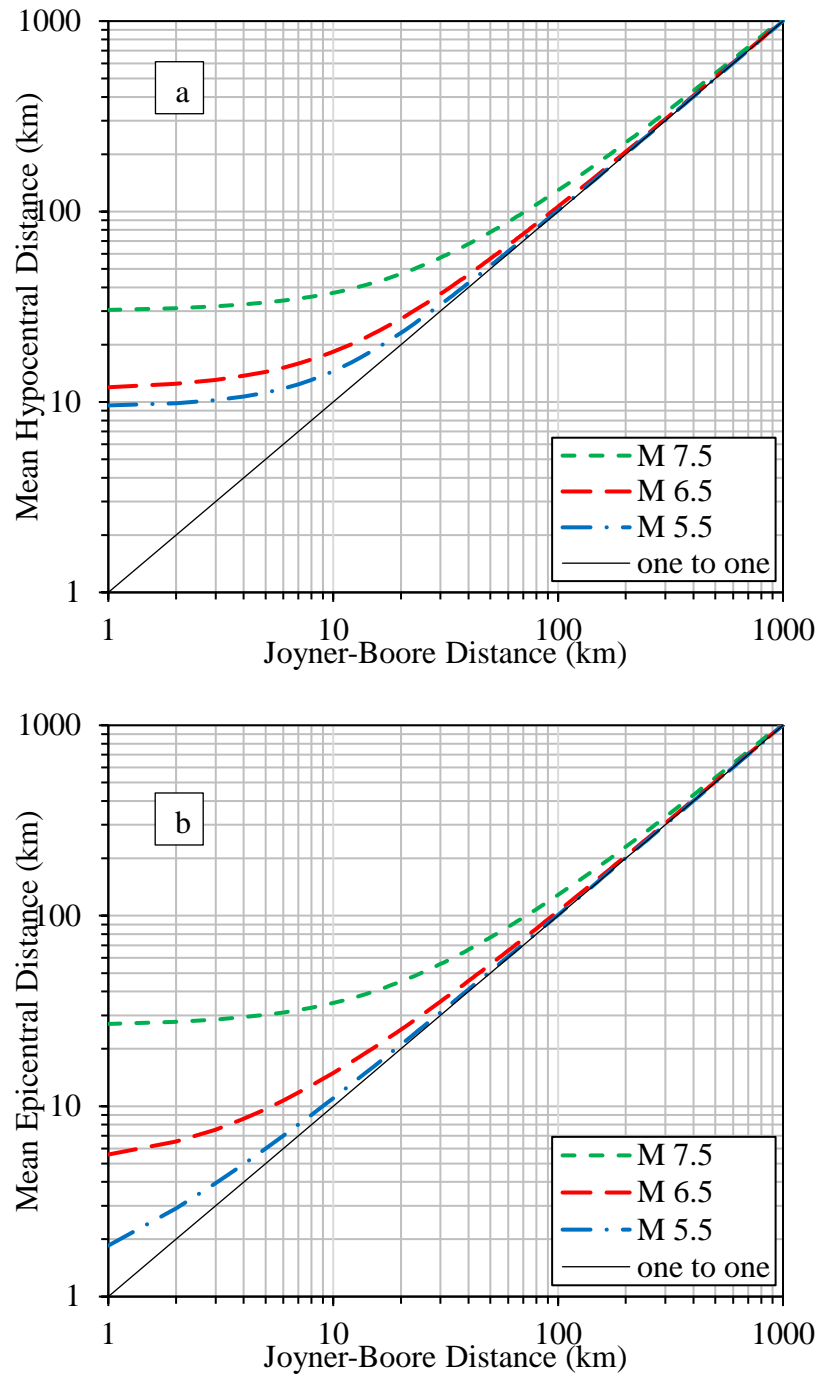
Figure 4-3. Distance adjustments along a vertical strike-slip fault as a function of Joyner-Boore distance for three selected magnitudes of **M** 5.5, **M** 6.5, and **M** 7.5; a) Hypocentral, b) Epicentral
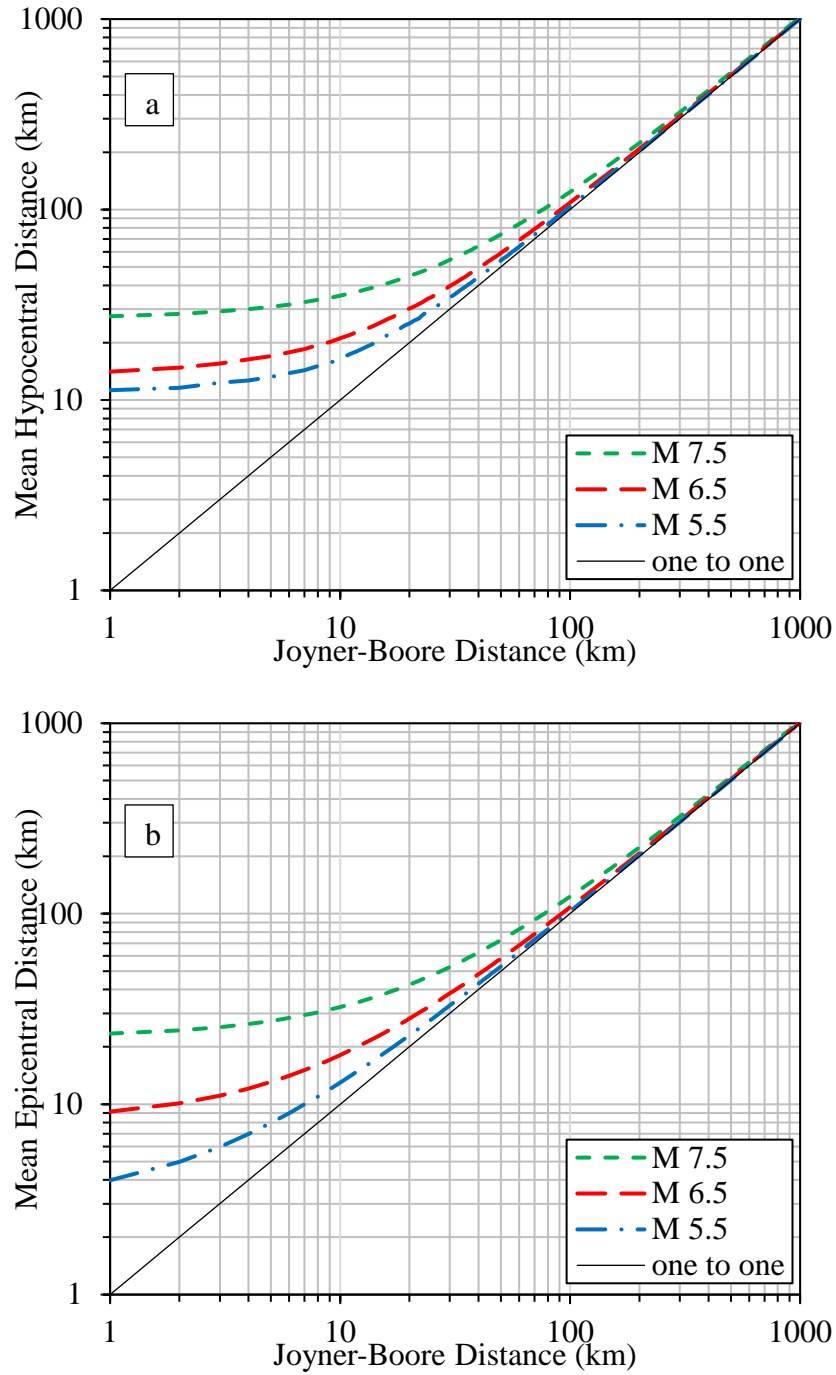
Figure 4-4. Distance adjustments along a 50˚-dip normal fault as a function of Joyner-Boore for three selected magnitudes of **M** 5.5, **M** 6.5, and **M** 7.5; a) Hypocentral, b) Epicentral
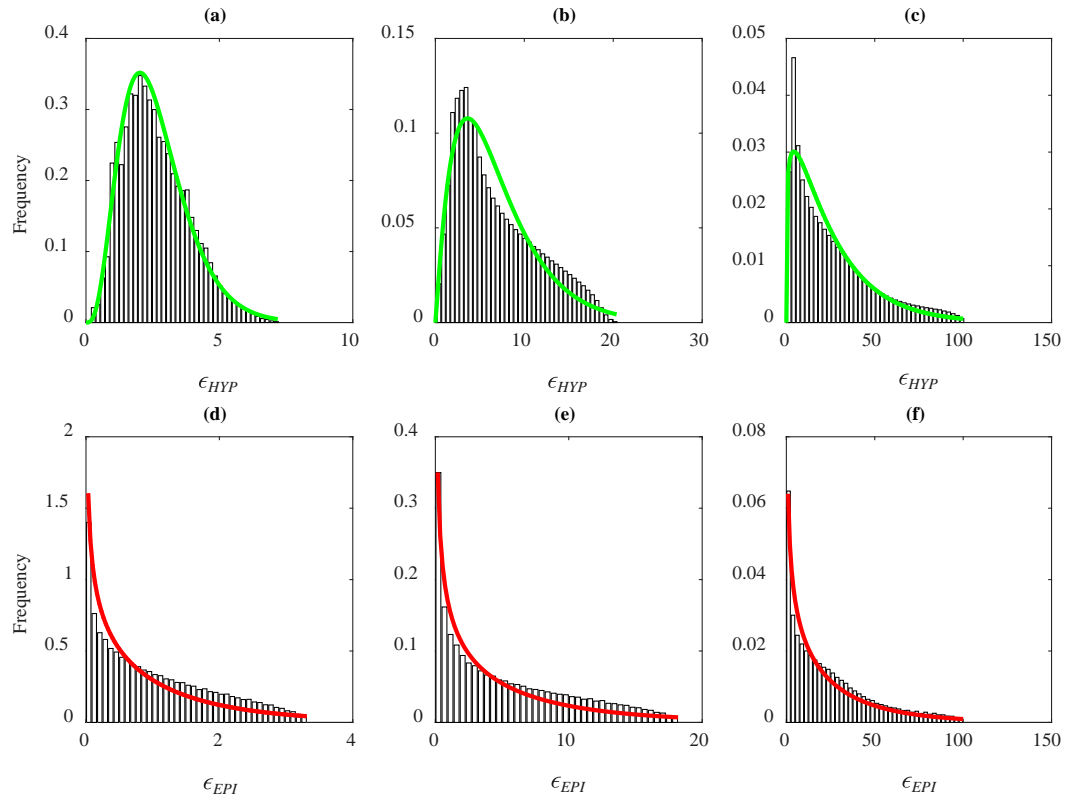
Figure 4-5. The frequency distribution of residuals fitted by a gamma distribution for a vertical strike-slip fault and a R_{JB} distance of 20 km; a) hypocentral and **M** 5.5, b) hypocentral and **M** 6.5, c) hypocentral and **M** 7.5, d) epicentral and **M** 5.5, e) epicentral and **M** 6.5, f) epicentral and **M** 7.5
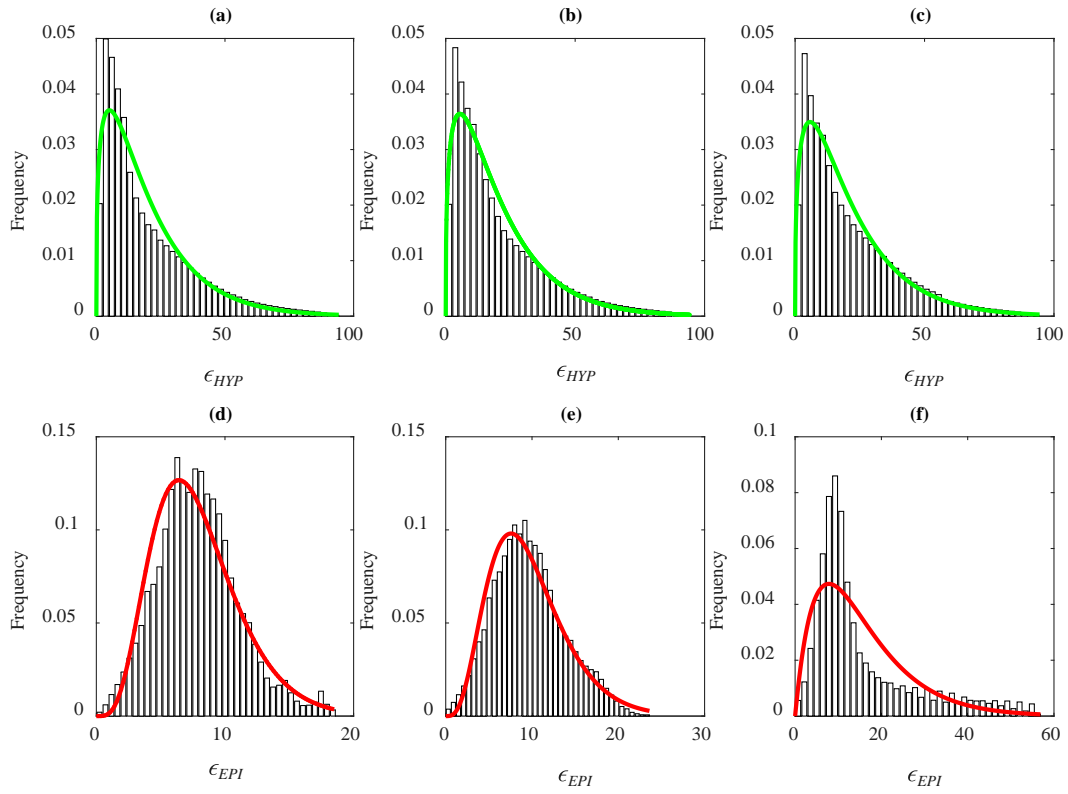
Figure 4-6. The frequency distribution of residuals fitted by a gamma distribution for a normal 50°-dip fault and a R_{JB} distance of 20 km; a) hypocentral and **M** 5.5, b) hypocentral and **M** 6.5, c) hypocentral and **M** 7.5, d) epicentral and **M** 5.5, e) epicentral and **M** 6.5, f) epicentral and **M** 7.5
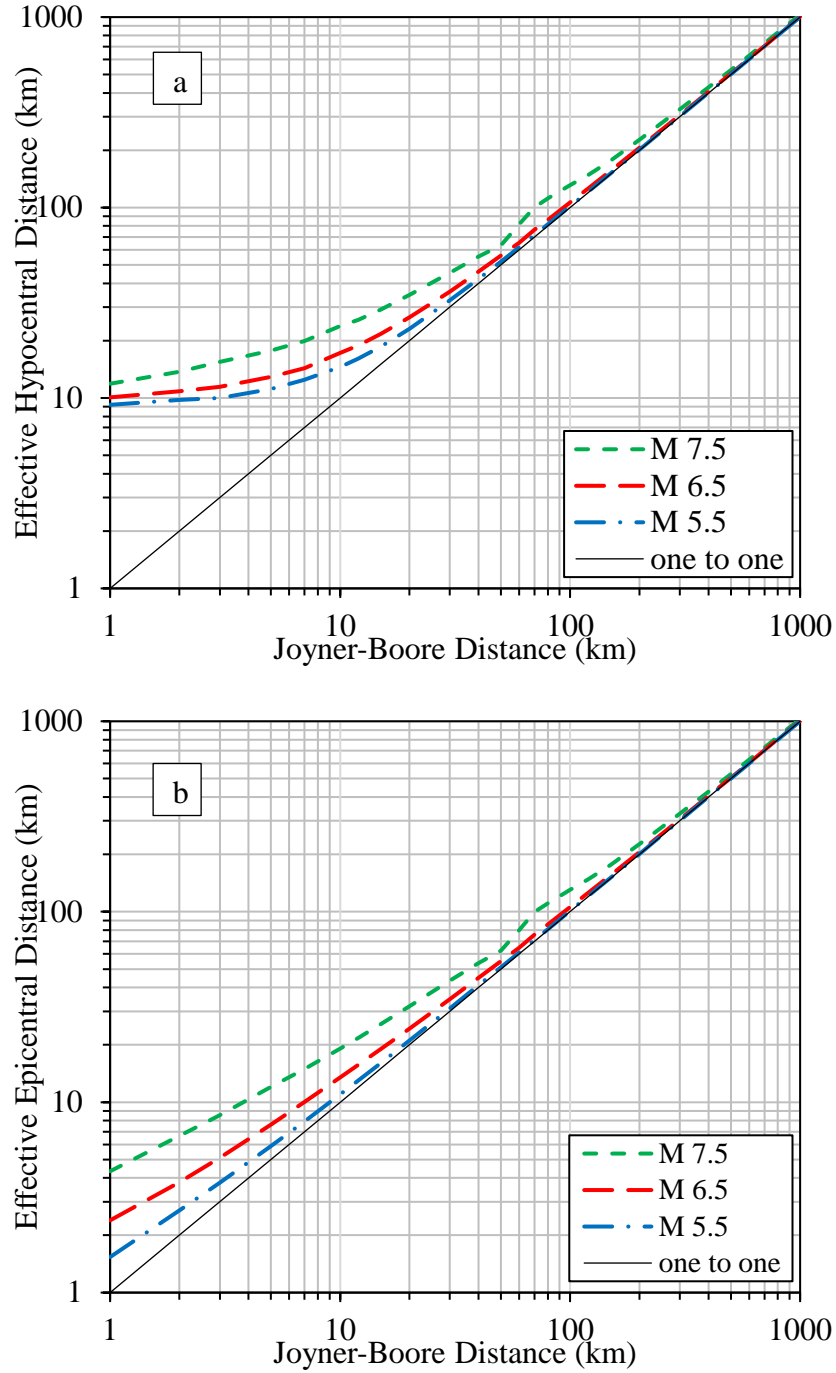
Figure 4-7. Effective distance adjustments along a vertical strike-slip fault as a function of Joyner-Boore distance for three selected magnitudes of **M** 5.5, **M** 6.5, and **M** 7.5; a) Hypocentral, b) Epicentral
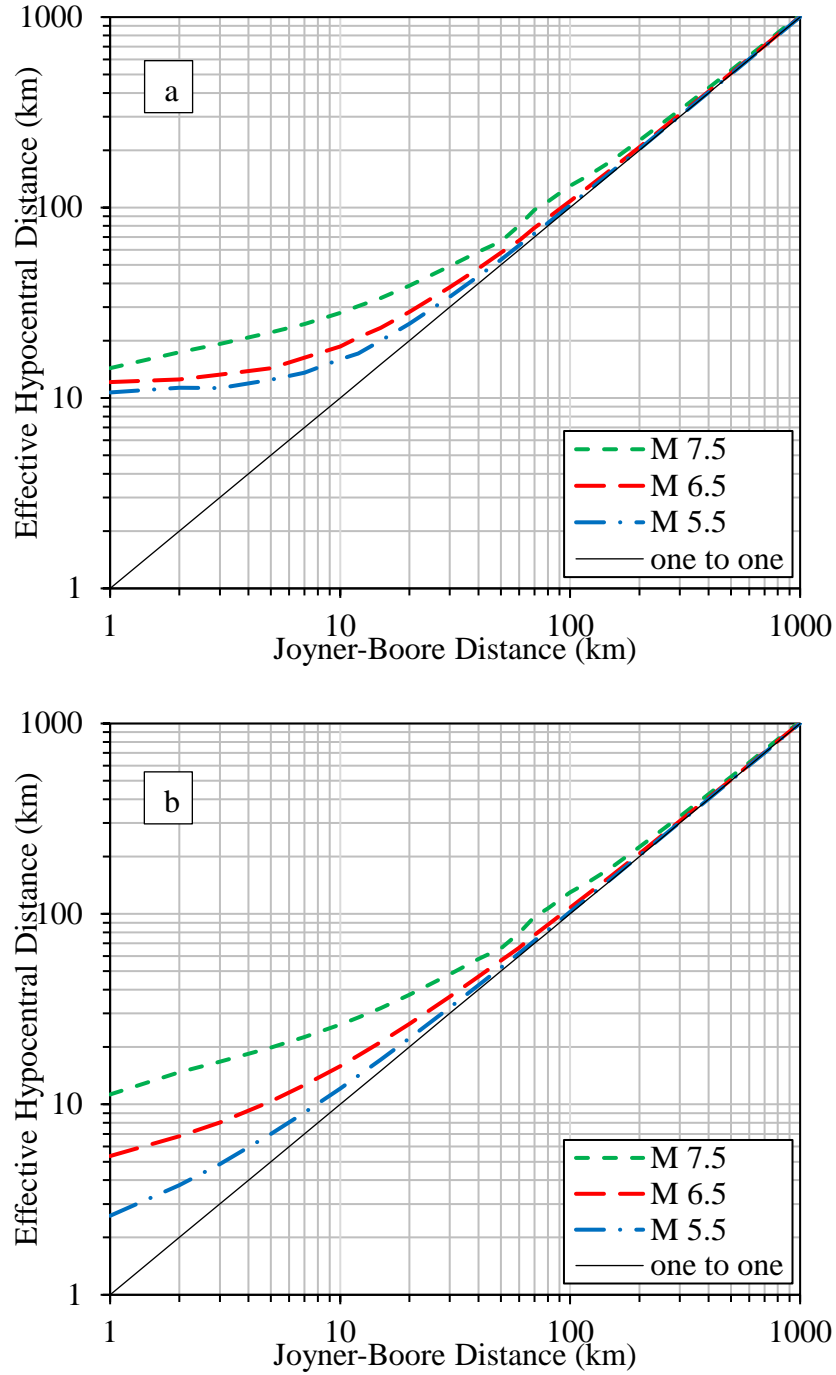
Figure 4-8. Effective distance adjustments along a 40˚-dip reverse fault as a function of Joyner-Boore distance for three selected magnitudes of **M** 5.5, **M** 6.5, and **M** 7.5; a) Hypocentral, b) Epicentral
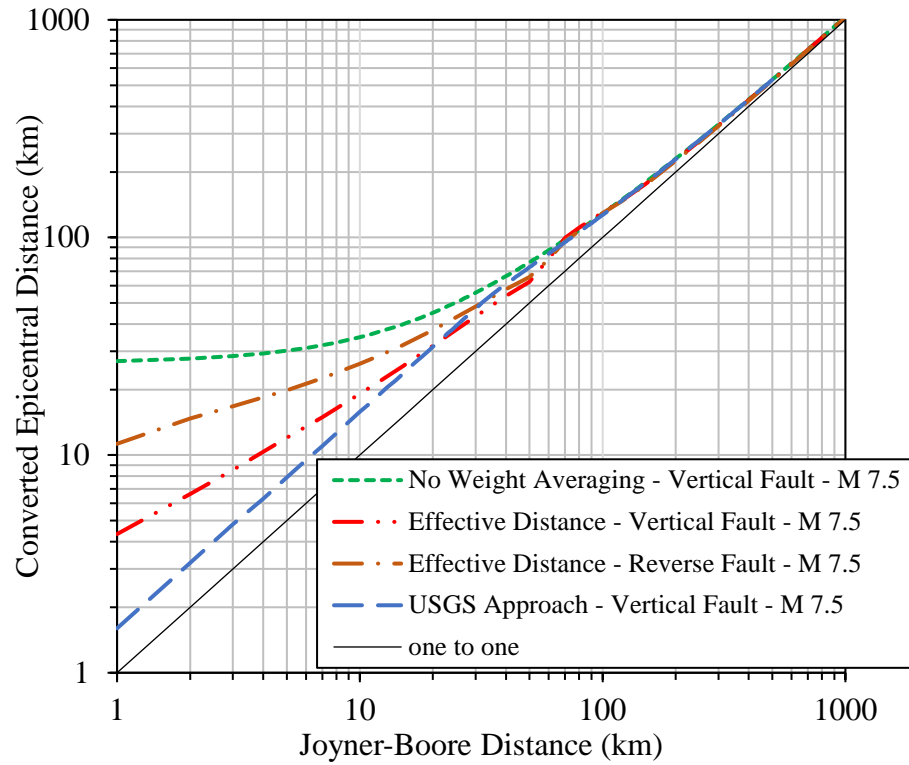
Figure 4-9. Epicentral distance adjustments along a vertical strike-slip fault and a 40˚-dip reverse fault as a function of Joyner-Boore distance in kilometer for a magnitude of **M** 7.5
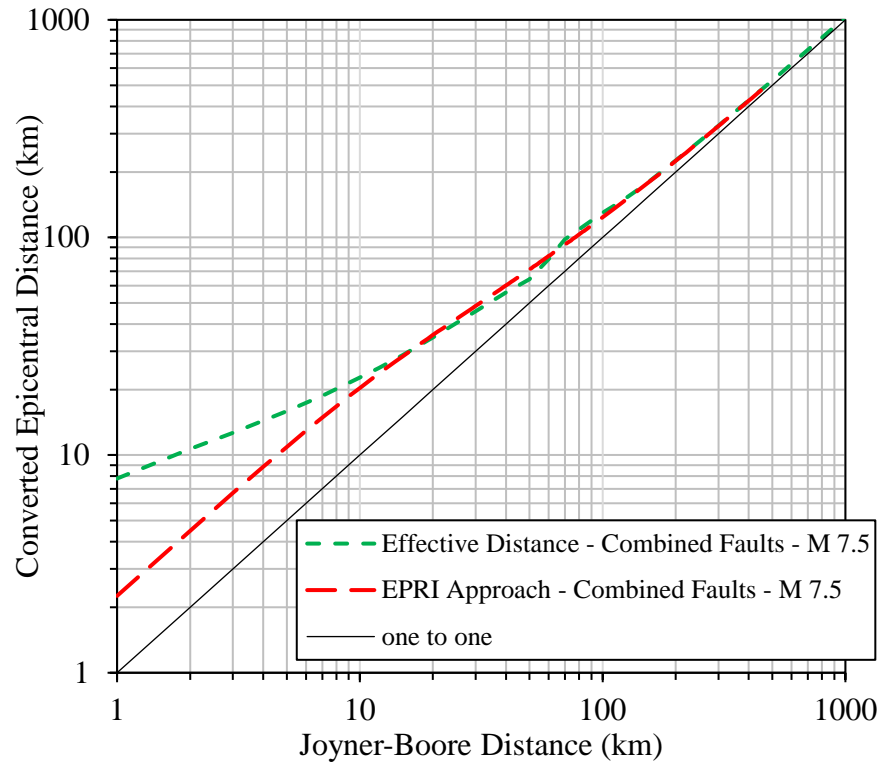
Figure 4-10. Epicentral distance adjustments along an equally combination of a vertical strike-slip fault and a 40˚-dip reverse fault as a function of Joyner-Boore distance in kilometer for a magnitude of **M** 7.5
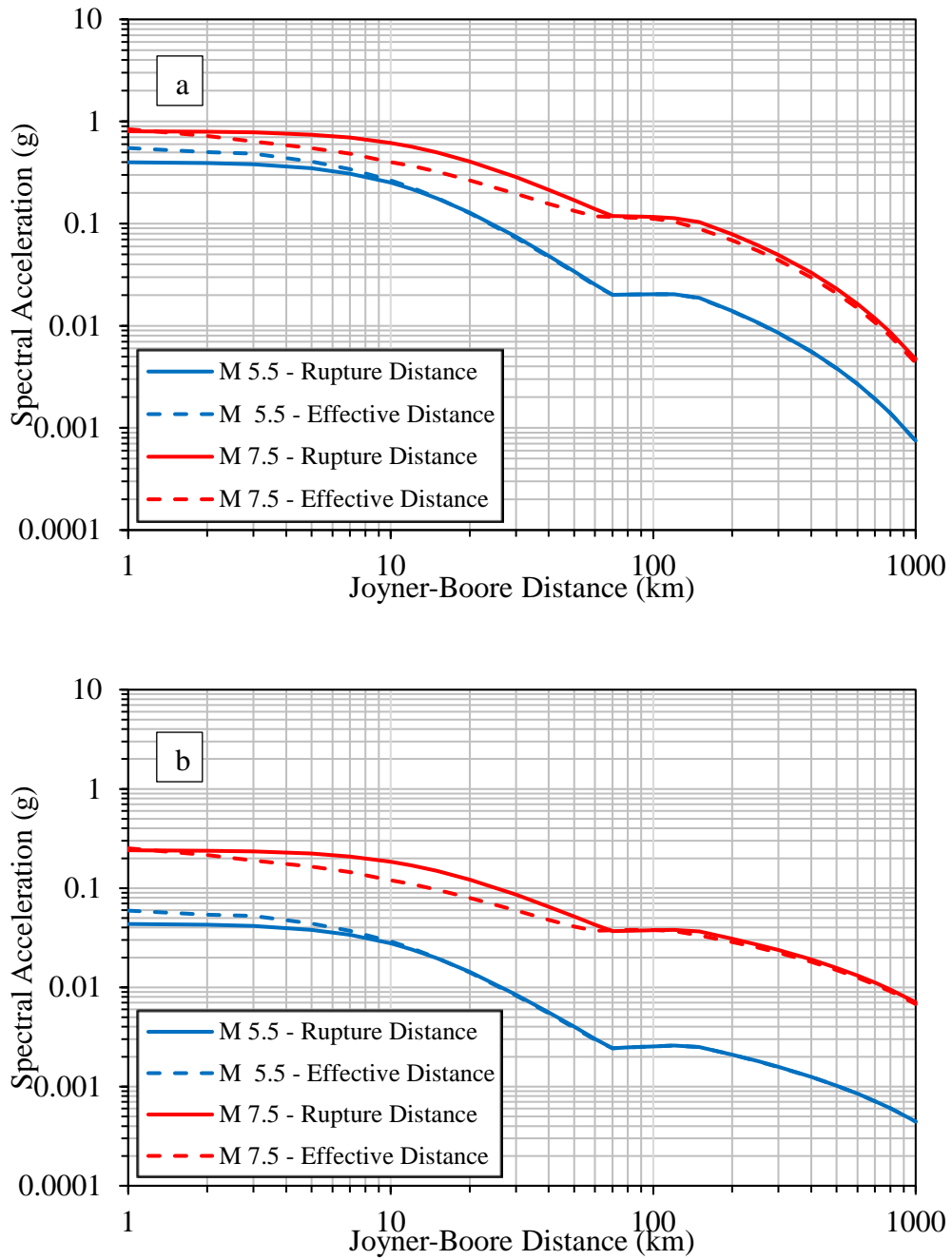
Figure 4-11. Influence of the effective R_{HYP} distance conversion on a given R_{JB}-based GMPE at a period of: a) 0.2 sec, b) 1.0 sec
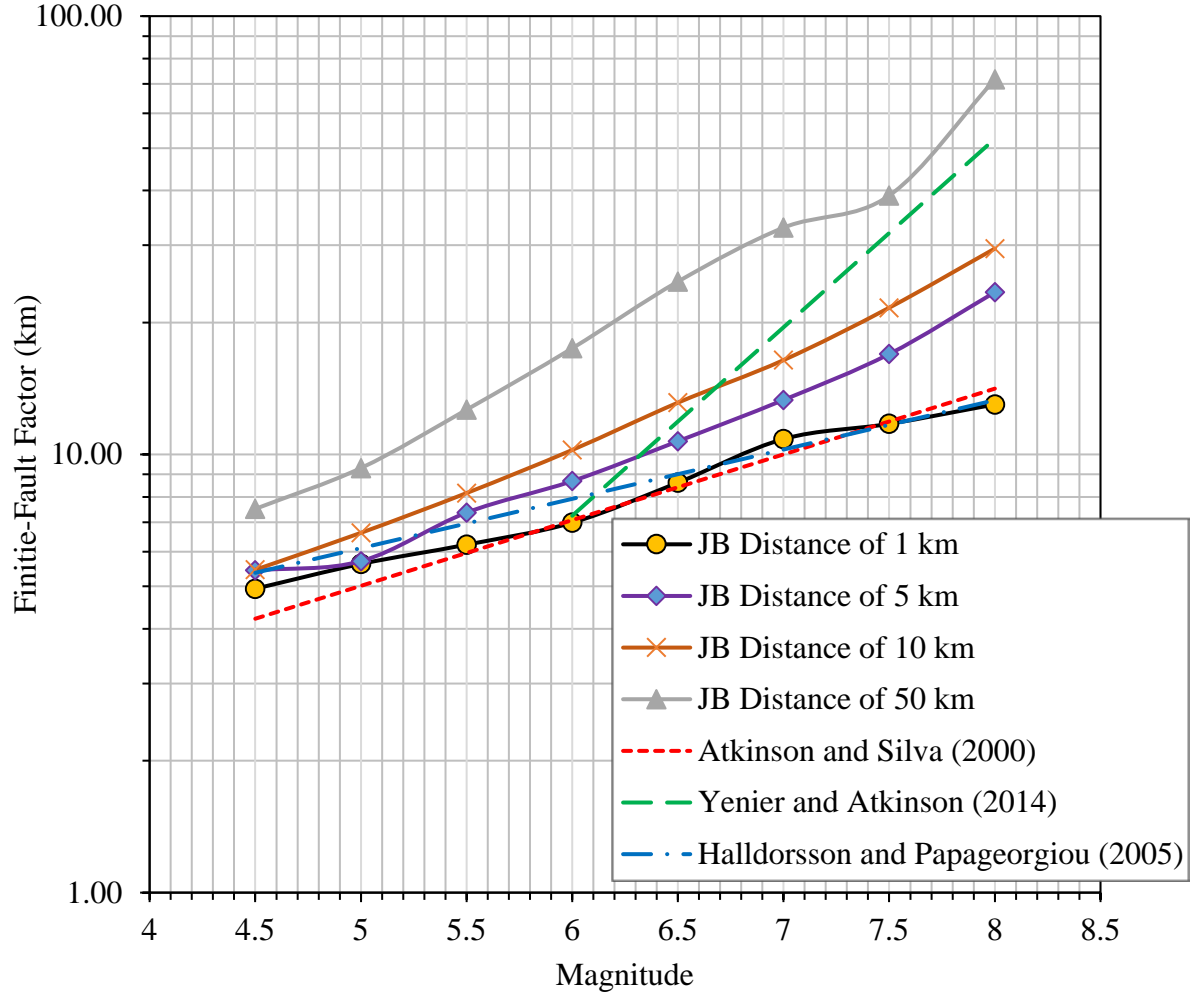
Figure 4-12. Different models proposed to obtain the finite-fault pseudo-depth at a reference distance of 1 km such as $\log(h) = -0.05 + 0.15\,\mathbf{M}$ by Atkinson and Silva (2000), $\log(h) = -1.72 + 0.43\,\mathbf{M}$ by Yenier and Atkinson (2014), and $\ln(h) = -0.515 + 0.259\,\mathbf{M}$ by Halldorsson and Papageorgiou (2005) as well as the analytical-based finite-fault depth values for different magnitudes at different R_{JB} distances
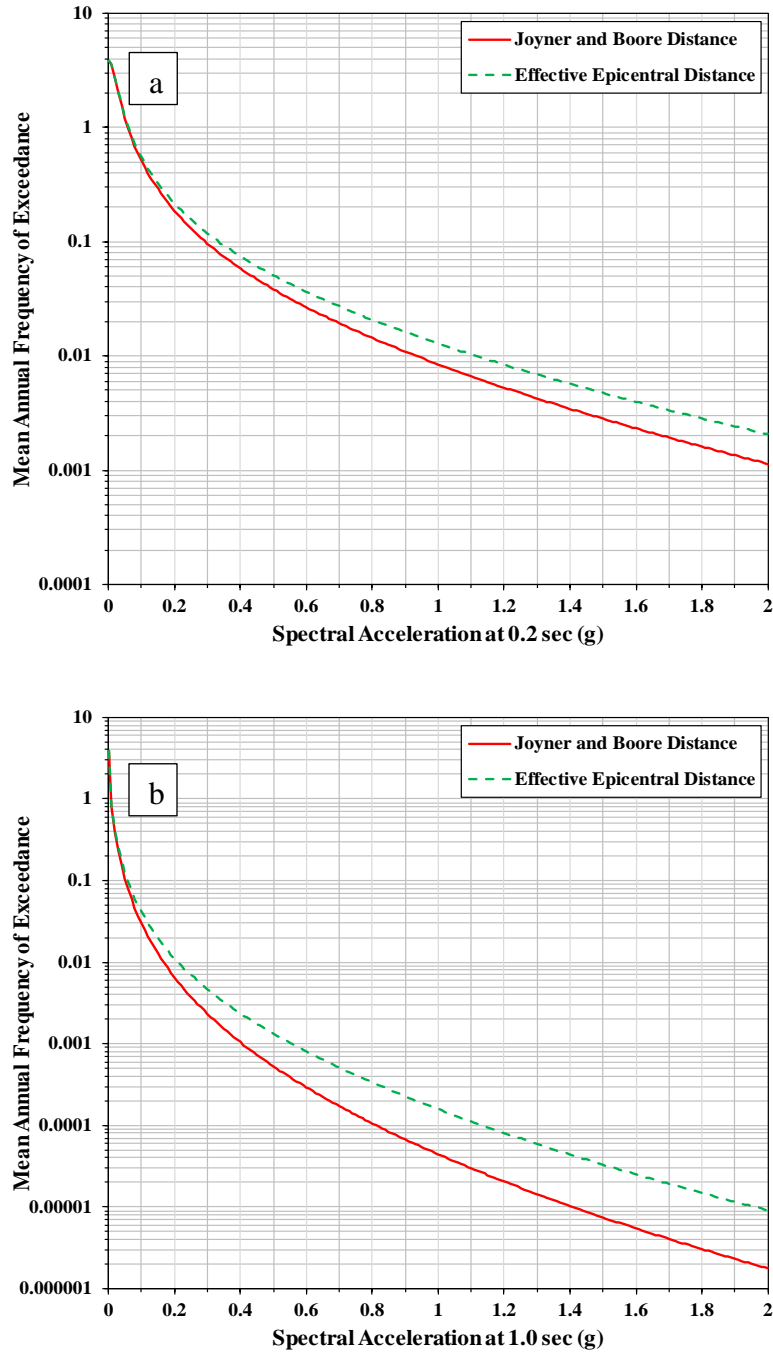
Figure 4-13. Seismic hazard curves for a rock site at the center of a circular high-seismicity source with a radius of 100 km and for a period of 0.2 sec (a) and a period of 1.0 sec (b) using an R_{JB}-based GMPE
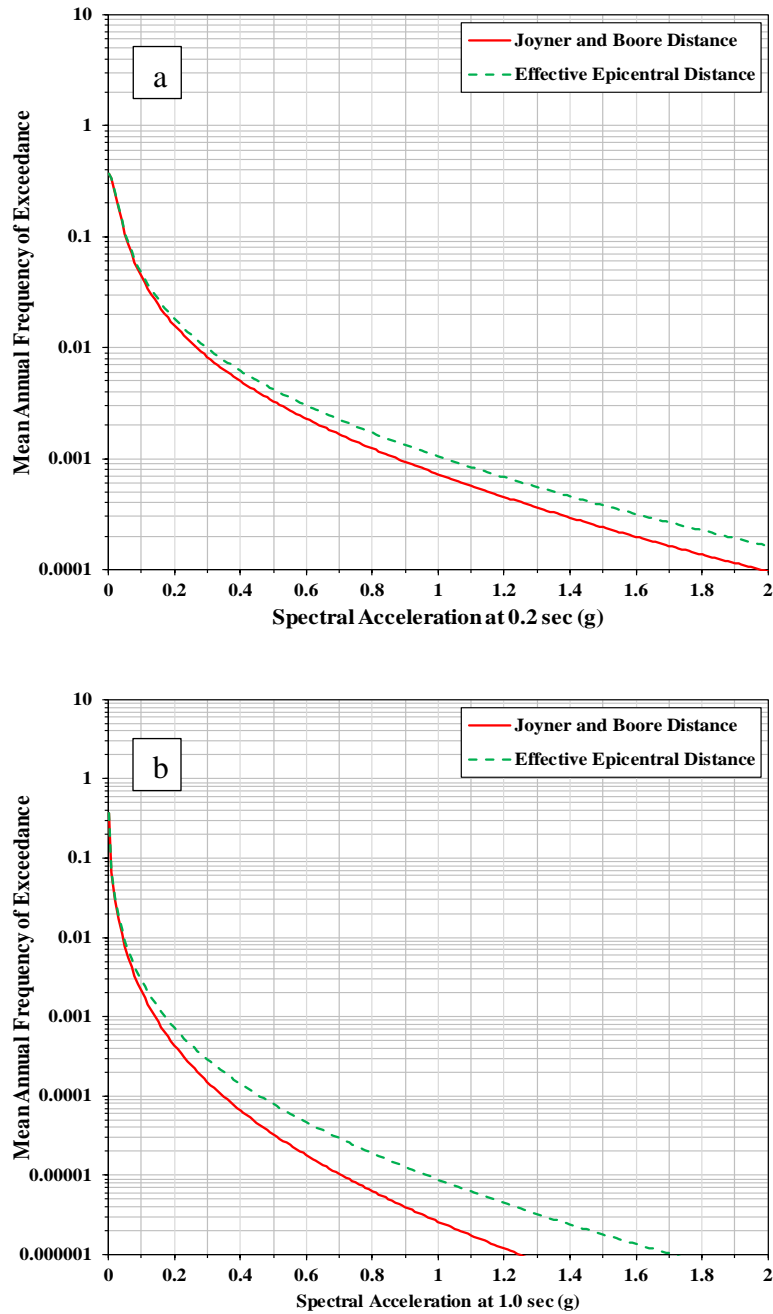
Figure 4-14. Seismic hazard curves for a rock site at the center of a circular low-seismicity

source with a radius of 100 km and for a period of 0.2 sec (a) and a period of 1.0 sec (b) using an

R_{JB}-based GMPE

5. SSGFM: A Software to Generate Time Histories Using the Stochastic Summation of Green's Function Method and Its Verification

Time histories are generally characterized by their amplitudes, durations, and frequency contents. In the stochastic summation of Green's function method (SSGFM) code, the summation scheme is defined such that the frequency content of the target event matches the frequency content of the expected large event. Thus, PGVs, PGAs, response spectra, durations (Trifunac and Brady, 1976), and Arias intensities (Arias, 1970) of the simulated time histories are generally good metrics to compare with the observed ones to validate the SSGFM.

It should be noted that the main goal of using different simulation techniques is not to produce synthetic time histories that match observed time histories wiggle for wiggle, but is to model realistic synthetic time histories with similar key features and properties of observed ground motion waveforms originated from amplitude, frequency content, and duration (Anderson, 2004; Olsen and Mayhew, 2010; Dreger *et al.*, 2015; Goulet *et al.*, 2015). The combined effect of all these characteristics can be captured with the elastic response spectra of a 5% damped single-degree-of-freedom system with different periods, called the pseudo-spectral acceleration (5% damped PSA). In this study, a similar procedure such as the one proposed by the Southern California Earthquake Center (SCEC) platform validation group (Goulet *et al.*, 2015) is used. The current validation process by the SCEC group concentrates only on median PSA values. In this regard, to quantify the validation results, the goodness of fit (GOF) of simulations with observed ground motions are employed. A set of criteria are defined to accept/reject (pass/fail) simulations. In fact, the performance of the simulation approach is evaluated by investigating the ability of matching PSAs from the simulations with the PSAs estimated from recorded ground motions (part A) and predicted median PSAs from GMPEs (part B). In summary, to assess the performance of the presented technique compared to the other ground motion simulation techniques, we need to evaluate the capability of the SSGFM to simulate strong ground motions using smaller ground motions as input (EGF).

In this chapter, various approaches proposed to measure the goodness of simulations are discussed. Then, synthetic and real ground motions data are used to verify the accuracy of SSGFM using the TSP1 and TSP2. Since the Ordaz *et al*. (1995) and Kohrs *et al*. (2005) models are similar to TSP1 and TSP2, respectively, they are not included in the comparisons. Key features of ground motions are compared to determine whether the SSGFM code can be used to simulate realistic ground motions.

5.1 Validation Procedure

5.1.1 SCEC Validation Exercise Part A – Against Observed Ground Motions

In the civil engineering design process, single-degree-of-freedom structural response spectra or earthquake time histories are employed as inputs to analyze structures. The SCEC broadband platform validation committee has developed a procedure to compare response spectra of the simulated ground motions with the observed data. The main goal of this exercise is to assess the ability of various ground motion simulation methods to generate reasonable average PSAs. This validation exercise was presented as a collaboration of SCEC with the Pacific Earthquake Engineering Research (PEER) center.

The current validation exercise only employs median PSA values, not their aleatory uncertainty. The first step to evaluate simulations via part A of the SCEC validation exercise is to define residuals (the difference between the natural logarithm of the observed PSA values and the PSA values from simulations)

$$\text{Res} = \ln(\text{PSA}_{\text{obs}}) - \ln(\text{PSA}_{\text{sim}}) = \ln(\frac{\text{PSA}_{\text{obs}}}{\text{PSA}_{\text{sim}}}) \tag{5-1}$$

where a positive residual represents underprediction of PSA and a negative residual denotes overprediction of PSA. This metric is called GOF. The SCEC-part A validation results in a GOF versus spectral period plot. Due to a large number of simulations at each spectral period, the difference between the average residual and zero indicates the bias at that period. The term bias is defined as

$$\text{bias} = \frac{1}{N} \sum_{j=1}^{N} \text{Res}_j \tag{5-2}$$

in which N is the number of simulations at a specified spectral period. The SCEC validation exercise part A suggests using 50 realizations for simulating each case at a given location to capture the variability of the source process (Goulet *et al*., 2015). A lower bias indicates a better set of simulations at a particular spectral period and the optimal bias is zero. The acceptance/rejection criterion is defined as (Dreger *et al*., 2015):

- Failure threshold is defined once the GOF value from simulations is more than twice or less than the half of the observed values. Thus, failure threshold is ln (2) = 0.69 ≈ 0.70. A GOF less than a factor of 0.35 (ln (1.4)) is given a "pass" condition. A GOF with a factor between 0.35 and 0.70 is considered as a "potential issue" condition.

5.1.2 Duration

The total duration of the event not only affects the feature of the ground motion in the time domain, but also significantly affects the response spectrum. Between two records having the same amount of energy, the one with longer duration has lower GMIMs and a lower response. Thus in addition to comparing response spectra, the duration is compared. The effective 95%-5% significant duration is defined by (Boore and Thompson, 2014)

$$D'_{95-5} = 2\left(D_{80} - D_{20}\right) \tag{5-3}$$

where D_{20} and D_{80} are the times at which 20% and 80% of the total cumulative squared acceleration (normalized Arias intensity) are reached, respectively. D_{20} and D_{80} are used instead of D_5 and D_{95} to pass the instability within the beginning and end of seismograms (Boore and Thompson, 2014).

Arias intensity is defined by

$$I_A = \int a^2(t)dt \tag{5-4}$$

in which $a(t)$ is the acceleration time history. Then, the normalized Arias intensity is given by

$$\text{Normalized intensity} = \frac{\int_0^t a^2(t)dt}{\int_0^{end} a^2(t)dt} \tag{5-5}$$

162

where t is the desired time to calculate the Arias intensity and the end represents the entire seismogram.

5.2 Verification Using Synthetic Motions

5.2.1 Using SMSIM to Simulate Synthetic Weak Motions

To generate synthetic weak motions for a small earthquake which is effectively a point source (Boore, 1983; Boore, 2003), the Stochastic-Method SIMulation (SMSIM) code (Boore, 2003; Boore, 2005) is used. The latest version, SMSIM 6.20 (http://www.daveboore.com/software_online.html; last accessed: 10/15/2017) is used. In addition to the source function explained in Chapter 1, the path and site functions should be defined. In the point-source model, the total Fourier amplitude spectrum (FAS) of the ground motion, Y, due to shear-wave propagation in an elastic half space can be expressed by the following equation (Boore, 2003)

$$Y(M_0, f, R) = S(M_0, f) \times P(f, R) \times G(f) \times I(f) \tag{5-6}$$

where M_0 is the seismic moment (dyne-cm), R is the source-to-site distance (km), f is frequency (Hz), $S(M_0, f)$ is the source spectrum, $P(f, R)$ is the path attenuation function, $G(f)$ is the site-response function, and $I(f)$ is a filter representing the type of GMIM. the recent seismological parameters determined for CENA to obtain the source, path, and site functions are used. Table 5-1 tabulates values employed for use in SMSIM. In the following sections, the path, and the site terms are breifly described.

Path Parameters

$P(f, R)$ describes the effects of the propagation path on seismic waves and consists of geometrical spreading and attenuation (scattering and anelastic attenuation). The geometrical spreading is defined as the decay of seismic wave amplitudes due to expansion on a spherical surface and Q represents the Earth's structure in which seismic waves propagate and is usually found out to be frequency dependent $P(f, R)$ is given by (Boore, 2003)

$$P(f, R) = Z(R) \exp\left(-\frac{\pi f R}{Q V_Q}\right) \tag{5-7}$$

where $Z(R)$ is the geometrical spreading function defined as a function of $R^{-\alpha}$ (α is the geometrical spreading exponent). V_Q denotes the average group velocity of the desired phase of seismic waves through the propagation path.

Six attenuation models were provided by the PEER NGA-East project (Silva *et al*., 2002; Atkinson, 2004; Atkinson and Boore, 1995; Boore *et al*. 2010; Boatwright and Seekins, 2011; Atkinson and Boore, 2014). Boore (2015) compared these models and concluded that models with $1/R^{1.3}$ as the geometrical spreading functions cannot fit the observed data at periods of 1.0 and 2.0 sec. In addition, a very large stress drop is required to match the data at periods of 0.1 and 0.2 sec. A similar observation has made by Sedaghati and Pezeshk (2016c) and Pezeshk *et al*. (2018a) for the New Madrid seismic zone (NMSZ) which is a part of CENA. Furthermore, Boore (2015) suggests using the Boatwright and Seekins (2011) attenuation model since it matches the observed data well compared to other attenuation models. This attenuation model is very similar to the attenuation model derived by Nazemi *et al*. (2017) for the NMSZ. Hence, we will use the Boatwright and Seekins (2011) attenuation model given by

$$Q(f) = 410f^{\,0.50}$$
$$G(R) = \begin{cases} R^{-1} & R \le 50 \text{ km} \\ R^{-0.5} & R > 50 \text{ km} \end{cases} \tag{5-8}$$

It is interesting that the inversion results from Darragh *et al*. (2015) also confirm using the bilinear geometrical spreading proposed by Boatwright and Seekins (2011).

The next path parameter is the path-dependent duration. Table 5-2 reports the path duration model for a stable continental region determined by Boore and Thompson (2015). Note that the total duration is the summation of the source-dependent duration ($T_S = 1/f_c$) and path duration (T_P).

Site Parameters

The $G(f)$ function represents the combined effects of the diminution function (near site path independent attenuation introduced by Anderson and Hough, 1984) and the crustal amplification factor (Boore, 2003). The site response is obtained from

$$G(f) = A(f) \times D(f) \tag{5-9}$$

in which $A(f)$ and $D(f)$ represent the amplification and diminution functions. The diminution function can be explained by an exponential function given by

$$D(f) = \exp(-\pi f \kappa_0) \qquad (5\text{-}10)$$

where κ_0 is the path-independent loss of energy which occurs due to the damping at the site and can be obtained by the decay rate of the FAS on a log-linear plot (Anderson and Hough, 1984). The site amplification function indicates that the response of the low-velocity layers near the surface which corresponds to the shear-wave velocity, density, and damping ratio of the soil layers and can be estimated theoretically or experimentally. Table 5-3 lists the value of amplification factors derived using the quarter wavelength method (Boore and Thompson, 2015). For simulation purposes, the typically adopted value of 0.006 sec is used as κ_0 (Campbell *et al.*, 2014).

Source Parameters

I will use a single corner frequency (SCF) source model with a constant stress drop. Equations to calculate the seismic moment and corner frequency were given in Chapter 1. Thus, to model the spectral shape at high frequencies, we need to have the stress drop value. Boore (2015) inverted the data in CENA and obtained that the median stress parameter is equal to 172 bars based on the Boatwright and Seekins (2011) attenuation model. The average radiation pattern, shear-wave velocity near the source, and density of the rock near the source are assumed to be 0.55, 3.7 km/sec, and 2.8 g/cc, respectively. All these explained parameters are chosen to be consistent with each other. Since they are correlated, changing one parameter will result in changing the other parameters.

Time domain analysis

It is worth mentioning that having a smaller time step for the recorded small earthquake time history yields better and more accurate results, since the delay times will be adjusted to this vector. A value of 0.005 sec was used as the time step.

5.2.2 Verification Procedure

Example of the SCF source model using SMSIM

For the first example, all values tabulated in Table 5-1 are ued to generate an **M**3.0 earthquake ($\Delta\sigma$ = 172 bar) using SMSIM 6.2 at a point-source distance of 40 km. The distance used in SMSIM is the effective point-source distance. Since SSGFM requires that the equivalent point-sources of both target and EGF are located at the same place, the effective point-source distance for the large event should be 40 km as well. To generate a large earthquake with magnitude of 6.0 and a point-source distance of 40 km, the stress drop is updated with a value of 350 bars while the remaining parameters are the same. Figure 5-1 and Figure 5-2 illustrate the acceleration, velocity, and displacement time series for the small event (EGF) and the target event, respectively. To check the accuracy of the written code, the velocity and displacement time histories determined from the SSGFM code and from SMSIM are plotted. As can be seen, they are the same suggesting that this part of the code works correctly. Using equations (2-53) and (2-54), the number of summands and the scaling factor are obtained to be

$$
\begin{aligned}
N &= 387805 \\
\xi &= 0.0815 \\
f_{cs} &= 14.2421 \\
f_{ct} &= 0.5707
\end{aligned}
\tag{5-11}
$$

First, the TSP1 approach is used and simulate 50 sets of rupture times. Using the generated rupture times, scaling factor, and the number of summands, 50 different realizations are simulated to account for the source rupture variability. Figure 5-3 demonstrates the FAS of the EGF, the FAS of the target, and all realizations as well as the average FAS. The average FAS is obtained from the rms (root mean square) mean of all 50 realizations, given by

$$
\text{FAS}_{\text{mean}} = \sqrt{\frac{\sum_{i=1}^{N} FAS_i^2}{N}}
\tag{5-12}
$$

As can be seen, the FAS of realizations perfectly follows the trend of the FAS of the target event. Figure 5-4 displays the response spectra for the EGF, target event, each realization, and the average. The geometric mean of response spectra of realizations is used to determine the average response spectrum (Boore, 2003). Figure 5-4 also shows the bias of the realizations and based on

that, simulations match the target event very well. The effective significant duration (equation (5-3)) for the target event is 21.66 sec and the average effective significant duration from all 50 realizations is 21.02 sec, indicating the simulations have very similar durations to the target event. Finally, Figure 5-5 presents two different simulated time histories compared to the target event. Values of PGA, PGV, and PGD for each time series are written. All values from synthetics are within ±15% of the observed values.

Now, the TSP2 approach is used to simulate another 50 realizations. Figure 5-6, Figure 5-7, and Figure 5-8 show the FAS, response spectra, and time series plots for the target event and all realizations. According to these plots, the simulated time histories perfectly match all desired characteristics of the target event.

Note that the difference between the TSP1 and TSP2 approaches is clearly visible in the FAS plot, response spectrum plot, and the time histories plot. All simulations from the one-stage summation scheme are similar, while each simulation from the two-stage method is different than the other simulations. In fact, simulations from the two-stage method on average match the energy distribution, response spectrum, and FAS of the target event. Therefore, the two-stage method can better capture the variability of ground motions caused by the rupture process whereas simulations from the one-stage summation scheme produce very similar results.

Example of the DCF source model using SMSIM

To perform the second example, all parameters except the SCF source model from Table 5-1 are used to simulate two earthquakes with magnitude 5 (EGF) and magnitude 7 (target) having the same stress parameters. Both events are simulated at an effective point source distance of 70 km. To model the source, the additive double corner frequency model suggested by Atkinson and Silva (2000) for ENA (equation (3-33)) is used. Figure 5-9 and Figure 5-10 illustrate the acceleration, velocity and displacement time series for the small event (EGF) and the target event, respectively. Using equations (2-53) and (2-54), the number of summands and the scaling factor are given by

$$N = 10000$$
$$\xi = 0.01$$
$$f_{cs} = 1.4242,\ f_{as} = 0.5023,\ f_{bs} = 2.9257 \qquad (5\text{-}13)$$
$$f_{ct} = 0.1424,\ f_{at} = 0.0512,\ f_{bt} = 0.5196$$
$$f_{cd} = 0.2533,\ f_{ad} = 0.1603,\ f_{bd} = 0.5909$$

The TSP1 approach is skipped since it generates very similar time histories and the results from the two-stage summation scheme have a more realistic shape since the energy is not concentrated in the middle like the one-stage summation scheme. Using the TSP2 approach, 50 different simulations are produced. Figure 5-11 demonstrates the FASs for all realizations and the small and target event as well as the average FAS. As can be seen, the FAS of the simulated time histories on average match the FAS of the target event, while the FAS of each realization can deviate from the FAS of the target event. Figure 5-12 depicts that the average of the 50 spectra matches the target response spectrum very well, although the spectrum of each simulation may deviate from the average at some frequencies. In addition, this figure shows that the bias is near to zero, indicating the simulations can mimic the characteristics of the target event. The effective significant duration (equation (5-3)) for the target event is 36.82 sec and the average effective significant duration from all 50 realizations is 33.23 sec, indicating the simulations have very similar durations to the target event. Simulated acceleration time series as well as their resulting velocity and displacement time histories are shown in Figure 5-13. All PGA, PGV, PGD values are within ±20% of the observed values, indicating that the results from the synthetics are satisfactory.

Example of the SCF source model using EXSIM

The next step for verification of the proposed method and written codes is to generate two events with magnitudes 7 and 8 using the EXSIM software. EXSIM (EXtended-finite fault-method SIMulation) is an open-source FORTRAN code to simulate ground motions (Motazedian and Atkinson, 2005; Boore, 2009; Assatourians and Atkinson, 2012). In this regard, weak ground motions for subsources are generated using the stochastic point source model. Then, time series are normalized and shifted in the time domain to construct the time histories of the large event. The basic idea of EXSIM is very similar to SSGFM. The advantage of SSGFM is that if a recorded weak motion is available, it is not required to have detailed information of the path and

site parameters such as geometrical spreading and attenuation. Also, SSGFM needs fewer input parameters related to the source compared to EXSIM.

To generate **M**7.0 and **M**8.0 events, the Wells and Coppersmith (1994) relationships to estimate the width and length of the fault is used. All parameters used for the **M**8.0 event are reported in Table 5-4 and the distance is 7 km. For the **M**7.0 event, the length and width of the fault are equal to 46.737 and 10.707 km, respectively, and the distance is 15 km. To generate time series, the time step is chosen to be 0.01 sec.

Using equations (2-53) and (2-54), the number of summands and the scaling factor are given by

$$
\begin{aligned}
N &= 150 \\
\xi &= 0.22 \\
f_{cs} &= 0.14 \\
f_{ct} &= 0.04
\end{aligned}
\tag{5-14}
$$

I use the TSP2 scheme to scale, shift, and sum up time histories from the **M**7.0 event to simulate 50 different time histories from an **M**8.0 event. Figure 5-14 demonstrates the FASs for all realizations and the small and target event as well as the average FAS. As can be seen, the FAS of the simulated time histories on average match the FAS of the target event, while the FAS of each realization can deviate from the FAS of the target event. Figure 5-15 depicts that the average of the 50 spectra matches the target response spectrum very well, although the spectrum of each simulation may deviate from the average at some frequencies. Note that with increasing frequency the deviation from the average gets larger, whereas all realizations are very close to the average at low frequencies. In addition, this figure shows that the bias is near to zero, indicating the simulations can mimic the characteristics of the target event. The effective significant duration (equation (5-3)) for the target event is 31.38 sec and the average effective significant duration from all 50 realizations is 27.63 sec, indicating the simulations have very similar durations to the target event. The simulated acceleration time series as well as their resulting velocity and displacement time histories are shown in Figure 5-16. All PGA, PGV, PGD values are within ±20% of the observed values, indicating the results from the synthetics are satisfactory.

5.3 Verification Using Observed Ground Motions

The 11 March 2011 Tohoku, Japan, megathrust earthquake with **M**9.0 is one of the recorded largest subduction earthquakes. About 23,000 people were killed due to this earthquake and the tsunami generated by this event. The source of this earthquake approximately has a length of 450 km and a width of 200 km with a maximum slip of 30 m (Kurahashi and Irikura, 2011; Ghofrani *et al*., 2012). Detailed investigations of this event reveal that the source model is a combination of areas with large slip velocity or high stress drop (asperities) and areas with large slip (background source). This kind of rupture model is called compound (Frankel, 2016). The comprehensive description of this event can be found in Kurahashi and Irikura (2011). This earthquake was selected since a rich dataset of strong motions from this earthquake can be obtained from the National Research Institute for Earth Science and Disaster Prevention (NIED) and it is freely available to download via *http://www.kyoshin.bosai.go.jp/* (last accessed Jan 2018). To select an appropriate small earthquake for use in the SSGFM, both events must have the same radiation pattern and also propagation path and site effects. Therefore, the **M**6.8 10 March 2011 Tohoku, Japan, earthquake is selected since its hypocenter is very close to the hypocenter of the target event and their source characteristics are similar. Table 5-5 provides general information about source parameters of the main event (target) and the small event (EGF).

Two popular NIED strong motion seismograph networks are K-NET and KiK-net. The K-NET network consists of more than 1,000 stations, installed on the ground surface throughout Japan, distributed uniformly every 20 km. The KiK-net network has 687 pairs of strong-motion seismographs installed on the ground surface and in boreholes within Japan. In this study, three-component accelerograms from KiK-net in boreholes is used, since recordings of these large earthquakes from the ground surface are strongly affected by the soil nonlinearity and the SSGFM cannot capture this effect. Therefore to have better simulation results, borehole data is used. A total of 10 KiK-net stations was selected in which both events were recorded at the bottom of boreholes with JB distances ranging from 35 to 120 km. Table 5-6 tabulates the location of stations and their details and Figure 5-17 demonstrates the location of the selected sites as well as the location of the target event and its EGF. As can be seen from this figure, all stations are above half of the fault's length. Note that stations located beneath half of the fault's

length were not employed since the effective distance for them is significantly different; and therefore, those stations will need another EGF with a hypocenter located near the equivalent point-source of the target event.

To perform the SSGFM, we need to have stress drop values or corner frequencies of both events as inputs. The corner frequency of the small event is obtained by Kurahashi and Irikura (2011) and is equal to 0.22 Hz. The corner frequency of the target event is obtained in this report based on a trial and error approach by minimizing the sum of the squared residuals, obtained from fitting the Fourier acceleration spectra of all waveforms by a SCF source model. The estimated corner frequency for the target event is equal to 0.0225. Therefore, the number of summand and the scaling factor are

$$
N = 9140
$$
$$
\xi = 0.2125
$$

(5-15)

I use the TSP2 scheme and simulate 50 different realizations for each component recorded at each station, to account for variations in the source rupture process. Thus, there are 1500 synthetics based on 30 input ground motions.

Figure 5-18, Figure 5-19, and Figure 5-20 present the comparison of the FAS of the target event to each realization, as well as the average FAS for stations AKTH19 (N-S direction), YMTH14 (E-W direction), and YMTH15 (vertical direction), respectively. Overall, there is a reasonable agreement between the target FASs and the average FAS. There are some sparks in FAS of different stations which may be attributed to the reverberation in data caused by site response (Frankel, 2016; Sedaghati *et al*., 2018) or the presence of surface waves (Ghofrani *et al*., 2013). The SSGFM perfectly models these sparks in the FAS of the simulations. It should be mentioned the average FAS in a few stations falls below the target FAS at high frequencies. The reason for this issue is that the equivalent point-source of the target event for these stations is located closer to the site, but the EGF used in the simulation process is farther to the site. Therefore, it affects the FAS at high frequencies.

To obtain the response spectrum, normalized Arias intensity, and time series plots, the acceleration waveforms (both data and synthetics) filtered between 0.10 and 15 Hz is used. Following Ghofrani *et al*. (2012), the lower cut-off frequency is selected by the inspection of data somehow the displacement spectrum has a flat portion at low frequencies resulting in well-

shaped displacement time histories. The upper cut-off frequency is chosen based on the characteristics of the seismographs (Ghofrani *et al*., 2012). A zero-phase (acausal) four-pole Butterworth filter to avoid changing the size and location of peak amplitudes (Sedaghati and Pezeshk, 2016c) is used.

The comparison between the response spectra of simulations and target event as well as bias plots are depicted in Figure 5-21, Figure 5-22, and Figure 5-23 for stations AKTH19 (N-S direction), YMTH14 (E-W direction), and YMTH15 (vertical direction), respectively. As can be seen, the bias lines bracket the zero-line indicating that there is no systematic underestimation or overestimation of the responses.

Table 5-7 compares the durations derived from different definitions for time histories of stations AKTH19 (N-S direction), YMTH14 (E-W direction), and YMTH15 (vertical direction), respectively. The duration of the synthetics is often longer than the target event. The reason for this issue is that the EGF is located further, compared to the equivalent point source of the target event. Therefore, the EGFs have longer total duration due to the effect of path-dependent duration. The longer duration of the EGF is accumulated within the simulation process and produces synthetics with longer duration compared to the target event.

Acceleration, velocity, and displacement time histories of the EGF, the target event, and two different realizations for stations AKTH19 (N-S direction), YMTH14 (E-W direction), and YMTH15 (vertical direction) are shown in Figure 5-24, Figure 5-25, and Figure 5-26, respectively. The peak values are also denoted on the plots. Regarding these figures, all PGA, PGV, and PGD values from synthetics match the observed values within a factor of 1.4 indicating that the results are satisfactory. It is interesting to note that the other stochastic methods such as EXSIM fail to reproduce the velocity and displacement waveforms for very large earthquakes since they are strongly affected by the integration of the slip across the entire fault plane (Ghofrani *et al*., 2013). The method presented in this report can reproduce well-simulated velocity and displacement waveforms that look reasonable and coherent.

Eventually, the final bias is determined from averaging the three components captured at all stations. As can be seen in Figure 5-27, the broadband synthetics overall produce PSAs with low bias compared to the data. Therefore, the resultant simulations even at close distances are in good agreement with the recorded data. The upper plot shows the residuals from each realization

172

as well as the average and the standard deviation. The lower plot depicts the average, 90% confidence interval, and standard deviation lines. Note that the improved SSGFM is a simple stochastic method that works with a few input parameters that aim to mimic the effects of rupture propagation, rupture inhomogeneity, and a fault's geometry without any specific details of the physics of the rupture process. Thus, synthetics may sometimes miss coherent pulses and phasing information. In fact, the produced synthetics match the key characteristics of ground motions such as response spectrum and duration although they can have different shapes of time series compared to the observed ones.

5.4 Tables

Table 5-1. Parameters of the stochastic model for use in SMISM

Source Parameters
Source spectrum, SCF ω^2 model
Stress drop, $\Delta\sigma = 172$ bars
Radiation pattern coefficient $= 0.55$
Velocity, $\beta_S = 3.7$ km/sec
Density, $\rho = 2.8$ g/cc
Source duration, $T_S = 1/f_c$ where f_c is the corner frequency

Path Parameters
Geometrical spreading, $Z(R) = R^{-1.0}$ for $R \leq 50$; and $R^{-0.5}$ beyond 50 km
Quality factor, $Q(f) = 410f^{0.5}$ (from Boatwright and Seekins, 2011)
Path duration, T_P see Table 5-2 (from Boore and Thompson, 2015)

Site Parameters
Partition factor $= 0.707$
Free-surface factor $= 2.0$
Site attenuation, $\kappa_0 = 0.006$ sec
Site amplification, $A(f)$ see Table 5-3 (from Boore and Thompson, 2015)

Table 5-2. The path duration function for CENA (from Boore and Thompson, 2015)

Rupture distance (km)	T_P (sec)
0	0.0
15	2.6
35	17.5
50	25.1
125	25.1
200	28.5
392	46.0
600	69.1
Slope of last segment	0.111

Table 5-3. Crustal amplification factors for CENA for a reference hard-rock site

f (Hz)	$A(f)$
0.001	1.000
0.008	1.003
0.023	1.010
0.04	1.017
0.061	1.026
0.108	1.047
0.234	1.069
0.345	1.084
0.508	1.101
1.09	1.135
1.37	1.143
1.69	1.148
1.97	1.150
2.42	1.151

Table 5-4. Parameters of the stochastic model for use in EXSIM

```
Fault Strike              =       0.00
Fault dip                 =      90.00
Fault depth to upper edge =       2.00
Fault length from Wells and Coppersmith for fault type S, using a reference stress of    70.0
Fault Length              =    194.830
Fault width from Wells and Coppersmith for fault type S, using a reference stress of    70.0
Fault Width               =     19.937
ratio of rupture to s-wave velocity =     0.80
FaultLat                  =       0.00
FaultLon                  =       0.00
No.of subs along strike   =      129
No.of subs along dip      =       13
subfault length           =      1.51
subfault width            =      1.53
i_rise_time (1=orig,2=1/f0) =  2
iseed, nsims =          -40    5
-----------------------------------------------
input hypocenter at position    =  -1.000E+00 -1.000E+00
input hypocenter at subfault    =    0    0
n_hypocenters     =    2
Mag.                      =       8.00
-----------------------------------------------
dt (sec)                  =     0.0100
beta (km/s)               =       3.70
density (rho), gr/cm3     =       2.80
prtitn                    =       0.71
rtp                       =       0.55
fs                        =       2.00
pulsing Percentage        =      50.00
iflagscalefactor (1=vel^2; 2=acc^2;  3=asymptotic acc^2 (dmb)) = 2
flocut, nslope            =     0.000  8
iflagfas_avg              = 3
iflagpsa_avg_over_hypos   = 2
iflagpsa_avg_over_sims    = 1
stress parameter (bars)   =     140.00
fmax                      =       0.00
kappa                     =     0.0050
-----------------------------------------------
Corner Frequency
Dynamic Corner Frequency Flag is  ON =     1
-----------------------------------------------
fr1, qr1, s1q, ft1, ft2, fr2, qr2, s2q, c_q, qt1, stq  =
1.00000000 1000.00000 0.00000000E+00 1.42420006 1.42420006 1.00000000 893.000000 0.319999993
3.70000005 1000.00000 0.00000000E+00
Path duration: ndur_hinges, rpathdur, pathdur, durslope:
4
0.0    0.00
10.0    0.00
70.0    9.60
130.0    7.80
0.040
gspread: i, nsprd_segs, r_ref, rlow, a_s, b_s, m_s
1 3 1.00000000 1.00000000 -1.29999995 0.00000000E+00 6.50000000
2 3 1.00000000 70.0000000 0.200000003 0.00000000E+00 6.50000000
3 3 1.00000000 140.000000 -0.500000000 0.00000000E+00 6.50000000
-----------------------------------------------
window applied               = Saragoni-Hart
-----------------------------------------------
Crustal amps from file crustal_amps_sample.txt
freq      amp
0.500   1.000
1.000   1.130
2.000   1.220
5.000   1.360
10.000   1.410
-----------------------------------------------
site amps from file site_amps_sample.txt
freq      amp
```

```
1.000   1.000
----------------------------------------------
----------------------------------------------
Analytical Pulse parameters
----------------------------------------------
Analytical Flag is  OFF   =     0
tpadl, tpadt, dt(sec)                        :    50.000    20.000     0.010
For site   1 siteLocation coordinates 1&2 =     98.12     0.71
For site   2 siteLocation coordinates 1&2 =    105.90     8.49
Site may have been moved to midpoint or end of surface projection of upper edge of fault
For site   1 elapsed time (sec) = 183.27
For site   2 elapsed time (sec) = 183.36
```

Table 5-5. Source parameters of the small event and the main shock

	Source	Origin Time (UT)	Latitude	Longitude	Depth (km)	M	Strike (°)	Dip (°)	Rake (°)	M_0 (N.m)
Small Event	JMA[*]	2011/03/09 21:23:59.00	38.1722	143.0448	9.30	6.8				
	Manual[**]				20.00	6.5	22 ; 213	68 ; 23	85 ; 101	5.51E+18
Main Shock	JMA[*]	2011/03/11 05:46:18.12	38.1035	142.8610	23.74	9.0				
	Manual[**]				20.00	8.7	22 ; 200	63 ; 27	91 ; 88	1.07E+22

[*]JMA: Japan Meteorological Agency
[**]Manual: From F-net website, *http://www.fnet.bosai.go.jp/top.php*

179

Table 5-6. Locations of the selected station from KiK-net

	Site Code	Site Name	Latitude	Longitude	Altitude (m)	Depth (m)
1	AKTH01	NISHIKI-N	39.8147	140.5790	318	100
2	AKTH02	NISHIKI-S	39.6634	140.5721	95	100
3	AKTH06	OGACHI	38.9801	140.4952	285	100
4	AKTH19	YUZAWA	39.1913	140.4710	74	180
5	IWTH12	KUNOHE	40.1533	141.4245	365	100
6	MYGH02	NARUKO	38.8587	140.6513	345	203
7	YMTH02	YAMAGATA	38.2693	140.2583	130	150
8	YMTH07	YONEZAWA	37.8960	140.0278	352	200
9	YMTH14	NISHIKAWA-W	38.3860	139.9916	465	103
10	YMTH15	NISHIKAWA-E	38.4257	140.1249	305	100

Table 5-7. Comparison between the durations of synthetics and observed recording at the three selected stations

	$D'_{95\text{-}5}$ (sec)	
Stations	Observed	Synthetics
AKTH19	143.60	134.80
YMTH14	147.18	162.01
YMTH15	129.04	147.60

5.5 Figures
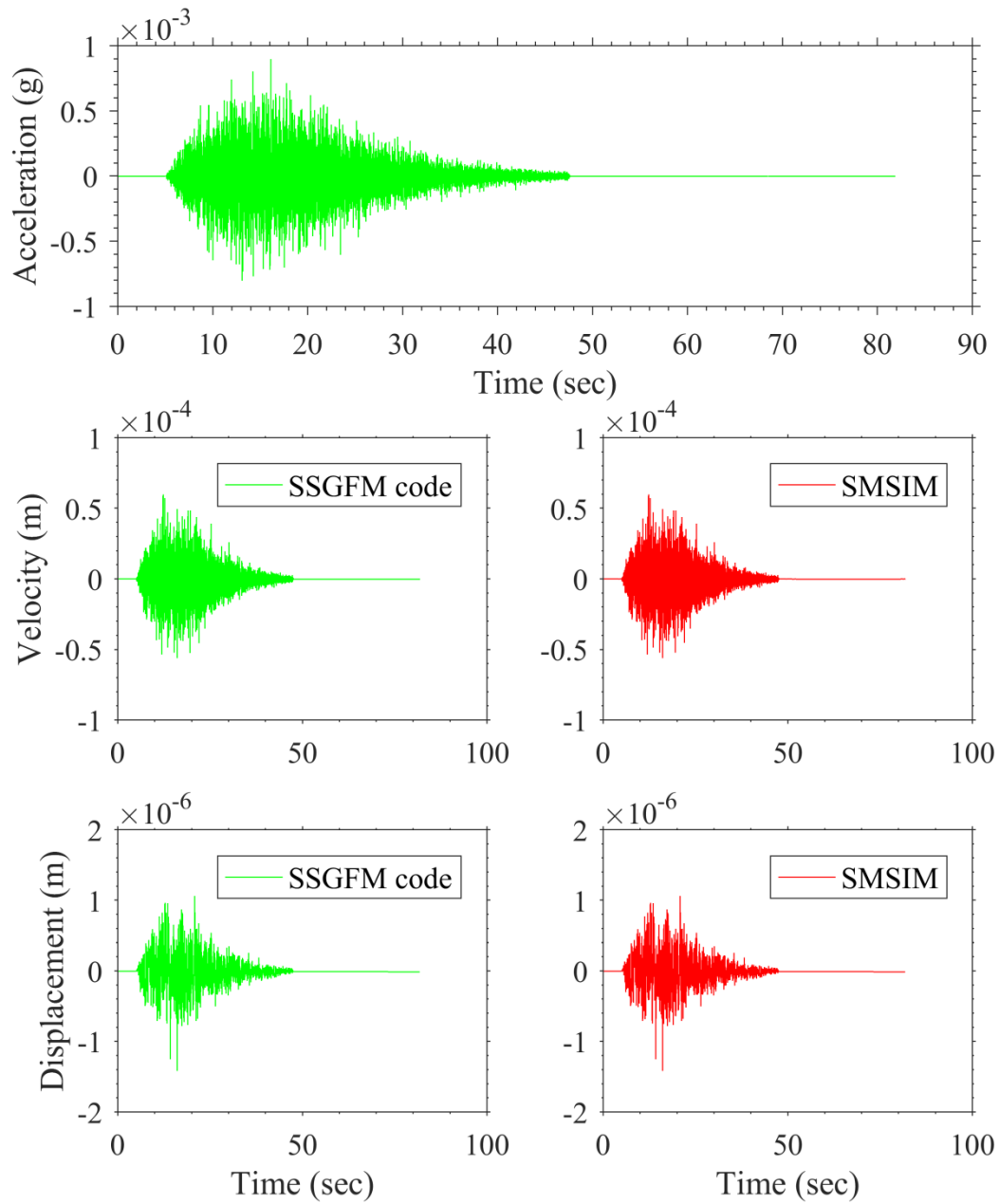
Figure 5-1. Time series for an **M** 3.0 earthquake following a SCF source model for use as EGF
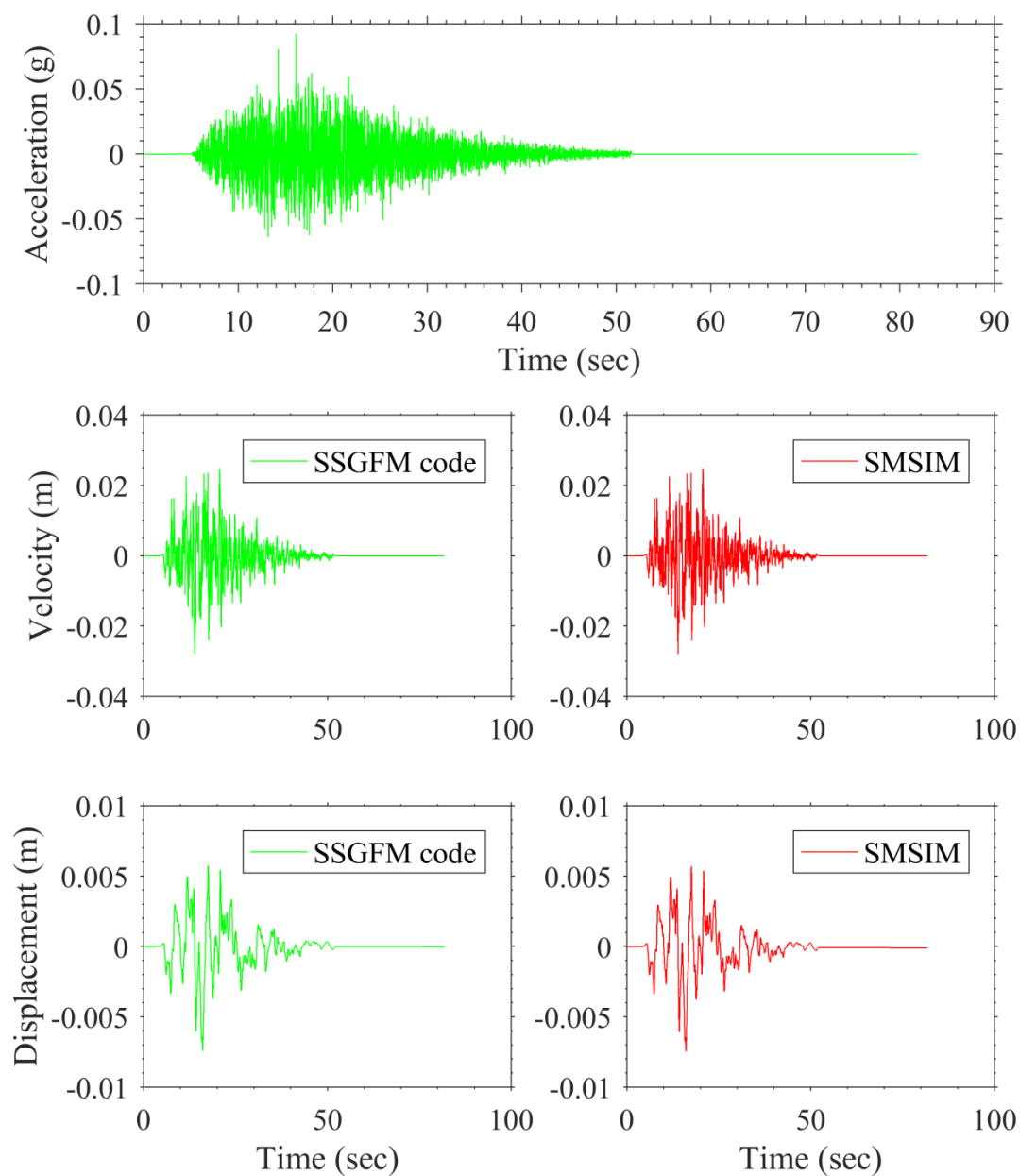
Figure 5-2. Time series for an **M** 6.0 earthquake following a SCF source model for use as target
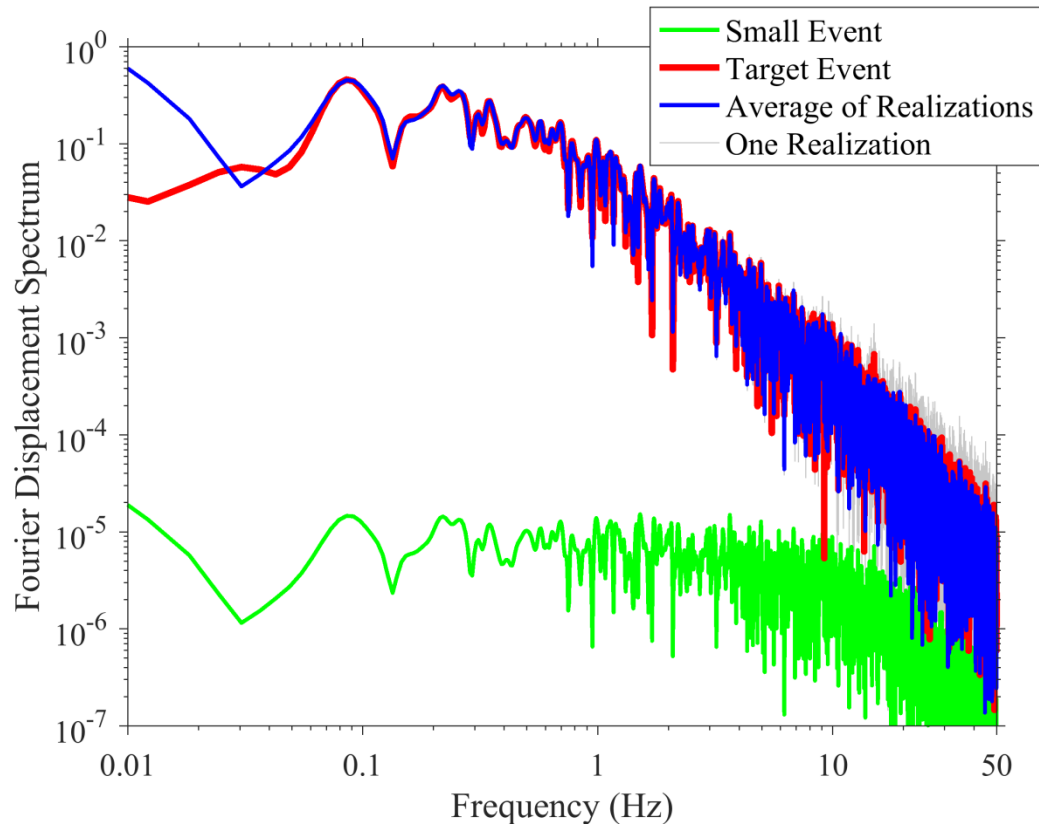
Figure 5-3. Comparison of the FASs of the target event, each realization, and the average for a SCF source model using the TSP1 scheme

Figure 5-4. Comparison of the response spectra computed from the target event, each realization, and the average for a SCF source model using the TSP1 scheme
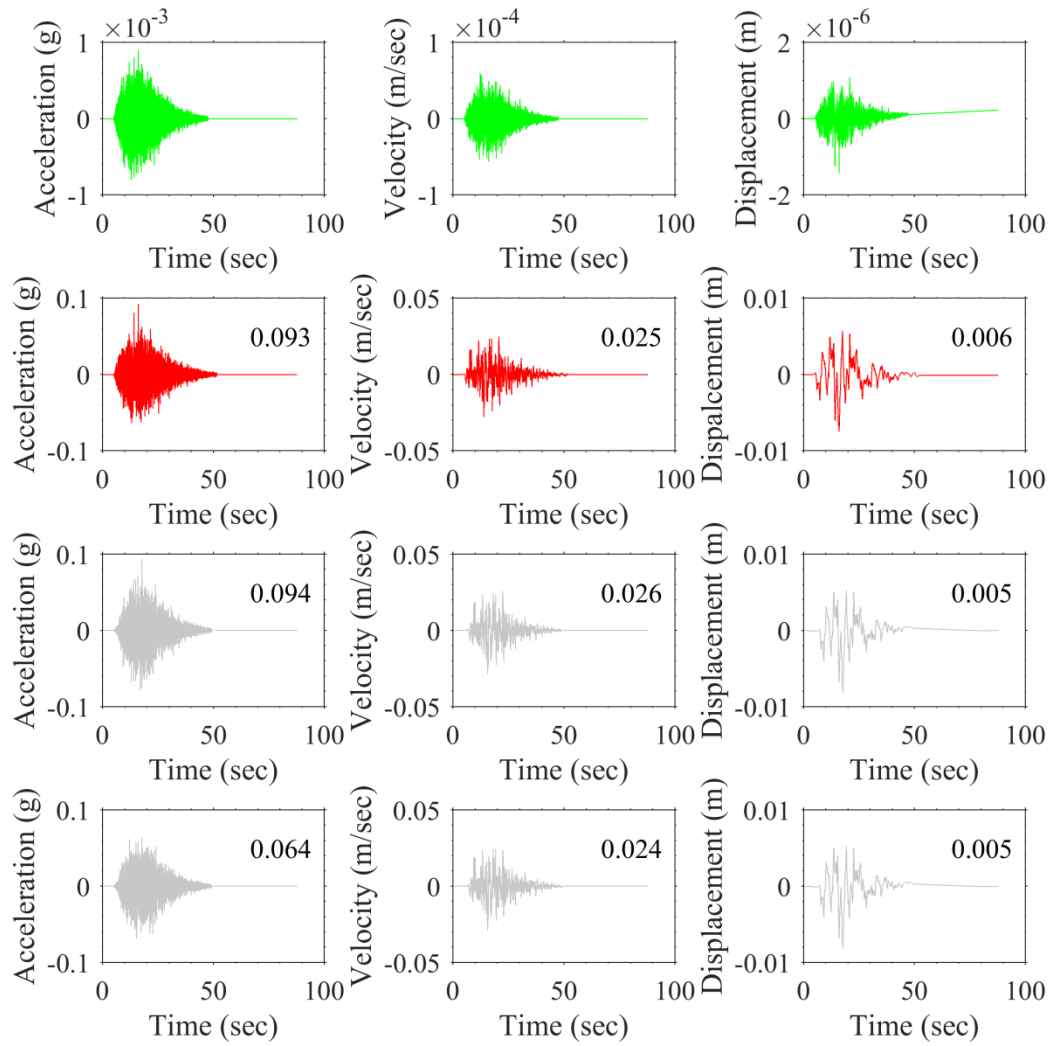
Figure 5-5. EGF, target event, and two synthetic time series for a SCF source model using the TSP1 scheme. Values on the plots represent the peak value.
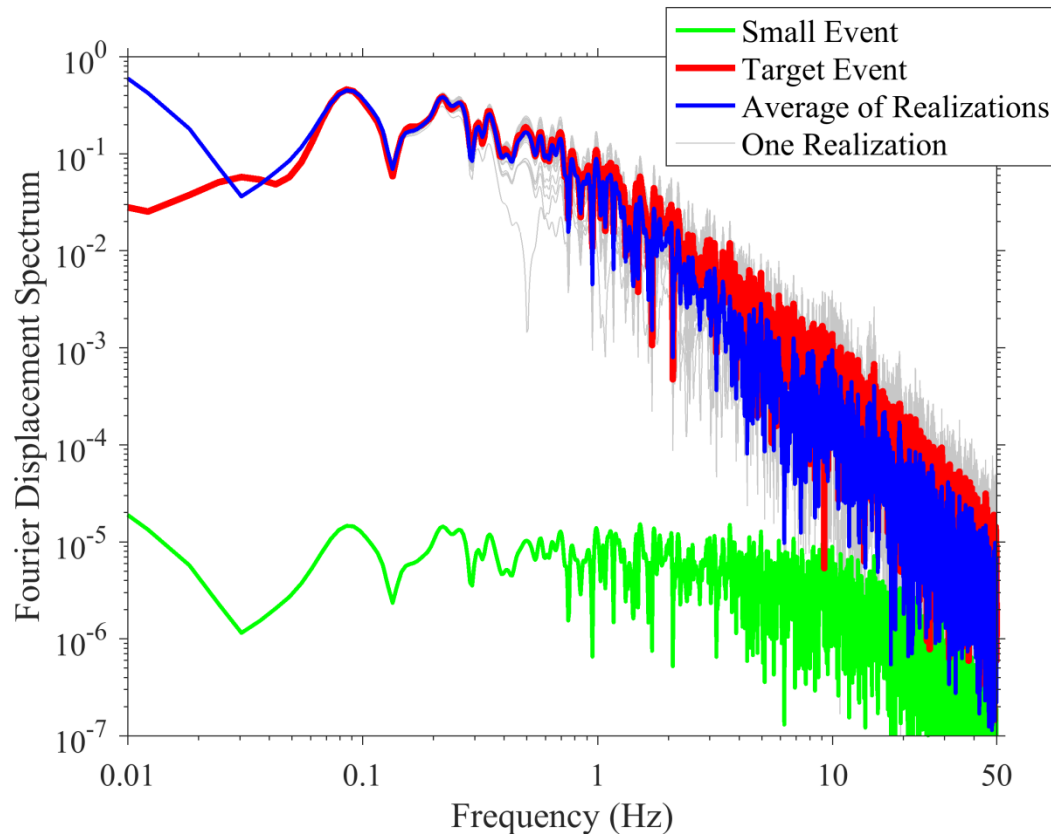
Figure 5-6. Comparison of the FASs of the target event, each realization, and the average for a SCF source model using the TSP2 scheme

Figure 5-7. Comparison of the response spectra computed from the target event, each realization, and the average for a SCF source model using the TSP2 scheme
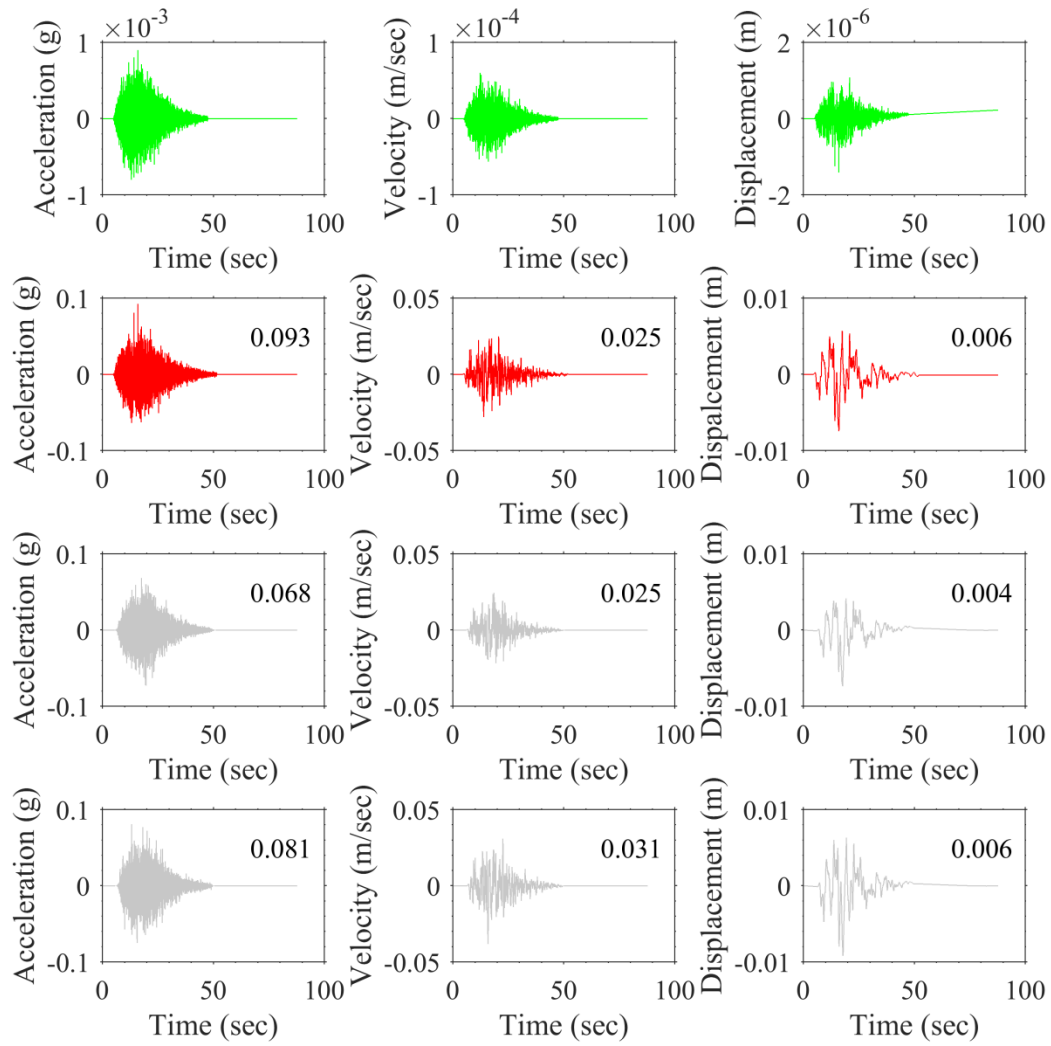
Figure 5-8. EGF, target event, and two synthetic time series for a SCF source model using the TSP2 scheme. Values on the plots represent the peak value.
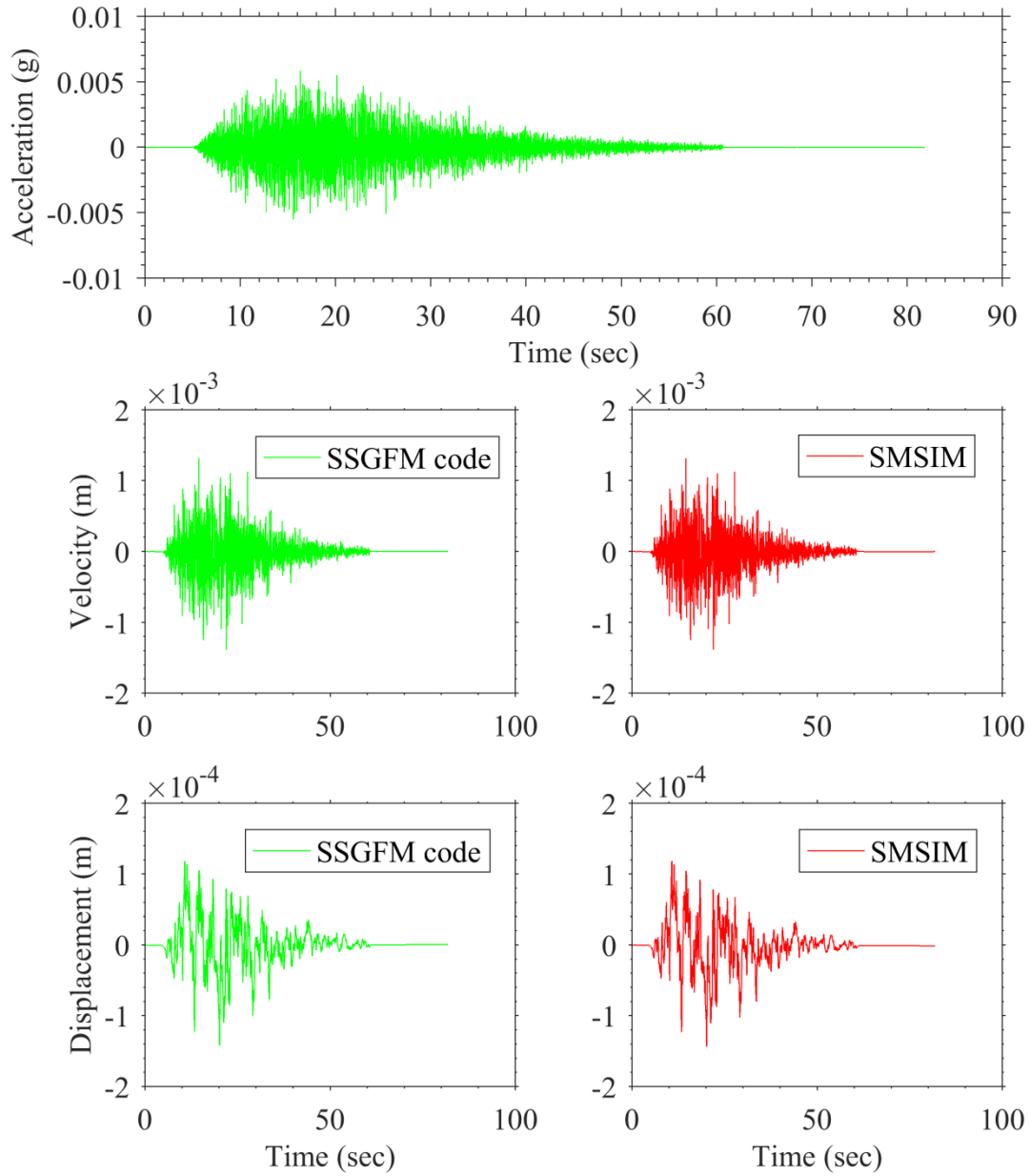
Figure 5-9. Time series for an **M** 5.0 earthquake following a DCF source model for use as EGF
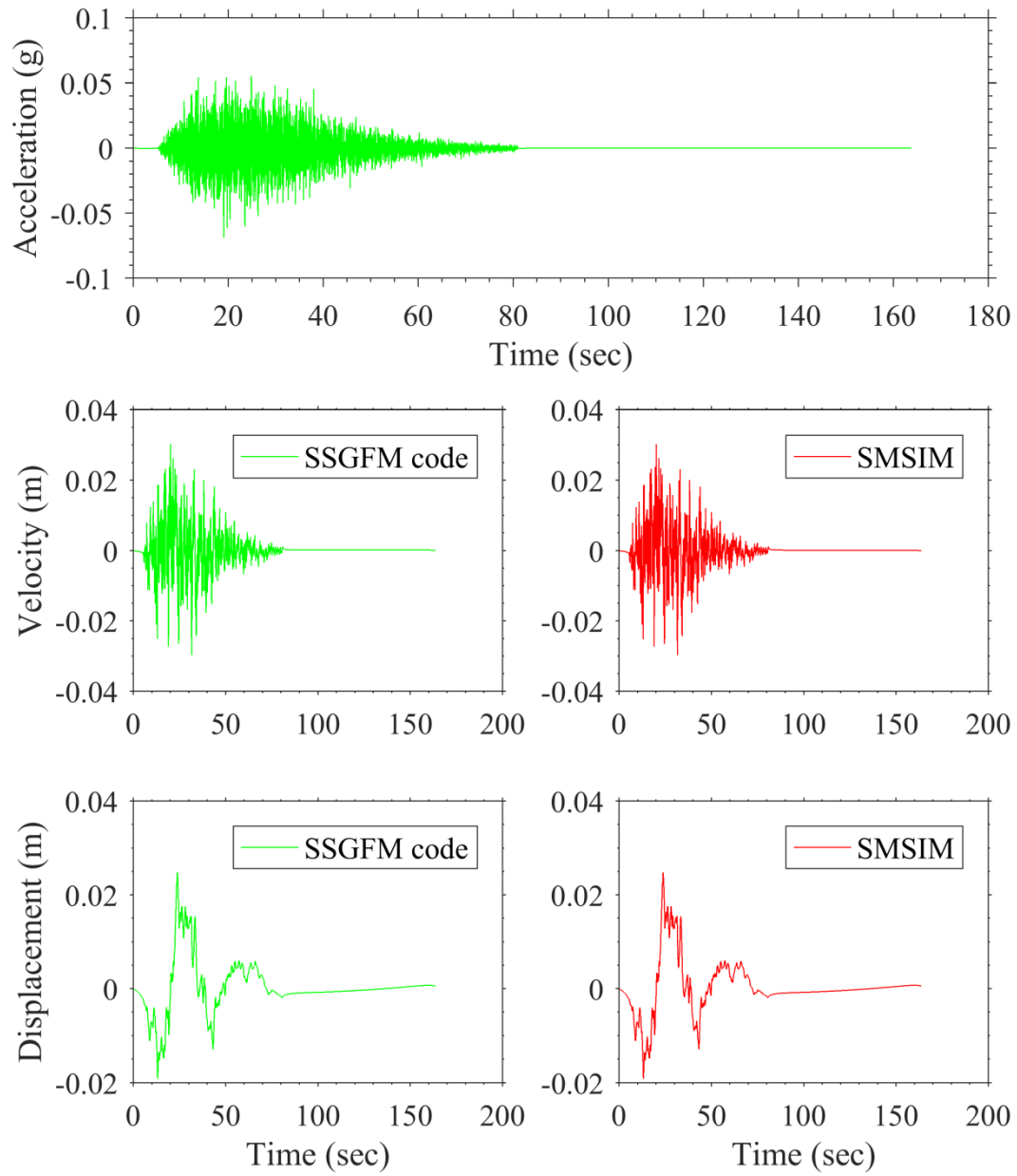
Figure 5-10. Time series for an **M** 7.0 earthquake following a DCF source model for use as target
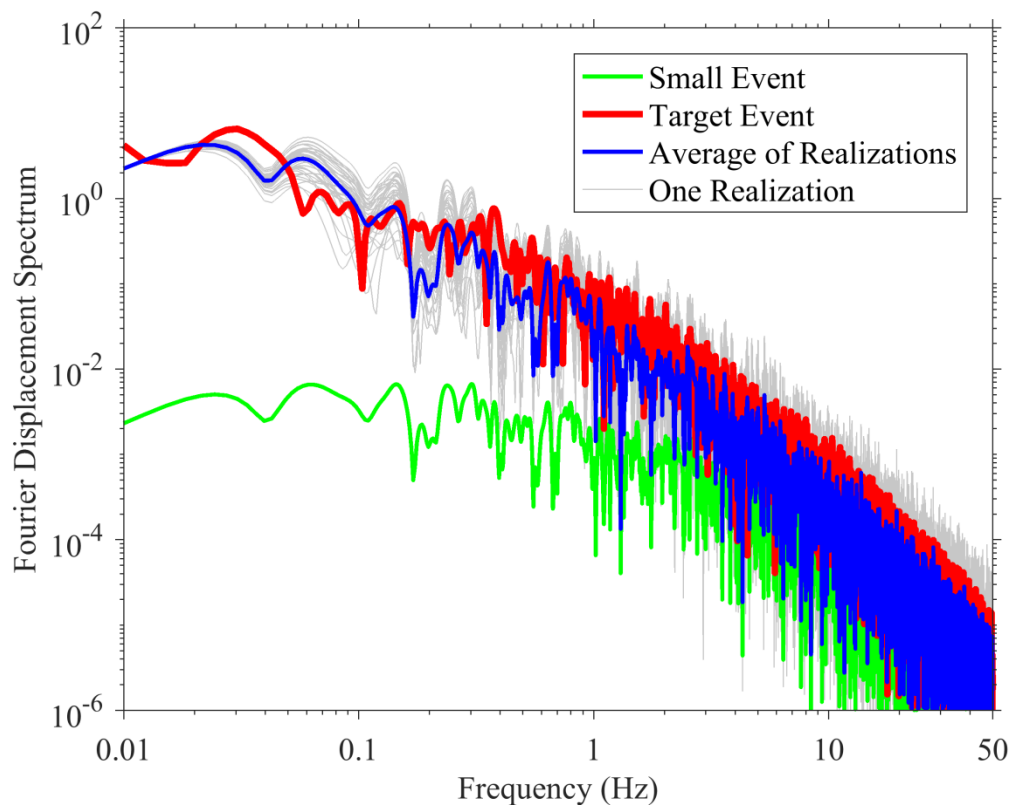
Figure 5-11. Comparison of the FASs of the target event, each realization, and the average for a

DCF source model using the TSP2 scheme
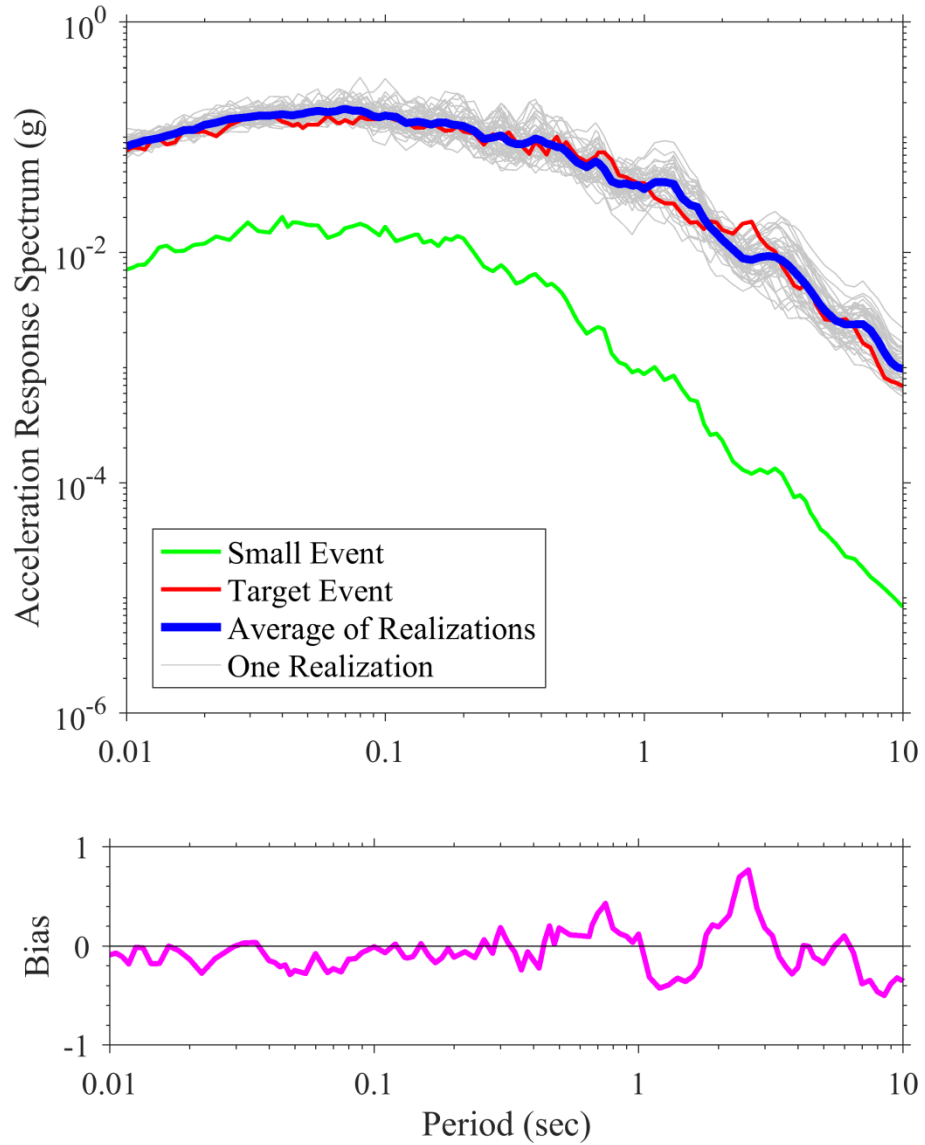
Figure 5-12. Comparison of the response spectra computed for the target event, each realization, and the average for a DCF source model using the TSP2 scheme
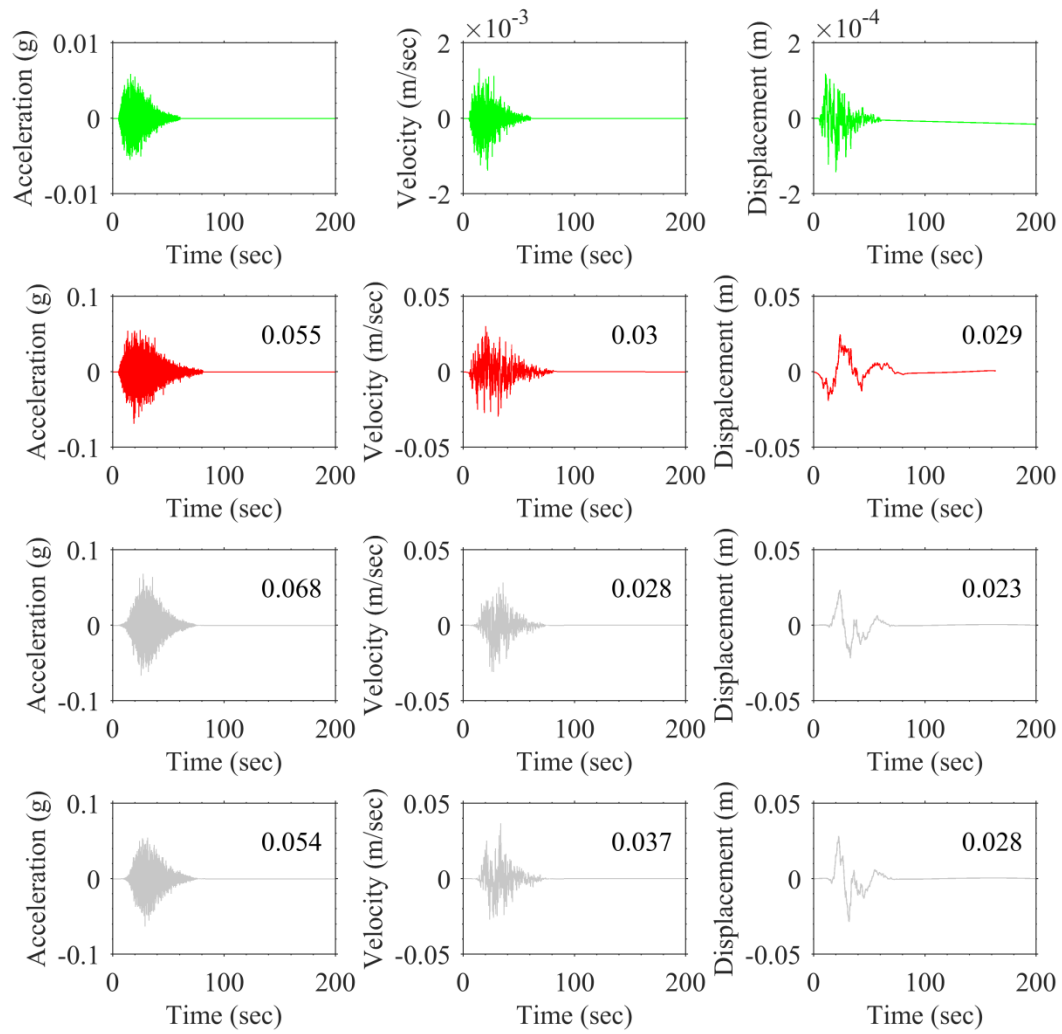
Figure 5-13. EGF, target event, and two synthetic time series for a DCF source model using the TSP2 scheme. Values on the plots represent the peak value.
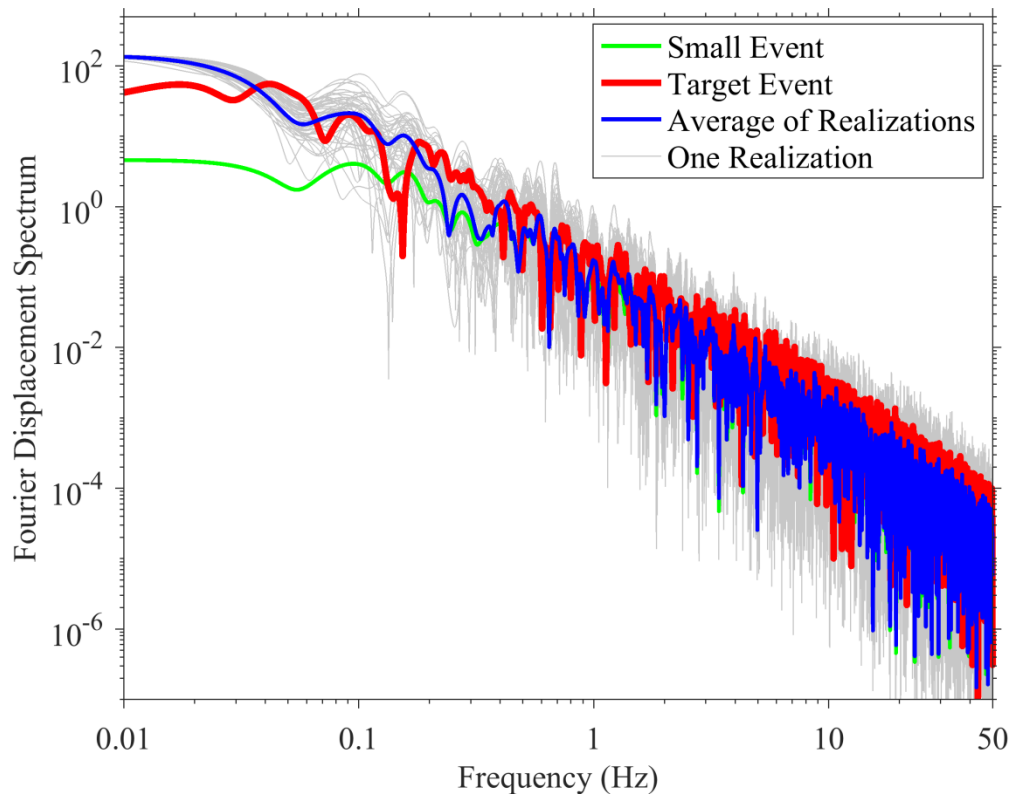
Figure 5-14. Comparison of the FASs of the target event generated using EXSIM, each realization, and the average for a SCF source model using the TSP2 scheme
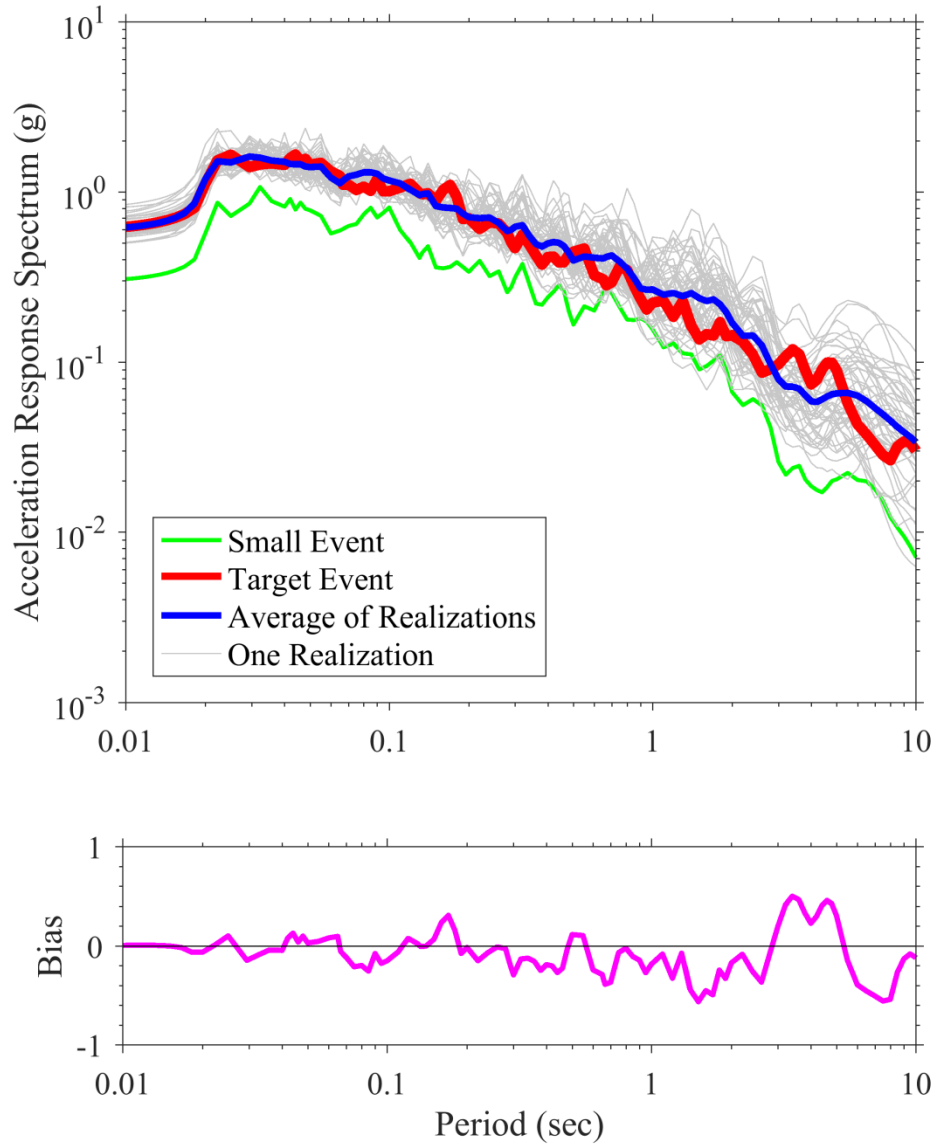
Figure 5-15. Comparison of the response spectra computed for the target event generated using EXSIM, each realization, and the average for a SCF source model using the TSP2 scheme
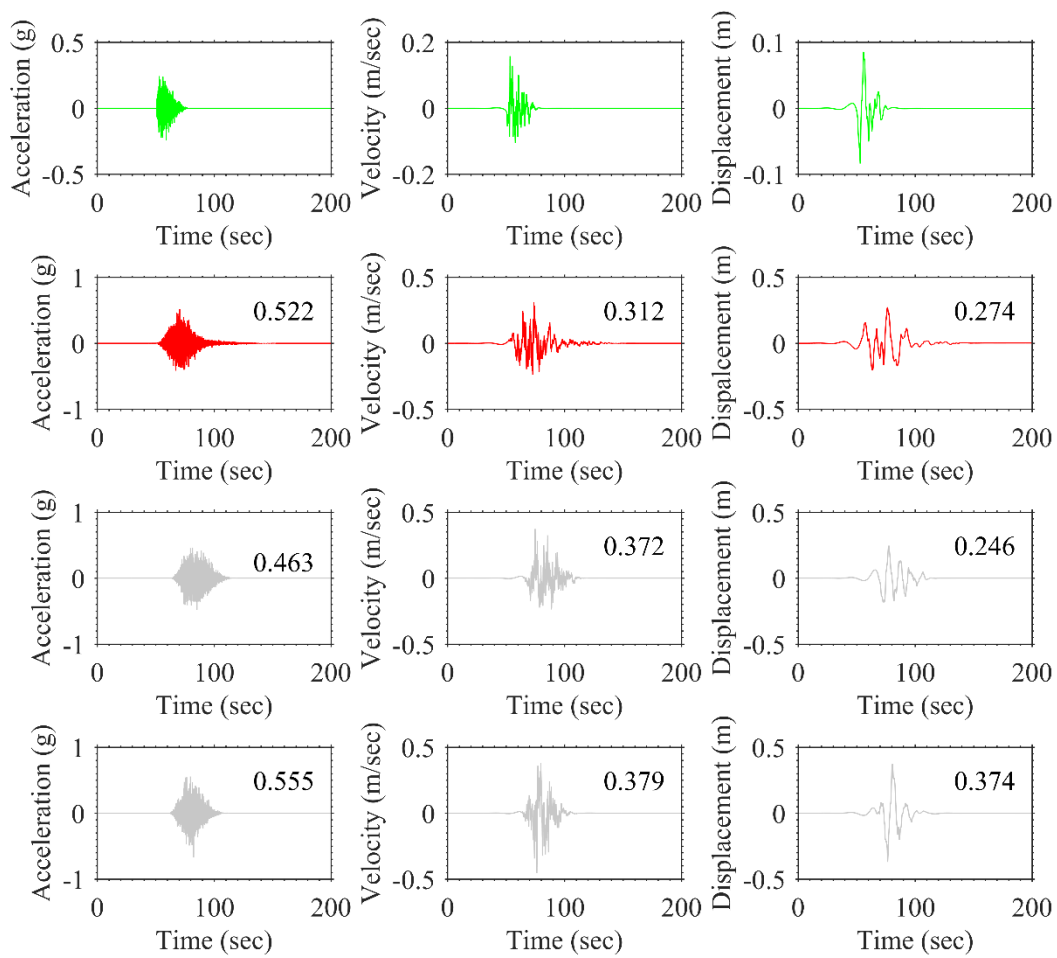
Figure 5-16. EGF, target event generated using EXSIM, and two synthetic time series for a SCF source model using the TSP2 scheme. Values on the plots represent the peak value.
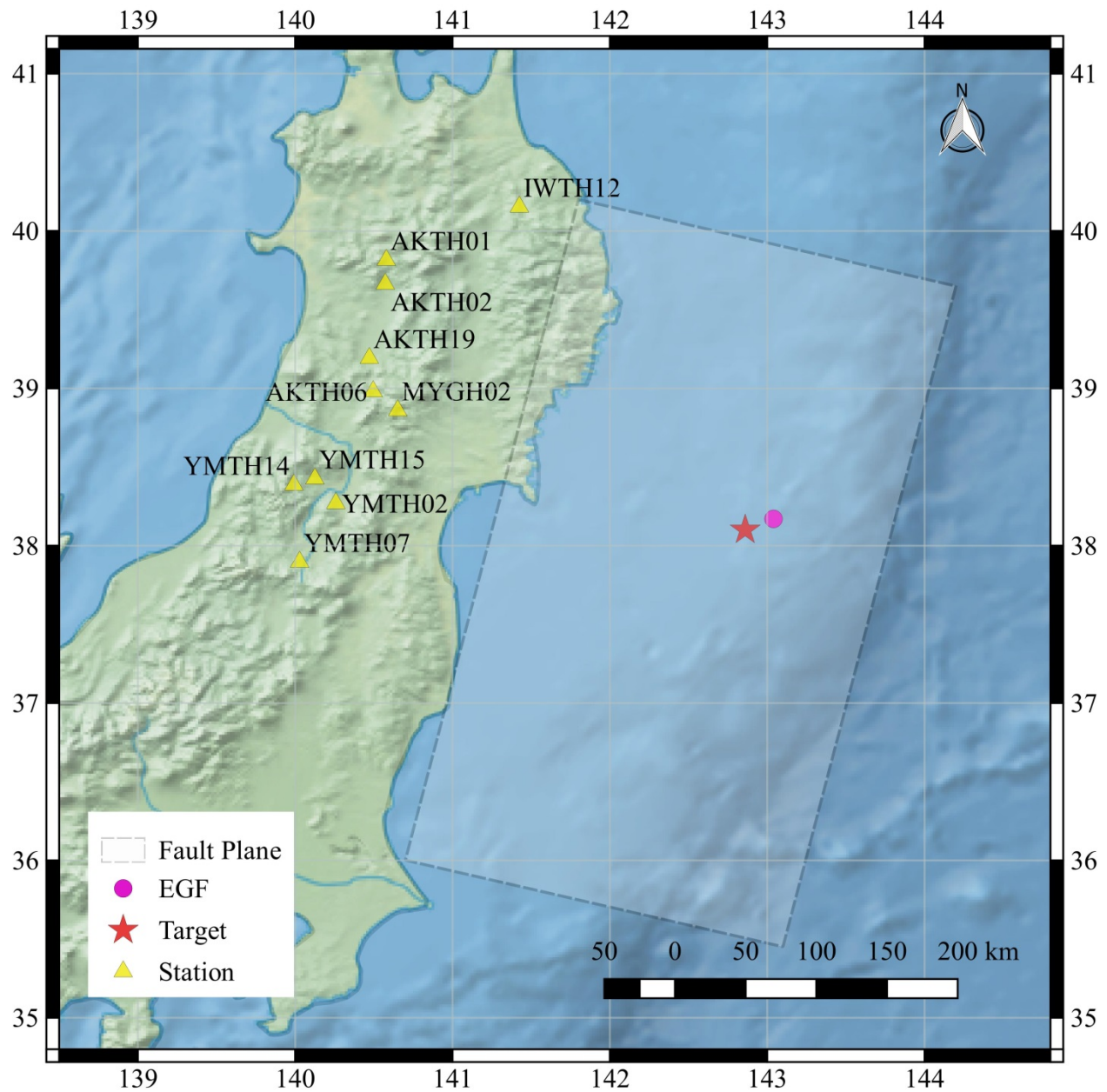
Figure 5-17. Map showing the location of the selected KiK-net stations and fault plane of the target event as well as the location of the epicenter of the target event and EGF (this plot is generated using QGIS 2.18.12)
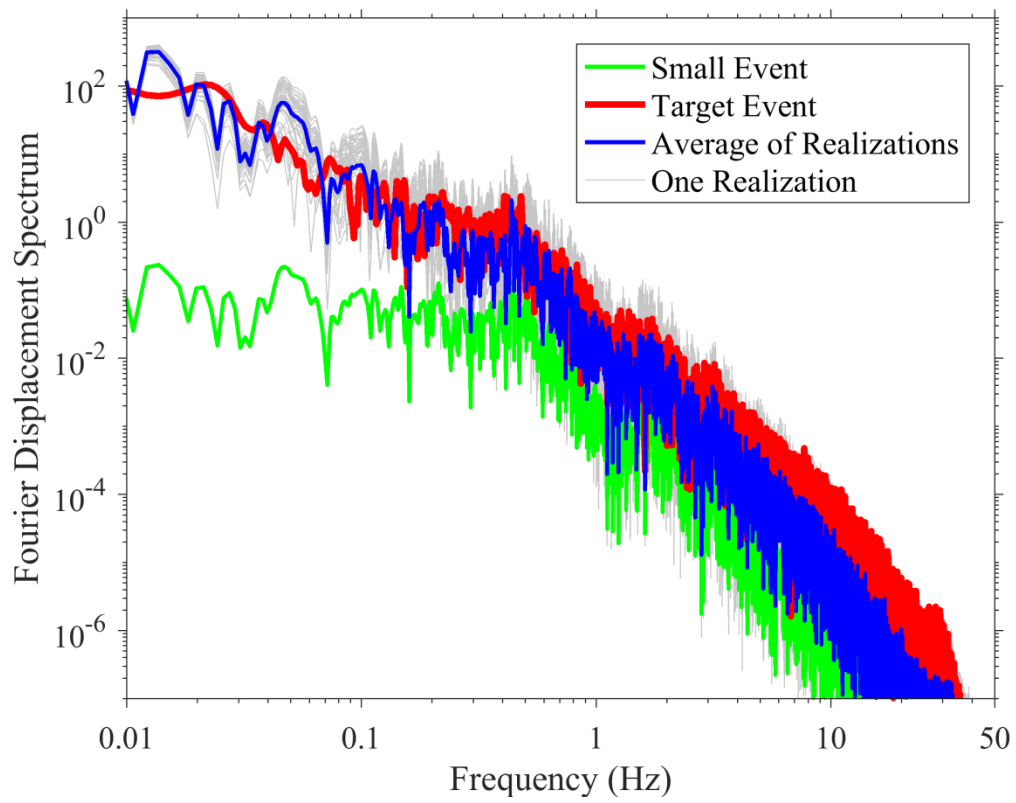
Figure 5-18. Comparison of the FASs of the target event, each realization, and the average from waveforms captured at AKTH19 (N-S direction)
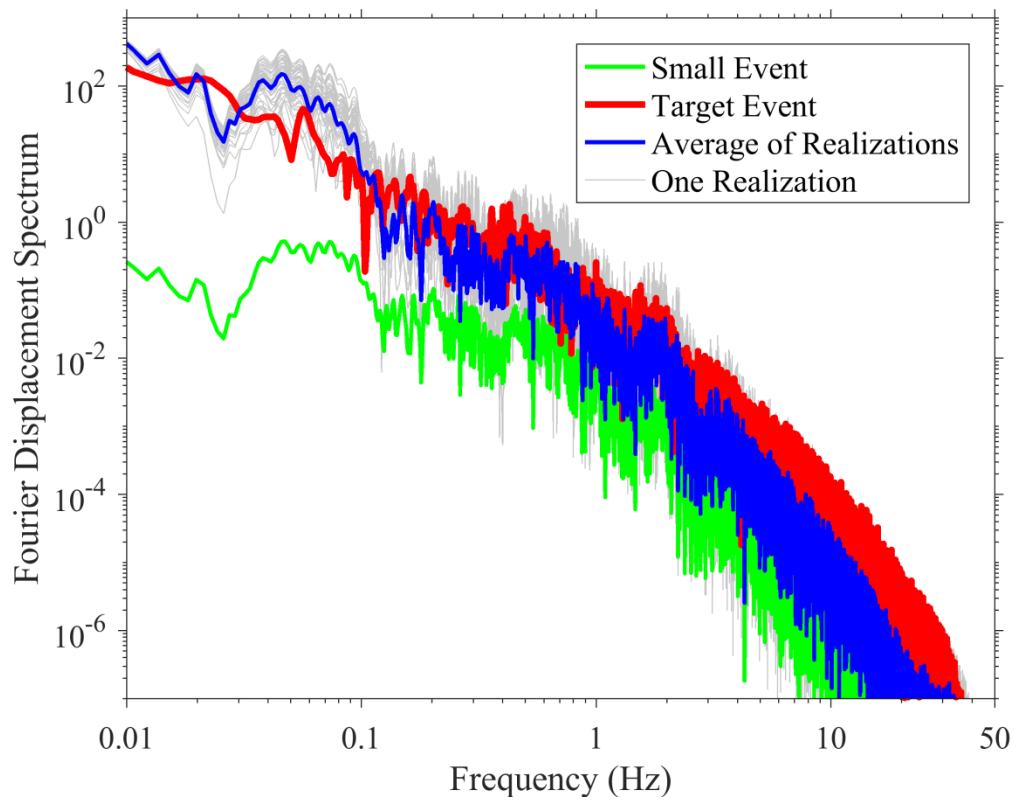
Figure 5-19. Comparison of the FASs of the target event, each realization, and the average from waveforms captured at YMTH14 (E-W direction)
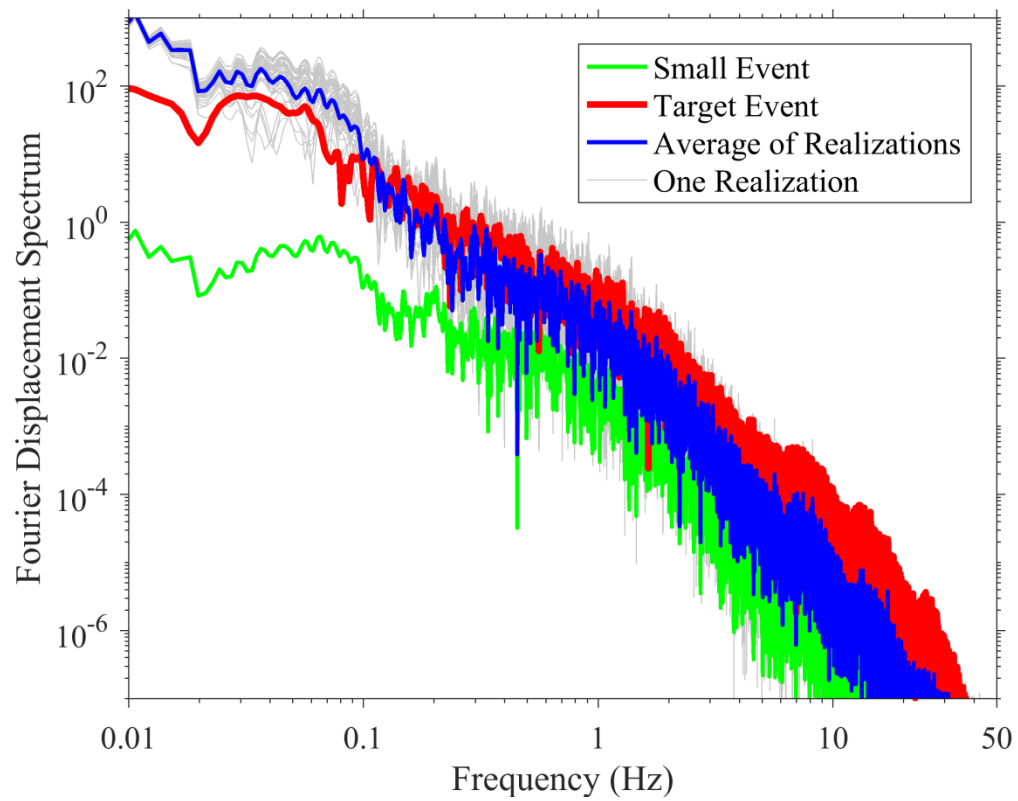
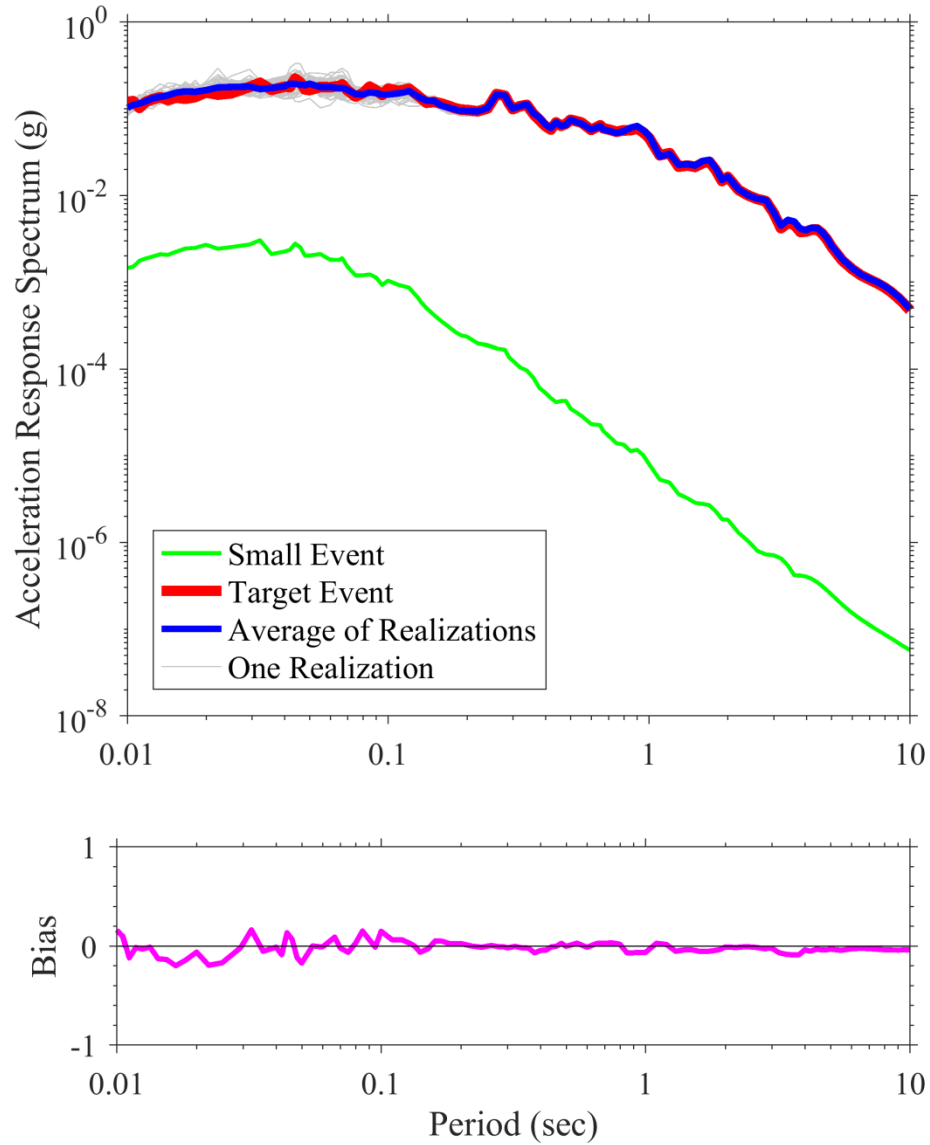Figure 5-20. Comparison of the FASs of the target event, each realization, and the average from waveforms captured at YMTH15 (vertical direction)
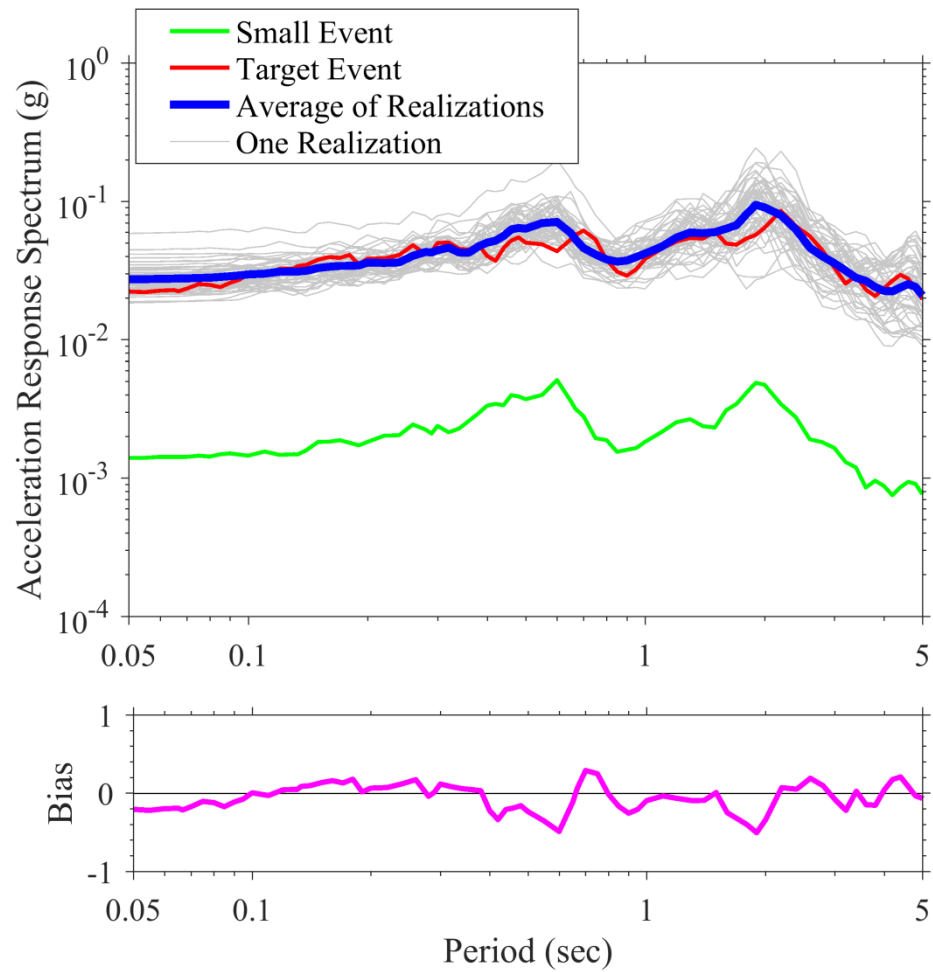
Figure 5-21. Comparison of the response spectra computed for the target event, each realization, and the average from waveforms captured at AKTH19 (N-S direction)
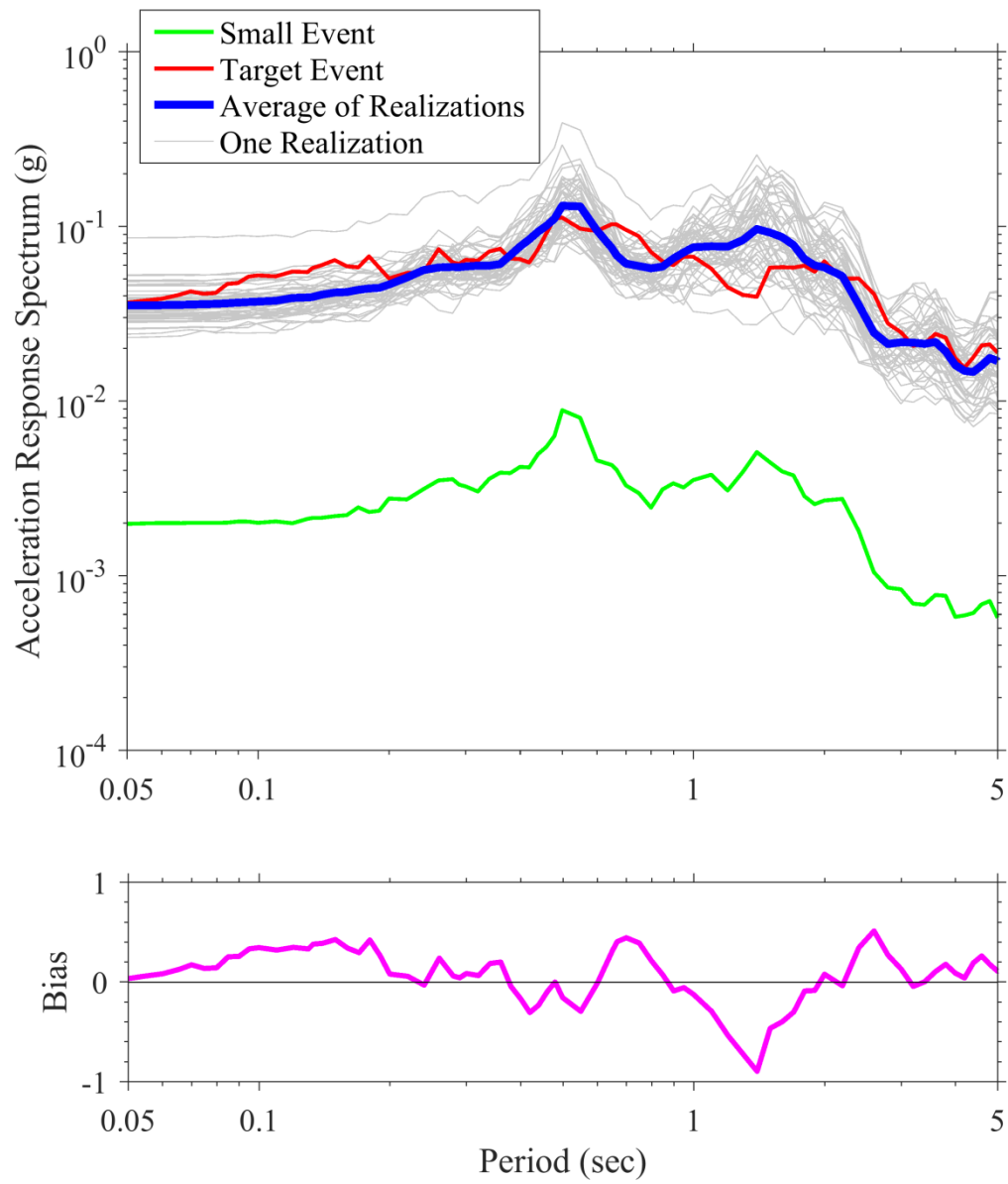
Figure 5-22. Comparison of the response spectra computed for the target event, each realization, and the average from waveforms captured at YMTH14 (E-W direction)
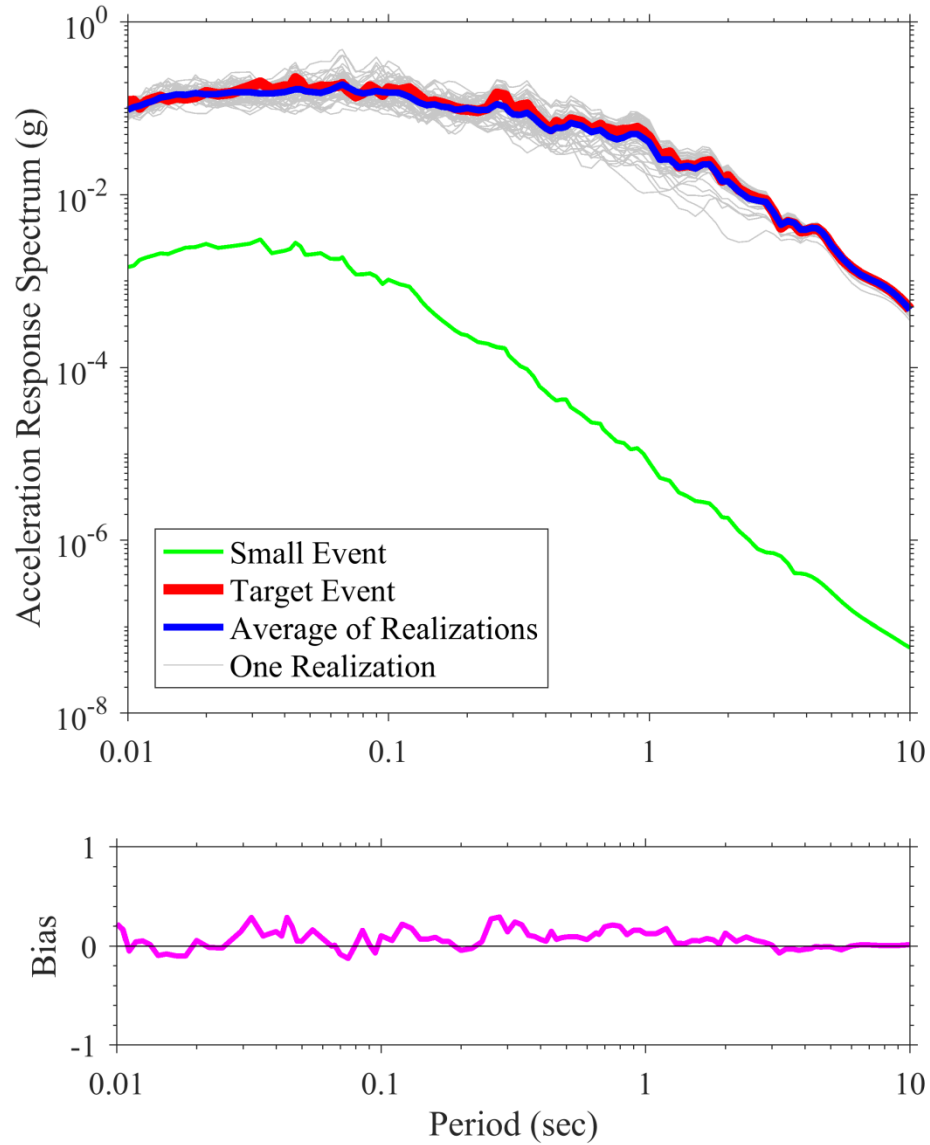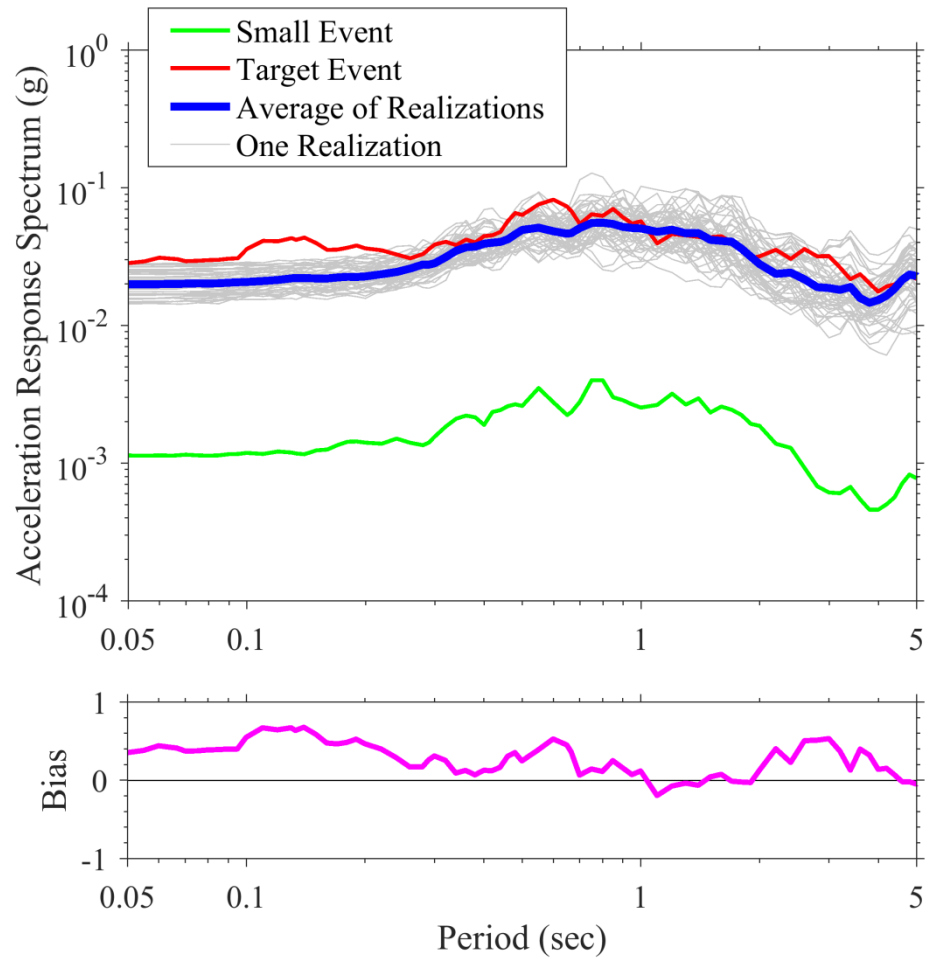
Figure 5-23. Comparison of the response spectra computed for the target event, each realization, and the average from waveforms captured at YMTH15 (vertical direction)
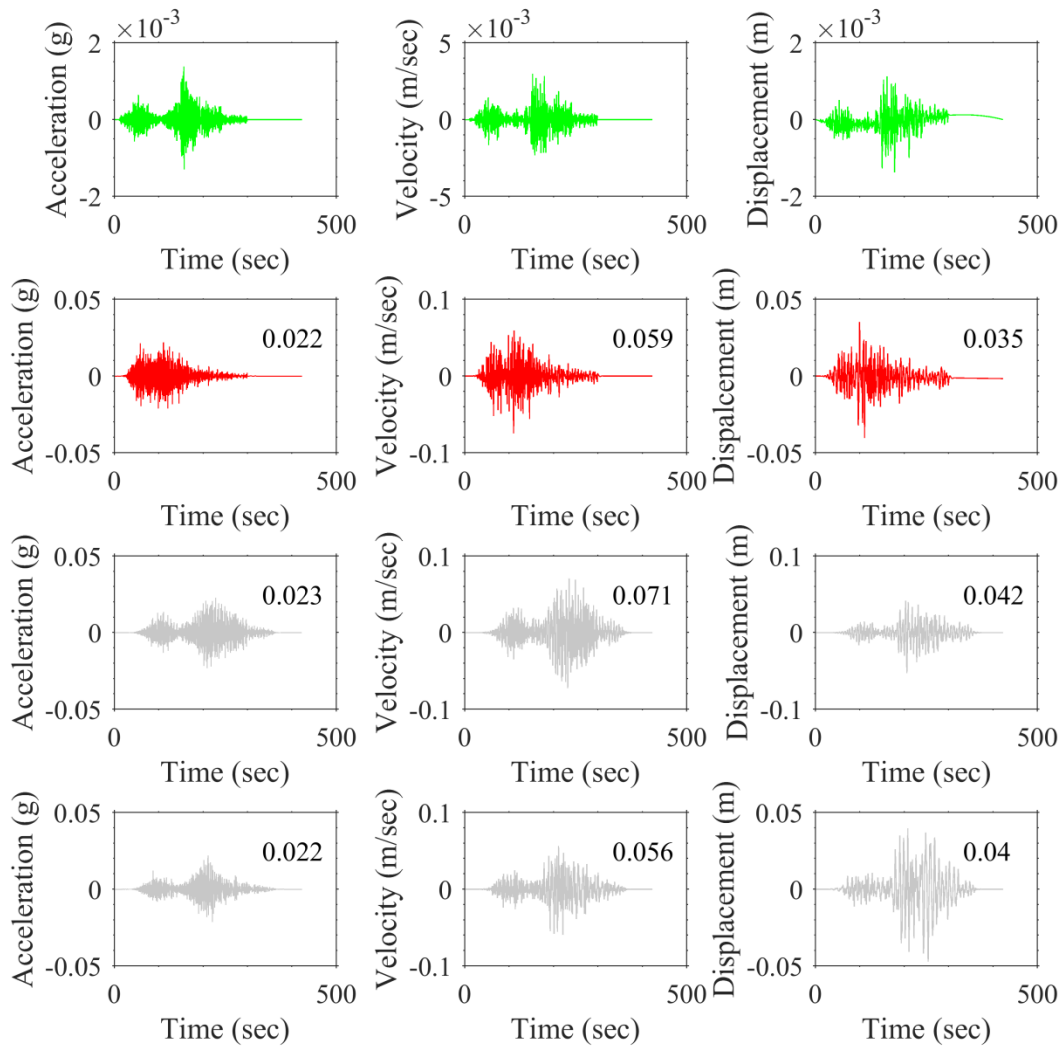
Figure 5-24. EGF, target event, and two synthetic time series from waveforms captured at AKTH19 (N-S direction). Values on the plots represent the peak value.
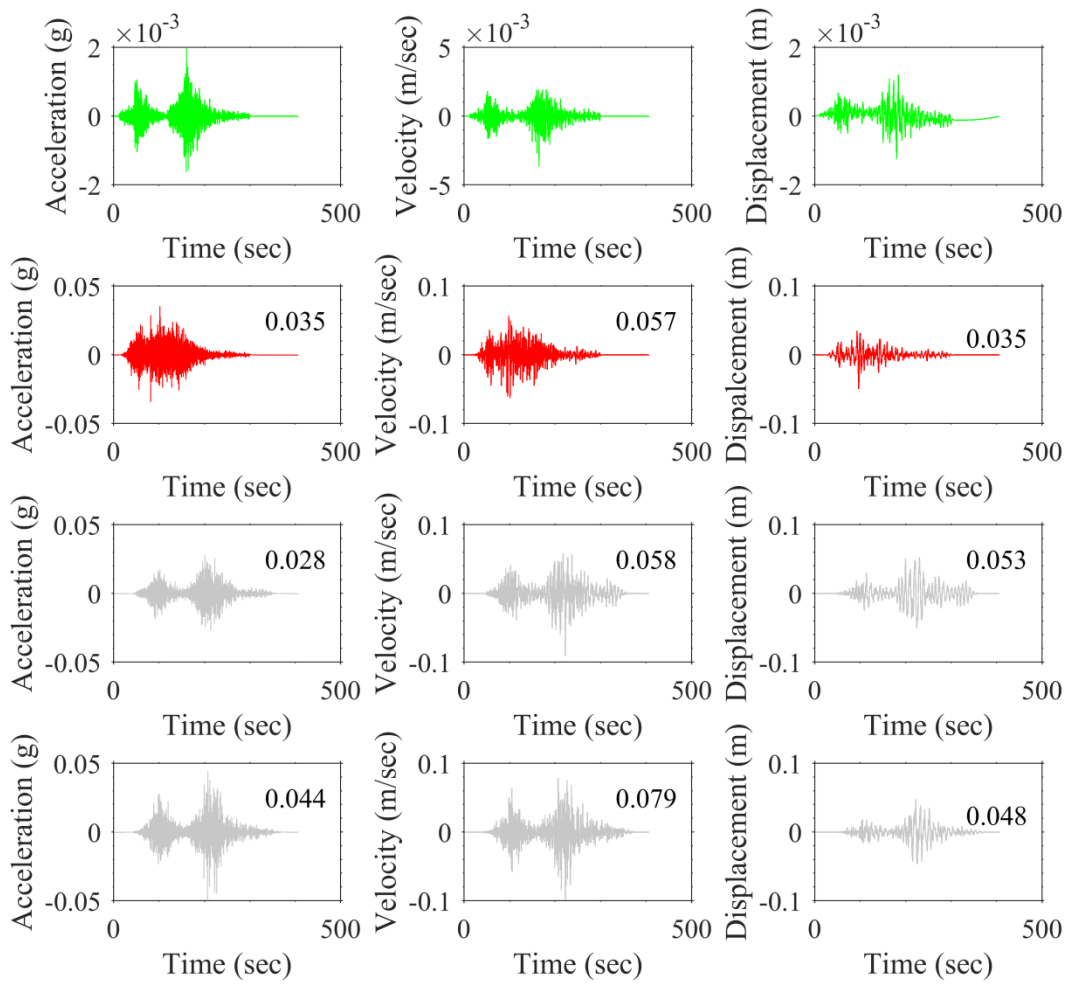
Figure 5-25. EGF, target event, and two synthetic time series from waveforms captured at YMTH14 (E-W direction). Values on the plots represent the peak value.
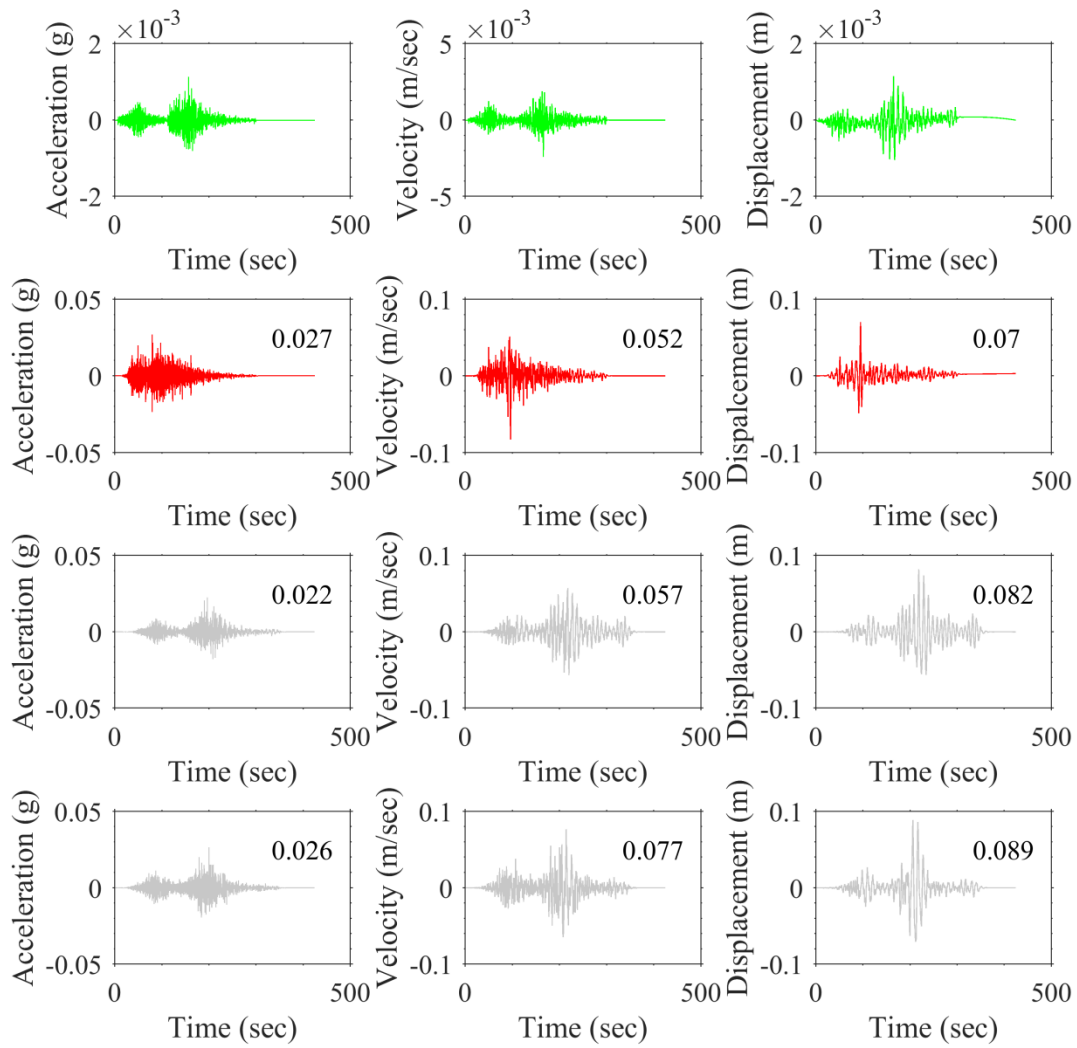
Figure 5-26. EGF, target event, and two synthetic time series from waveforms captured at YMTH15 (vertical direction). Values on the plots represent the peak value.
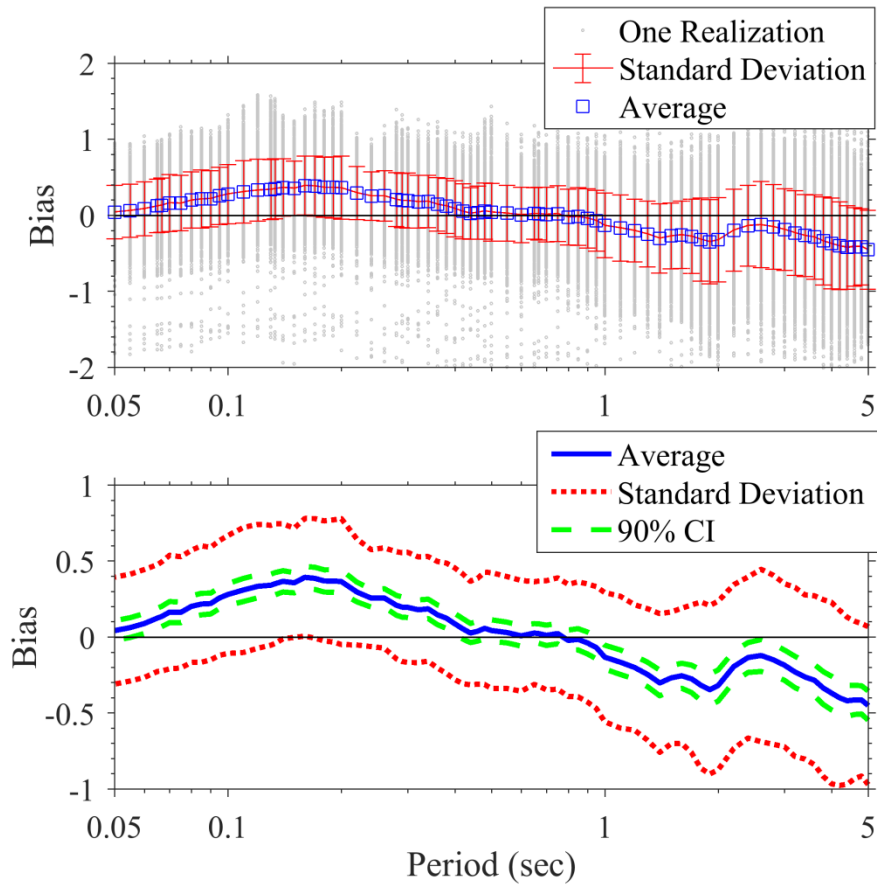
Figure 5-27. Average bias and its uncertainty over all 1500 simulations. CI: confidence interval.

6. An Application to Central and Eastern North America (CENA) and Development of Ground Motion Prediction Equations for This Region

6.1 Introduction

Due to the low level of seismicity in central and eastern North America (CENA), the database for this region is not robust in terms of magnitude and distance, particularly for large magnitudes and close distances. Therefore, a significant issue exists in selecting appropriate ground motions for structural design and development of ground motion prediction equations (GMPEs) in this region. Employing synthetic ground motions generated based on the seismological characteristics of CENA is one of the solutions for this issue.

The main objective of this chapter is to provide peak ground velocity (PGV), peak ground acceleration (PGA), and 5%-damped pseudo-spectral acceleration (PSA) values at spectral periods of 0.01 to 10 sec and to develop GMPEs for CENA. To achieve this goal, the geological and seismological characteristics of this region is used to construct region-specific input ground motions into the SSGFM code instead of using site-specific observed ground motions. The region-specific synthetics, generated using SMSIM, are then employed as input Green's functions (GF) into the SSGFM code. Using the improved SSGFM code considering the effective distance, the effects of finite-fault geometry as well as rupture propagating and rupture inhomogeneity are taken into account.

In the following page, a detailed discussion is provided on why the point-source stochastic simulation of Boore (2003) is used to generate GFs. The Southern California Earthquake Center (SCEC) broadband platform validation committee compared 5 different finite-fault simulation approaches. These 5 models are listed in Table 6-1. Based on the results shown in Figure 6-1 and Figure 6-2, it can be concluded that although all methods, except EXSIM, are assumed to generate broadband synthetics, all of them, except EXSIM, failed in validation exercises at long periods (Goulet *et al*., 2014; Dreger *et al*., 2014). The SCEC validation exercise-part B considered 12 well-recorded earthquakes (7 in CA, 2 in Japan, and 3

in ENA) to compare 5 simulation methods. Figure 6-1 shows the bias normalized with the GMPEs' predictions presenting the performance of each model for the selected earthquakes at different periods and distance ranges. All simulation methods mostly produce fail conditions for the distance range of 0 to 5 km. Also, bias increases with increasing period. However, EXSIM noticeably works better than the other simulation methods. This is very interesting since other methods are supposed to produce more accurate broadband ground motions at low frequencies, not overestimating the median PSAs. But EXSIM, which is developed based on a bandlimited stochastic white noise method, produces better results at low frequencies compared to physic-based and hybrid methods (see Figure 6-2). It should be mentioned that EXSIM constructs weak motions using the similar procuedure used in SMSIM and then scales and shifts the weak motions to generate large earthquake time series. The second reason to use SMSIM for simulating weak motions instead of other methods is that for small events in which the length and width of the faults is small, even a close distance site can be considered as far-field. Therefore, using SMSIM to generate weak motions as input ground motions in the SSGFM code is reasonable. The third reason is that the SSGFM itself cannot capture the effect of directivity and it just accumulates the effect of directivity if it exists in the simulated ground motions through summation. Therefore, if we include directivity effect in the input weak motion, all large earthquake simulations would be biased and they do not reflect the average trend.

Regarding these 3 reasons, weak motions for CENA using SMSIM is generated first. Then, these weak motions are used as input GFs to the improved SSGFM code to synthesize strong ground motions. From the simulated time series, PGV, PGA, and PSA values are calculated and these values are compared and validated with the predicted PGA and PSA values from GMPEs developed for CENA. Finally, a new suite of GMPEs for this region are developed. The simulated time histories can be employed for nonlinear structural analysis and performance-based design applications. The developed GMPEs can be used for seismic hazard analysis for CENA.

6.2 Simulation of Synthetic Seismograms for CENA

The latest version of SMSIM is used to generate region-specific stochastic simulations for **M**3.5, **M**4.0, and **M**4.5 events at 26 equivalent point-source (effective point-source) distances

of 9.2, 10, 11, 12.5, 14, 15, 20, 25, 30, 40, 50, 60, 70, 80, 100, 120, 150, 200, 250, 300, 400, 500, 600, 700, 800, and 1000 km (http://www.daveboore.com/software_online.html; last accessed: 10/15/2017). These effective distances are equivalent to JB distances of 1 to 1000 km based on tables generated at the end of Chapter 4. Ground motions in this report are simulated for a reference hard rock site with V_{S30} = 3.0 km/sec. Note that it is very important to select seismological and geological parameters that are internally consistent. In fact, it is unreasonable to use a stress drop from a particular study and then to use the path attenuation from another study. Boore (2015) and Boore (2018) have calculated the stress drop for 6 different attenuation models (combination of Q and the geometrical spreading) determined from the inversion of PSA values at spectral periods of 0.1 and 0.2 sec within 200 km and 600 km. The Atkinson and Boore (2014) attenuation model is used with a frequency independent geometrical spreading function which Boore (2018) referred to as AB14mod2. Table 6-2 lists the seismological and geological characteristics which are used as the representative values in CENA to construct ground motions based on the stochastic point-source approach. A key feature of the source model for these simulations is a constant stress drop for all magnitudes (magnitude-independent stress drop). Constant stress drop is accepted as a first order approximation for moderate to large earthquakes (Aki, 1967; Hutching and Viegas, 2012; Frankel, 2015). Frankel (2015) used 200 bars as the stress drop value for constructing high frequency stochastic synthetics for ENA. Pezeshk *et al*. (2015) used a constant stress drop value of 400 bars. The selected parameters are also consistent with the ones used in Chapter 4 to determine effective distances.

For each small magnitude-distance pair, 5 different simulations are generated using SMSIM. Therefore, a total of 5*3*26 = 390 weak motions are generated. The simulated weak motions are used as input GFs into the SSGFM code and are scaled, shifted, and added together to synthesize motions from large earthquakes with magnitudes of 5.0, 5.5, 6.0, 6.5, 7.0, 7.5, and 8.0 at those effective point-source distances. For each input GFs, 10 realizations are generated to account for the effect of slip variability. Therefore, for each large magnitude magnitude-distance pair, 50 various synthetics are generated. Overall, a database containing 50*26*7 + 390 = 9490 synthetics with magnitudes varying from 3.5 to 8 and effective distances ranging from 9.2 to 1000 km is created. To simulate synthetics of **M**5.0 and **M**5.5, time histories of **M**3.5 is used as the seeds, to simulate synthetics of **M**6.0 to **M** 7.0, time histories of **M**4.0 is used as the seeds, and for simulations of **M**7.5 and **M**8.0, time series of **M**4.5 are employed as the seeds. A total of

24 ground motion intensity measures (GMIMs) including PGV (cm/sec), PGA (g), and 5%-damped PSA (g) from 0.01 to 10 sec are calculated for each synthesized time series. The distance range, magnitude range, and spectral ordinates considered in this study are consistent with the PEER NGA-East project (Goulet *et al*., 2014).

The equivalent JB distance to each effective point-source distance-magnitude pair is determined based on Table 4-1 assuming faults are all strike-slip. Observed data reveals that the rate of increasing ground motions with magnitude decreases for larger magnitude earthquakes due to saturation effects. To capture the effects of magnitude and distance saturation, there are two different approaches (Darragh *et al*., 2015): 1) using a magnitude-dependent stress drop which decreases with increasing magnitude; and 2) incorporating an additional term in distance metric called the fictitious depth (Boore, 2009; Yenier and Atkinson, 2014; Tavakoli et *al*., 2018) discussed in Chapter 4. In this study, the effective point-source distance tables developed in Chapter 4 are employed. In fact, when a small earthquake is used within the framework of the SSGFM, the GF is supposed to be located at the effective point (equivalent point-source location) of the target event. In other words, to simulate a large earthquake, the effective point of the target event is placed at the effective point of the GF. For instance, to simulate an **M**7 earthquake with a JB distance of 10 km, the effective distance is 19.56 km (see Table 4-1). Thus, if the GF is a **M**4.5 event, we need to have a record at a JB distance of around 17 km which has an effective distance similar to the target event. This correction actually resolves the shortcoming of the point-source approach in modeling the magnitude and distance saturation. Since Table 4-1 is used to convert effective distances to JB distances, all shaking scenarios are defined for a strike-slip faulting mechanism with a 90º dip angle having the characteristics (depth, width, and length) explained in Chapter 4.

6.3 Validation Procedure: Against Appropriate GMPEs (SCEC Validation Exercise-Part B)

According to the SCEC validation exercise-part B, the simulated ground motions are compared with GMPEs developed for the region where synthetic ground motions are generated. This approach was first proposed by Frankel (2009). To this end, first medians, minima, maxima, and standard deviations of all realizations are identified. Then, the boxplots indicating the

median, standard deviations, and extrema are drawn on the PSA versus spectral period plot. The next step is to plot the median of predicated PSAs from selected relevant GMPEs. Finally, the pass/fail limits are determined as follows (Dreger *et al*., 2015):

- The upper bound is determined by the largest positive departure of any individual GMPE from the overall median plus 15% and then adding the difference to the overall median uniformly at all periods.
- The lower bound is determined by the largest negative departure of any individual GMPE from the overall median minus 15% and then subtracting the difference from the overall median uniformly at all periods.

Therefore, if the median of realizations is placed out of the lower and upper bounds, it implies that simulations are not consistent with the selected GMPEs.

Various GMPEs have been developed for CENA based on different approaches such as the hybrid empirical method (Tavakoli and Pezeshk, 2005; Pezeshk *et al*., 2011; Pezeshk *et al*., 2015), the point-source stochastic method (Boore, 2018), and the finite-fault stochastic method (Atkinson and Boore, 2006). Pezeshk *et al*. (2018b), Pezeshk *et al*. (2011), Atkinson and Boore (2006) which has been modified by Atkinson and Boore (2011), Boore (2018), and Al Noman and Cramer (2015) with updated parameters (hereafter referred to as: PZCT18, PZT11, AB06 (revised), Boore18, and AC16, respectively) are selected as the representative GMPEs developed for CENA. These GMPEs for use in this analysis are selected somehow to cover different methodologies and input seismological and geological parameters such as stress drop and attenuation to capture the effect of epistemic uncertainty. Figure 6-3, Figure 6-4, Figure 6-5, and Figure 6-6 illustrate the variation of response spectra for selected GMPEs at rupture distances of 5, 10, 100, and 300 km, respectively. Note that since AC16 is derived using observed ground motions and is not simulation-based, the magnitude and distance ranges of applicability are limited to magnitudes up to 5.8 and distances beyond 50 km.

To assess and evaluate the accuracy of the simulations, the median and standard deviation of 50 simulations at each distance-magnitude bin are determined and are compared against the median PSAs predicted by selected GMPEs. As can be seen from Figure 6-7 to Figure 6-14, the estimated values from synthetics generated using the proposed method (improved SSGFM), fall between the defined acceptance criteria indicating acceptable performance of the synthetics at all

magnitude and distance ranges. Note that since the selected GMPEs use the rupture distance, this distance metric is converted to the JB distance (using equations explained in Chapter 4) to be consistent with the distance of simulations.

6.4 Ground Motion Prediction Equations for CENA

Regarding the shape of the geometrical spreading function used to generate GFs by SMSIM, the functional form is given by

$$
\begin{aligned}
\mathrm{Ln}(Y) = &C_1 + C_2 M + C_3 M^2 + (C_4 + C_5 M) \times \min\left(\log(R), \log(10)\right) + \\
&(C_6 + C_7 M) \times \max\left(\min\left(\log(R/10), \log(50/10)\right), 0\right) + \\
&(C_8 + C_9 M) \times \max\left(\log(R/50), 0\right) + C_{10} R
\end{aligned}
\tag{5-16}
$$

in which

$$
R = \sqrt{R_{JB}^2 + C_{11}^2}
\tag{5-17}
$$

and C_1 to C_{11} are the coefficients of the functional form, **M** is the moment magnitude, R_{JB} is the Joyner-Boore distance (km) defined as the closest horizontal distance to the surface projection of the rupture plane, and $\mathrm{Ln}(Y)$ is the natural logarithm of the GMIM of interest (PGV in cm/sec and PGA and 5%-damped PSAs in *g* unit). A nonlinear least-squares regression is then employed to derive the model coefficients and its standard deviations. Table 6-3 tabulates the model coefficients and the regression standards deviation for 23 spectral periods from 0 to 10 sec as well as PGV. The proposed GMPEs for CENA are applicable for magnitudes ranging from 3.5 to 8.0 and JB distances up to 1000 km for generic hard rock sites with $V_{S30} = 3000$ m/sec. For other site conditions, the estimated GMIMs should be modified based on V_{S30} (*e.g.*, Stewart *et al.*, 2017; Parker *et al.*, 2018). It is worth mentioning that all simulations are directly used in the regression analysis to derive GMPEs and the regression analysis is not based on only the geometric mean or median spectral acceleration at each period for each distance-magnitude bin.

It should be mentioned that the calculation of aleatory uncertainty is a part of GMPE development. The GMPEs proposed in this report are for generic hard rock site with $V_{S30} = 3000$ m/sec; while the Next Generation Attenuation-East (NGA-East) database (Goulet *et al.*, 2014) includes events recorded on sites having different V_{S30}. Therefore, the NGA-East data must be

adjusted for the generic hard rock site. The impact of epistemic uncertainty is not considered in this study. The most important part of epistemic uncertainty is related to the seismological and geological parameters used in the simulations such as stress drop, attenuation, and duration. Epistemic uncertainty is often handled by using different GMPEs constructed based on various assumptions within the framework of logic trees.

Figure 6-15 depicts the decay rate of the estimated spectral accelerations with distance at different spectral periods. As observed from this figure, because of selection of a geometrical spreading function with three hinge points, there are three different segments in the distance-scaling plots. Since the decay trends are linear at close distances, it indicates that the effect of geometrical spreading overcomes Q up to 50 km. However, beyond this distance, the higher effect of Q causes the presence of curvature in plots. Furthermore, although the distance and magnitude saturation effects are obvious in the plots, we do not observe oversaturation at large magnitudes and very short distances. Figure 6-16 demonstrates the median response spectra for sites located at Joyner-Boore distances of 10, 30, 100, and 300 km. These plots again reveal the presence of saturation, but not oversaturation. Moreover, it is interesting to note that the predominant period increases with increasing magnitude. This pattern has been observed in other studies such as Boore *et al*. (2014) and Sedaghati and Pezeshk (2017).

6.4.1   Comparison with Previous Models Developed for CENA

Figure 6-17, Figure 6-18, Figure 6-19, and Figure 6-20 present the comparison of the GMPEs developed in this study (hereafter PST18: Pezeshk, Sedaghati, and Tavakoli 2018) at 4 different spectral periods with 3 selected GMPEs derived for CENA: Shahjouei and Pezeshk (2016), Gupta *et al*. (2017) which is a modified version of Shahjouei and Pezeshk (2016), and Pezeshk *et al*. (2011) (referred to as SP16, SP16scaled, and PZT11, respectively). Upper plots compare the decay rate of selected GMPEs for **M**5 and **M**7 and lower plots compare the decay rate of selected GMPEs for **M**4 and **M**6 for PGA and PSA at 0.2, 1.0, and 5.0 sec. Note that PZT11 is constructed using the rupture distance. Therefore, the rupture distance is converted to the JB distance using equations explained in Chapter 4 to have a consistent distance metrics. It should be also mentioned that the seismological parameters employed for each set of GMPEs are different. For instance, the stress drop values used for PZT11 and PST18 are 250 and 229 bar, respectively. SP16 used equally weighted simulations based on stress parameters of 400 and 600

bars. In addition, the geometrical spreading and the quality factor function for these GMPEs are completely different. In SP16scaled, Gupta *et al*. (2017) updated the coefficents of the functional form proposed by Shahjouei and Pezeshk (2016) to follow the trend of recorded small to moderate ground motions with distances less than 200 km in CENA. Overall, the proposed model is placed between other models. At close distances, the proposed model in this study predicts spectral amplitudes pretty similar to SP16scaled. At longer distances, spectral amplitudes estimated from PST18 are similar to SP16. Note that SP16 was developed for magnitudes larger than 5 and as can be seen in these figures, SP16 significantly overestimates spectral amplitudes for **M**4 events. On the other hand, since SP16scaled is modified based on recorded small to moderate magnitude earthquakes in CENA, it should predict reasonable spectral amplitudes. For the small magnitude range, PST18 and SP16scaled have similar trends in the JB distance range of 1 to 200 km and both result in comparable spectral amplitudes.

6.4.2 Comparison with Observed Ground Motions in CENA

The NGA-East database (Goulet *et al*., 2014) contains ground motions recorded on different soil conditions in CENA. Therefore, the ground motions for sites other than reference hard rock should be adjusted. There are many practical limits to perform site adjustment and all of them include severe uncertainty (Pezeshk *et al*., 2015; Hassani and Atkinson, 2016). In this regard, we use only observed data of NGA-East database with $V_{S30} > 1000$ m/sec to reduce the impact of uncertainty inherent in the site adjustment factor. To account for the effect of different site-damping coefficient and amplification factors, the adjustment factor explained in Pezeshk *et al*. (2018) (see Figure 9 of Pezeshk *et al*., 2018b) is used to modify the GMIMs of interest for a reference hard rock site. This compiled dataset is then combined with a dataset of Gupta *et al*. (2017). The Gupta *et al*. (2017) dataset consists of 46,178 recordings from 2873 small to moderate earthquakes with distances up to 200 km captured at 1069 stations located within CENA. This database of ground motions is available at https://github.com/abhineetgupta/groundMotionsDatabase_CEUS (last accessed Feb 2018). The recordings of this database have been corrected for the effects of site using the site amplification model of Seyhan and Stewart (2014) to convert for a site with $V_{S30} = 760$ m/sec. Note that the used site amplification model is developed for the NGA-west2 database; and therefore, it may not be appropriate to use in CENA (Hassani and Atkinson, 2016). However, since the objective

216

here is only visual comparison, we add this dataset to the NGA-East dataset. The site condition for the Gupta *et al.* (2017) (referred to as GKE17) dataset is not adjusted to V_{S30} of 3000 m/sec to avoid incorporating more uncertainty into the GMIMs.

Figure 6-21, Figure 6-22, and Figure 6-23 compare recorded ground motions from NGA-East and Gupta *et al.* (2017) (referred to as GKE17) datasets with the median spectral accelerations estimated from GMPEs developed in this study for **M**4.0, **M**4.5, and **M**5.0 events, respectively, at different spectral ordinates. Overall, comparisons demonstrate good agreement between the proposed model and observed ground motions. The proposed model perfectly follows the trend of recorded ground motions at even very close distances. For very long periods at very long distances, the proposed model slightly underpredicts spectral acceleration compared to observed recordings which may attribute to the attenuation function (higher attenuation compared to reality) or stress drop (lower compared to reality).

6.5 **Tables**

Table 6-1. List of the different simulation schemes used in SCEC broadband platform

Approach	Contact(s) and Institution	Name
Broadband deterministic	J. Anderson (UNR)	Composite source model
	Archuleta and Cremoien (UCSB)	UCSB
Hybrid: LF deterministic and HF stochastic	Graves (USGS)	Graves and Pitarka
	Olsen (SDSU)	SDSU (BB toolbx)
Stochastic finite fault	Assatourians and Atkinson (UWO)	EXSIM

Table 6-2. Parameters of the stochastic model for use in SMISM

Source Parameters
Source spectrum, SCF ω^2 model
Stress drop, $\Delta\sigma$ = 229 bars
Radiation pattern coefficient = 0.55
Velocity, β_S = 3.7 km/sec
Density, ρ = 2.8 g/cc
Source duration, T_S = $1/f_c$ where f_c is the corner frequency

Path Parameters
Geometrical spreading, $Z(R) = R^{-1.0}$ for $R \leq 10$; $R^{-1.3}$ for $10 < R \leq 50$; and $R^{-0.5}$ beyond 50 km
Quality factor, $Q(f) = 525f^{0.45}$ (from Atkinson and Boore, 2014)
Path duration, T_P see Table 5-2 (from Boore and Thompson, 2015)

Site Parameters
Partition factor = 0.707
Free-surface factor = 2.0
Site attenuation, κ_0 = 0.006 sec
Site amplification, $A(f)$ see Table 5-3 (from Boore and Thompson, 2015)

Table 6-3. Derived coefficients of the functional form defined for CENA in this study

Period	C_1	C_2	C_3	C_4	C_5	C_6	C_7	C_8	C_9	C_{10}	C_{11}	σ_{Reg}
PGV	-9.9497	3.1354	-0.1464	-0.0097	-0.0859	-2.9860	0.2703	-1.7261	0.1884	-0.00204	1.8432	0.2800
PGA	-9.7886	2.5152	-0.1345	-0.0322	-0.1053	-3.0052	0.2499	-1.9066	0.1609	-0.00273	2.6190	0.2094
0.01	-9.1259	2.4536	-0.1302	-0.0015	-0.1185	-3.0982	0.2488	-2.1473	0.1778	-0.00248	2.8313	0.1996
0.02	-8.1691	2.3487	-0.1282	-0.2608	-0.0741	-2.8021	0.2042	-2.5160	0.1939	-0.00212	2.4712	0.2206
0.03	-8.3106	2.2761	-0.1172	-0.0485	-0.0940	-2.6971	0.1980	-2.4199	0.1820	-0.00239	2.2830	0.2522
0.04	-8.4363	2.3203	-0.1177	-0.1567	-0.0908	-2.5013	0.1798	-2.2608	0.1711	-0.00276	2.8045	0.2699
0.05	-8.3931	2.2794	-0.1184	-0.1076	-0.0821	-2.7732	0.2236	-2.0211	0.1485	-0.00307	1.8654	0.2886
0.08	-8.7766	2.3018	-0.1069	0.1284	-0.1415	-2.7992	0.2330	-1.5607	0.1118	-0.00368	3.5379	0.3224
0.10	-9.0902	2.3307	-0.1084	0.1271	-0.1343	-2.7158	0.2268	-1.3249	0.0984	-0.00409	3.3217	0.3528
0.15	-10.5794	2.6042	-0.1317	0.1841	-0.1139	-2.8045	0.2420	-1.0109	0.0722	-0.00401	2.0199	0.3459
0.20	-11.9932	2.9406	-0.1543	0.2604	-0.1255	-2.7546	0.2450	-0.9989	0.0703	-0.00375	2.3634	0.3531
0.25	-12.9046	3.2242	-0.1796	0.0814	-0.0979	-2.6531	0.2350	-0.9174	0.0648	-0.00369	1.9677	0.3679
0.30	-14.3076	3.5189	-0.1971	0.1581	-0.1051	-2.6124	0.2325	-0.8457	0.0562	-0.00343	1.7414	0.3629
0.40	-16.6885	4.1629	-0.2353	0.3396	-0.1539	-2.7406	0.2440	-0.7492	0.0403	-0.00300	3.5677	0.3757
0.50	-18.9354	4.6095	-0.2655	0.5704	-0.1560	-2.5803	0.2284	-0.6233	0.0274	-0.00294	1.7632	0.3966
0.75	-22.9284	5.4859	-0.3183	1.0055	-0.2061	-2.4381	0.1965	-0.7504	0.0638	-0.00299	0.7383	0.4073
1.00	-24.3573	5.9099	-0.3522	0.6829	-0.1670	-2.6300	0.2332	-0.8903	0.0650	-0.00232	0.9506	0.4106
1.50	-25.1991	6.1462	-0.3688	-0.0828	-0.0851	-2.6507	0.2481	-0.5505	0.0275	-0.00238	1.7931	0.4209
2.00	-24.6729	5.9743	-0.3611	-0.8591	0.0177	-2.2927	0.2014	-0.7699	0.0677	-0.00236	2.4364	0.4164
3.00	-27.1609	6.2135	-0.3628	-0.7059	0.0300	-2.4647	0.2181	-0.6717	0.0278	-0.00119	1.9928	0.3936
4.00	-28.3079	6.1956	-0.3330	-0.1525	-0.0857	-2.5172	0.2331	-0.8686	0.0661	-0.00176	3.5658	0.4085
5.00	-28.7753	6.0708	-0.3087	0.1557	-0.1482	-2.6554	0.2547	-0.9352	0.0697	-0.00157	3.5803	0.4150
7.50	-28.1283	5.4054	-0.2568	0.0158	-0.0839	-2.5556	0.2422	-1.2105	0.1044	-0.00113	1.4088	0.3753
10.00	-26.5872	4.7754	-0.2013	-0.2719	-0.0594	-2.6764	0.2545	-1.1911	0.0995	-0.00101	2.7920	0.3784

C_1 to C_{11} are the functional form coefficients and σ_{Reg} is the regression standard deviation in the natural logarithm unit.

6.6 Figures

Combined Metric Performance Level

| Within Threshold | Potential Issues | Problematic |

Rrup = [0-5] km

Event (MW, Mech.)	0.01 ≤ PSA Period Range ≤ 0.1 s					0.1 < PSA Period Range ≤ 1 s					1 < PSA Period Range ≤ 3 s					PSA > 3s				
	UCSB	EXSIM	G&P	SDSU	GMPE	UCSB	EXSIM	G&P	SDSU	GMPE	UCSB	EXSIM	G&P	SDSU	GMPE	UCSB	EXSIM	G&P	SDSU	GMPE
Chino Hills (5.39, ROBL)																				
Alum Rock (5.45, SS)		1.04	0.94	0.65	1.33		1.15	1.11	0.78	1.33		1.15	1.32	1.32	1.77		0.96	1.11	1.05	1.66
Whittier Narrows (5.89, REV)																				
North Palm Springs (6.12, ROBL)	0.25	0.38	0.13	0.36	0.16	0.96	0.23	0.11	0.27	0.16	0.93	0.20	0.47	0.51	0.15	0.41	0.08	0.94	0.95	0.50
Tottori (6.59, SS)	0.28	1.18	0.13	0.40	0.23	1.08	0.41	0.59	0.46	0.62	1.25	0.19	0.14	0.17	0.11	1.11	0.23	0.30	0.31	0.41
Niigata (6.65, REV)																				
Northridge (6.73, REV)																				
Loma Prieta (6.94, ROBL)	0.27	0.29	0.18	0.26	0.25	0.58	0.29	0.25	0.33	0.21	0.76	0.73	0.30	0.33	0.59	0.43	0.34	0.39	0.39	0.31
Landers (7.22, SS)	1.16	0.73	0.91	0.92	1.05	1.58	0.28	0.55	0.45	0.69	2.04	0.61	0.58	0.53	0.94	2.25	1.13	0.45	0.44	1.17
Riviere-du-Loup (4.6 REV)																				
Mineral (5.68 REV)																				
Saguenay (5.81 REV)																				
Average CA	0.45	0.33	0.27	0.34	0.35	0.86	0.25	0.25	0.29	0.34	1.05	0.50	0.45	0.47	0.46	1.16	0.54	0.40	0.39	0.45
Average CENA																				
Average ALL	0.38	0.36	0.25	0.29	0.30	0.90	0.27	0.29	0.31	0.30	1.09	0.43	0.41	0.43	0.41	1.15	0.43	0.38	0.37	0.43

Rrup = [5-20] km

Event (MW, Mech.)	0.01 ≤ PSA Period Range ≤ 0.1 s					0.1 < PSA Period Range ≤ 1 s					1 < PSA Period Range ≤ 3 s					PSA > 3s				
	UCSB	EXSIM	G&P	SDSU	GMPE	UCSB	EXSIM	G&P	SDSU	GMPE	UCSB	EXSIM	G&P	SDSU	GMPE	UCSB	EXSIM	G&P	SDSU	GMPE
Chino Hills (5.39, ROBL)		0.27	0.17	0.23	0.45		0.39	0.31	0.34	0.26		0.64	0.73	0.65	0.15		0.80	0.80	0.84	0.27
Alum Rock (5.45, SS)		0.32	0.52	0.19	0.48		0.28	0.43	0.21	0.33		0.38	0.42	0.44	0.34		0.71	0.43	0.43	0.43
Whittier Narrows (5.89, REV)	0.40	0.28	0.36	0.36	0.30	0.76	0.32	0.27	0.28	0.21	0.46	0.21	0.47	0.55	0.44	0.21	0.37	1.02	1.01	0.81
North Palm Springs (6.12, ROBL)	0.48	0.23	0.31	0.22	0.25	0.64	0.27	0.33	0.29	0.28	0.65	0.26	0.42	0.48	0.39	0.31	0.29	0.15	0.15	0.45
Tottori (6.59, SS)	0.39	0.47	0.36	0.31	0.60	0.44	0.21	0.40	0.23	0.60	0.47	0.21	0.27	0.25	0.22	0.54	0.37	0.25	0.24	0.22
Niigata (6.65, REV)	0.43	0.34	0.36	0.34	0.48	0.62	0.39	0.32	0.23	0.42	0.18	0.34	0.63	0.67	0.47	0.26	0.34	0.61	0.62	0.61
Northridge (6.73, REV)	0.56	0.31	0.20	0.22	0.21	0.80	0.38	0.37	0.29	0.37	0.54	0.39	0.22	0.25	0.36	0.37	0.36	0.21	0.21	0.29
Loma Prieta (6.94, ROBL)	0.20	0.37	0.20	0.27	0.24	0.47	0.31	0.21	0.30	0.27	0.41	0.24	0.35	0.36	0.20	0.46	0.33	0.27	0.27	0.23
Landers (7.22, SS)	0.73	0.43	0.45	0.48	0.33	0.65	0.32	0.27	0.28	0.33	0.53	0.43	0.41	0.44	0.22	0.44	0.41	0.85	0.85	0.42
Riviere-du-Loup (4.6 REV)		0.63	0.24	0.19	0.59		0.58	0.67	0.65	0.58		0.64	0.66	0.80	0.44		1.14	1.17	1.20	0.87
Mineral (5.68 REV)	0.74	0.46	0.43	0.66	0.71	0.66	0.20	0.27	0.68	0.36	0.97	0.20	0.05	0.23	0.32	0.57	0.28	0.03	0.25	0.19
Saguenay (5.81 REV)																				
Average CA	0.31	0.26	0.26	0.22	0.27	0.68	0.29	0.22	0.23	0.23	0.50	0.27	0.32	0.35	0.26	0.39	0.44	0.30	0.29	0.26
Average CENA	0.74	0.57	0.30	0.35	0.63	0.66	0.40	0.52	0.58	0.44	0.97	0.59	0.54	0.48	0.38	0.57	0.93	0.84	0.90	0.70
Average ALL	0.28	0.23	0.23	0.24	0.23	0.65	0.29	0.24	0.24	0.28	0.48	0.27	0.33	0.36	0.26	0.36	0.26	0.63	0.31	0.32

Rrup = [20-70] km

Event (MW, Mech.)	0.01 ≤ PSA Period Range ≤ 0.1 s					0.1 < PSA Period Range ≤ 1 s					1 < PSA Period Range ≤ 3 s					PSA > 3s				
	UCSB	EXSIM	G&P	SDSU	GMPE	UCSB	EXSIM	G&P	SDSU	GMPE	UCSB	EXSIM	G&P	SDSU	GMPE	UCSB	EXSIM	G&P	SDSU	GMPE
Chino Hills (5.39, ROBL)		0.39	0.26	0.24	0.50		0.33	0.28	0.26	0.42		0.46	0.35	0.29	0.24		0.64	0.61	0.59	0.28
Alum Rock (5.45, SS)		0.77	1.04	0.76	1.01		0.80	1.03	0.75	0.84		0.63	0.52	0.84	0.88		0.22	0.56	0.57	0.42
Whittier Narrows (5.89, REV)	0.43	0.40	0.26	0.35	0.31	1.00	0.35	0.28	0.38	0.27	0.79	0.30	0.47	0.56	0.52	0.37	0.14	0.46	0.49	0.31
North Palm Springs (6.12, ROBL)	0.35	0.62	0.45	0.41	0.42	0.90	0.31	0.26	0.26	0.29	0.85	0.44	0.24	0.29	0.41	0.14	0.34	0.43	0.43	0.09
Tottori (6.59, SS)	0.21	0.31	0.78	0.37	1.08	0.35	0.34	0.33	0.31	0.53	0.38	0.50	0.63	0.66	0.49	0.35	0.20	0.51	0.51	0.36
Niigata (6.65, REV)	0.36	0.31	0.38	0.24	0.48	0.39	0.29	0.43	0.33	0.33	0.52	0.52	0.99	1.01	0.67	0.92	0.40	1.11	1.11	0.72
Northridge (6.73, REV)	0.53	0.20	0.30	0.55	0.32	0.26	0.28	0.34	0.42	0.24	0.29	0.57	0.35	0.38	0.38	0.43	0.35	0.57	0.57	0.27
Loma Prieta (6.94, ROBL)	0.59	0.25	0.50	0.38	0.34	0.25	0.27	0.43	0.30	0.24	0.23	0.37	0.50	0.51	0.24	0.49	0.39	0.27	0.27	0.48
Landers (7.22, SS)	0.94	0.22	0.36	0.31	0.27	0.38	0.37	0.38	0.36	0.27	0.44	0.67	0.58	0.60	0.46	0.32	0.41	0.74	0.74	0.38
Riviere-du-Loup (4.6 REV)		0.36	0.37	0.28	0.96		0.53	0.29	0.34	0.43		0.45	0.32	0.37	0.82		0.28	0.26	0.28	0.72
Mineral (5.68 REV)	0.25	0.70	0.37	0.24	1.42	0.46	0.32	0.55	1.19	0.38	0.90	0.69	0.53	0.73		0.43	1.35	0.05	0.09	0.68
Saguenay (5.81 REV)	1.73	0.58	1.04	0.30	1.61	1.28	0.59	0.21	1.33	0.35	0.29	1.46	1.06	1.98	1.46					
Average CA	0.44	0.27	0.40	0.38	0.40	0.54	0.32	0.42	0.39	0.36	0.38	0.44	0.45	0.49	0.44	0.45	0.33	0.27	0.49	0.25
Average CENA	0.89	0.42	0.44	0.26	1.09	0.87	0.45	0.29	0.55	0.41	0.36	0.53	0.34	0.40	0.78	0.43	0.41	0.73	0.26	0.64
Average ALL	0.40	0.29	0.32	0.32	0.32	0.50	0.30	0.40	0.39	0.34	0.30	0.43	0.52	0.56	0.49	0.44	0.26	0.63	0.63	0.40

Rrup = [70-200 or 300] km

Event (MW, Mech.)	0.01 ≤ PSA Period Range ≤ 0.1 s					0.1 < PSA Period Range ≤ 1 s					1 < PSA Period Range ≤ 3 s					PSA > 3s				
	UCSB	EXSIM	G&P	SDSU	GMPE	UCSB	EXSIM	G&P	SDSU	GMPE	UCSB	EXSIM	G&P	SDSU	GMPE	UCSB	EXSIM	G&P	SDSU	GMPE
Chino Hills (5.39, ROBL)		0.54	0.51	0.43	0.33		0.43	0.46	0.46	0.31		0.44	0.50	0.46	0.30		0.65	0.75	0.75	0.48
Alum Rock (5.45, SS)		0.79	0.82	0.67	1.02		0.89	0.88	0.63	0.89		0.27	0.63	0.86	0.36		0.16	0.86	0.86	0.21
Whittier Narrows (5.89, REV)																				
North Palm Springs (6.12, ROBL)	0.26	0.15	0.09	0.25	0.25	0.52	0.46	0.36	0.48	0.43	0.83	0.46	0.37	0.30	0.35	0.27	0.81	0.45	0.45	0.32
Tottori (6.59, SS)	0.49	0.54	0.77	0.44	0.63	0.37	0.53	0.40	0.59	0.36	0.31	0.52	0.50	0.53	0.73		0.31	0.56	0.31	0.32
Niigata (6.65, REV)	0.35	0.31	0.35	0.42	0.49	0.37	0.44	0.79	0.33	0.81	0.70	0.52	1.33	1.35	1.05	1.35	0.23	1.50	1.50	0.92
Northridge (6.73, REV)	0.30	0.28	0.31	0.17	0.18	0.31	0.32	0.40	0.34	0.40	0.27	0.86	0.43	0.44	0.56	0.03	0.56	0.31	0.31	0.13
Loma Prieta (6.94, ROBL)	0.24	0.61	0.41	0.54	0.45	0.63	0.64	0.58	0.76	0.73	0.94	0.68	0.74	0.72	1.19	0.66	0.49	0.33	0.33	0.79
Landers (7.22, SS)	0.18	0.08	0.10	0.15	0.19	0.45	0.33	0.20	0.25	0.22	0.69	0.37	0.23	0.21	0.45	0.96	0.33	0.25	0.25	0.73
Riviere-du-Loup (4.6 REV)		0.45	0.44	0.23	1.51		0.69	0.51	0.34	0.88		0.84	0.70	0.62	0.64		0.97	0.69	0.58	0.16
Mineral (5.68 REV)	0.61	0.33	0.46	0.21	1.31	1.38	0.32	0.36	0.41	1.03	1.46	0.57	0.87	0.80	0.64	0.46	1.08	0.25	0.24	0.76
Saguenay (5.81 REV)	2.56	0.49	1.05	0.21	1.68	3.57	0.77	1.43	0.30	1.47	2.91	0.52	1.63	0.56	0.67	0.66	0.12	0.37	0.13	0.26
Average CA	0.16	0.27	0.24	0.25	0.35	0.48	0.37	0.37	0.29	0.35	0.70	0.31	0.34	0.36	0.39	0.93	0.29	0.35	0.35	0.54
Average CENA	1.71	0.41	0.62	0.20	1.52	2.62	0.60	0.85	0.34	1.18	2.13	0.60	1.12	0.68	0.60	0.48	0.98	0.27	0.23	0.68
Average ALL	0.50	0.34	0.38	0.29	0.52	0.82	0.34	0.37	0.36	0.44	0.70	0.34	0.50	0.51	0.42	0.58	0.51	0.69	0.69	0.42

Figure 6-1. Comparison of combined goodness of fit values obtained from different simulation schemes (from Dreger *et al*., 2015)
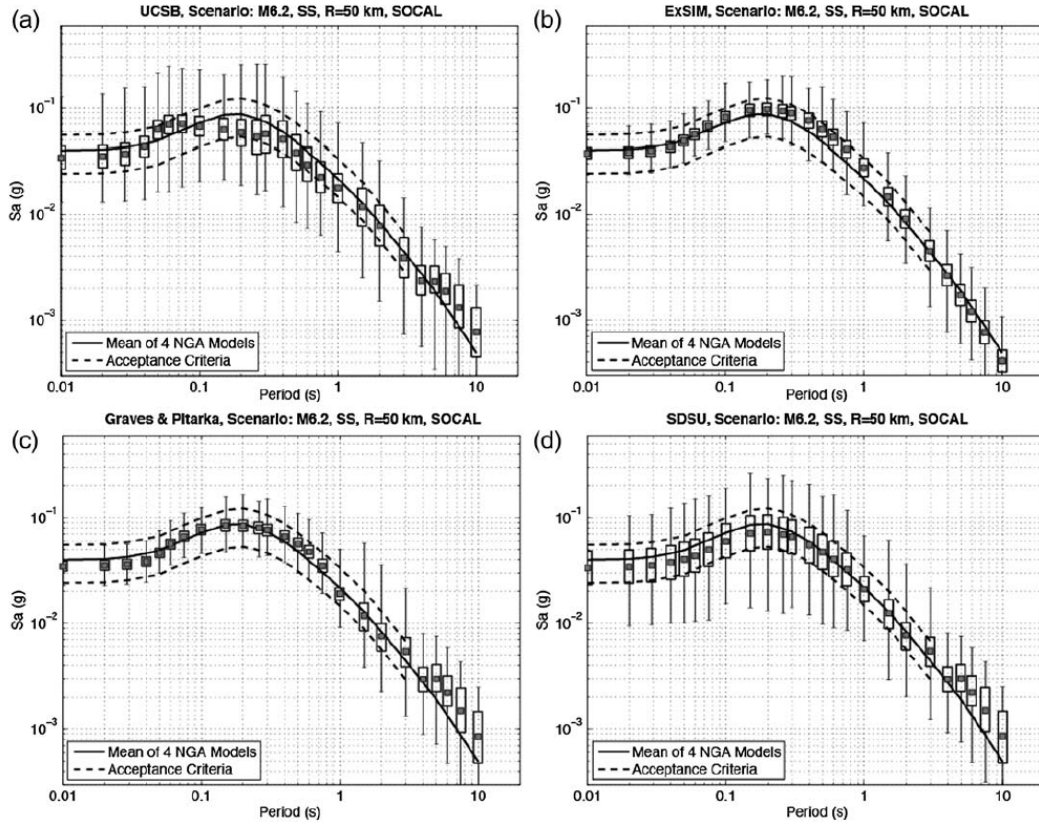
Figure 6-2. Comparison of the average response spectrum from simulations with the average response spectrum obtained from NGA-west 2 GMPEs based on the SCEC validation exercise part B for an **M** 6.2, strike-slip event at a distance of 50 km (from Dreger *et al*., 2015)
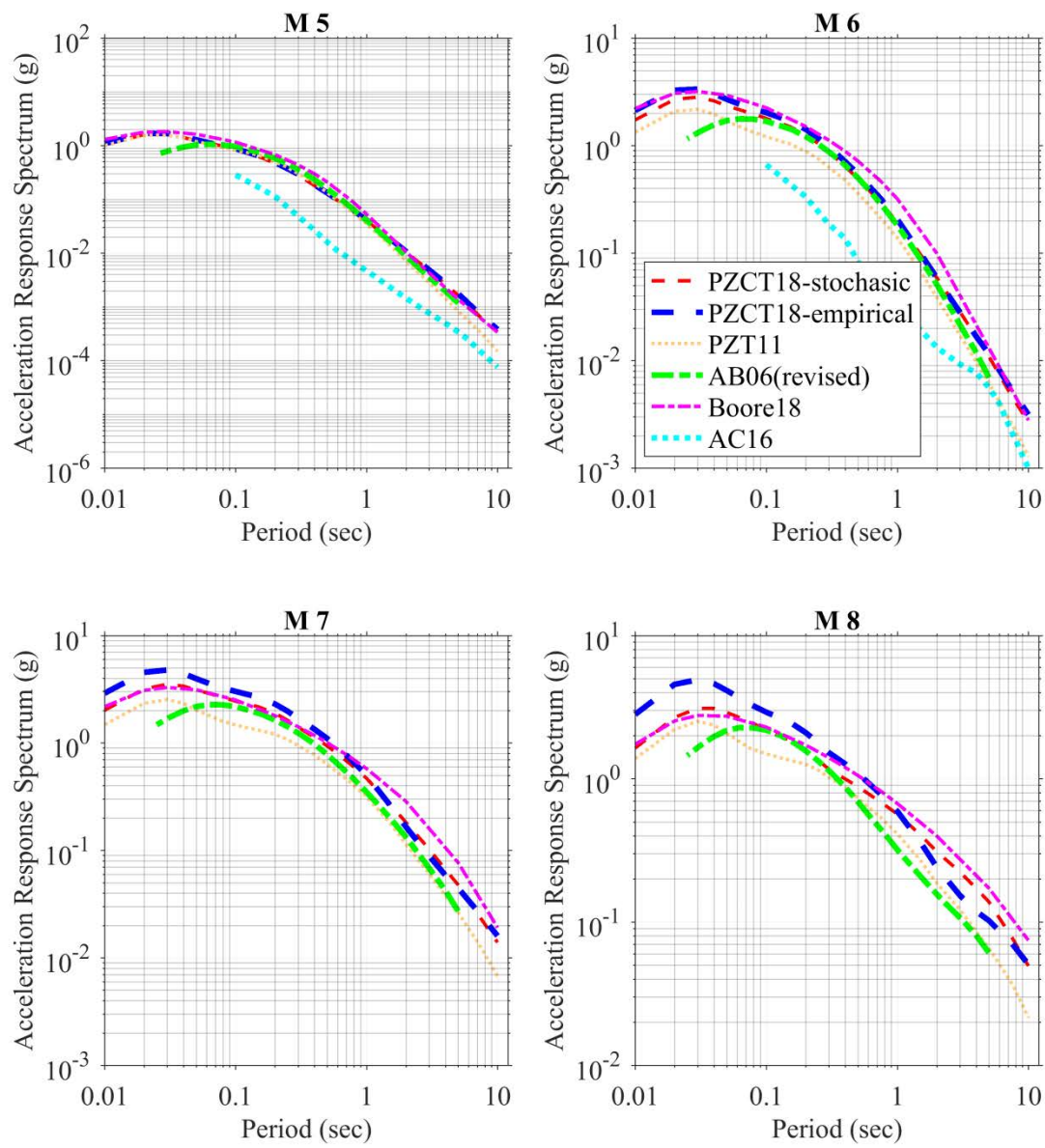
Figure 6-3. Response spectra predicted from the considered GMPEs developed for CENA at a
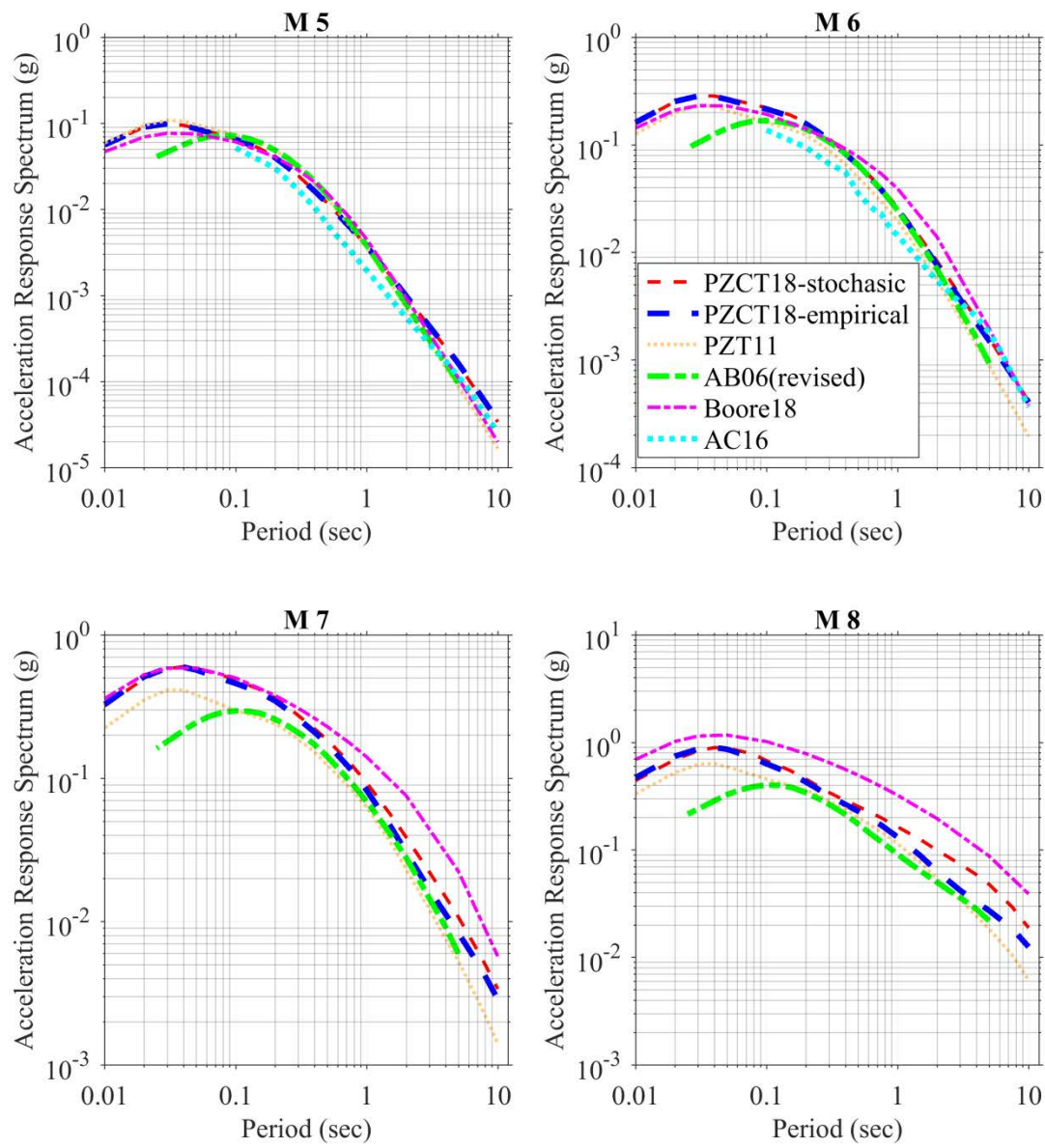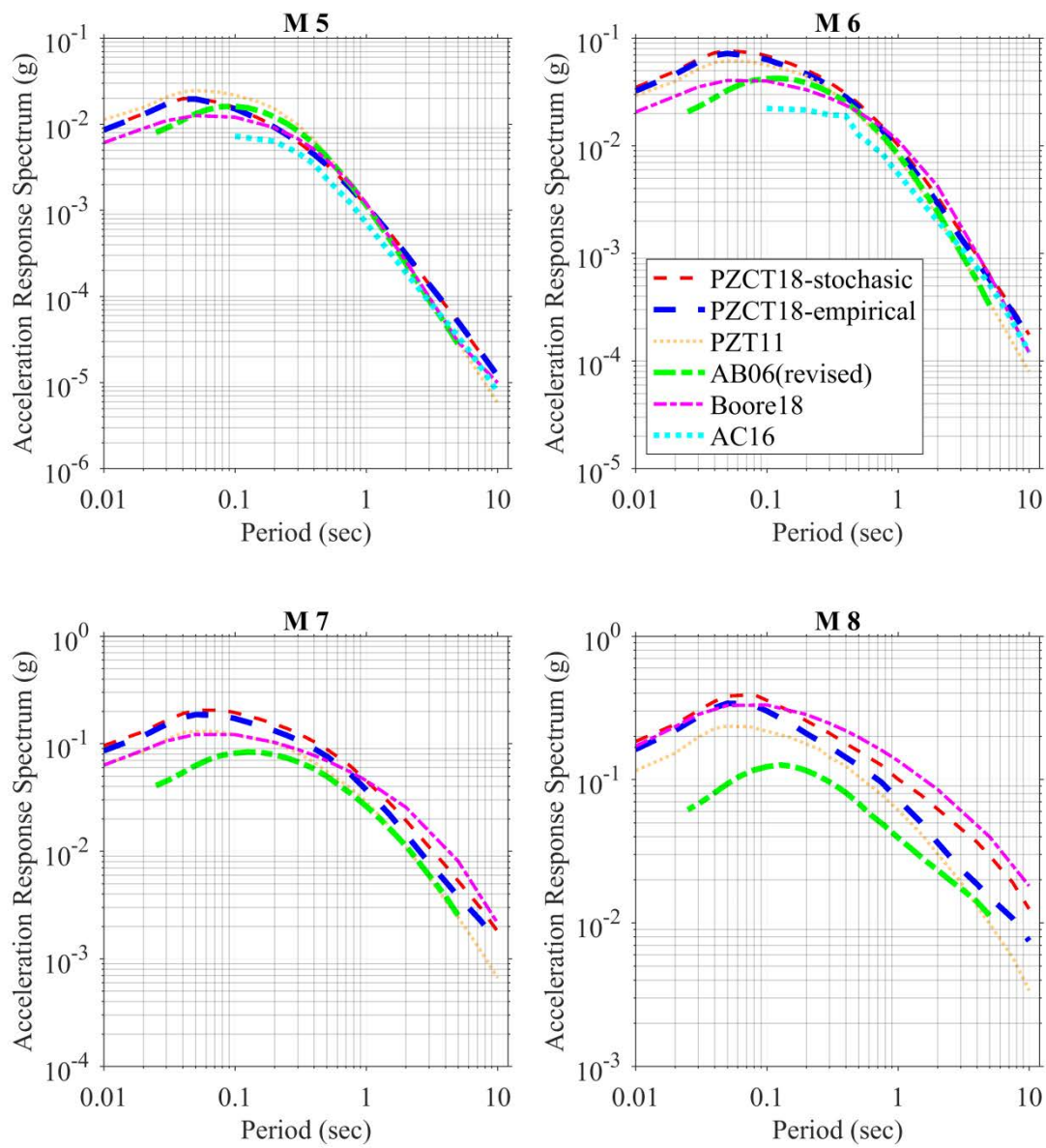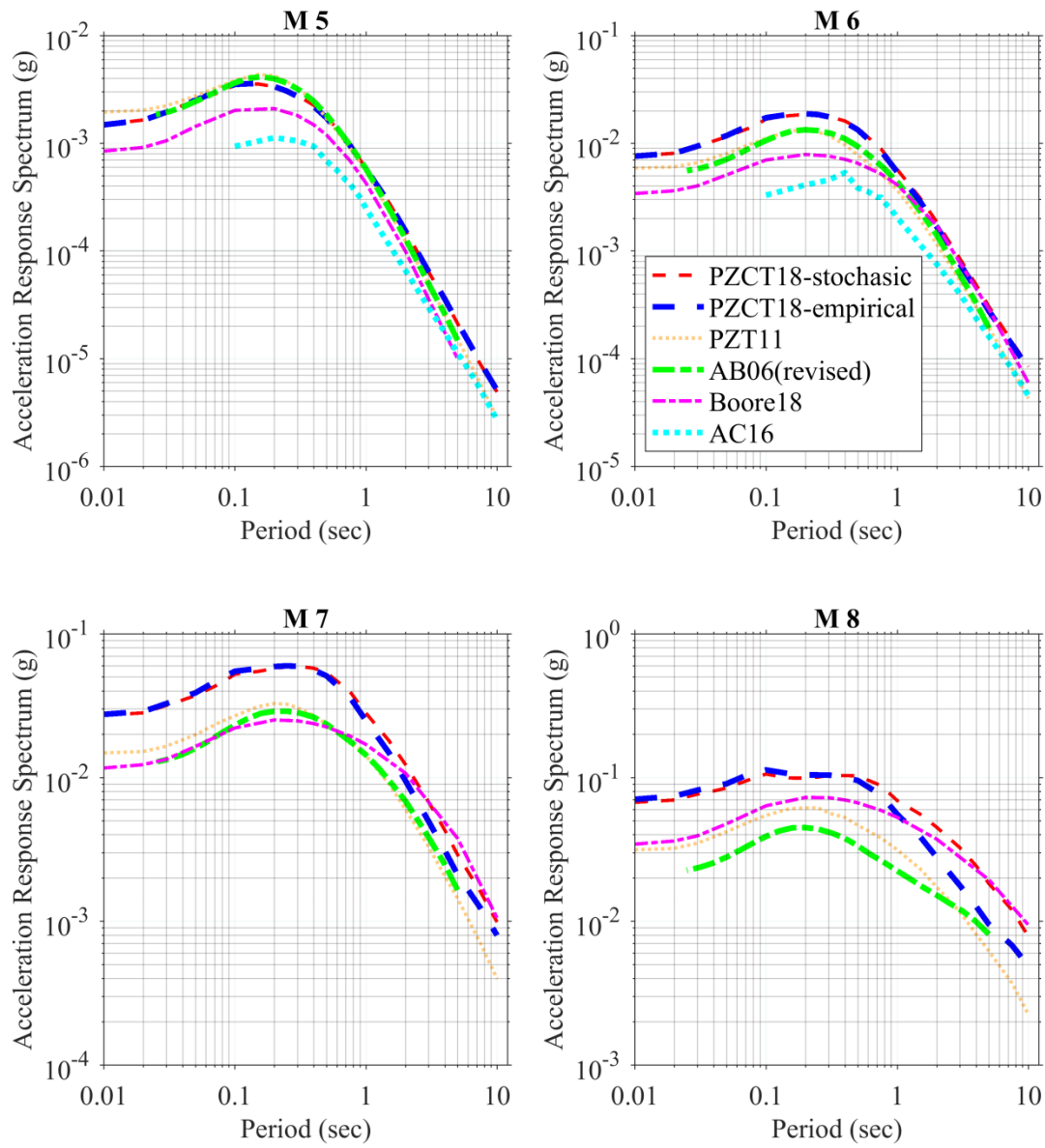rupture distance of 5 km for implementation in the SCEC-Part B validation exercise.

Figure 6-4. Response spectra predicted from the considered GMPEs developed for CENA at a rupture distance of 30 km for implementation in the SCEC-Part B validation exercise.
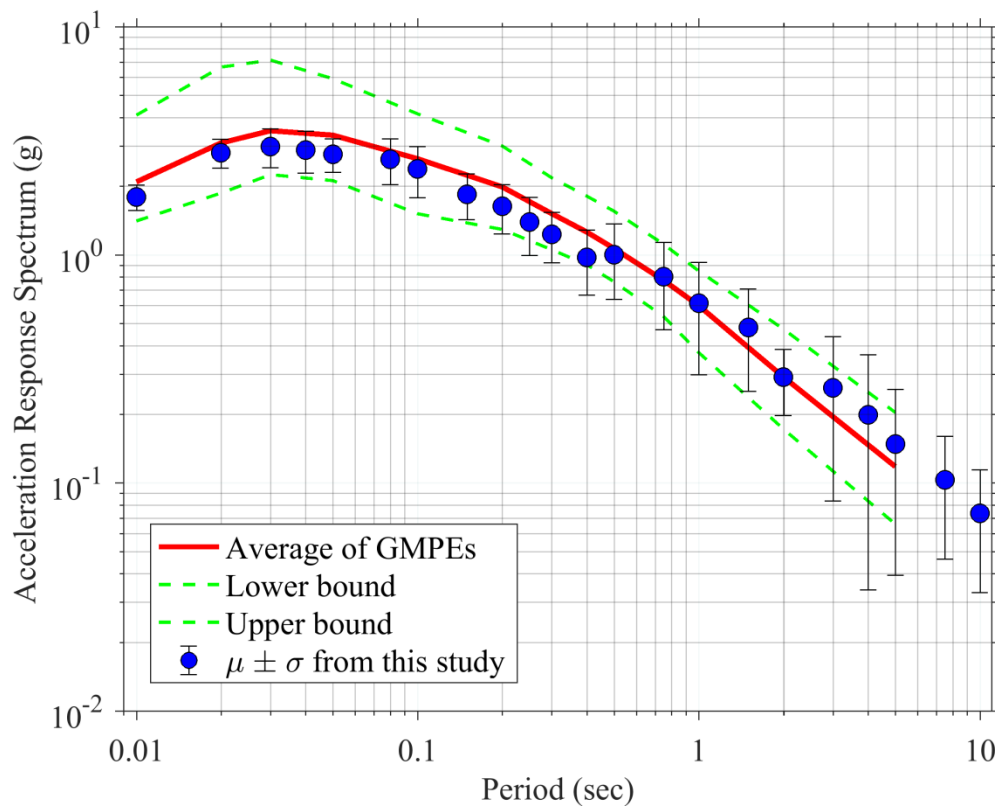
Figure 6-5. Response spectra predicted from the considered GMPEs developed for CENA at a rupture distance of 100 km for implementation in the SCEC-Part B validation exercise.

Figure 6-6. Response spectra predicted from the considered GMPEs developed for CENA at a rupture distance of 300 km for implementation in the SCEC-Part B validation exercise.
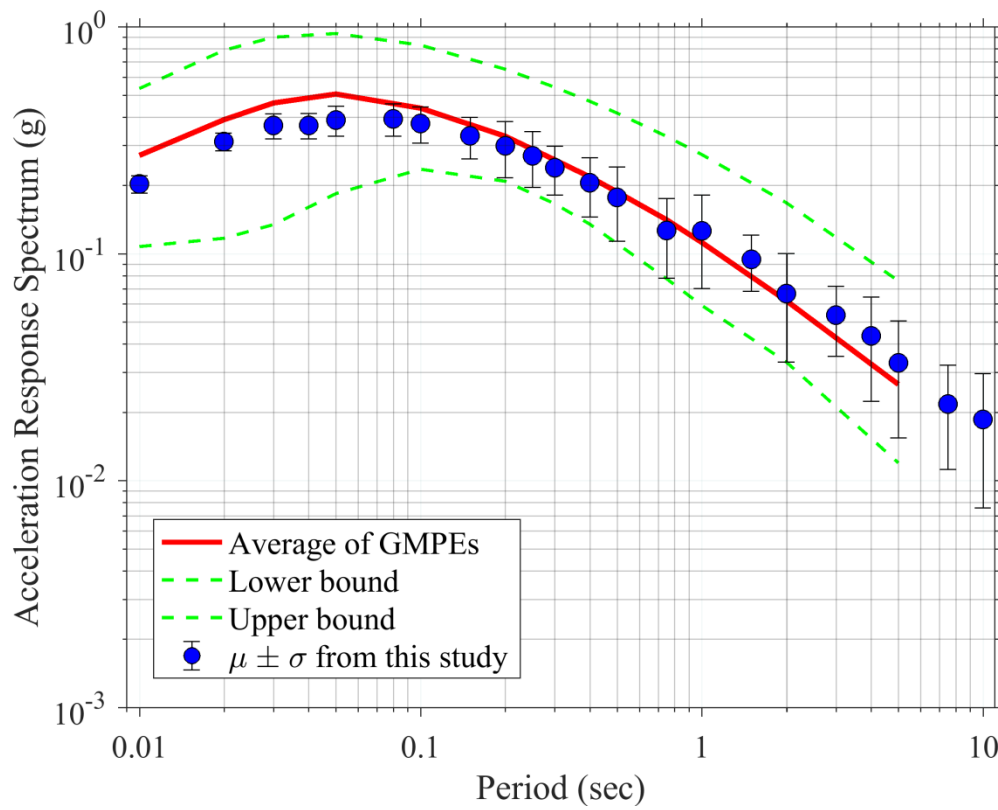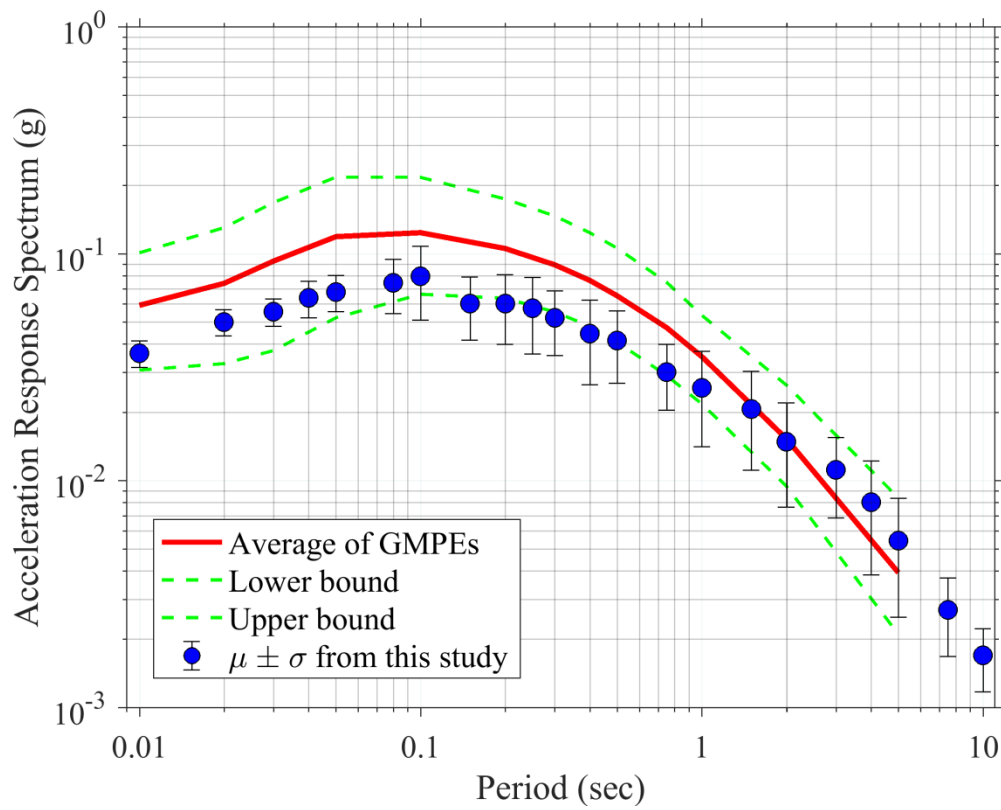
Figure 6-7. Comparison of the average (median) response spectrum obtained from the considered GMPEs for CENA and its acceptance criteria with the median spectral accelerations ±1 standard deviations determined from synthetics simulated in this study for an **M**8 event at a JB distance of 2.2 km.

Figure 6-8. Comparison of the average (median) response spectrum obtained from the considered GMPEs for CENA and its acceptance criteria with the median spectral accelerations ±1 standard deviations determined from synthetics simulated in this study for an **M**8 event at a JB distance of 40 km.
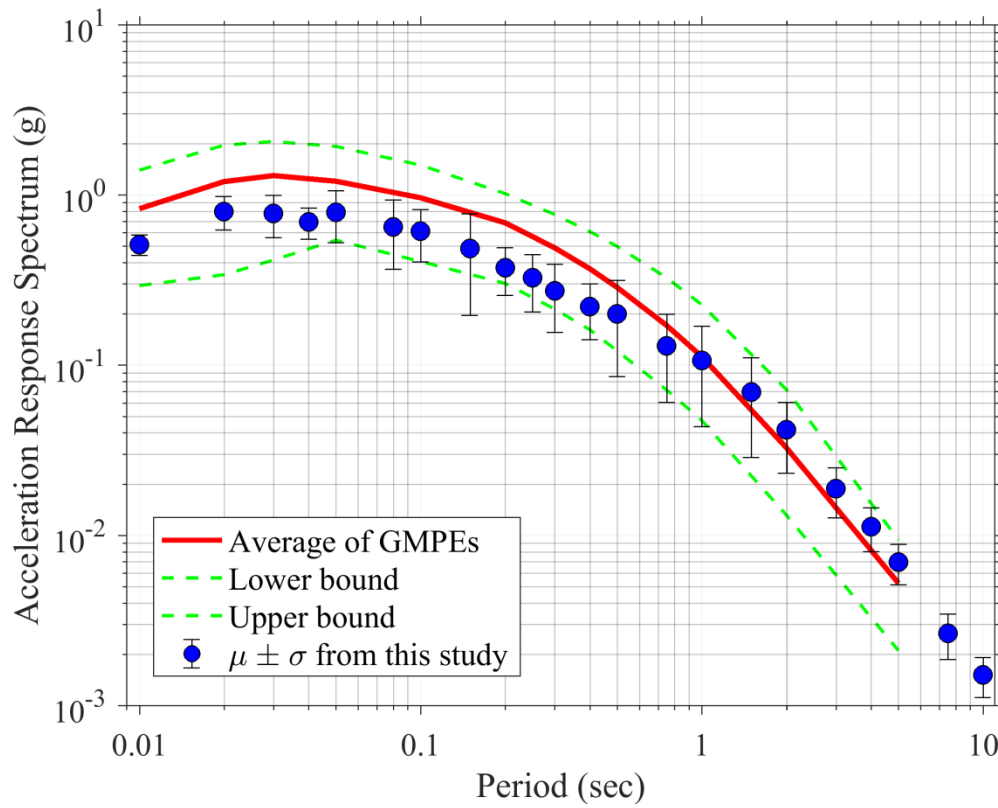
Figure 6-9. Comparison of the average (median) response spectrum obtained from the considered GMPEs for CENA and its acceptance criteria with the median spectral accelerations ±1 standard deviations determined from synthetics simulated in this study for an **M**7 event at a JB distance of 110 km.

Figure 6-10. Comparison of the average (median) response spectrum obtained from the considered GMPEs for CENA and its acceptance criteria with the median spectral accelerations ±1 standard deviations determined from synthetics simulated in this study for an **M**6 event at a JB distance of 8 km.
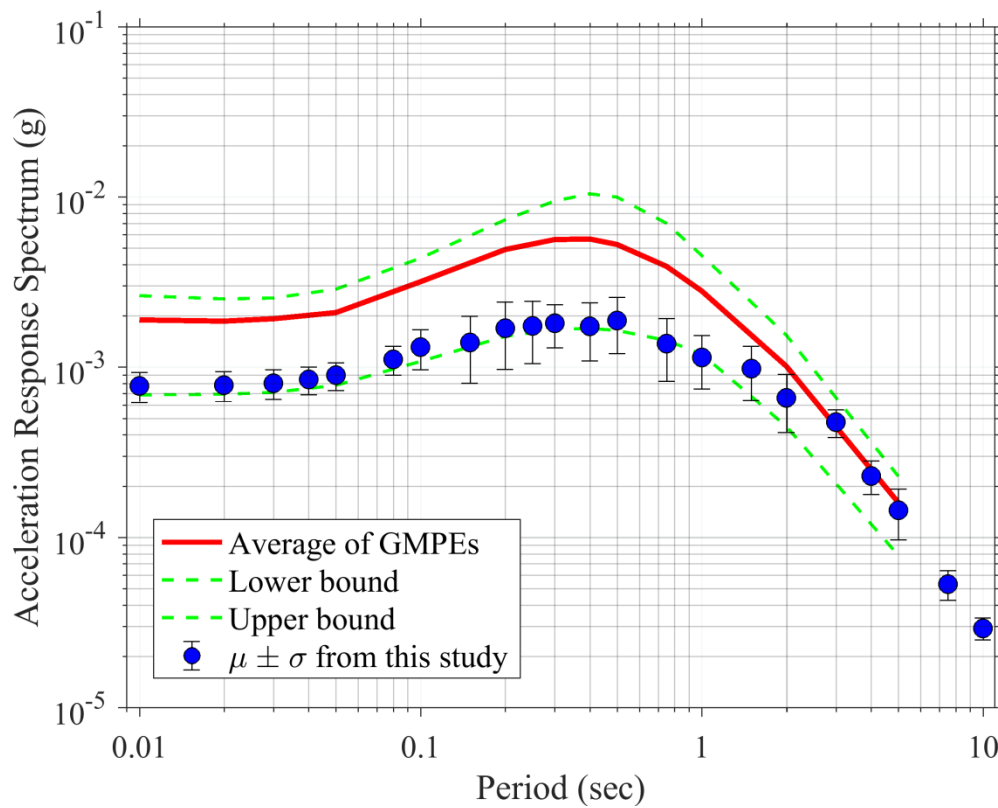
Figure 6-11. Comparison of the average (median) response spectrum obtained from the considered GMPEs for CENA and its acceptance criteria with the median spectral accelerations ±1 standard deviations determined from synthetics simulated in this study for an **M**6 event at a JB distance of 496 km.
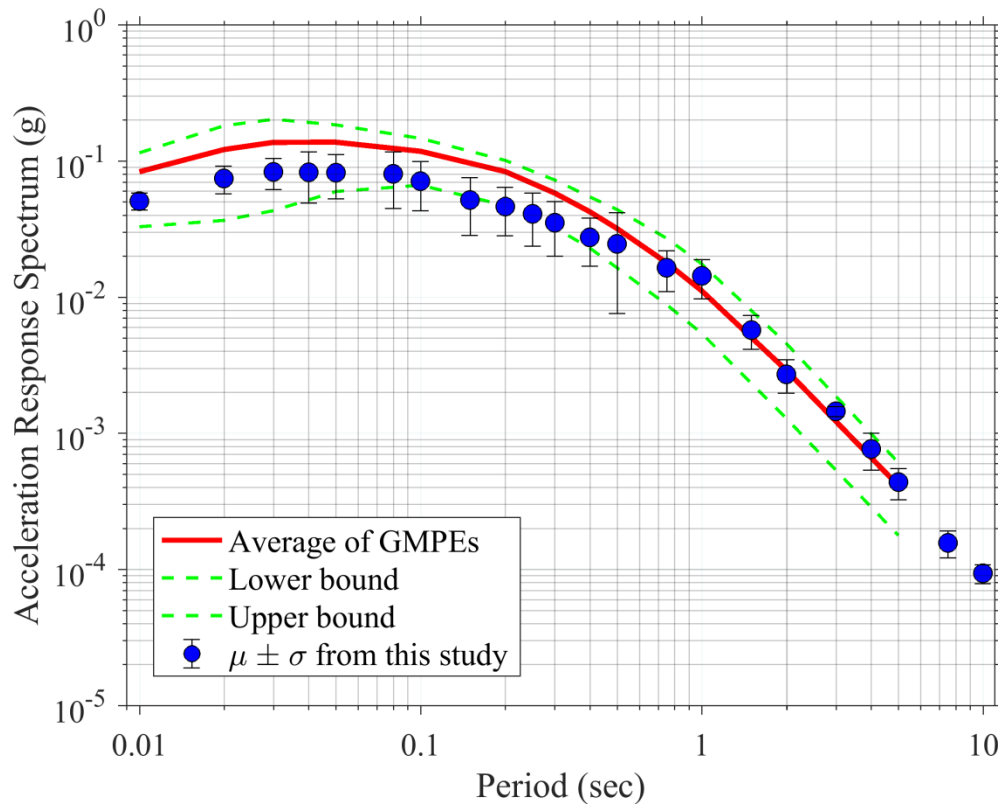
Figure 6-12. Comparison of the average (median) response spectrum obtained from the
considered GMPEs for CENA and its acceptance criteria with the median spectral accelerations
±1 standard deviations determined from synthetics simulated in this study for an **M**5.5 event at a
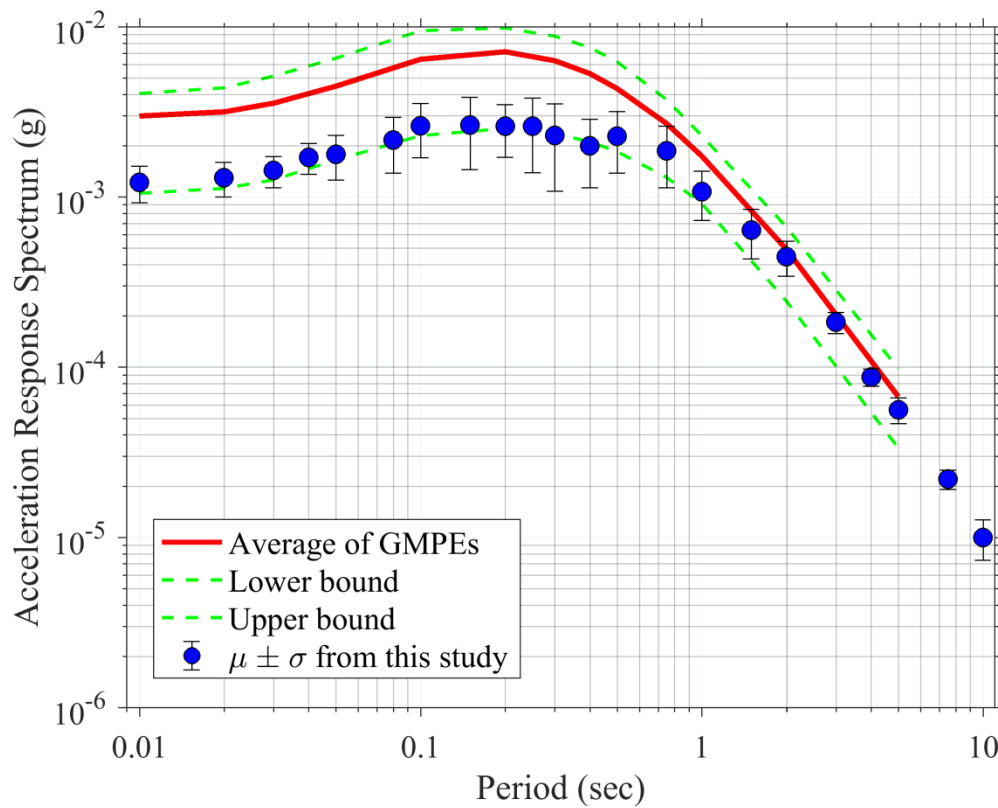JB distance of 26 km.

Figure 6-13. Comparison of the average (median) response spectrum obtained from the considered GMPEs for CENA and its acceptance criteria with the median spectral accelerations ±1 standard deviations determined from synthetics simulated in this study for an **M**5.5 event at a JB distance of 297 km.
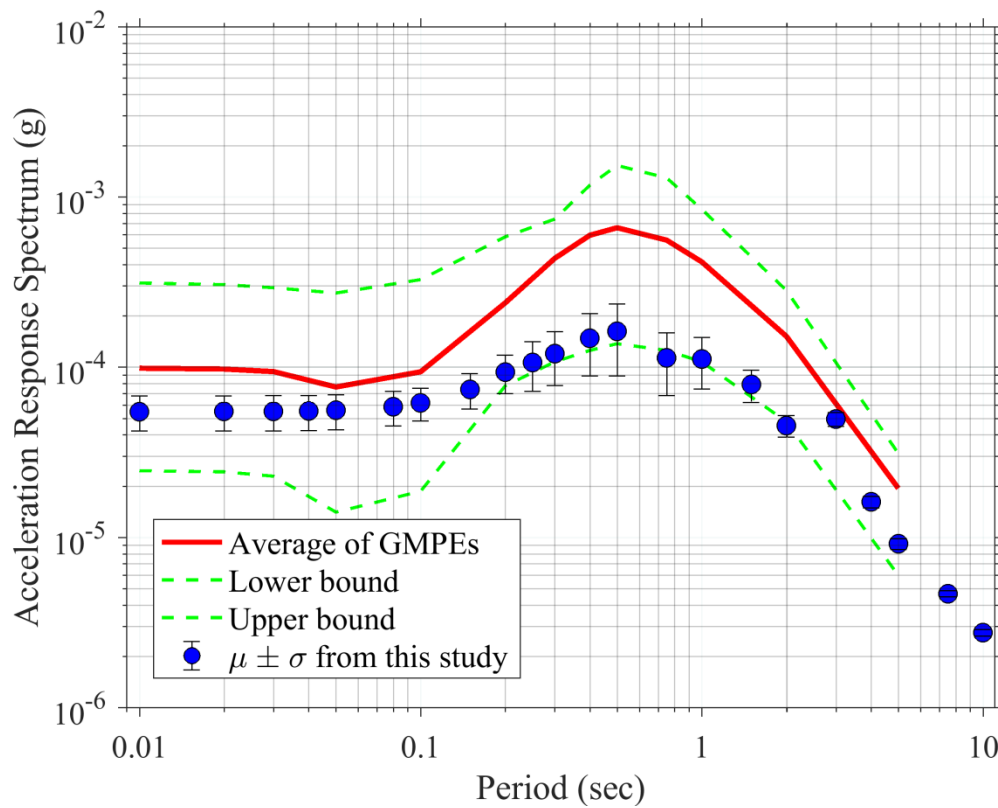
Figure 6-14. Comparison of the average (median) response spectrum obtained from the considered GMPEs for CENA and its acceptance criteria with the median spectral accelerations ±1 standard deviations determined from synthetics simulated in this study for an **M**5.5 event at a JB distance of 998 km.
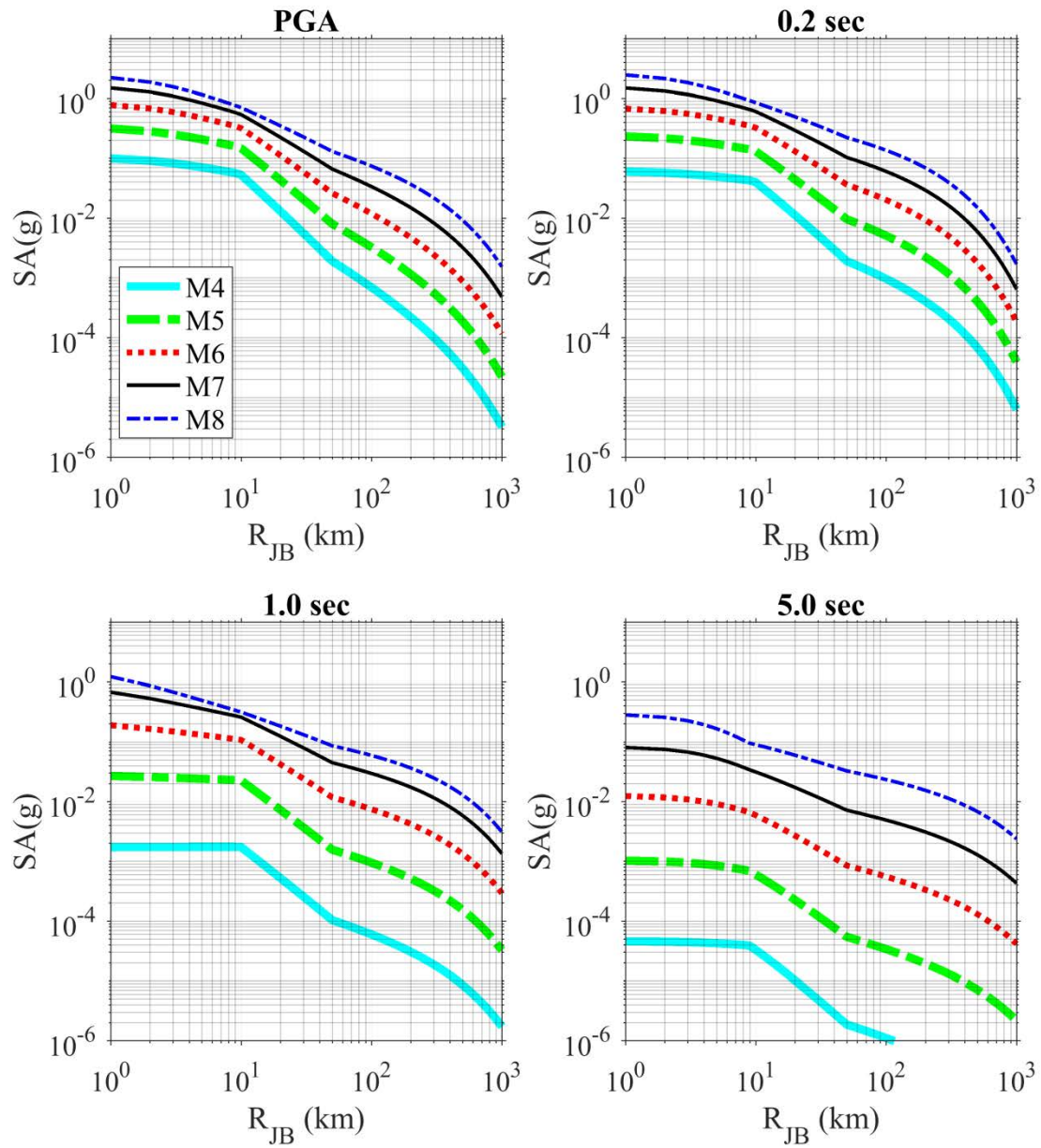
Figure 6-15. Distance scaling characteristics of the proposed GMPEs for a reference hard rock site with V_{S30} of 3000 m/sec at spectral periods of PGA, 0.2, 1.0, and 5.0 sec.
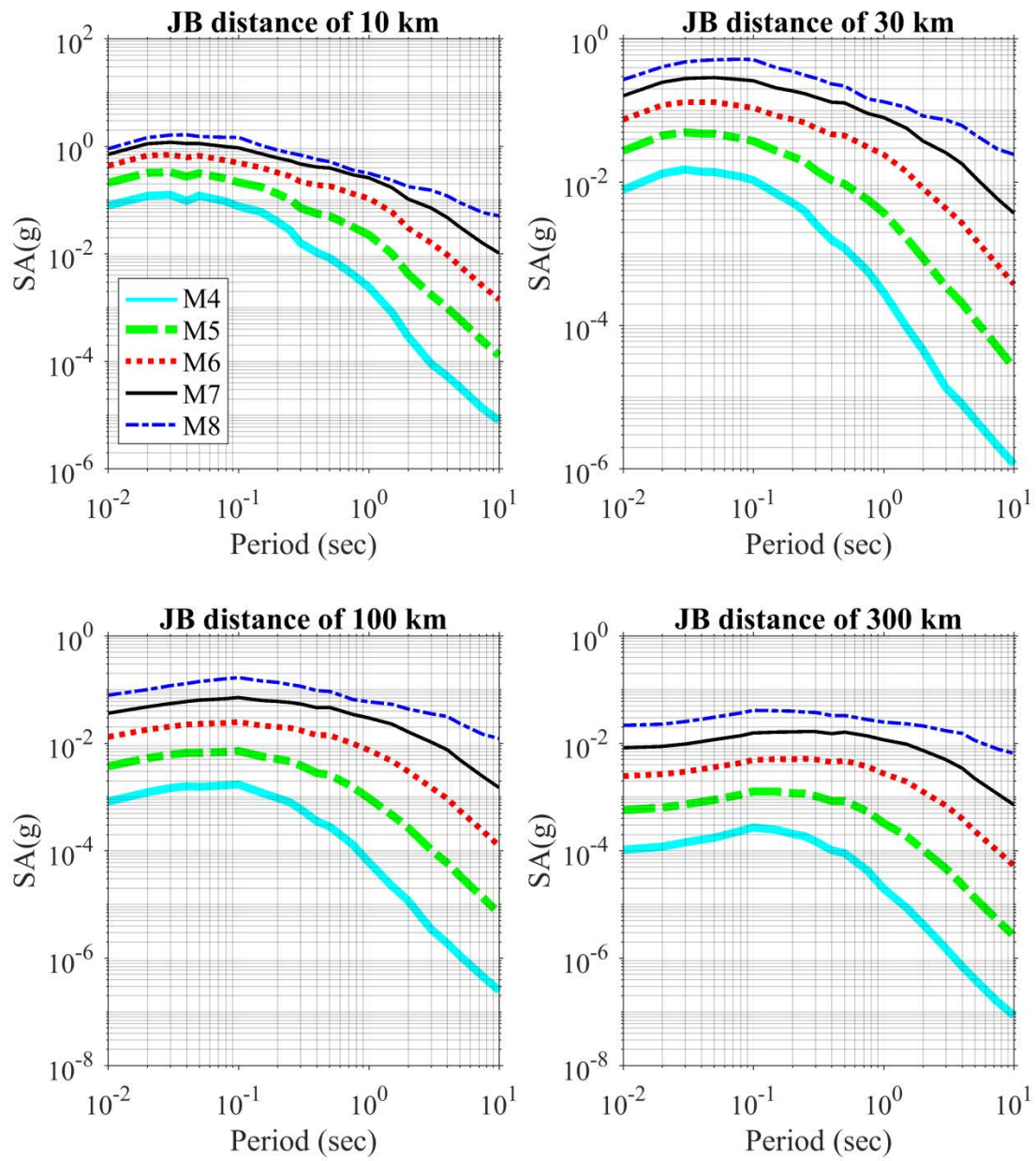
Figure 6-16. Variation of median estimates of response spectra versus spectral period at JB distances of 10, 30, 100, and 300 km
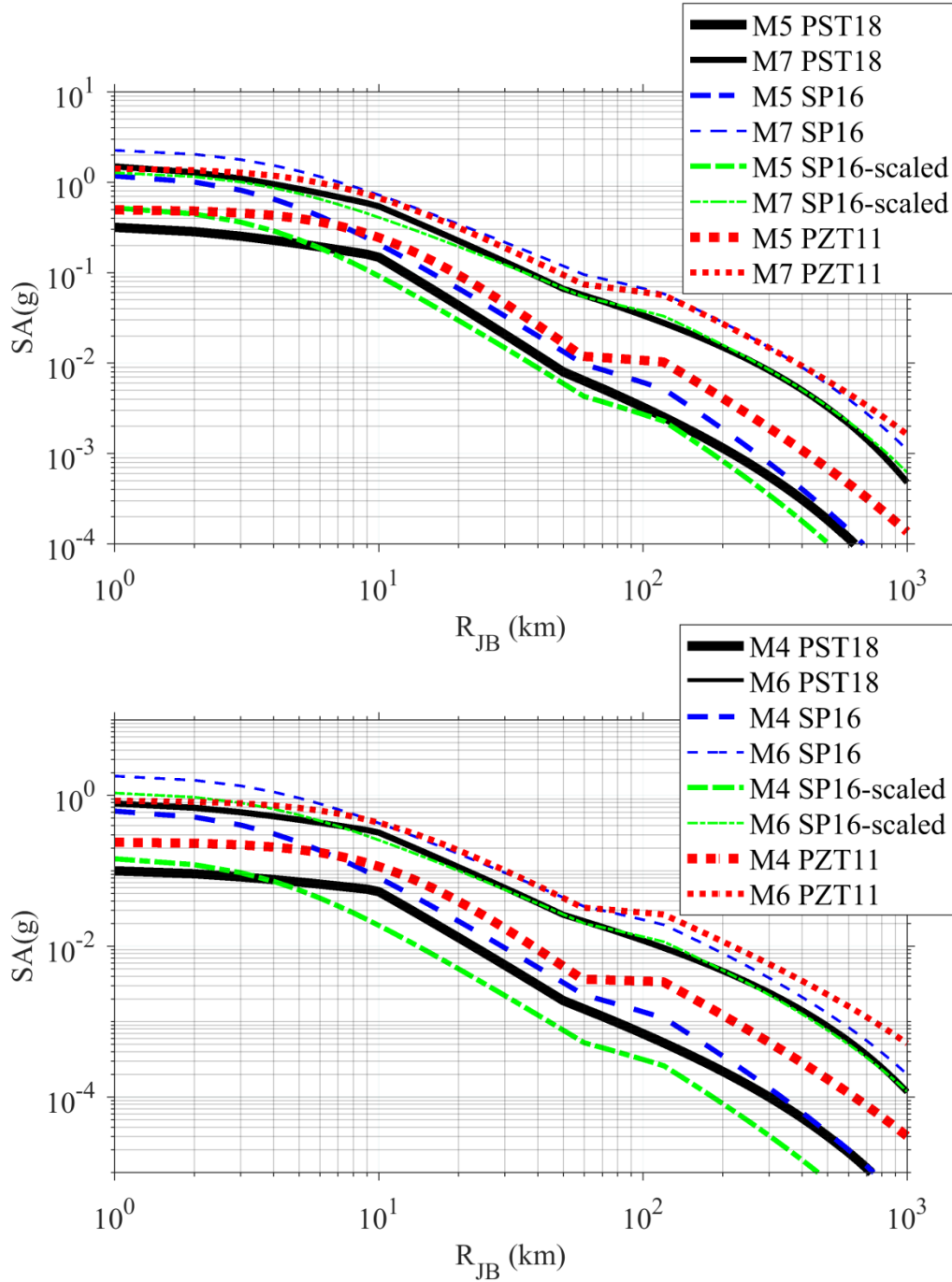
Figure 6-17. Comparison of estimated PGA values from the GMPEs proposed in this study with the predicted values by other GMPEs developed for CENA. **M**4 and **M**5 are the lower curves and **M**6 and **M**7 are the upper curves; PST18 (Pezeshk, Sedaghati, and Tavakoli, 2018); SP16 (Shahjouei and Pezeshk, 2016); SP16scaled (Gupta *et al.*, 2017); PZT11 (Pezeshk *et al.*, 2011).

Figure 6-18. Comparison of estimated SA values at 0.2 sec from the GMPEs proposed in this study with the predicted values by other GMPEs developed for CENA. **M**4 and **M**5 are the lower curves and **M**6 and **M**7 are the upper curves; PST18 (Pezeshk, Sedaghati, and Tavakoli, 2018); SP16 (Shahjouei and Pezeshk, 2016); SP16scaled (Gupta *et al*., 2017); PZT11 (Pezeshk *et al*., 2011).
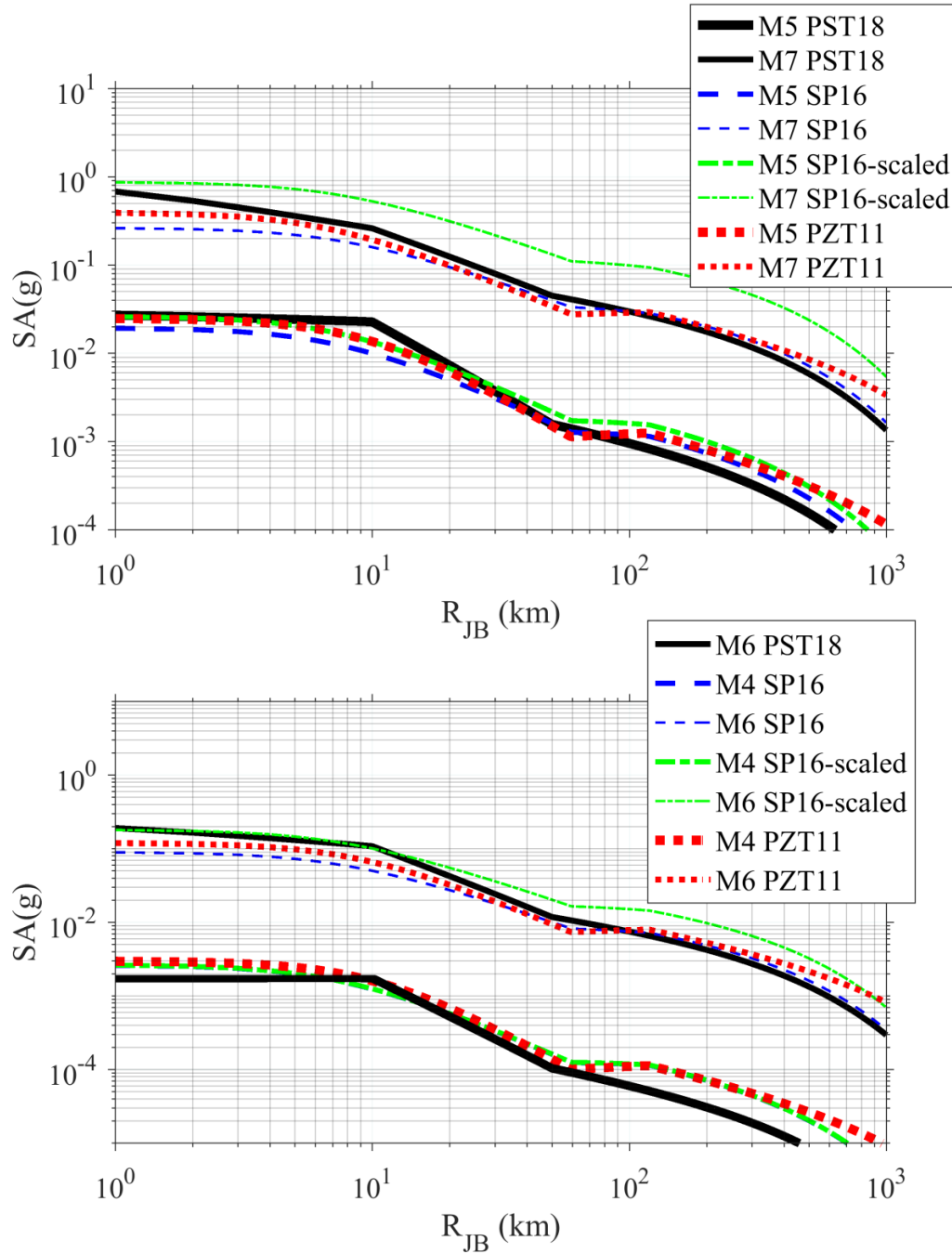
Figure 6-19. Comparison of estimated SA values at 1.0 sec from the GMPEs proposed in this study with the predicted values by other GMPEs developed for CENA. **M**4 and **M**5 are the lower curves and **M**6 and **M**7 are the upper curves; PST18 (Pezeshk, Sedaghati, and Tavakoli, 2018); SP16 (Shahjouei and Pezeshk, 2016); SP16scaled (Gupta *et al.*, 2017); PZT11 (Pezeshk *et al.*, 2011).
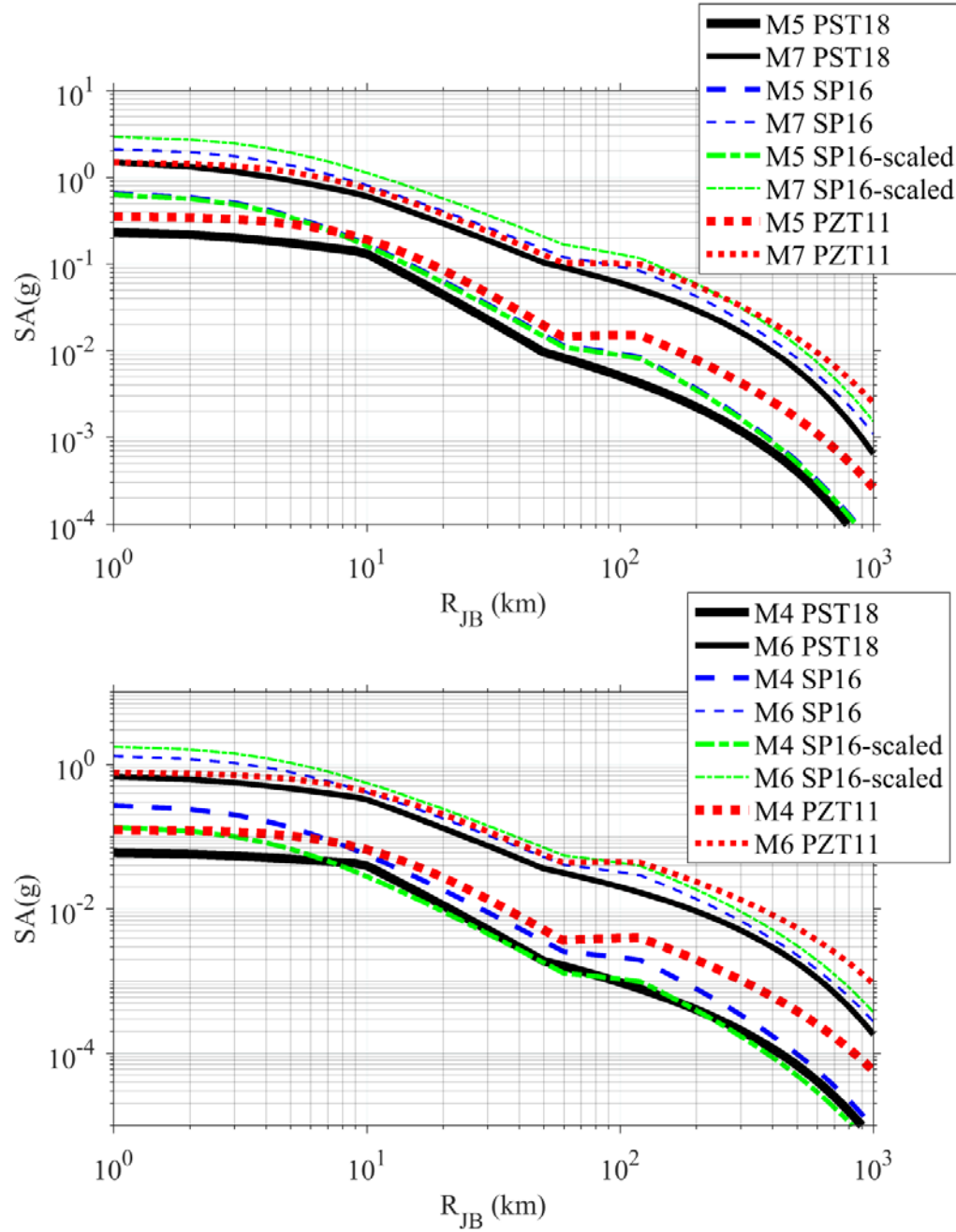
Figure 6-20. Comparison of estimated SA values at 5.0 sec from the GMPEs proposed in this study with the predicted values by other GMPEs developed for CENA. **M**4 and **M**5 are the lower curves and **M**6 and **M**7 are the upper curves; PST18 (Pezeshk, Sedaghati, and Tavakoli, 2018); SP16 (Shahjouei and Pezeshk, 2016); SP16scaled (Gupta *et al*., 2017); PZT11 (Pezeshk *et al*., 2011).

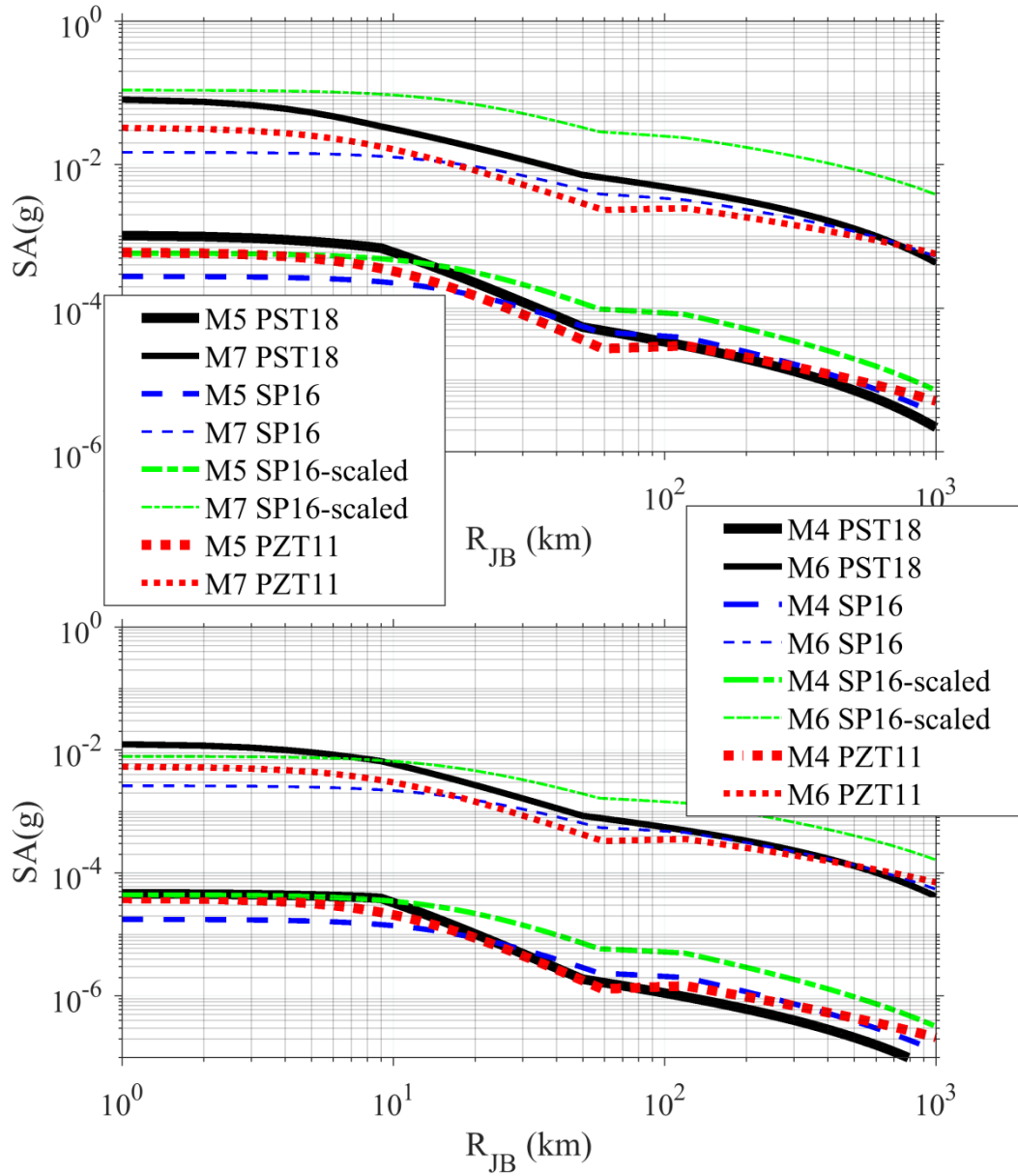Figure 6-21. Comparison of the median spectral acceleration predicted from the derived GMPEs in this study for the **M**4 case with the GMIMs of observed ground motions with magnitudes ranging from 3.75 to 4.25 at spectral ordinates of PGA, 0.2 sec, 1.0 sec, and 5.0 sec.

Figure 6-22. Comparison of the median spectral acceleration predicted from the derived GMPEs in this study for the **M**4.5 case with the GMIMs of observed ground motions with magnitudes ranging from 4.25 to 4.75 at spectral ordinates of PGA, 0.2 sec, 1.0 sec, and 5.0 sec.
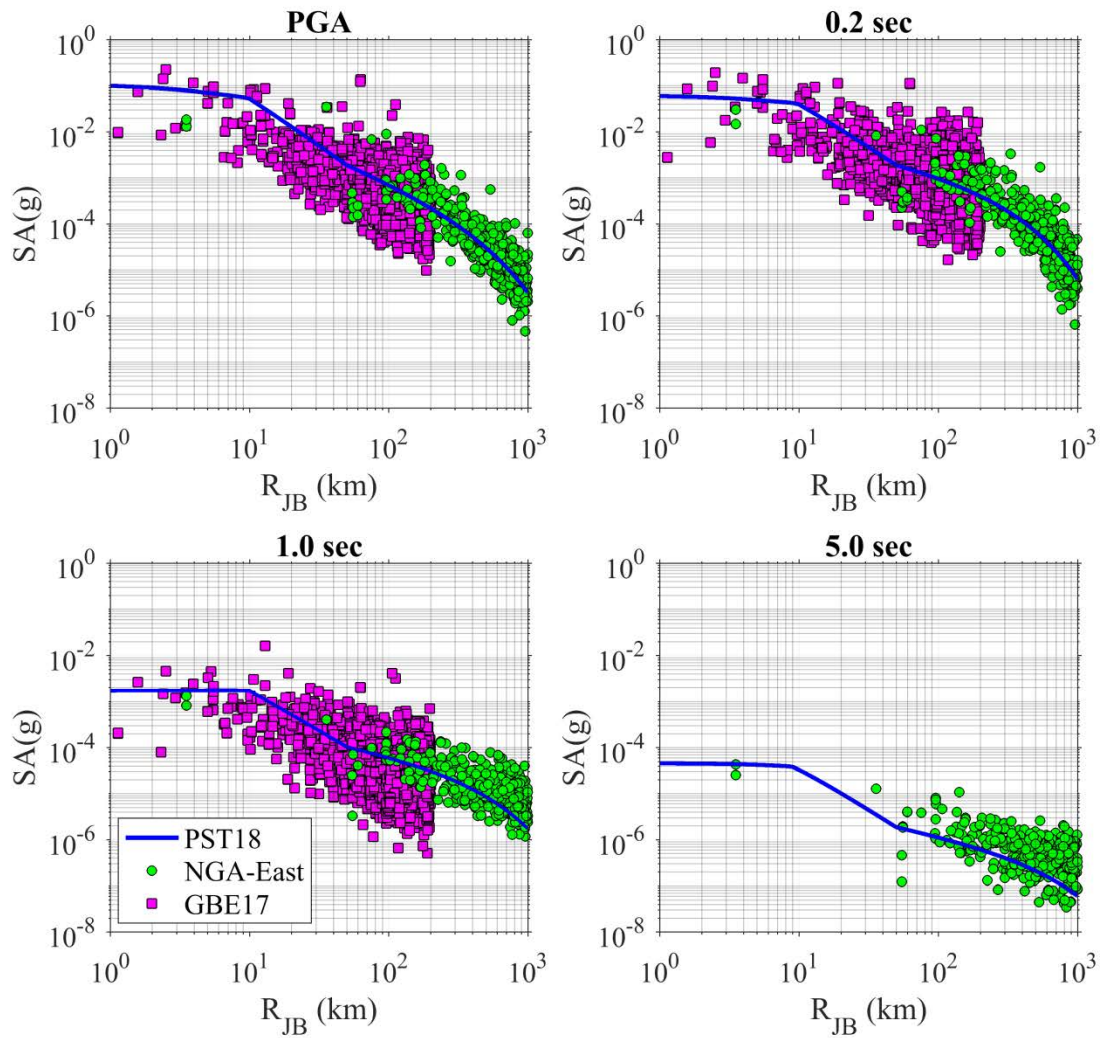
Figure 6-23. Comparison of the median spectral acceleration predicted from the derived GMPEs in this study for the **M**5 case with the GMIMs of observed ground motions with magnitudes ranging from 4.75 to 5.25 at spectral ordinates of PGA, 0.2 sec, 1.0 sec, and 5.0 sec.
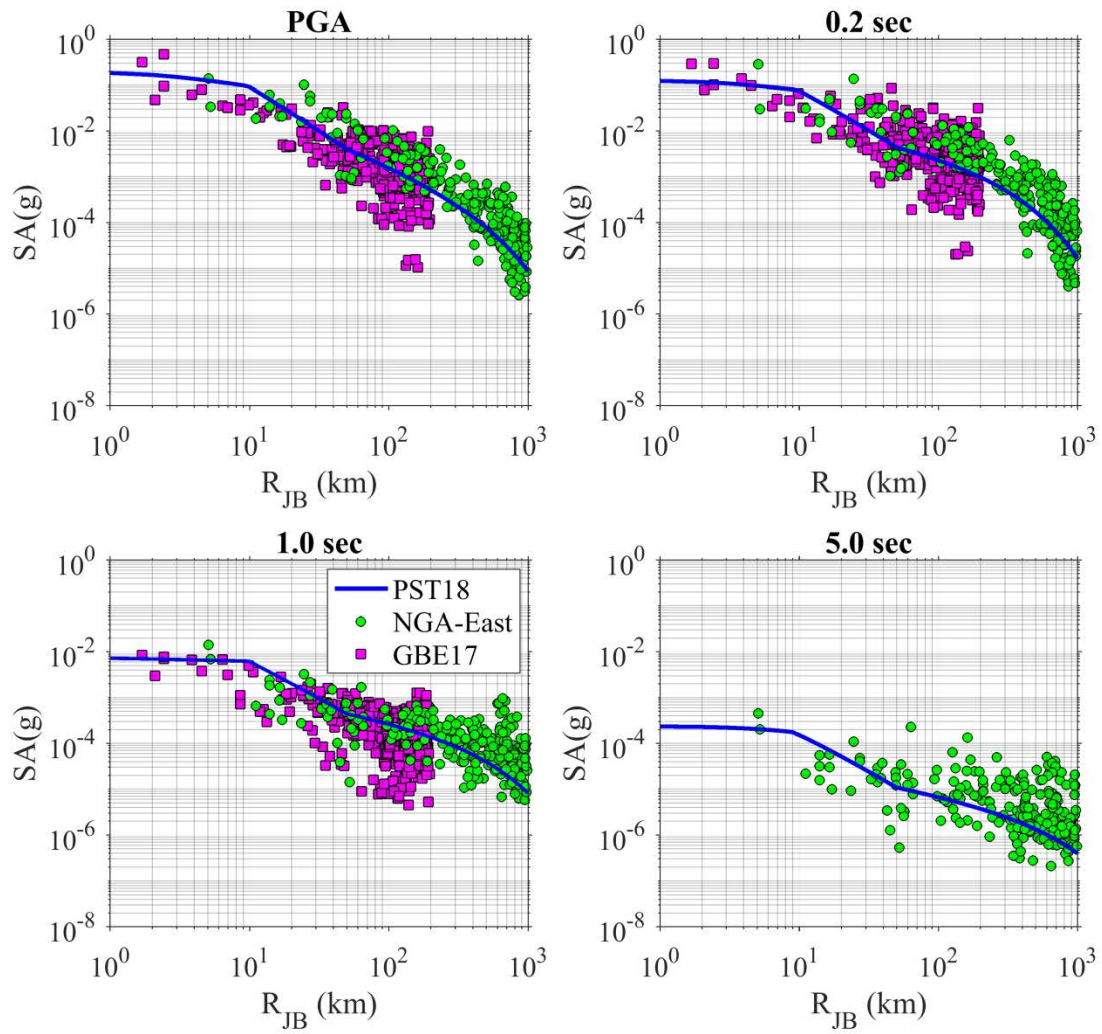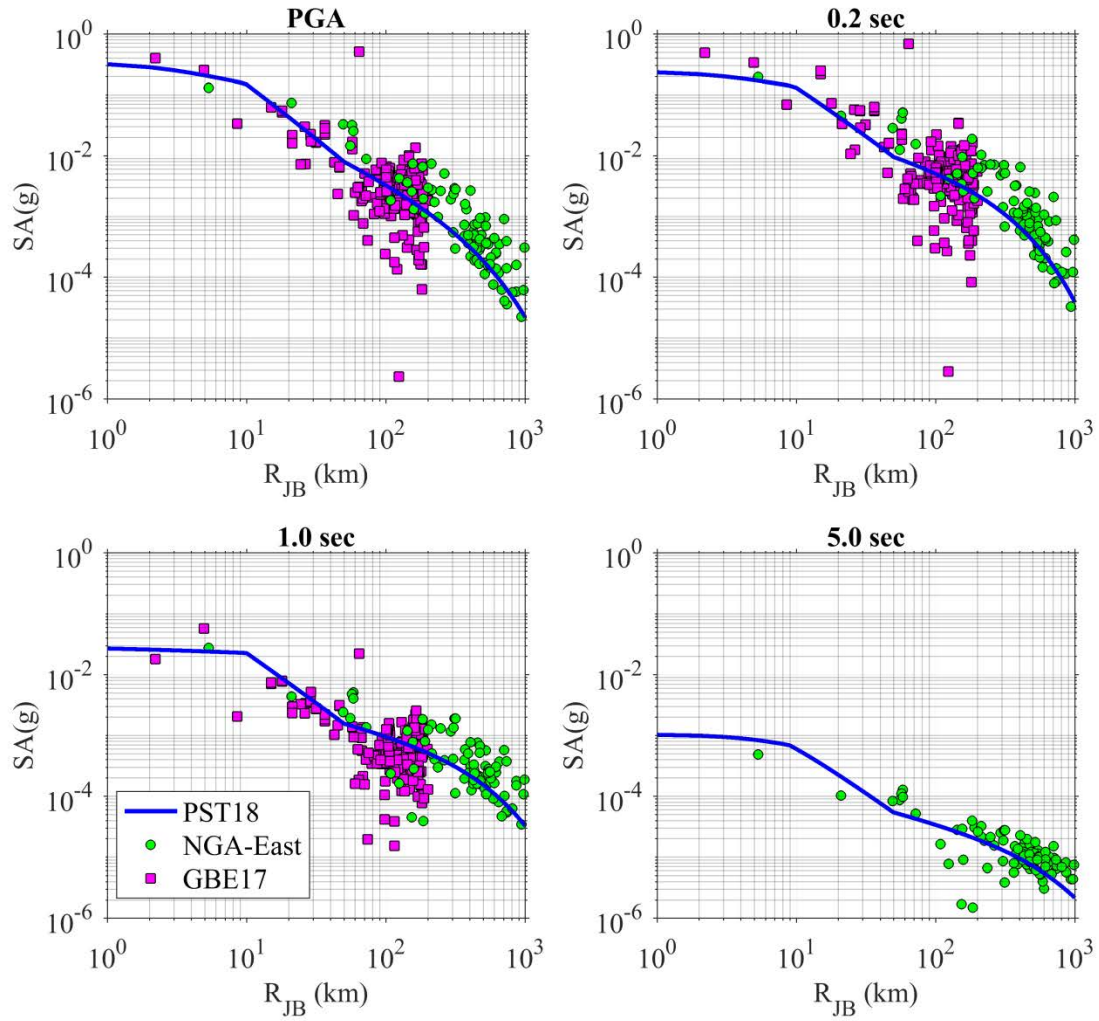
7. Summary, Conclusions, and Future Work

7.1 Summary of the Current Study

Near source and high magnitude recordings of ground motions are of great interest to both seismologists and engineers particularly for performing probabilistic seismic hazard assessment (PSHA) and engineering design. In seismically active areas, there are many near source and high magnitude events to create a robust database. However, there is an essential need to use synthetic data regions such as central and eastern North America where there is a scarcity of recorded large events. Furthermore, there is a great need for strong motion time histories in case of nonlinear performance for complex structures such as tall buildings, long span bridges, structures with base isolations, or structures supported by damping devices.

Many different techniques have been proposed to simulate synthetic time histories including physics-based, stochastic, and hybrid approaches. The problem of physics-based and hybrid approaches is that they require many input parameters and details about the source, path, and site terms. In addition, these methods are often computationally expensive. On the other hand, most stochastic methods particularly those constructed based on point-source models ignore important characteristics of finite fault rupture such as source-to-site geometry, rupture propagation, and asperities. In this report, the two-stage stochastic summation of Green's functions method (SSGFM) is combined with the definition of the effective point-source distance to employ the simplicity of the stochastic method and to augment the accuracy of simulations. Using this method, three components of a strong ground motion can be simultaneously predicted in the whole frequency range.

The required input parameters for SSGFM are values of the stress drop and the moment magnitude of both the target and small events. Then, the time series of the postulated large (target) earthquake can be simulated as a linear combination of observed small earthquakes. In this simulation technique, the target fault is divided into a specific number of identical sub-faults having the same characteristics of the small event fault. Then, time series from the considered sub-faults are shifted and are added together to construct the large target earthquake time series. Since deterministic or theoretic Green's functions are difficult to obtain due to the complex

244

nature of the propagation path and site through which seismic waves propagate. Hartzell (1978) suggested using small earthquakes which have effectively impulse source time function, and thereby, they reflect the effects of the propagation path (geometrical spreading and attenuation) and site responses (amplification and near-site distance independent). In fact, these small events can be considered as empirical Green's function (EGF).

In Chapter 1, two improvements were proposed to extend SSGFM. In Chapters 2 and 3, the first improvement was achieved, which is the generalization and extension of the summation scheme to the general SCF and DCF source models. In Chapter 4, the second improvement was achieved, which is the definition of another distance metric, called effective point-source distance, to capture the effect of source-to-site geometry of the fault on simulations. In Chapter 5, we tested and verified the proposed summation schemes and developed codes using a variety of synthetics and real ground motions. Finally in Chapter 6, the improved SSGFM was employed for CENA to generate region-specific time series and the derived PGV, PGA, and PSA values were used to develop a new set of GMPEs for CENA. Comparing the results with other exsiting GMPEs developed for CENA and observed ground motions in this region, we concluded that the SSGFM can reproduce ground motions that the PGV, PGA, and PSA values estimated from synthetics match well the estimated values from observed ground motions.

7.2 Achievements and Conclusions

The significant achievements and findings of this study are summarized as follows:

- Generalization of the summation scheme: one-stage and two-stage summation schemes for the SCF and DCF source models following the general forms proposed by Boore *et al*. (2014) were defined to follow the source scaling relationships.
- Analytical equations to obtain the effective distance: analytical equations were derived to obtain the effective distance for a given JB distance based on general input parameters such as the geometrical spreading and anelastic attenuation functions.
- Application to very large earthquakes: using the synthetic ground motions and observed ground motions of the 2011 **M**9 Tohoku Japan subduction earthquake, it was shown that SSGFM is capable of generating and simulating time series for very large earthquakes.

- Application to CENA and to develop time series for this region: using the developed method in this report, the improved SSGFM, which was combined with the definition of the effective point-source distance, a large set of time series was synthesized for CENA. Then, the latest and the most updated seismological and geological characteristics were incorporated in simulations. The synthetics generated in this study can be employed for structural analysis and design purposes in this region considering the effects of finite-fault rupture.

- Development of a new suite of GMPEs for CENA for implementation in seismic hazard assessment: the derived GMPEs are applicable for earthquakes with moment magnitudes ranging from 3.5 to 8.0 and Joyner-Boore distances up to 1000 km for sites with V_{S30} of 3 km/sec.

7.3 Recommendations for Future Studies

The research presented in this report can be considered as a reference point in the simulation of large earthquakes by the stochastic summation of Green's functions. However, several studies are recommended to improve and extend the various topics presented in this study as follows:

- Generalized summation scheme for the case that the GF has a SCF source model and the target event has a DCF source model: in this report, both GF and target event follow identical source models (both follow the SCF source model or both follow the DCF source model). As an improvement, the summation scheme can be updated to use GFs following the SCF source model and to construct large earthquakes conforming the DCF source model.

- Multiple-stage summation scheme: the summation schemes developed in this study are performed in one stage or two stages. The new recommended scheme would be similar to EXSIM with a dynamic corner frequency in which the corner frequency of subsources decrease (see Atkinson and Assatourians, 2015: SCEC). In the dynamic corner frequency model, the frequency content of a radiated seismic wave moves towards lower frequencies as the rupture propagates. To do summation in multiple-stages, many small to moderate events between the GF and the target event should be defined and those small

to moderate events are scaled, shifted, and added gradually to follow the source scaling relationships.

- Evaluating the aleatory uncertainty of the developed GMPEs: if the recorded data are correctly modified to adjust for hard rock sites, then the between-event and within-event components of the aleatory uncertainty can be determined using a regression analysis.

- Accounting for epistemic uncertainty: different input parameters such as stress drop and geometrical spreading and anelastic attenuation can be used in simulations to capture the effect of epistemic uncertainty.

- Development of GMPEs for CENA based on the DCF source model instead of the SCF: in this report, it was assumed that the source scaling follows a SCF model. Following the proposed DCF source models for CENA, a new set of simulations and thus GMPEs can be derived.

References

1) Abercrombie, R. E. (1995). Earthquake source scaling relationships from -1 to 5 ML using seismograms recorded at 2.5-km depth, *J. Geophys. Res.* **100**, 24,015–24,036.

2) Abrahamson, N. A., and P. G. Somerville (1996). Effects of the Hanging Wall and Footwall on Ground Motions Recorded during the Northridge earthquake, *Bull. Seism. Soc. Am.* **86**, 93–99.

3) Aki, K. (1967). The scaling law of seismic spectrum, *J. Geophys. Res.* **72**, 1217–1231.

4) Aki, K. (1968). Seismic displacements near a fault, *J. Geophys. Res.* **73**, 5359–5376.

5) Aki, K. (1982). Strong motion prediction using mathematical modeling techniques, *Bull. Seism. Soc. Am.* **72**, S29–S41.

6) Aki, K. (1984). Asperities, barriers, characteristic earthquakes and strong motion prediction, *J. Geophys. Res.* **89**, 5867–5872.

7) Aki, K., M. Bouchon, B. Chouet, and S. Das (1977). Quantitative prediction of strong motion for a potential earthquake fault, *Ann. Geofis.* **30**, 341–368.

8) Aki, K., and P. G. Richards (2002). *Quantitative Seismology*, *Second Ed.*, University Science Books, Sausalito, California.

9) Al Noman, M., and C. H. Cramer (2015). Point-Source Stochastic-Method Simulations of Ground Motions for the PEER NGA-East Project, Chapter 8 in NGA-East: Median Ground-Motion Models for the Central and Eastern North America Region, *PEER Report 2015/04*, Pacific Earthquake Engineering Research Center, 193–212.

10) Anderson, J. G. (2004). Quantitative measure of the goodness-of-fit of synthetic seismograms. *In: 13th world conference on earthquake engineering conference proceedings*, Vancouver, Canada, Paper.

11) Anderson, J. G., and S. E. Hough (1984). A model for the shape of the Fourier amplitude spectrum of acceleration at high frequencies, *Bull. Seism. Soc. Am.* **74**, 1969–1993.

12) Anderson, J. G., P. Bodin, J. N. Brune, J. Prince, S. K. Singh, R. Quaas, and M. Onate (1986). Strong ground motion from the Michoacan, Mexico, earthquake, *Science* **233**, 1043-1049.

13) Andrews, D. J. (2001). A suggestion for fitting ground-motion attenuation near an extended earthquake source, *Seismol. Res. Lett.* **72**, 454–461.

14) Archuleta, R. J., and C. Ji (2016). Moment rate scaling for earthquakes $3.3 \leq \mathbf{M} \leq 5.3$ with implications for stress drop, *Geophys. Res. Lett.* **43(23)**, 1-18.

15) Arias, A. (1970). *A measure of earthquake intensity, in Seismic Design for Nuclear Power Plants*, R. J. Hansen (Editor), MIT Press, Cambridge, Massachusetts, 438–483.

16) Atkinson, G. (2004). Empirical attenuation of ground motion spectral amplitudes in southeastern Canada and the northeastern United States, *Bull. Seism. Soc. Am.* **94**, 1079–1095.

17) Atkinson, G. M. and D. M. Boore (1995). Ground motion relations for eastern North America, *Bull. Seismol. Soc. Am.* **85**, 17–30.

18) Atkinson, G. M., and W. Silva (2000). Stochastic modeling of California ground motions, *Bull. Seismol. Soc. Am.* **90**, 255–274.

19) Atkinson, G. M. and E. Sonley (2003). Ground-motions for the M 5.0 Au sable Forks earthquake, *Seismol. Res. Lett.* **74**, 339–349.

20) Atkinson, G. M., and D. M. Boore (2006). Earthquake ground-motion prediction equations for eastern North America, *Bull. Seism. Soc. Am.* **96(6)**, 2181–2205.

21) Atkinson, G. M., K. Assatourians, D. M. Boore, K. Campbell, and D. Motazedian (2009). A guide to differences between stochastic point-source and stochastic finite-fault simulations, *Bull. Seism. Soc. Am.* **99(6)**, 3192–3201.

22) Atkinson, G. M., and D. M. Boore (2011). Modifications to existing ground-motion prediction equations in light of new data, *Bull. Seismol. Soc. Am.* **101**, 1121–1135.

23) Atkinson, G. M., and D. M. Boore (2014). The attenuation of Fourier amplitudes for rock sites in eastern North America, *Bull. Seism. Soc. Am.* **104(1)**, 513–528.

24) Baker, J. W. (2011). Conditional mean spectrum: Tool for ground-motion selection, *J. Struct. Eng.* **137**, 322–331.

25) Bender, B., and D. M. Perkins (1987). SEISRISK III, A computer program for seismic hazard estimation, *U.S. Geol. Surv. Bull.* **1772**, 1–20.

26) Beresnev, I. A., and G. M. Atkinson (1997). Modeling finite-fault radiation from the ω^n spectrum, *Bull. Seism. Soc. Am.* **87(1)**, 67–84.

27) Beresnev, I. A., and G. M. Atkinson (1998). FINSIM: A FORTRAN program for simulating stochastic acceleration time histories from finite faults, *Seismol. Res. Lett.* **69**, 27–32.

28) Boatwright, J. (1981). Quasi-dynamic models of simple earthquake: an application to an aftershock of the 1975 Oroville, California earthquake, *Bull. Seis. Soc. Am.* **71**, 69–94.

29) Boatwright, J. (1988). The seismic radiation from composite models of faulting, *Bull. Seism. Soc. Am.* **78**, 489–508.

30) Boatwright, J. (1994), Regional propagation characteristics and source parameters of earthquakes in northeastern North America, *Bull. Seismol. Soc. Am.* **84**, 1–15.

31) Boatwright, J., and L. Seekins (2011). Regional spectral analysis of three moderate earthquakes in northeastern North America, *Bull. Seismol. Soc. Am.* **101**, 1769–1782.

32) Bommer, J. J., and S. Akkar (2012). Consistent source-to-site distance metrics in ground-motion prediction equations and seismic source models for PSHA, *Earthq. Spectra* **28**, 1–15.

33) Boore, D. M. (1973). The effect of simple topography on seismic waves: Implications for the accelerations recorded at Pacoima dam, San Fernando Valley, California, *Bull. Seism. Soc. Am.* **63**, 1603–1609.

34) Boore, D. M. (1983). Stochastic simulation of high-frequency ground motions based on seismological models of the radiated spectra, *Bull. Seism. Soc. Am.* **73**, 1865–1894.

35) Boore, D. M. (1999). Basin waves on a seafloor recording of the 1990 Upland, California, earthquake: Implications for ground motions from a larger earthquake, *Bull. Seism. Soc. Am.* **89(1)**, 317–324.

36) Boore, D. M. (2003). Simulation of ground motion using the stochastic method, *Pure Appl. Geophys.* **160**, 635–676.

37) Boore, D. M. (2005). SMSIM; FORTRAN programs for simulating ground motions from earthquakes: Version 2.3 A revision of OFR 96-80-A, *U.S. Geol. Surv. Open-File Rept.* (a modified version of OFR 00-509, describing the program as of 15 August 2005 [version 2.30]).

38) Boore, D. M. (2009). Comparing stochastic point-source and finite-source ground-motion simulations: SMSIM and EXSIM, *Bull. Seism. Soc. Am.* **99**, 3202–3216.

39) Boore, D. M. (2015). Point-Source Stochastic-Method Simulations of Ground Motions for the PEER NGA-East Project, Chapter 2 in NGA-East: Median Ground-Motion Models for the Central and Eastern North America Region, *PEER Report 2015/04*, Pacific Earthquake Engineering Research Center, 11–49.

40) Boore, D. M. (2018). Ground-motion models for very-hard rock sites in eastern North America: An update, *Seismol. Res. Lett.* **89**.

41) Boore, D. M., and J. Boatwright (1984). Average body-wave radiation coefficients, *Bull. Seism. Soc. Am.* **74(5)**, 1615–1621.

42) Boore D. M., K. W. Campbell, and G. M. Atkinson (2010). Determination of stress parameters for eight well-recorded earthquakes in eastern North America, *Bull. Seismol. Soc. Am.*, **100**, 1632–1645.

43) Boore D. M., and E. M. Thompson (2014). Path durations for use in the stochastic-method simulation of ground motions, *Bull. Seism. Soc. Am.* **104**, 2541–2552.

44) Boore, D. M., C. Di Alessandro, and N. A. Abrahamson (2014). A generalization of the double-corner-frequency source spectral model and its use in the SCEC BBP Validation Exercise, *Bull. Seism. Soc. Am.* **104(5)**, 2387–2398.

45) Boore, D. M., J. P. Stewart, E. Seyhan, and G. M. Atkinson (2014). NGA-West2 Equations for Predicting PGA, PGV, and 5% Damped PSA for Shallow Crustal Earthquakes, *Earthq. Spectra* **30**, 1057–1085.

46) Boore, D. M., and E. M. Thompson (2015). Revisions to some parameters used in stochastic-method simulations of ground motion, *Bull. Seism. Soc. Am.* **105(2)**, 1029–1041.

47) Bouchon, M. (1981). A simple method to calculate Green's functions for elastic layered media, *Bull. Seism. Soc. Am.* **71(4)**, 959–971.

48) Bouchon, M. (2003). A review of the discrete wavenumber method, *Pure Appl. Geophys.* **160**, 445–465.

49) Bour, M., and M. Cara (1997). Test of a simple empirical Green's function method on moderate size earthquake, *Bull. Seism. Soc. Am.* **87**, 668–683.

50) Bozorgnia, Y., M. M. Hachem, and K. W. Campbell (2010). Ground motion prediction equation ("Attenuation Relationship") for inelastic response spectra, *Earthq. Spectra* **26**, 1–23.

51) Brune, J. N. (1970). Tectonic stress and the spectra of seismic shear waves from earthquakes, *J. Geophys. Res.* **75**, 4997–5009.

52) Brune, J. N. (1971). Correction, *J. Geophys. Res.* **76**, 5002.

53) Burridge, R., and L. Knopoff (1964). Body force equivalents for seismic dislocations, *Bull. Seism. Soc. Am.* **54**, 1875–1888.

54) Campbell, K. W., and Y. Bozorgnia (2014). NGA-West2 Ground Motion Model for the Average Horizontal Components of PGA, PGV, and 5% Damped Linear Acceleration Response Spectra, *Earthq. Spectra* **30**, 1087–1115.

55) Campbell, K.W., Y. M. A. Hashash, B. Kim, A. R. Kottke, E. M. Rathje, W. J. Silva, J. P. Stewart (2014). Reference rock site conditions for Central and Eastern North America: Part II – Attenuation definition, *PEER Report 2014-12*, Pacific Earthquake Engineering Research Center, University of California, Berkeley, CA, 1–80.

56) Chapman, M. C., and R. W. Godbee (2012). Modeling geometrical spreading and the relative amplitudes of vertical and horizontal high frequency ground motions in eastern North America, *Bull. Seismol. Soc. Am.* **102**, 1957–1975.

57) Choy, G. L., and J. W. Dewey (1988). Rupture process of an extended earthquake sequence: teleseismic analysis of the Chilean earthquake of March 3, 1985, *J. Geophys. Res.* **93**, 1103–1118.

58) Conte, J. (1992). Nonstationary ARMA modeling of seismic motions, *Soil Dyn. Earthq. Eng.* **11**, 411–426.

59) Dabaghi, M. N. (2014). *Stochastic Modeling and Simulation of Near-Fault Ground Motions for Performance-Based Earthquake Engineering*, Ph.D. thesis, Department of Civil and Environmental Engineering, University of California, Berkeley, CA.

60) Das, S., and K. Aki (1977). Fault planes with barriers: a versatile earthquake model, *J. Geophys. Res.* **82**, 5648–5670.

61) Donahue, J. L., and N. A. Abrahamson (2014). Simulation-based hanging wall effects model, *Earthq. Spectra*, **30**, 1269–1284.

62) Douglas, J., and H. Aochi (2008). A survey of techniques for predicting earthquake ground motions for engineering purposes, *Surv. Geophys.* **29**, 187–220.

63) Dreger, D. S., G. C. Beroza, S. M. Day, C. A. Goulet, T. H. Jordan, P. A. Spudich, and J. P. Stewart (2014). Validation of the SCEC broadband platform v14. 3 simulation methods using pseudospectral acceleration data, *Seismol. Res. Lett.* **86(1)**, 39–47.

64) Electric Power Research Institute, EPRI (2004). *CEUS Ground Motion Project: Final Report*, EPRI Report 1009684 Palo Alto, CA.

65) Eshelby, J. D. (1957). The determination of the elastic field of an ellipsoidal inclusion, and related problems, *Proc. Roy. Soc. Lond. Math. Phys. Sci.* **241**, 376–396.

66) Frankel, A. (1995). Simulating strong motions of large earthquakes using recordings of small earthquakes: the Loma Prieta mainshock as a test case, *Bull. Seism. Soc. Am.* **85(4)**, 1144–1160.

67) Frankel, A. (2009). A constant stress-drop model for producing broadband synthetic seismograms: comparison with the Next Generation Attenuation relations, *Bull. Seism. Soc. Am.* **99**, 664–680.

68) Frankel, A. (2015). Decay of S-wave amplitudes with distance for earthquakes in the Charlevoix, Quebec, area: Effects of radiation pattern and directivity, *Bull. Seismol. Soc. Am.* **105**, 850–857.

69) Frankel, A. (2017). Modeling strong-motion recordings of the 2010 M_w 8.8 Maule, Chile, earthquake with high stress-drop subevents and background slip, *Bull. Seism. Soc. Am.* **107(1)**, 372–386.

70) Ghofrani, H., G. M. Atkinson., and K. Goda (2012). Implications of the 2011 **M** 9.0 Tohoku Japan earthquake for the treatment of site effect large earthquakes, *Bull. Earthq. Eng.,* **11**, 171–203.

71) Ghofrani, H., G. Atkinson, K. Goda, and K. Assatourians (2013). Stochastic finite-fault simulations of the 2011 Tohoku, Japan, earthquake, *Bull. Seismol. Soc. Am.* **103**, 1307–1320.

72) Goda, K., and G. M. Atkinson (2014). Variation of source-to-site distance for megathrust subduction earthquakes: effects on ground motion prediction equations, *Earthq. Spectra* **30**, 845–866.

73) Goda, K., H. P. Hong, and G. M. Atkinson (2010). Impact of using updated seismic information on seismic hazard in western Canada, *Can. J. Civ. Eng.* **37**, 562–575.

74) Goulet, C. A., N. A. Abrahamson, P. G. Somerville, and K. E. Wooddell (2014). The SCEC broadband platform validation exercise: Methodology for code validation in the context of seismic-hazard analyses, *Seismol. Res. Lett.* **86(1)**, 17–26.

75) Goulet, C. A., C. H. Cramer, R. B. Darragh, W. J. Silva, Y. M. A. Hashash, J. Harmon, J. P. Stewart, K. E. Wooddell, and R. R. Youngs (2014). PEER NGA-East database, *PEER Report Number 2014/17*, Pacific Earthquake Engineering Research Center, Berkeley, California.

76) Graves, R. W., and A. Pitarka (2010). Broadband ground-motion simulation using a hybrid approach, *Bull. Seism. Soc. Am.* **100**, 2095–2123.

77) Graves, R., A. Pitarka, N. Collins, and P. Somerville (1999). Goodness of Fit in Simulated Near-Fault Long Period Ground Motions, *Final Report, PG&E-PEER Directed Studies Program, Phase II*, URS Greiner Woodward Clyde, Pasadena, CA.

78) Gupta, A., J. W. Baker, and W. L. Ellsworth (2017). Assessing ground-motion amplitudes and attenuation for small-to-moderate induced and tectonic earthquakes in the central and eastern United States, *Seismol. Res. Lett.* **88(5)**, 1379–1389.

79) Haji-Soltani, A. (2017). A comprehensive site-specific probabilistic seismic hazard analysis for a liquid natural gas tank located in the gulf coast region, *Ph.D. Dissertation*, The University of Memphis, Memphis, Tennessee.

80) Haji-Soltani, A., and S. Pezeshk (2017). A comparison of different approaches to incorporate site effects into PSHA: a case study for a liquefied natural gas tank, *Bull. Seismol. Soc. Am.* **107**, 2927–2947.

81) Haji-Soltani, A., S. Pezeshk, M. Malekmohammadi, and A. Zandieh (2017). A study of vertical-to-horizontal ratio of earthquake components in the Gulf coast region, *Bull. Seismol. Soc. Am.* **107**, 2055–2066.

82) Halldorsson, B., and A. S. Papageorgiou (2005). Calibration of the specific barrier model to earthquakes of different tectonic regions, *Bull. Seismol. Soc. Am.* **95**, 1276–1300.

83) Hanks, T. C., and H. Kanamori (1979). A moment magnitude scale, *J. Geophys. Res.* **84**, 2348–2350.

84) Hanks, T. C., and R. K. McGuire (1981). The character of high frequency strong ground motion, *Bull. Seism. Soc. Am.* **71**, 2071–2095.

85) Hartzell, S. H. (1978). Earthquake aftershocks as Green's functions, *Geophys. Res. Lett.* **5**, 1–4.

86) Hartzell, S., M. Guatteri, G. Mariagiovanna, P. M. Mai, P.-C. Liu, and M. Fisk (2005). Calculation of broadband time histories of ground motion, Part II: Kinematic and dynamic modeling using theoretical Green's functions and comparison with the 1994 Northridge earthquake, *Bull. Seism. Soc. Am.* **95**, 614–645.

87) Haskell, N. (1964). Total energy and energy spectral density of elastic wave radiation from propagating faults, *Bull. Seism. Soc. Am.* **54**, 1811–1842.

88) Haskell, N. (1966). Total energy and energy spectral density of elastic wave radiation from propagating faults, 2, A statistical source model, *Bull. Seism. Soc. Am.* **56**, 125–140.

89) Haskell, N. A. (1969). Elastic displacements in the near-field of a propagating fault, *Bull. Seism. Soc. Am.* **59**, 865–908.

90) Hassani, B., and G. M. Atkinson (2016). Applicability of the NGAWest2 site-effects model for central and eastern North America, *Bull. Seismol. Soc. Am.* **106**, 1331–1341.

91) Hiramatsu, Y., H. Yamanaka, K. Tadokoro, K. Nishigami, and S. Ohmi (2002). Scaling law between corner frequency and seismic moment of microearthquakes: Is the

breakdown of the cube law a nature of earthquakes?, *Geophys. Res. Lett.* **29(8)**, 52-1–52-3.

92) Hutchings, L. J. (1987). Modeling near-source earthquake ground motion with empirical Green's functions. *Ph.D. Dissertation. Department of Geological Sciences, State University of New York, Binghamton, New York*, 1–180.

93) Hutchings, L. (1992). Modeling Earthquake Ground Motion with an Earthquake Simulation Program (EMPSYN) that Utilizes Empirical Green's Functions, *Lawrence Livermore National Lab.* **UCRL-ID-105890**, 1–119.

94) Hutchings, L. (1994). Kinematic Earthquake Models and Synthesized Ground Motion Using Empirical Green's Functions, *Bull. Seism. Soc. Am.* **84**, 1028–1050.

95) Hutchings, L., and F. Wu (1990). Empirical Green's Functions from small earthquakes: A waveform study of locally recorded aftershocks of the 1971 San Fernando Earthquake, *J. Geophys. Res.* **95**, 1187–1214.

96) Hutchings, L., and G. Viegas (2012). Application of empirical Green's functions in earthquake source, wave propagation and strong motion studies. In: D'Amico, S. (Ed.), *Earthquake Research and Analysis–New Frontiers in Seismology*. InTech, Rijeka, Croatia, pp. 87–140, ISBN: 978–953–307–840–3.

97) Ide, S., and G. C. Beroza (2001). Does apparent stress vary with earthquake size?, *Geophys. Res. Lett.* **28**, 3349–3352.

98) Irikura, K. (1983). Semi-empirical estimation of strong ground motions during large earthquakes, *Bull. Disaster. Prevention. Res. Inst. (Kyoto University)* **32**, 63–104.

99) Irikura, K. (1986). Prediction of strong acceleration motion using empirical Green's function, *Proc. 7th Japan Earthq. Eng. Symp.* **151**, 151–156.

100) Irikura, K., and K. Kamae (1994). Estimation of strong ground motion in broad-frequency band based on a seismic source scaling model and an empirical Green's function technique, *Ann. Geofis.* **37**, 1721–1743.

101) Izutani, Y., and H. Kanamori (2001). Scale-dependence of seismic energy-to-moment ratio for strike-slip earthquakes in Japan, *Geophys. Res. Lett.* **28**, 4007–4010.

102) Jarpe, S. P., and P. W. Kasameyer (1996). Validation of a Procedure for Calculating Broadband Strong-Motion Time Histories with Empirical Green's Functions, *Bull. Seism. Soc. Am.* **86**, 1116–1129.

103) Joyner, W. B. (1984). A scaling law for the spectra of large earthquakes, *Bull. Seismol. Soc. Am.* **74(4)**, 1167–1188.

104) Joyner, W. B., and D. M. Boore (1986). On simulating large earthquakes by Green's function addition of smaller earthquakes, in *Earthquake Source Mechanics*, Vol. 37, *Maurice Ewing Series 6,* S. Das, J. Boatwright, and C. H. Scholtz (Editors), American Geophysical Union, Washington, D.C., 269–274.

105) Joyner, W. B., and D. M. Boore (1988). Measurement, characterization, and prediction of strong ground motion, in *Earthquake Engineering and Soil Dynamics If-Recent Advances in Ground Motion Evaluation*, J. L. Von Thun (Editor), A.S.C.E., New York, 43–102.

106) Kaklamanos, J., L. G. Baise, and D. M. Boore (2011). Estimating unknown input parameters when implementing the NGA ground-motion prediction equations in engineering practice, *Earthq. Spectra* **27**, 1219–1235.

107) Kamae, K., K. Irikura, and A. Pitarka (1998). A technique for simulating strong ground motions using hybrid Green's functions, *Bull. Seismol. Soc. Am.* **88**, 357–367.

108) Kanamori, H. (1979). A semi-empirical approach to prediction of long-period ground motions from great earthquakes, *Bull. Seism. Soc. Am.* **69**, 1654–1670.

109) Kanamori, H., J. Mori, E. Hauksson, T. Heaton, L. K. Hutton, and L. M. Jones (1993). Determination of earthquake energy release and Ml using Terrascope, *Bull. Seism. Soc. Am.* **83**, 330–346.

110) Kanamori, H., and L. Rivera (2004). Static and dynamic relations for earthquakes and their implications for rupture speed and stress drop, *Bull. Seism. Soc. Am.* **94**, 314–319.

111) Kanamori, H., and G. S. Stewart (1978). Seismological aspects of the Guatemala earthquake of February 4, 1976, *J. Geophys. Res.* **83**, 3427–3434.

112) Keilis-Borok, V. (1959). On estimation of the displacement in an earthquake source and of source dimensions, *Ann. Geofisc.* **12**, 17–20.

113) Kohrs-Sansorny, C., F. Courboulex, M. Bour, and A. Deschamps (2005). A two-stage method for strong ground motions simulations using stochastic summation of small earthquakes, *Bull. Seism. Soc. Am.* **95**, 1387–1400.

114) Kramer, S. L. (1996). *Geotechnical Earthquake Engineering*. Prentice-Hall, Upper Saddle River, New Jersey.

115) Kurahashi, S., and K. Irikura (2011). Source model for generating strong ground motions during the 2011 off the Pacific coast of Tohoku earthquake, *Earth Planets Space* **63**, 571–576.

116) Li, V. C., and R. Dmowska (1981). Asperity model for precursory seismicity patterns for some large earthquakes, *EOS* **62**, 328.

117) Luco, N., and P. Bazzurro (2007). Does amplitude scaling of ground motion records result in biased nonlinear structural drift responses? *Earthq. Eng. Struct. Dynam.* **36**, 1813–1835.

118) Ma, S., and G. Atkinson (2006). Focal depth distribution for earthquakes with MN ≥ 2.8 in western Quebec, southern Ontario and northern New York, *Bull. Seism. Soc. Am.* **96**, 609–623.

119) Madariaga, R. (1976). Dynamics of an expanding circular fault, *Bull. Seism. Soc. Am.* **66**, 636–666.

120) Madariaga, R. (1977). Implications of stress-drop models of earthquakes for the inversion of stress drop from seismic observations, *Stress in the Earth. Birkhäuser Basel*, 301–316.

121) Madariaga, R. (2007). *Seismic source theory, in Treatise on Geophysics*, vol. 4, edited by H. Kanamori, and G. Schubert, pp. 59–82, Elsevier, Amsterdam.

122) Mai, P. M., and G. Beroza (2003). A hybrid method for calculating near-source, broadband seismograms: application to strong motion prediction, *Phys. Earth Planet. Int.* **137**, 183–199.

123) Mai, P. M., P. Spudich, and J. Boatwright (2005). Hypocenter locations in finite-source rupture models, *Bull. Seism. Soc. Am.* **95**, 965–980.

124) Mai, P. M., W. Imperatori, and K. B. Olsen (2010). Hybrid broadband ground-motion simulations: Combining long-period deterministic synthetics with high-frequency multiple S-to-S backscattering, *Bull. Seismol. Soc. Am.* **100**, 2124–2142.

125) McGuire, R. K. (1976). FORTRAN computer program for seismic risk analysis, *U.S. Geol. Surv. Open-File Rept.* 76–67.

126) Moczo, P., J. Kristek, M. Galis, P. Pazak, and M. Balazovjech (2007). The finite-difference and finite-element modeling of seismic wave propagation and earthquake motion, *acta physica slovaca* **57**, 177–406.

127) Motazedian, D., and G. M. Atkinson (2005). Stochastic finite-fault modeling based on a dynamic corner frequency, *Bull. Seism. Soc. Am.* **95**, 995–1010.

128) Munguia, L., and J. N. Brune (1984). Simulations of strong ground motion for earthquakes in the Mexicali-Imperial Valley region, *Geophys. J. Int*, **79**, 747–771.

129) Nazemi, N., S. Pezeshk, and F. Sedaghati (2017). Attenuation of Lg waves in the New Madrid seismic zone of the central United States using the coda normalization method, *Tectonophysics* **712-713**, 623–633.

130) Nozu, A., and K. Irikura (2008). Strong-motion generation areas of a great subduction-zone earthquake: waveform inversion with empirical Green's functions for the 2003 Tokachi-oki earthquake, *Bull. Seismol. Soc. Am.* **98**, 180–197.

131) Ohno, S., T. Ohta, T. Ikeura, and M. Takemura (1993). Revision of attenuation formula considering the effect of fault size to evaluate strong motion spectra in near field, *Tectonophysics*. **218**, 69–81.

132) Ólafsson, S., S. Remseth, and R. Sigbjörnsson (2001). Stochastic models for simulation of strong ground motion in Iceland, *Earthq. Eng. Struct. Dynam.* **30(9)**, 1305–1331.

133) Olsen, K. B. (1994). Simulation of three-dimensional wave propagation in the Salt Lake basin, *Ph.D. Dissertation,* University of Utah, Salt Lake City, Utah, 157 pp.

134) Olsen, K. B., and J. E. Mayhew (2010). Goodness-of-fit criteria for broadband synthetic seismograms, with application to the 2008 Mw 5.4 Chino Hills, CA, earthquake, *Seismol. Res. Lett.* **81**, 715–723.

135) Ordaz, M., J. Arboleda, and S. K. Singh (1995). A scheme of random summation of an empirical Green's function to estimate ground motions from future large earthquakes, *Bull. Seism. Soc. Am.* **85**, 1635–1647.

136) Ou, G.-B., and R. B. Herrmann (1990). Estimation theory for strong ground motion, *Seism. Res. Lett*. **61**, 99–107.

137) Papadimitrios, K. (1990). Stochastic characterization of strong ground motion and applications to structural response. *Report NO. EERL 90-03, Earthquake Engineering Research Laboratory*, California Institute of Technology, Pasadena, CA.

138) Parker, G. A., J. P. Stewart, Y. M. A. Hashash, E. M. Rathje, K. W. Campbell, and W. J. Silva (submitted). Empirical linear seismic site amplification in central and eastern North America, *Earthq. Spectra*.

139) Petersen, M. D., A. D. Frankel, S. C. Harmsen, C. S. Mueller, K. M. Haller, R. L. Wheeler, R. L. Wesson, Y. Zeng, O. S. Boyd, D. M. Perkins, N. Luco, E. H. Field, C. J. Wills, and K. S. Rukstales (2008). Documentation for the 2008 Update of the United States National Seismic Hazard Maps, *U.S. Geol. Surv. Open-File Rept.,* 2008–1128, 1–128.

140) Pezeshk, S., F. Sedaghati, and N. Nazemi (2018a). Near Source Attenuation of High Frequency Body Waves beneath the New Madrid Seismic Zone, *J. Seismol.* **22**, 455–470, https://doi.org/10.1007/s10950-017-9717-6.

141) Pezeshk, S., A. Zandieh, K. W. Campbell, and B. Tavakoli (2018b). Ground Motion Prediction Equations for Central and Eastern North America Using the Hybrid Empirical Method and NGA-West2 Empirical Ground Motion Models, *Bull. Seism. Soc. Am.*

142) Pezeshk, S., A. Zandieh, and A. Haji-Soltani (2017). Hybrid empirical ground-motion prediction equations for the Gulf coast region, *USGS Technical Report*, USGS Award number: G16AP00138.

143) Pezeshk, S., A. Zandieh, and B. Tavakoli (2011). Hybrid empirical ground-motion prediction equations for eastern North America using NGA models and updated seismological parameters, *Bull. Seism. Soc. Am.* **101**, 1859–1870.

144) Pezeshk, S., A. Zandieh, K. W. Campbell, and B. Tavakoli (2015). Ground motion prediction equations for eastern North America using the hybrid empirical method and NGA-West2 empirical ground motion model, in NGA-East: *Median Ground Motion Models for the Central and Eastern North America Region, Chapter 5, PEER Rept. No. 2015/04*, Pacific Earthquake Engineering Research Center, University of California, Berkeley, California, 119–147.

145) Randall, M. J. (1973). The spectral theory of seismic sources, *Bull. Seism. Soc. Am.* **63(3)**, 1133–1144.

146) Raoof, M., R. B. Herrmann, and L. Malagnini (1999). Attenuation and excitation of three-component ground motion in southern California, *Bull. Seismol. Soc. Am.* **89**, 888–902.

147) Rathje, E. M., F. Faraj, S. Russell, and J. D. Bray (2004). Empirical relationships for frequency content parameters of earthquake ground motions, *Earthq. Spectra* **20(1)**, 119–144.

148) Rezaeian, S. (2010). *Stochastic modeling and simulation of ground motions for performance-based earthquake engineering*. Ph.D. Dissertation, Department of Civil and Environmental Engineering, University of California, Berkeley, CA.

149) Sato, H., and M. C. Fehler (1998). *Seismic Wave Propagation and Scattering in the Heterogeneous Earth*, American Institute of Physics Press, New York, New York.

150) Scherbaum, F., J. Schmedes, and F. Cotton (2004). On the conversion of source-to-site distance measures for extended earthquake source models, *Bull. Seism. Soc. Am.* **94(3)**, 1053–1069.

151) Sedaghati, F., and S. Pezeshk (2016a). Investigation of regional differences in strong ground motions for the Iranian plateau, World Academy of Science, Engineering and Technology, *International Journal of Environmental, Chemical, Ecological, Geological and Geophysical Engineering*, **10(6)**, 556–559.

152) Sedaghati, F., and S. Pezeshk (2016b). Comparative study on parameter estimation methods for attenuation relationships, *J. Geophys. Eng.* **13(6)**, 912–927.

153) Sedaghati, F., and S. Pezeshk (2016c). Estimation of the coda-wave attenuation and geometrical spreading in the New Madrid seismic zone, *Bull. Seism. Soc. Am.* **106(4)**, 1482–1498.

154) Sedaghati, F., and S. Pezeshk (2017). Partially nonergodic empirical ground motion models for predicting horizontal and vertical PGV, PGA, and 5% damped linear acceleration response spectra using data from the Iranian plateau, *Bull. Seism. Soc. Am.* **107(2)**, 934–948.

155) Sedaghati, F., S. Pezeshk, and N. Nazemi (2018). Site Amplification within the Mississippi Embayment of the Central United States: Investigation of Possible Differences among Various Phases of Seismic Waves and Presence of Basin Waves, *Soil Dyn. Earthq. Eng.* (submitted).

156) Seyhan, E., and J. P. Stewart (2014). Semi-empirical nonlinear site amplification from NGA-West2 data and simulations, *Earthq. Spectra* **30**, 1241–1256.

157) Shahbazian, A., and S. Pezeshk. (2010). Improved velocity and displacement time histories in frequency-domain spectral-matching procedures. *Bull. Seism. Soc. Am.* **100(6)**, 3213–3223.

158) Shahjouei, A., and S. Pezeshk (2015). Synthetic seismograms using a hybrid broadband ground-motion simulation approach: application to central and eastern United States. *Bull. Seism. Soc. Am.* **105**, 686–705.

159) Shahjouei, A., and S. Pezeshk (2016). Alternative hybrid empirical ground-motion model for central and eastern North America using hybrid simulations and NGA-West2 models, *Bull. Seism. Soc. Am.* **106(2)**, 734–754.

160) Silva, W. J., N. Gregor, and R. B. Darragh (2002). Development of regional hard rock attenuation relations for central and eastern North America, *Report to Pacific Engineering and Analysis*, El Cerrito, CA.

161) Singh, S. K., M. Ordaz, J. G. Anderson, M. Rodriguez, R. Quaas, E. Mena, and D. Almora (1989). Analysis of near-source strong-motion recordings along the Mexican subduction zone, *Bull. Seism. Soc. Am.* **79**, 1697–1717.

162) Somerville, P. G., J. P. McLaren, C. K. Saikia, and D. V. Helmberger (1990). The 25 November 1988 Saguenay, Quebec, earthquake: source parameters and the attenuation of strong ground motion, *Bull. Seism. Soc. Am.* **80**, 1118–1143.

163) Somerville, P. G., M. Sen, and B. Cohee (1991). Simulation of strong ground motions recorded during the 1985 Michoacan, Mexico and Valparaiso, Chile earthquakes, *Bull. Seism. Soc. Am.* **81(1)**, 1–27.

164) Somerville, P. G., N. Collins, N. A. Abrahamson, R. Graves, and C. K. Saikia (2001). "Ground Motion Attenuation Relations for the Central and Eastern United States," *Report to U.S. Geol. Surv. Open-File Rept., NEHRP External Research Program*, Award No. 99–HQ–GR–0098.

165) Spudich, P., and L. Xu (2003). *Software for calculating earthquake ground motions from finite-faults in vertically varying media, in IASPEI International Handbook of Earthquake and Engineering Seismology*, W. H. K. Lee, H. Kanamori, P. C. Jennings, and C. Kisslinger (Editors), Chapter 85.14, Academic Press, New York, New York, 1633–1634.

166) Stewart, J. P., G. A. Parker, J. A. Harmon, G. M. Atkinson, D. M. Boore, R. B. Darragh, W. J. Silva, and Y. M. A. Hashash (2017). Expert Panel Recommendations for Ergodic Site Amplification in Central and Eastern North America, *PEER 2017/03*, Pacific Earthquake Engineering Research Center, University of California, Berkeley, California, 51 pp.

167) Tavakoli, B., and S. Pezeshk (2005). Empirical-stochastic ground-motion prediction for eastern North America, *Bull. Seism. Soc. Am.* **95**, 2283–2296.

168) Tavakoli, B., F. Sedaghati, and S. Pezeshk (2018). An Analytical effective point source-based distance conversion approach to mimic the effects of extended faults on seismic hazard assessment, *Bull. Seismol. Soc. Am.* **108(2)**, 742–760.

169) Triep, E. G., and L. R. Sykes (1997). Frequency of occurrence of moderate to great earthquakes in intracontinental regions: Implications for changes in stress, earthquake prediction, and hazard assessment, *J. Geophys. Res.* **102**, 9923–9948.

170) Triep, E. G., and L. R. Sykes. Catalog of shallow intracontinental earthquakes, www.ideo.columbia.edu/seismology/triep/intra.expl.html.

171) Trifunac, M. D., and A. G. Brady (1976). A study on the duration of strong earthquake ground motion, *Bull. Seismol. Soc. Am.* **65**, 581–626.

172) Tumarkin, A. G., and R. J. Archuleta (1994). Empirical ground motion prediction. *Ann. of Geofis.* **37**, 1691–1720.

173) Tumarkin, A. G., R. J. Archuleta, and R. Madariaga (1994). Scaling relations for composite earthquake models, *Bull. Seism. Soc. Am.* **84(4)**, 1279–1283.

174) Wells, D. L., and K. J. Coppersmith (1994). New empirical relationships among magnitude, rupture length, rupture width, rupture area, and surface displacement, *Bull. Seism. Soc. Am.* **84**, 974–1002.

175) Wennerberg, L. (1990). Stochastic summation of empirical Green's functions, *Bull. Seism. Soc. Am.* **80**, 1418–1432.

176) Wesson, R. L., R. O. Burford, and W. L. Ellsworth (1973). Relationship between seismicity, fault creep and crustal loading along the Central San Andreas Fault, Proc. Conf. Tectonic Problems of the San Andreas Fault System, *Stanford Univ. Publ. Geol. Sci.* **13**, 303–320.

177) Wu, F. T. (1978). Prediction of Strong Ground Motion using Small Earthquakes, *Proc. 2nd International Microzonation Conference* **2**,70 l–704.

178) Wu, F. T. (1981). Ground Motion Prediction and Eastern U.S. Earthquake Monitoring, *U.S. Geol. Surv. Open-File Rept.* **81-944**, 1–6.

179) Yamamoto, Y., and J. W. Baker (2011). Stochastic model for earthquake ground motion using wavelet packets, *Technical Report Blume Center Report* **176**, Stanford, California.

180) Yamamoto, Y., and J. W. Baker (2013). Stochastic model for earthquake ground motion using wavelet packets, *Bull. Seism. Soc. Am.* **103(6)**, 3044–3056.

181) Yenier, E., and G. M. Atkinson (2014). Equivalent point-source modeling of moderate-to-large magnitude earthquakes and associated ground-motion saturation effects, *Bull. Seism. Soc. Am.* **104(3)**, 1458–1478.

182) Yenier, E., and G. M. Atkinson (2015). An equivalent point-source model for stochastic simulation of earthquake ground motions in California, *Bull. Seism. Soc. Am.* **105(3)**, 1435–1455.

183) Zandieh, A., and S. Pezeshk (2010). Investigation of geometrical spreading and quality factor functions in the New Madrid seismic zone, *Bull. Seism. Soc. Am.* **100**, 2185–2195.

184) Zandieh, A., and S. Pezeshk (2011). A study of horizontal-to-vertical component spectral ratio in the New Madrid seismic zone, *Bull. Seism. Soc. Am.* **101**, 287–296.

185) Zeng, Y. H. (1993). Theory of scattered P- and S-wave energy in a random isotropic scattering medium, *Bull. Seismol. Soc. Am.* **83**, 1264–1276.

186) Zeng, Y. H., F. Su, and K. Aki (1991). Scattered wave energy propagation in a random isotropic scattering medium–Part 1. Theory, *J. Geophys. Res.* **96**, 607–619.

187) Zeng, Y., J. G. Anderson, and G. Yu (1994). A composite source model for computing realistic synthetic strong ground motions, *Geophys. Res. Lett.* **21**, 725–728.

188) Zeng, Y. H., J. G. Anderson, and F. Su (1995). Subevent rake and random scattering effects in realistic strong ground motion simulation, *Geophys. Res. Lett.* **22**, 17–20.

189) Zhu, L., and L. Rivera (2002). A note on the dynamic and static displacement from a point source in multilayered media, *Geophys. J. Int.* **148**, 619–627.

Appendix A. Examples

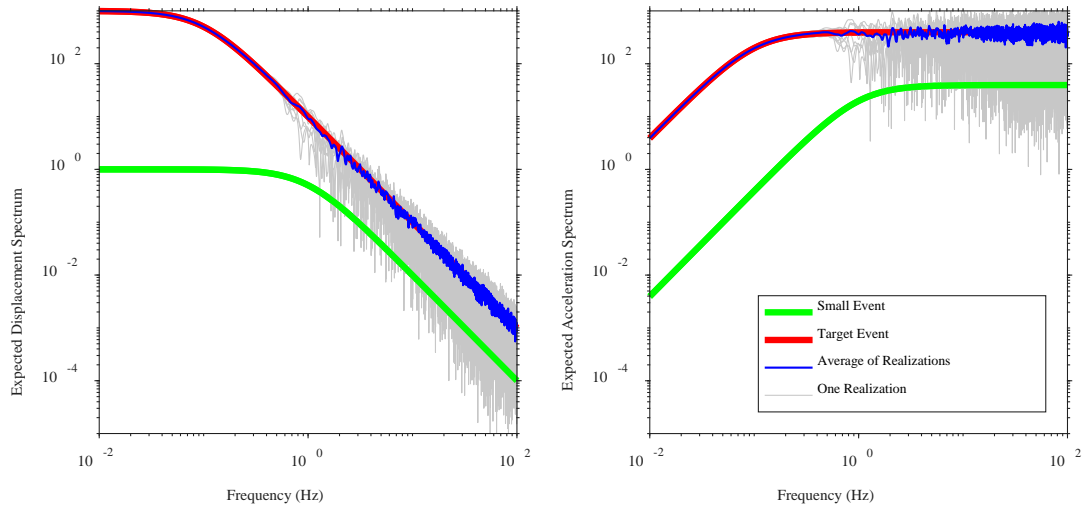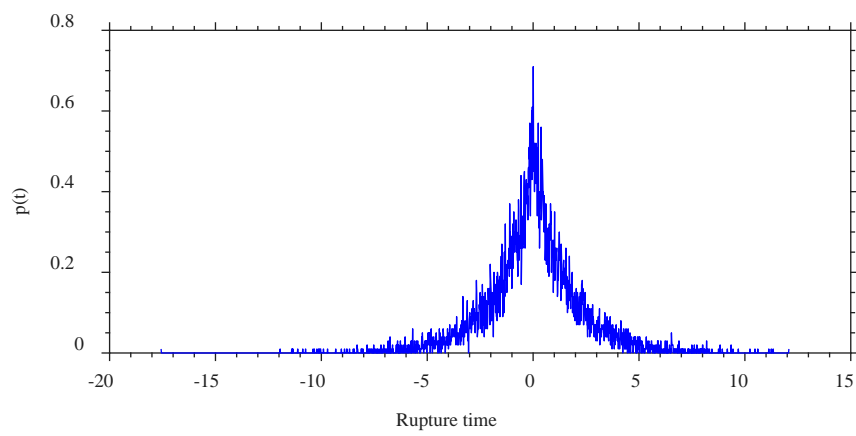Example 2: with $f_{cs} = 1$ Hz, $\Delta\sigma_s = 1$ and $f_{ct} = 0.1$ Hz, $\Delta\sigma_t = 1$
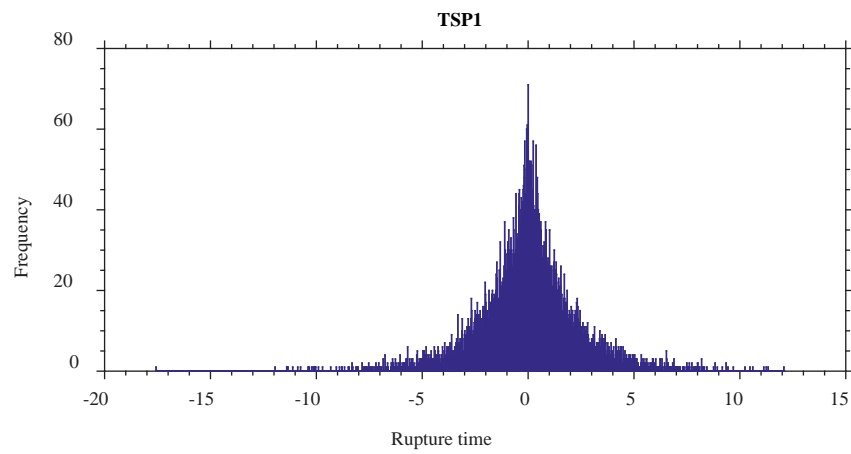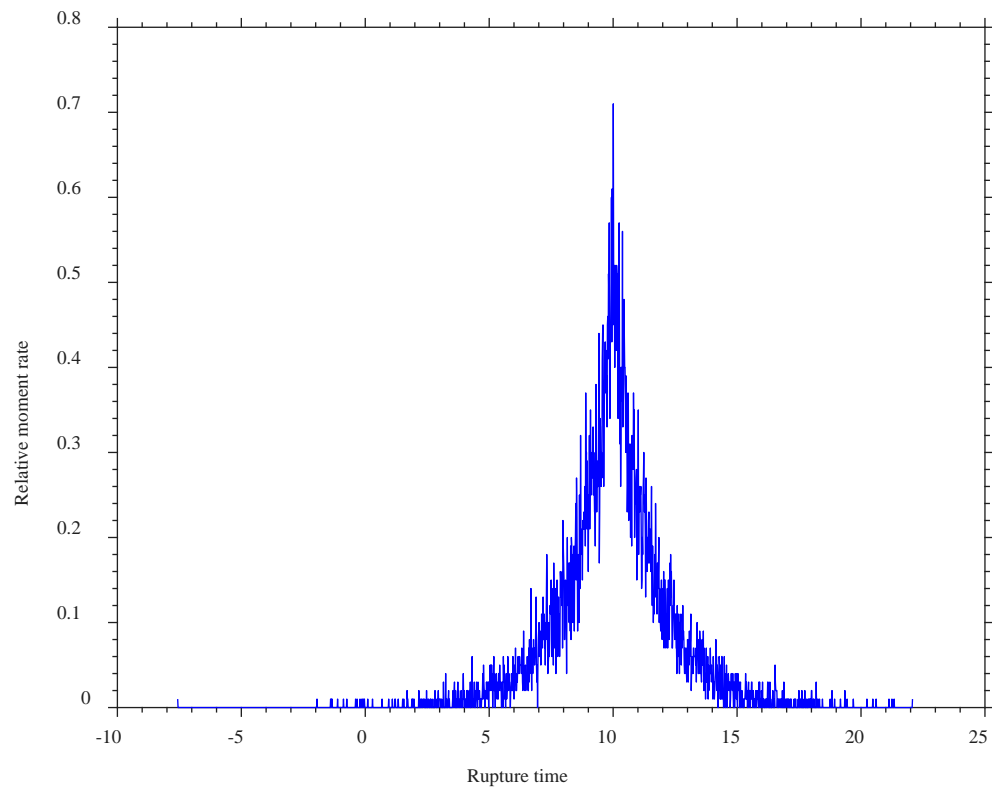
$$M_t = 1$$
$$M_s = 0.001$$
$$f_{ct} = 1$$
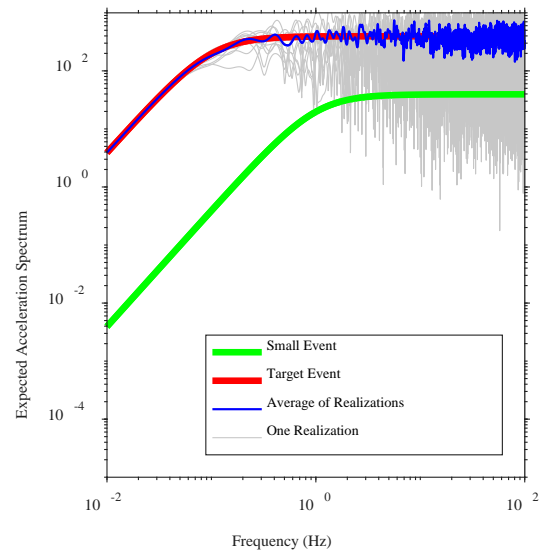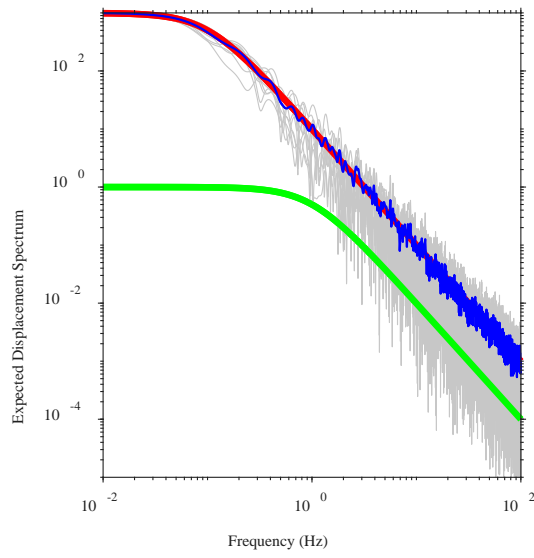$$f_{cs} = 10$$
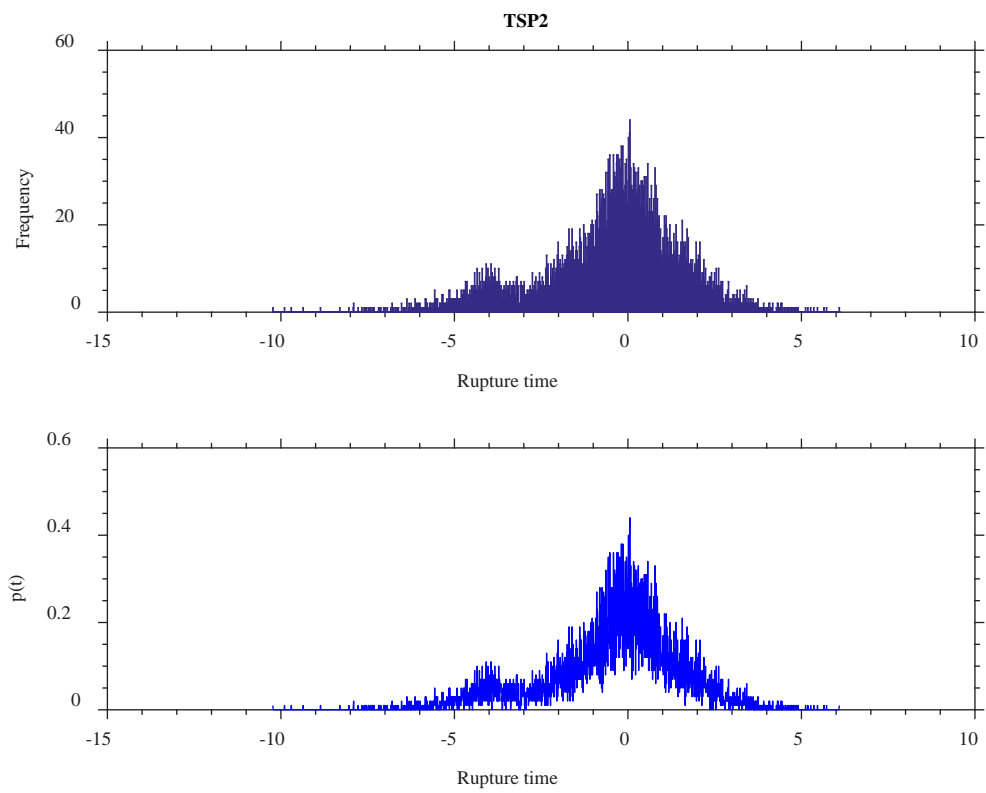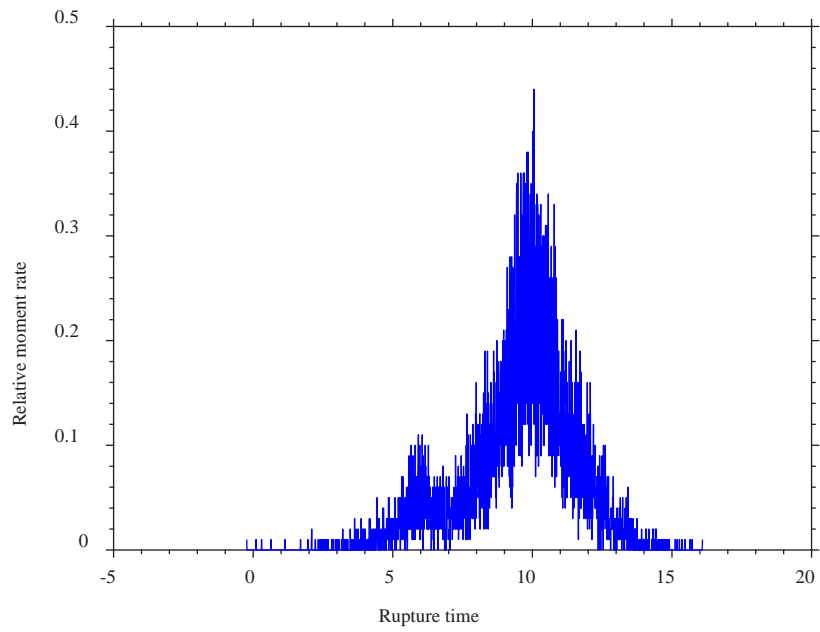
7.3.1.1 *TSP1*

TSP1

TSP2

TSP2

263

Example 3: with f_{cs} = 5 Hz, $\Delta\sigma_s$ = 0.5 and f_{ct} = 0.5 Hz, $\Delta\sigma_t$ = 2
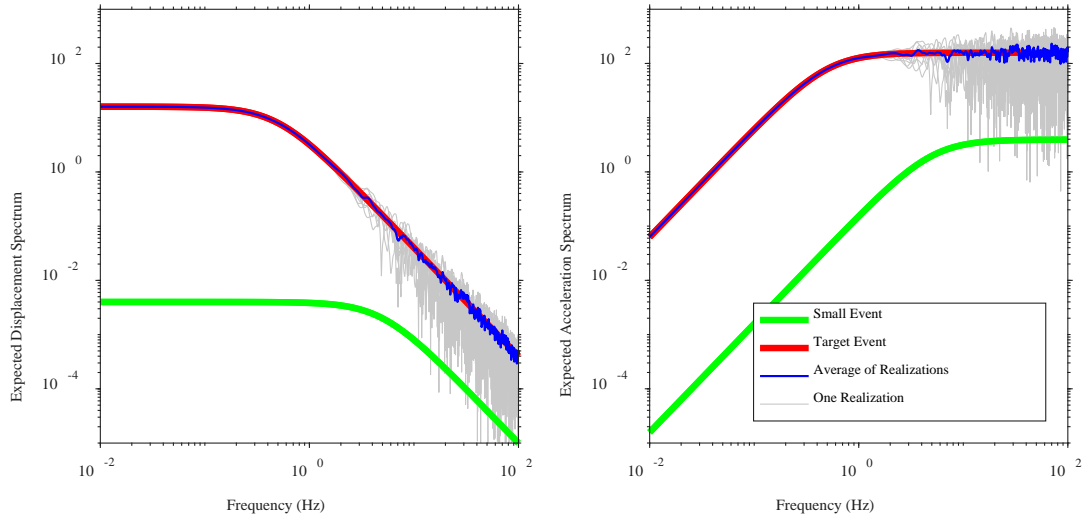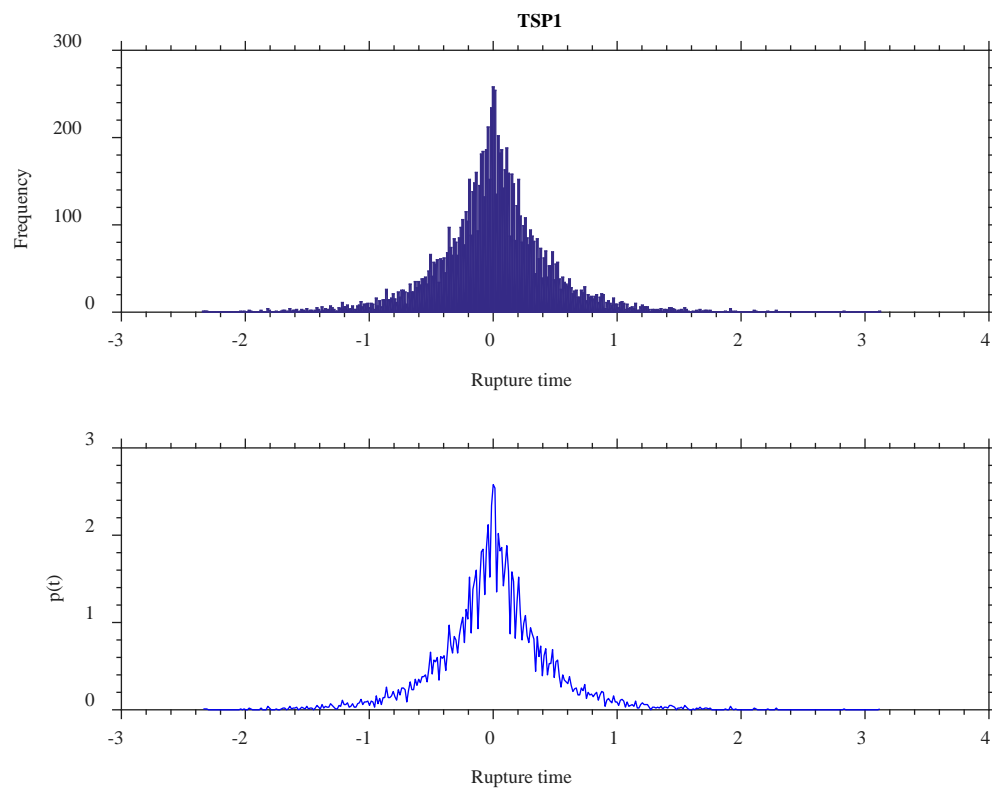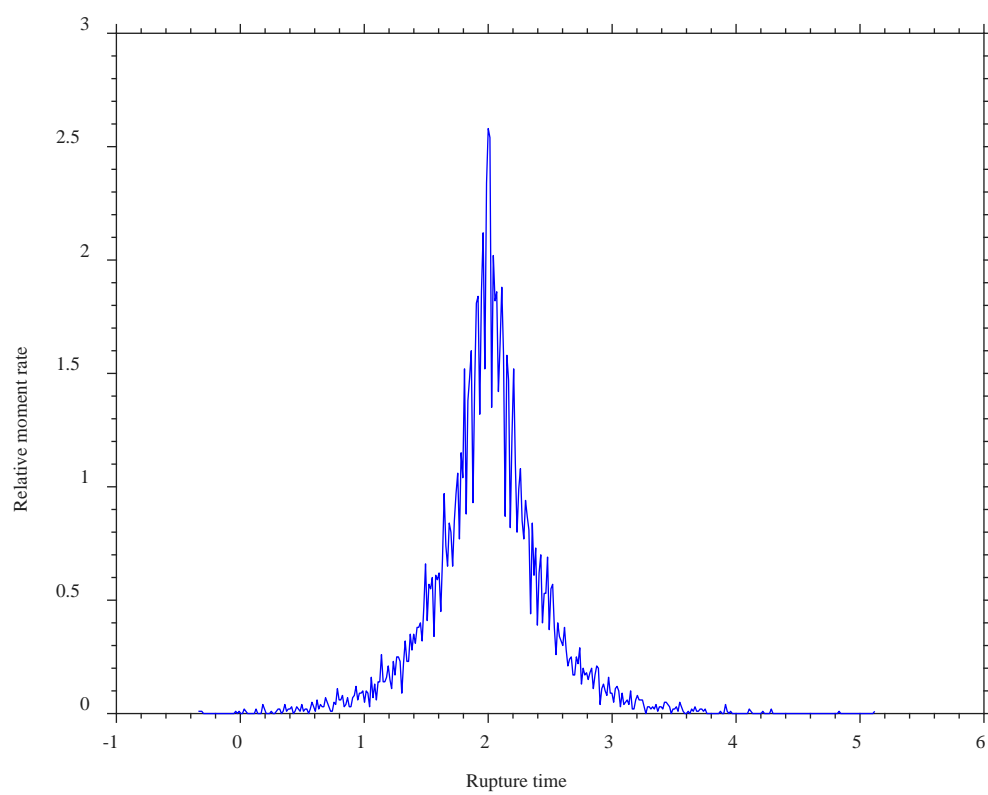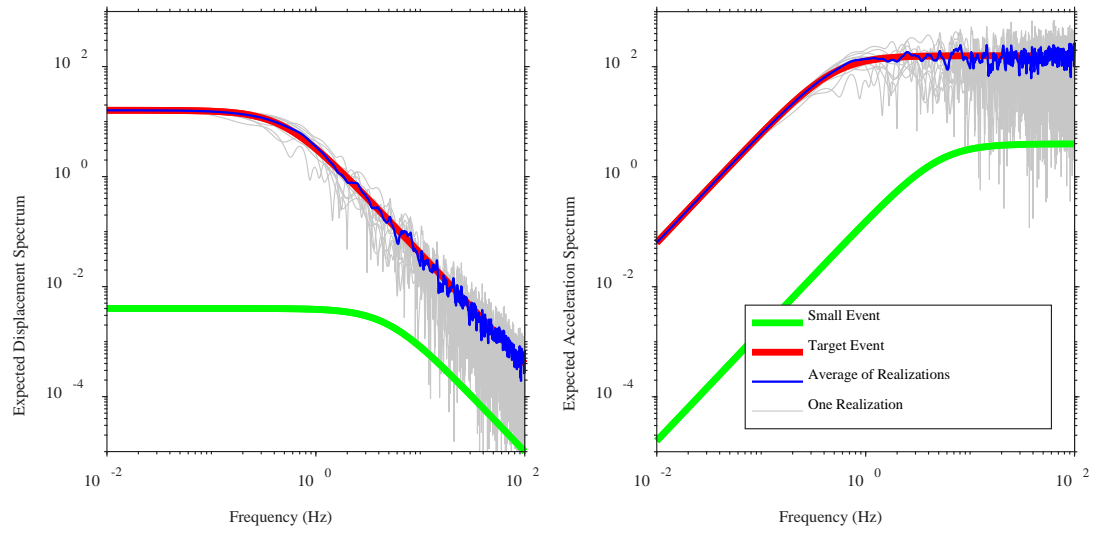
$$M_t = 1$$
$$M_s = 0.001$$
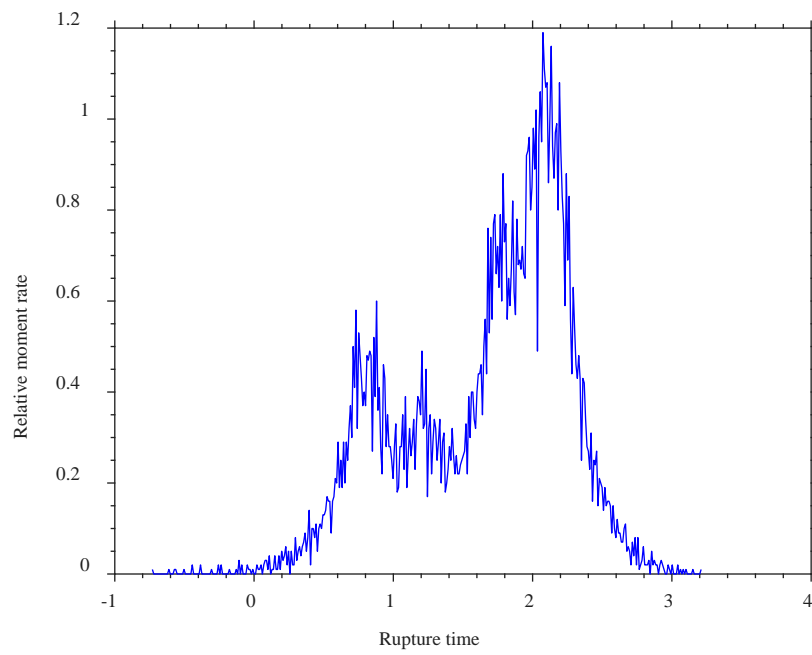$$f_{ct} = 1$$
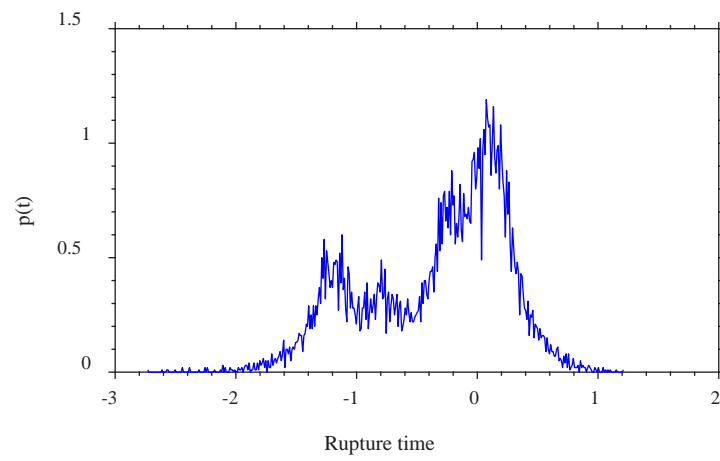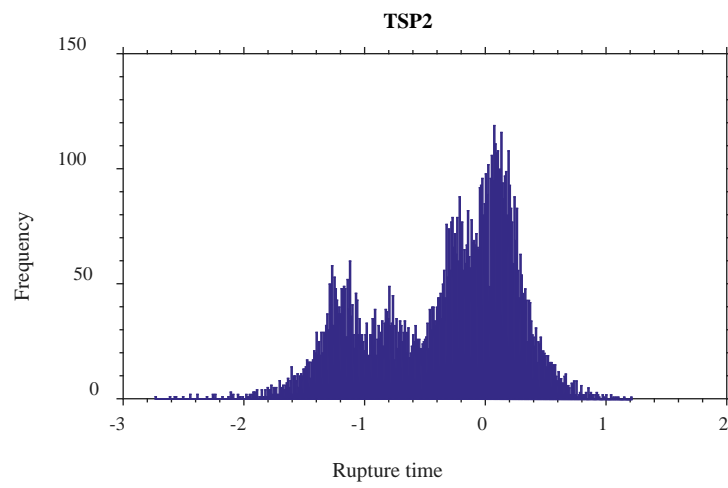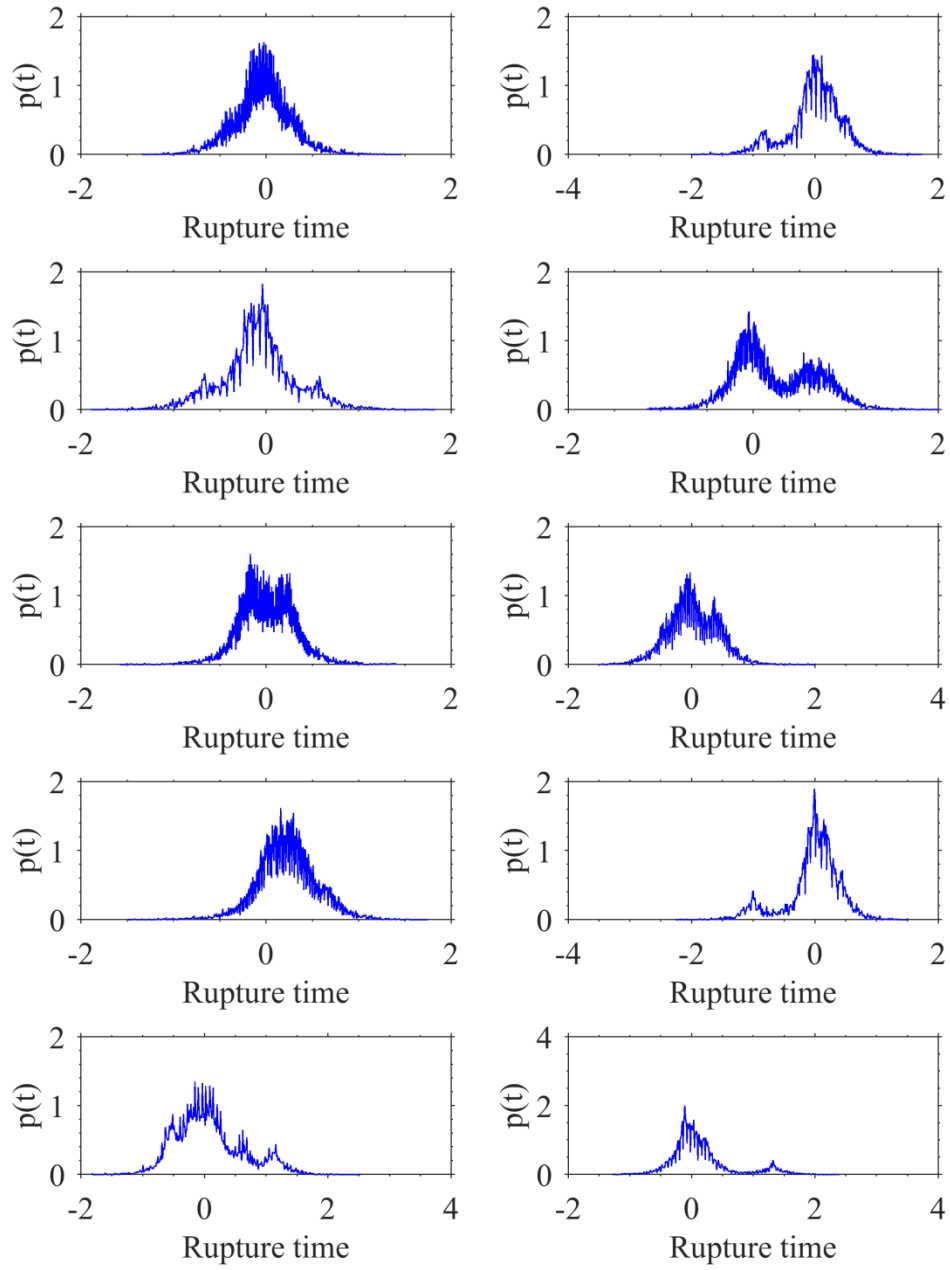$$f_{cs} = 10$$

TPS1

TSP1

266

TSP2

10 different generated delay times using the TSP2 method for example 3

Appendix B. List of Publications Resulted for This Research

Refereed Publications

Tavakoli, B., F. Sedaghati, and S. Pezeshk (2018). "An analytical effective point-souce based distance-conversion approach to mimic the effects of extended faults on seismic hazard assessment." *Bulletin of the Seismological Society of America*; 108(2): 742–760.

Nazemi, N., S. Pezeshk, and Farhad Sedaghati. (2017). "Attenuation of Lg waves in the New Madrid seismic zone of the central United States using the coda normalization method." *Tectonophysics* 08/2017; 712:623-633., DOI:10.1016/j.tecto.2017.06.026.

Sedaghati, F., S. Pezeshk, and N. Nazemi. (2018). "Site amplification within the Mississippi embayment of the central United States: Investigation of possible differences among various phases of seismic waves and presence of basin waves." *Soil Dynamics and Earthquake Engineering*, 04, DOI:10.1016/j.soildyn.2018.04.017.

Pezeshk, S., F. Sedaghati, and N. Nazemi. (2018). "Near Source Attenuation of High Frequency Body Waves beneath the New Madrid Seismic Zone." *Journal of Seismology*, **03**; 22(2), pp. 455–470, DOI:10.1007/s10950-017-9717-6.

Conference Publications

Nazemi, N., S. Pezeshk, F. Sedaghati (2017). "Attenuation of Lg Waves in the Central United States Using Coda Normalization Method"- Earthquake Engineering Research Institute, *EERI 69th meeting*, March 7-10, 2017

Pezeshk, S., A. Haji-Soltani, and A. Zandieh (2017). "Hybrid Empirical Ground-Motion Prediction Equations for the Gulf Coast Region." *Seismological Society of America Annual Meeting*, April 18–20, Denver, CO.

Haji-Soltani, A., and S. Pezeshk (2017). "Relationships Among Various Definitions of Horizontal Spectral Accelerations in Central and Eastern North America." *Seismological Society of America Annual Meeting*, April 18–20, Denver, CO.

Nazemi, N., F. Sedaghati, and S. Pezeshk (2017). "Separation of Intrinsic and Scattering Attenuation in the New Madrid Seismic Zone." *Seismological Society of America Annual Meeting*, April 18–20, Denver, CO.

Nazemi, N., S. Pezeshk, F. Sedaghati (2017). "Attenuation of Lg waves in the New Madrid Seismic Zone using Coda Normalization Method." *Seismological Society of America Annual Meeting*, April 18–20, Denver, CO.

Nazemi, N., S. Pezeshk, F. Sedaghati (2017). "Attenuation of Lg waves in the New Madrid Seismic Zone." *Seismological Society of America Annual Meeting*, April 18–20, Denver, CO.

Sedaghati, F., and S. Pezeshk (2016). "Investigation of Regional Differences in Strong Ground Motions for the Iranian Plateau," *18th International Conference on Earthquake Engineering and Seismology*, San Francisco, CA.

Sedaghati, F., and S. Pezeshk. (2016). "Investigation of the Path Effect Term in the New Madrid Seismic Zone." *Seismological Society of America*, April 20–22, Reno, NV.

Nazemi, N., S. Pezeshk, F. Sedaghati (2016). "Frequency Dependent Quality Factor of L*g* Waves for the Central United States Using Coda Normalization Method." *Eastern Section of Seismological Society of America Annual Meeting*, October 24–26, Reston, Virginia.

Sedaghati, F., and S. Pezeshk (2016). "Attenuation of High Frequency Body Waves in the New Madrid Seismic Zone." *Eastern Section of Seismological Society of America Annual Meeting*, October 24–26, Reston, Virginia.

Sedaghati, F., and S. Pezeshk. (2015). "Coda quality in the New Madrid seismic zone." *Seismological Society of America Eastern Section*, October 4-6, Memphis, TN.